NASA/TM-2003-211621/Rev4-Vol.VI

Ocean Optics Protocols For Satellite Ocean Color Sensor Validation, Revision 4, Volume VI: Special Topics in Ocean Optics Protocols and Appendices

James L. Mueller, Giulietta S. Fargion and Charles R. McClain, Editors

J. L. Mueller, D. K. Clark, V. S. Kuwahara, G. Lazin, S.W. Brown, G. S. Fargion, M. A. Yarbrough, M. Feinholz, S. Flora, W. Broenkow, Y. S. Kim, B. C. Johnson, M. Yuen, P. G. Strutton, T. D. Dickey, M. R. Abbott, R. M. Letelier, M. R. Lewis, S. McLean, F. P. Chavez, A. Barnard, J. R. Morrison, A. Subramaniam, D. Manov, X. Zheng, L. W. Harding, Jr., R. A. Barnes, and K. R. Lykke, Authors.

National Aeronautical and
Space administration

Goddard Space Flight Space Center
Greenbelt, Maryland 20771

April 2003

NASA/TM-2003-211621/Rev4-Vol.VI

Ocean Optics Protocols For Satellite Ocean Color Sensor Validation, Revision 4, Volume V: Special Topics in Ocean Optics Protocols and Appendices

J. L. Mueller
CHORS, San Diego State University, San Diego, California
Giulietta S. Fargion
Science ApplicationsInternational Corp., Beltsville, Maryland
Charles R. McClain
NASA Goddard Space Flight Center, Greenbelt, Maryland
Dennis K. Clark and Marilyn Yuen
NOAA National Environmental Satellite Data Information Service, Suitland, Maryland
Victor S. Kuwahara, Peter G. Strutton and Francisco P. Chavez
Monterey Bay Aquarium Research Institute, Moss Landing, California
Gordina Lazin, Scott McLean and Marlon R. Lewis
Satlantic Inc., Halifax, Nova Scotia, Canada
Steven W. Brown, B. Carol Johnson and Keith R. Lykke
National Institute of Standards and Technology, Gaithersburg, Maryland
Mark A. Yarbrough, Mike Feinholz, Stephanie Flora and William Broenkow
Moss Landing Marine Laboratory, California
Yong Sung Kim
Data Systems Technologies, Inc., Rockville, Maryland
Tommy D. Dickey, Derek Manov and Xiaobing Zheng
Ocean Physics Lab., University of California, Santa Barbara, California
Mark R. Abbott and Ricardo M. Letelier
College of Oceanic and Atmospheric Sciences, Oregon State University, Corvallis, Oregon
Andrew Barnard
Bigelow Laboratory for Ocean Sciences, W. Boothbay Harbor, Maine
J. Ruairidh Morrison
Woods Hole Oceanographic Institution, Woods Hole, Massachusetts
Ajit Subramaniam
University of Maryland, College Park, Maryland
Lawrence W. Harding, Jr.
University of Maryland Center for Environmental Science, Maryland
Robert A. Barnes
Science ApplicationsInternational Corp., Beltsville, Maryland

National Aeronautical and
Space administration
Goddard Space Flight Space Center
Greenbelt, Maryland 20771

April 2003

Preface

This document stipulates protocols for measuring bio-optical and radiometric data for the Sensor Intercomparison and Merger for Biological and Interdisciplinary Oceanic Studies (SIMBIOS) Project activities and algorithm development. The document is organized into 6 separate volumes as:

Ocean Optics Protocols for Satellite Ocean Color Sensor Validation, Revision 4

Volume I: Introduction, Background and Conventions
Volume II: Instrument Specifications, Characterization and Calibration
Volume III: Radiometric Measurements and Data Analysis Methods
Volume IV: Inherent Optical Properties: Instruments, Characterization, Field Measurements and Data Analysis Protocols
Volume V: Biogeochemical and Bio-Optical Measurements and Data Analysis Methods
Volume VI: Special Topics in Ocean Optics Protocols and Appendices

The earlier version of *Ocean Optics Protocols for Satellite Ocean Color Sensor Validation*, *Revision 3* (Mueller and Fargion 2002, Volumes 1 and 2) is entirely superseded by the seven Volumes of Revision 4 listed above.

The new multi-volume format for publishing the ocean optics protocols is intended to allow timely future revisions to be made reflecting important evolution of instruments and methods in some areas, without reissuing the entire document. Over the years, as existing protocols were revised, or expanded for clarification, and new protocol topics were added, the ocean optics protocol document has grown from 45pp (Mueller and Austin 1992) to 308pp in Revision 3 (Mueller and Fargion 2002). This rate of growth continues in Revision 4. The writing and editorial tasks needed to publish each revised version of the protocol manual as a single document has become progressively more difficult as its size increases. Chapters that change but little, must nevertheless be rewritten for each revision to reflect relatively minor changes in, *e.g.*, cross-referencing and to maintain self-contained consistency in the protocol manual. More critically, as it grows bigger, the book becomes more difficult to use by its intended audience. A massive new protocol manual is difficult for a reader to peruse thoroughly enough to stay current with and apply important new material and revisions it may contain. Many people simply find it too time consuming to keep up with changing protocols presented in this format - which may explain why some relatively recent technical reports and journal articles cite Mueller and Austin (1995), rather than the then current, more correct protocol document. It is hoped that the new format will improve community access to current protocols by stabilizing those volumes and chapters that do not change significantly over periods of several years, and introducing most new major revisions as new chapters to be added to an existing volume without revision of its previous contents.

The relationships between the Revision 4 chapters of each protocol volume and those of Revision 3 (Mueller and Fargion 2002), and the topics new chapters, are briefly summarized below:

Volume I: This volume covers perspectives on ocean color research and validation (Chapter 1), fundamental definitions, terminology, relationships and conventions used throughout the protocol document (Chapter 2), requirements for specific *in situ* observations (Chapter 3), and general protocols for field measurements, metadata, logbooks, sampling strategies, and data archival (Chapter 4). Chapters 1, 2 and 3 of Volume I correspond directly to Chapters 1, 2 and 3 of Revision 3 with no substantive changes. Two new variables, Particulate Organic Carbon (POC) and Particle Size Distribution (PSD) have been added to Tables 3.1 and 3.2 and the related discussion in Section 3.4; protocols covering these measurements will be added in a subsequent revision to Volume V (see below). Chapter 4 of Volume I combines material from Chapter 9 of Revision 3 with a brief summary of SeaBASS policy and archival requirements (detailed SeaBASS information in Chapter 18 and Appendix B of Revision 3 has been separated from the optics protocols).

Volume II: The chapters of this volume review instrument performance characteristics required for *in situ* observations to support validation (Chapter 1), detailed instrument specifications and underlying rationale (Chapter 2) and protocols for instrument calibration and characterization standards and methods (Chapters 3 through 5). Chapters 1 through 5 of Volume II correspond directly to Revision 3 chapters 4 through 8, respectively, with only minor modifications.

Volume III: The chapters of this volume briefly review methods used in the field to make the *in situ* radiometric measurements for ocean color validation, together with methods of analyzing the data (Chapter 1), detailed measurement and data analysis protocols for in-water radiometric profiles (Chapter 2), above water measurements of remote sensing reflectance (Chapter III-3), determinations of exact normalized water-leaving radiance (Chapter 4), and atmospheric radiometric measurements to determine aerosol optical thickness and sky radiance distributions (Chapter 5). Chapter 1 is adapted from relevant portions of Chapter 9 in Revision 3. Chapter 2 of Volume III corresponds to Chapter 10 of Revision 3, and Chapters 3 through 5 to Revision 3 Chapters 12 through 14, respectively. Aside from reorganization, there are no changes in the protocols presented in this volume.

Volume IV: This volume includes a chapter reviewing the scope of inherent optical properties (IOP) measurements (Chapter 1), followed by 4 chapters giving detailed calibration, measurement and analysis protocols for the beam attenuation coefficient (Chapter 2), the volume absorption coefficient measured *in situ* (Chapter 3), laboratory measurements of the volume absorption coefficients from discrete filtered seawater samples (Chapter 4), and *in situ* measurements of the volume scattering function, including determinations of the backscattering coefficient (Chapter 5). Chapter 4 of Volume IV is a slightly revised version of Chapter 15 in Revision 3, while the remaining chapters of this volume are entirely new contributions to the ocean optics protocols. These new chapters may be significantly revised in the future, given the rapidly developing state-of-the-art in IOP measurement instruments and methods.

Volume V: The overview chapter (Chapter 1) briefly reviews biogeochemical and bio-optical measurements, and points to literature covering methods for measuring these variables; some of the material in this overview is drawn from Chapter 9 of Revision 3. Detailed protocols for HPLC measurement of phytoplankton pigment concentrations are given in Chapter 2, which differs from Chapter 16 of Revision 3 only by its specification of a new solvent program. Chapter 3 gives protocols for Fluorometric measurement of chlorophyll *a* concentration, and is not significantly changed from Chapter 17of Revision 3. New chapters covering protocols for measuring, Phycoerythrin concentrations, Particle Size Distribution (PSD) and Particulate Organic Carbon (POC) concentrations are likely future additions to this volume.

Volume VI: This volume gathers chapters covering more specialized topics in the ocean optics protocols. Chapter 1 introduces these special topics in the context of the overall protocols. Chapter 2 is a reformatted, but otherwise unchanged, version of Chapter 11 in Revision 3 describing specialized protocols used for radiometric measurements associated with the Marine Optical Buoy (MOBY) ocean color vicarious calibration observatory. The remaining chapters are new in Revision 4 and cover protocols for radiometric and bio-optical measurements from moored and drifting buoys (Chapter 3), ocean color measurements from aircraft (Chapter 4), and methods and results using LASER sources for stray-light characterization and correction of the MOBY spectrographs (Chapter 5). In the next few years, it is likely that most new additions to the protocols will appear as chapters added to this volume.

Volume VI also collects appendices of useful information. Appendix A is an updated version of Appendix A in Revision 3 summarizing characteristics of past, present and future satellite ocean color missions. Appendix B is the List of Acronyms used in the report and is an updated version of Appenix C in Revision 3. Similarly, Appendix C, the list of Frequently Used Symbols, is an updated version of Appendix D from Rev. 3. The SeaBASS file format information given in Appendix B of Revision 3 has been removed from the protocols and is promulgated separately by the SIMBIOS Project.

In the Revision 4 multi-volume format of the ocean optics protocols, Volumes I, II and III are unlikely to require significant changes for several years. The chapters of Volume IV may require near term revisions to reflect the rapidly evolving state-of-the-art in measurements of inherent optical properties, particularly concerning instruments and methods for measuring the Volume Scattering Function of seawater. It is anticipated that new chapters will be also be added to Volumes V and VI in Revision 5 (2003).

This technical report is not meant as a substitute for scientific literature. Instead, it will provide a ready and responsive vehicle for the multitude of technical reports issued by an operational Project. The contributions are published as submitted, after only minor editing to correct obvious grammatical or clerical errors.

Table of Contents

Chapter 1

Introduction to Special Topics in Ocean Optics for Ocean Color Sensor Validation

James L. Mueller

Center for Hydro-Optics and Remote Sensing, San Diego State University, California

The overall purpose of the ocean optics protocols document is to provide the ocean color community with guidance for acquiring *in situ* data needed to develop algorithms and validate the performance of, and biogeochemical data sets derived from, satellite ocean color sensors. The first five volumes of this document first identify necessary and desired oceanic and atmospheric variables and appropriate instruments to measure them. Methods for characterizing and calibrating those instruments are covered next. Finally, detailed methods are described for measuring each category of variables at sea, and for processing and analyzing the data, to derive the essential information needed for all aspects of satellite ocean color validation.

The present volume provides a vehicle for describing important elements of the *in situ* ocean color validation process and infrastructure that don't fit cleanly into the integrated "variable – instrument – calibration – measurement – analysis" structure of the topics presented other volumes. As presently envisioned, appropriate subjects for chapters in this volume fall into 3 categories described below.

Ocean observatories use moored buoys instrumented for radiometric, bio-optical and interdisciplinary time-series measurements, together with supporting programs of survey cruises and/or drifting buoy deployments, to determine time and space scales of biogeochemical and physical variability in selected regional sites. The scientific goal of such observatories may be narrowly focused on acquiring ocean radiometric and optical data for vicarious calibration of satellite ocean color sensors, e.g the MOBY observatory described in ***Chapter 2*** of this volume [carried over unchanged from Chapter 11 of Revision 3 to the protocols (Mueller and Fargion, 2002)]. On the other hand, an interdisciplinary ocean observatory can combine comprehensive *in situ* observations with satellite remotely sensed data to derive synergistic descriptions of regional oceanographic features and their evolution in space and time, and provide validation data as well. Applications of moored and drifting instrumented buoys in the second, more general oceanographic context combined with ocean color validation are described in ***Chapter 3*** of this volume.

Airborne ocean color measurements, strictly speaking, are *in situ* observations closely related to shipboard radiometry topics covered elsewhere in the document. However, methods of airborne ocean color measurement also have much in common with satellite ocean color radiometry itself, including atmospheric corrections, and the avoidance and correction of sun and sky glint effects. From that perspective, protocols covering the full breadth of (satellite or aircraft) ocean color remote sensing technology and algorithms are beyond the scope of *Ocean Optics Protocols for Satellite Ocean Color Sensor Validation.* Certain aspects of radiometric and other measurements from aircraft are, nevertheless, relevant and within the scope of this document. These aspects include measurements from low altitude, which are closely akin to shipboard above-water radiance measurements (Vol. III, Ch. 3). Also appropriate are airborne measurements from any altitude to determine spatial variability, at scales ranging from m to 10 Km, in ocean color as a means of relating, *e.g.* shipboard, *in situ* measurements at a single point to concurrent satellite ocean color observations; such "sub-pixel" to small-scale regional bio-optical variability characterizations, using aircraft along-track or image data, become especially critical in Case II waters (Vol. I, Ch. 4). ***Chapter 4*** of this document describes the methods used in one approach to ocean color measurements using relatively simple radiometers mounted on light aircraft flown at low altitude, to detemine water-leaving radiance, and from radiance "spectral curvature" parameters, *Chl* (chlorophyll a concentration). Other important aspects that could form the basis for future chapters in this topic area include using along-track, nadir-viewing, combined measurements of hyperspectral ocean color radiance and oceanographic LIDAR at low altitude (*e.g.* Hoge and Swift 1986a, 1986b), or hyperspectral ocean color images, measured at spatial resolutions ranging less than a few m to 10's of m using imaging sensors flown at higher higher altitudes (*e.g.* Carder *et al*. 2003; Dierssen *et al*. 2003), to determine spatial distributions of water-leaving radiance and derived bio-optical variables.

Recent progress toward developing new, or improved, protocols is another subject of chapters to be included in this volume. ***Chapter 5*** of the present volume, for example, describes in detail the method by which LASER sources of monochromatic radiance and irradiance are used to characterize the stray light responsivity spectrographs, with particular application to those used in the MOBY ocean color observatory (Chapter 2). The chapter concludes with a brief description of ongoing research to apply tunable diode sources (Chapter 5, Fig. 5.39 and related text) to affordably transfer and extend this stray-light characterization approach to other spectrographs, and possibly filter radiometers. One can envision a future ***special topics*** chapter reporting progress in this critical area of research radiometric characterization, followed eventually by a more distilled protocol in a future revision (or replacement) of Vol. II, Chaper 3. Other future ***special topic*** chapters in the ***recent progress*** category might review reseach results on new and improved methods and uncertainty budgets for instrument self-shading and platform shading – especially by buoys (Chapter 3) - corrections to in-water upwelled radiance measurements (*e.g.* Gordon 1985; Gordon and Ding 1992; Doyle and Zibordi 2002), or for extrapolating in-water upwelled radiance profiles to the sea surface to derive water-leaving radiance. Special topic chapters on these subjects would precede, and provide the background for, new protocol method descriptions in a subsequent revision of Vol. III, Chapter 2. Reviews of results and methods for merging *in situ* data and remotely sensed ocean color data to support extended biogeochemical data products and models – sometimes mentioned examples include suspended particulate organic matter and marine primary productivity - might also be appropriate new chapter subjects in the future.

REFERENCES

Carder, K.L., C.-C. Liu, Z.P Lee, D.C. English, J. Patten, F.R.Chen, amd J.E. Ivey, 2003: Illumination and turbidity effects on observing faceted bottom elements with uniform Lambertian albedos. *Limnol. Oceanogr*., **48(1, part 2):** 355-363.

Dierssen, H.M., R.C. Zimmerman, R.A. Leathers, T.V. Downes, and C.O. Davis, 2003. Ocean color remote sensing of seagrass and bathymetry in the Bahamas Banks by high-resolution airborne imagery. *Limnol. Oceanogr*., **48(1, part 2):** 444-455.

Doyle, J.P. and G. Zibordi, 2002. Optical propagation within a three-dimensional shadowed atmosphere-ocean field: application to large deployment structures. . *Appl. Op*t., **41(21):** 4283-4306.

Gordon, H. R., 1985. Ship perturbation of irradiance measurements at sea. l: Monte Carlo simulations. Appl. Opt. 24(23): 4172-4182.

Gordon, H.R. and K. Ding, 1992. Self-shading of in-water optical instruments. Limnol. Oceanogr., 37(3): 491-500.

Hoge, F.E. and R.N. Swift, 1986a. Active-passive airborne ocean color measurement. 1: Instrumentation.. *Appl. Opt.* **25(1):** 48-57.

Hoge, F.E. and R.N. Swift, 1986b. Active-passive airborne ocean color measurement. 2: applications. *Appl. Opt*., **25(1):** 48-57.

Mueller, J.L. and G.S. Fargion [Eds.], 2002: Ocean Optics Protocols for SeaWiFS Validation, Revision 3. *NASA Tech. Memo. 2002–210004*, NASA Goddard Space flight center, Greenbelt, Maryland, 308 pp.

Chapter 2

MOBY, A Radiometric Buoy for Performance Monitoring and Vicarious Calibration of Satellite Ocean Color Sensors: Measurement and Data Analysis Protocols

Dennis K. Clark[1], Mark A. Yarbrough[2], Mike Feinholz[2], Stephanie Flora[2], William Broenkow[2], Yong Sung Kim[3], B. Carol Johnson[4], Steven W. Brown[4], Marilyn Yuen[1], and James L. Mueller[5]

[1]*NOAA National Environmental Satellite Data Information Service, Suitland, Maryland*
[2]*Moss Landing Marine Laboratory, California*
[3]*Data Systems Technologies, Inc., Rockville, Maryland*
[4]*National Institute of Standards and Technology, Gaithersburg, Maryland*
[5]*Center for Hydro-Optics and Remote Sensing, San Diego State University, California*

2.1 INTRODUCTION

The Marine Optical Buoy (MOBY) (Clark *et al.* 1997) is the centerpiece of the primary ocean measurement site for calibration of satellite ocean color sensors based on independent *in situ* measurements. Since late 1996, the time series of normalized water-leaving radiances $L_{WN}(\lambda)$ determined from the array of radiometric sensors attached to MOBY are the primary basis for the on-orbit calibrations of the USA Sea-viewing Wide Field-of-view Sensor (SeaWiFS), the Japanese Ocean Color and Temperature Sensor (OCTS), the French Polarization Detection Environmental Radiometer (POLDER), the German Modular Optoelectronic Scanner on the Indian Research Satellite (IRS1-MOS), and the USA Moderate Resolution Imaging Spectrometer (MODIS). The MOBY vicarious calibration $L_{WN}(\lambda)$ reference is an essential element in the international effort to develop a global, multi-year time series of consistently calibrated ocean color products using data from a wide variety of independent satellite sensors.

A longstanding goal of the SeaWiFS and MODIS (Ocean) Science Teams is to determine satellite-derived $L_{WN}(\lambda)$ with a relative combined standard uncertainty[1] of 5 % (Vol. I, Chapter 1). Other satellite ocean color projects and the Sensor Intercomparison for Marine Biology and Interdisciplinary Oceanic Studies (SIMBIOS) project have also adopted this goal, at least implicitly. Because water-leaving radiance contributes at most 10 % of the total radiance measured by a satellite sensor above the atmosphere (Gordon 1997), a 5 % uncertainty in $L_{WN}(\lambda)$ implies a 0.5 % uncertainty in the above-atmosphere radiance measurements. This level of uncertainty can only be approached using "vicarious-calibration" approaches as described below. In practice, this means that the satellite radiance responsivity is adjusted to achieve the best agreement, in a least-squares sense, for the $L_{WN}(\lambda)$ results determined using the satellite and the independent optical sensors (*e.g.* MOBY). The end result of this approach is to implicitly absorb unquantified, but systematic, errors in the atmospheric correction, incident solar flux, and satellite sensor calibration into a single correction factor to produce consistency with the *in situ* data (see *e.g.* Gordon 1981, 1987, 1988).

Clearly, the combined standard uncertainty of the *in situ* $L_{WN}(\lambda)$ determinations must be less than 5 % if the stated uncertainty goal is to be approached. The uncertainty budget of MOBY $L_{WN}(\lambda)$ determinations may be divided into environmental and radiometric factors. Environmental factors include uncertainties due to radiance and irradiance fluctuations associated with surface waves and platform motions during the radiometric measurements, and with extrapolation of upwelling radiance measurements from depths of 1 m or more to, and through, the sea surface. The uncertainties associated with these ambient conditions have been shown to be less than, but approaching, 5 % for upwelled radiance (Siegel *et al.* , 1995; Hooker and Maritorena, 2000). Radiometric uncertainty components associated with instrument characterization, calibration and stability, *i.e.* the radiance

[1] All uncertainties in this document are standard uncertainties, unless noted otherwise. Standard uncertainty is the uncertainty of the result of a measurement expressed as a standard deviation (Taylor and Kuyatt 1994).

measurements *per se*, must be summed in quadrature to yield the combined standard uncertainty of the MOBY $L_{WN}(\lambda)$ determinations.

The estimated combined standard uncertainty of MOBY radiance measurements is between 4 % and 8 % (Clark *et al.* 2001). This estimate is based on uncertainties of MOBY calibrations at less than 3 %, changes in pre- and post-deployment calibrations ranging from 1 % to 6 %, radiometric stability tests during deployments using internal reference sources that show changes less than 1 %, and diver-deployed external reference lamp responses that are stable within less than 3 % (the estimated uncertainty of the method) (Clark *et al.* 2001). The 8 % upper limit on the combined standard uncertainty estimate does not include preliminary results of recently undertaken stray light characterization of the MOBY spectrographs, which indicate systematic stray light offsets in $L_{WN}(\lambda)$ may have approximate magnitudes of +5 % and -3 % at blue and green wavelengths respectively (Sects. 2.4 and 2.8 below, and Clark *et al.* 2001). Once the stray light characterization is completed on all MOBY spectrographs, the entire MOBY $L_{WN}(\lambda)$ time series will be reprocessed with an expected combined standard uncertainty of less than 5 %. Variations in the measurement environment may add additional uncertainty.

The nature of, and data requirements for, vicarious calibration of a satellite ocean color sensor are briefly described in Vol. I, Chapter 1 (Sect. 1.5), and in more detail by Gordon (1981, 1987, 1988, 1997), Gordon *et al.* (1983), Evans and Gordon (1994), and Clark *et al.* (1997). A critical element of the procedure is the ability to monitor a satellite sensor's performance at daily to weekly intervals by comparing its derived $L_{WN}(\lambda)$ with concurrently derived *in situ* $L_{WN}(\lambda)$ meeting the uncertainty criteria described above. The most direct way of measuring $L_{WN}(\lambda)$ on a continuing daily basis over periods of several years is to utilize a specially designed array of radiometers mounted on a moored buoy. This buoy must be designed to mount the optical collectors well away from platform shading and reflections, artifacts similar to ship shadow, as discussed in Vol. III, Chapter 2 (Sect. 2.2). To minimize uncertainties due to extrapolation of upwelling radiance $L_u(z,\lambda)$ to the sea surface, the buoy must be moored at a location with consistently transparent case 1 waters and with negligible mesoscale to sub-mesoscale spatial variability. To assure frequent occurrences of matched satellite and buoy measurements, the site must be cloud free throughout most of the year. The mooring must be located close to an island based sun photometer and sky radiance sensor to allow concurrent determinations of aerosol optical thickness and sky radiance distribution. On the other hand, the atmospheric conditions at the mooring location must not be significantly influenced by the island's wake. Extraordinary calibration maintenance procedures are needed to assure low uncertainties in the buoy's radiometric measurements. In addition, comparative shipboard measurements must be made near the buoy to check the radiometric stability of its instrumentation, to determine spatial variability surrounding the buoy location, and to develop and validate bio-optical algorithms. Some of these measurements can be made during cruises staged to replace the mooring at 3 to 4 month intervals, but dedicated cruises of 1 to 2 week duration are also required. The logistical demands of buoy maintenance, calibration activities, deployment and relief, and ship support operations strongly argue for placing the buoy conveniently near a permanent support facility. The locations of the MOBY mooring, near the island of Lanai, and the associated support facilities in Honolulu, Hawaii closely satisfy all of the above conditions.

The radiometric measurements at a primary reference site for vicarious calibration of satellite ocean color sensors differ in several aspects from the radiometric in-water profiling methods described in the Vol. III, Chapter 2. A primary reference data set must consist of *in situ* determinations of band-averaged $L_{WN}(\lambda)$'s that reproduce the spectral response functions of each satellite sensor's bands with more accuracy than can be realized using off the shelf radiometers. The need for flexibility in the choice of spectral response weighting functions used to determine band-averaged $L_{WN}(\lambda)$ imposes a requirement for full-spectrum measurements with resolutions <1 nm. Instead of measuring radiometric profiles resolved at several samples per m (Vol. III, Chapter 2, Sect. 2.2), downwelling irradiance $E_d(z,\lambda)$ and upwelling radiance $L_u(z,\lambda)$ can be measured on a buoy at only a few fixed depths, which complicates the problem of accurately determining $L_u(0^-,\lambda)$ (just below the sea surface).

To be affordable, a moored array must typically be deployed and operated semi-autonomously for periods of 3 to 4 months. Provisions to assure radiometric stability through these extended period operations should include, as a minimum, pre- and post-deployment calibrations of all radiometers, combined with continuous monitoring of on-board light sources of known stability. Moreover, instruments suspended in seawater for periods of this duration experience fouling by biological organisms that, if not countered effectively using antifouling methods and frequent cleaning by divers, seriously degrade the performance of optical sensors. Affordable servicing and maintenance

during each deployment is limited to *circa* monthly visits by divers to clean instruments, check sensor calibrations against portable underwater lamp sources, and perform minimal maintenance.

Because of these uniquely different measurement requirements, platform related geometry, instrument characteristics, and operational conditions, the protocols applying to the MOBY instruments and methods of measurement and data analysis are presented separately in the present chapter. Where appropriate, certain protocols will be defined and described by reference to other chapters. This chapter documents the protocols used by the MOBY Operations Team to measure and derive the MOBY data sets that consist of the $L_{WN}(\lambda)$ time series. The information is intended as background for those wishing to apply this data to validate water-leaving radiances from one or more satellite ocean color sensors.

2.2 THE MOBY PRIMARY VICARIOUS CALIBRATION SITE

The primary components of the MOBY vicarious calibration site are located as shown in Fig. 2.1. A MOBY is continuously moored approximately 20 km west of the island of Lanai in 1200 m of water. During prevailing trade wind conditions, this location is sheltered in the lee of the island, yet it is far enough offshore to minimize atmospheric perturbations associated with the island's wake. CIMEL[2] sun photometers on Lanai and Oahu, operated by the Aerosol Robotic Network (AERONET) Project (Vol. II, Chapter 4 and Vol. III, Chapter 5), provide time series measurements of aerosol optical thickness and sky radiance distributions that are required to reduce the uncertainty budgets of atmospheric correction models used during vicarious calibration analyses. The MOBY Operation Site, located at the University of Hawaii (UH) Marine Facility in Honolulu, is staffed full time by personnel from the Moss Landing Marine Laboratory (MLML) for buoy maintenance, instrument maintenance and calibration, and for staging buoy relief and bio-optical sampling cruises. The UH's research vessels are used for cruises to support buoy deployments (L-series cruises identified in Table 2.1), Marine Optical Characterization Experiments (MOCE-series), and interim maintenance and quality control operations. During the MOCE and some L-series cruises (Table 2.1), *in situ* bio-optical measurements are made to validate MOBY $L_{WN}(\lambda)$ determinations, to characterize spatial variability near the mooring, and to develop and validate bio-optical algorithms. A subset of the MOBY data is transmitted, in real time via cellular telephone, to the MLML in California. The MOBY data are processed at MLML to produce and extract appropriately weighted band-averaged $L_{WN}(\lambda)$'s for SIMBIOS and SeaWiFS Project Offices at the National Aeronautics and Space Administration (NASA) Goddard Space Flight Center (GSFC), and/or to the MODIS Team at the University of Miami.

MOBY and the Marine Optical System (MOS)

MOBY is a 12 m spar buoy (including the lower instrument bay) uniquely designed as an optical bench for measurements of $E_d(z,\lambda)$ and $L_u(z,\lambda)$ at depths of 1 m, 5 m, 9 m, and 12 m (Fig. 2.2). The features of MOBY are summarized in Table 2.2. Fig. 2.3 is a schematic illustration of the MOBY system's sensors, operations and communications, while the mechanical layouts of the upper and lower instrument bays are illustrated in Fig. 2.4 and Fig. 2.5, respectively. The MOBY spar is tethered to a second surface buoy, which is slack moored, *i.e.* isolated by subsurface floats, to an anchor on the sea floor (Fig. 2.6). Sensors for wind speed, wind direction, air temperature, relative humidity, and barometric pressure are mounted on the main mooring buoy.

The Marine Optical System (MOS), the heart of MOBY, consists of two single-grating CCD spectrographs connected via an optical multiplexer and fiber optic cables to the $E_d(z,\lambda)$ and $L_u(z,\lambda)$ optical heads mounted at the ends of the buoy's 3 standoff arms (Fig. 2.2 and Fig. 2.3). To provide low-loss transmission at ultraviolet wavelengths, 1 mm diameter silica fiber-optic cables are used to connect the optical heads to MOS. $L_u(12,\lambda)$, at z = 12 m, is measured through a window in the bottom of the MOS housing itself. A seventh fiber optic cable connects a surface irradiance $E_S(\lambda)$ cosine collector, mounted at the top of the MOBY above-water mast, to the spectrographs. Each pair of in-water optical heads is mounted on a standoff arm to minimize radiometric artifacts due to shadows or

[2] Certain commercial equipment, instruments, or materials are identified in this document to foster understanding. Such identification does not imply recommendation or endorsement by the National Institute of Standards and Technology, nor does it imply that the materials or equipment identified are necessarily the best available for the purpose.

reflections from the buoy. To minimize self-shading by the $L_u(z,\lambda)$ radiometer (Vol. III, Chapter 2, Sect. 2.4; Gordon and Ding 1992), the underwater housings for the optical heads are very small in diameter (7 cm).

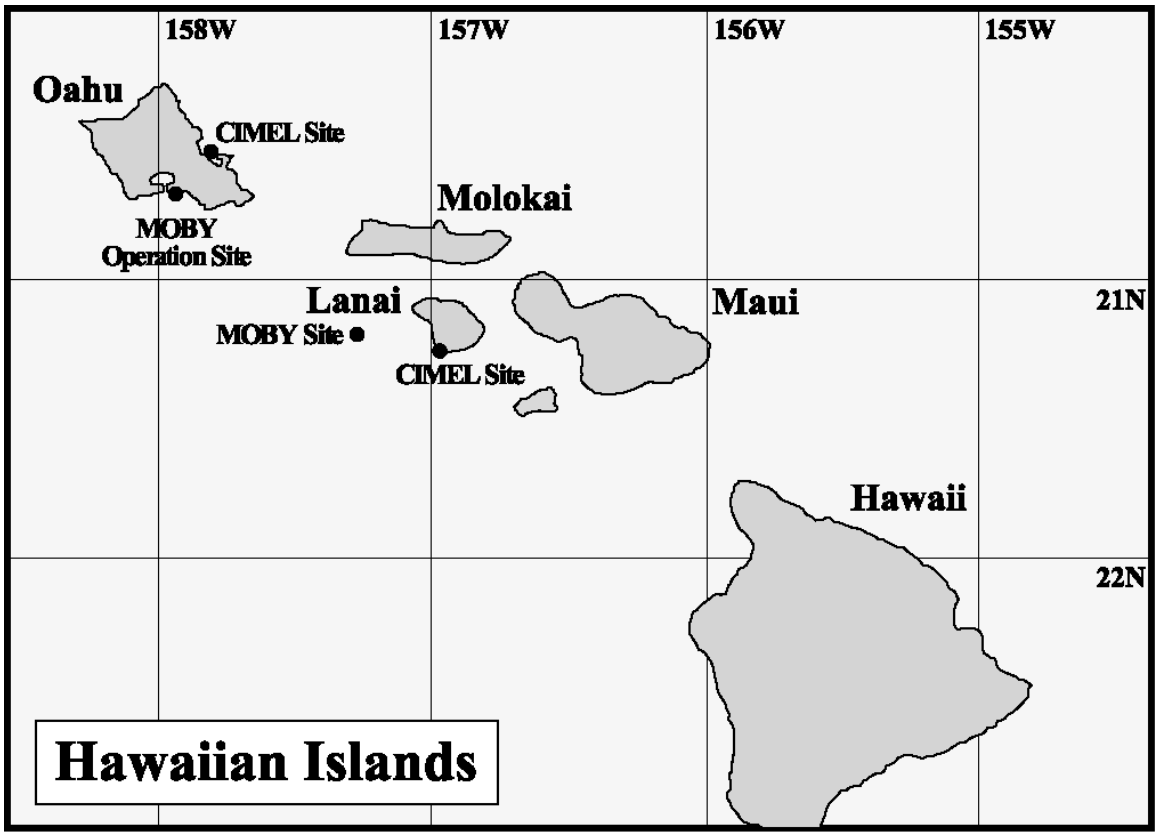

Figure 2.1: Chart showing locations of the MOBY mooring, the two CIMEL robotic sun photometers on Oahu and Lanai, cell phone relay stations used for data communications, and the MOBY Operations Site in Honolulu, Hawaii.

The principal characteristics of MOS are summarized in Table 2.3. The MOS system elements and optical layout are illustrated schematically in Fig. 2.7 and Fig. 2.8, respectively. Light from an $L_u(z,\lambda)$, $E_d(z,\lambda)$, or $E_s(\lambda)$ head enters the spectrograph package via its fiber optic cable and the multiplexer, is directed to a dichroic mirror that reflects light at wavelengths between 350 nm and 630 nm into one (blue) grating spectrograph, and transmits wavelengths greater than 630 nm to the other (red) spectrograph. The MOS spectrograph package is mounted in MOBY's lower instrument bay (Fig. 2.5), at a depth of approximately 12 m, primarily to isolate the package from the shock and vibration that surface waves inflict on the upper instrument bay. The deeper location also facilitates heat dissipation from the thermoelectric coolers used to maintain the operating temperature of the CCD arrays, and $L_u(12,\lambda)$ may be measured through the MOS optical window at the very bottom of the MOBY spar. Even more critically, the high current draw of the MOS requires that it be located close to the batteries, which themselves must be placed at the bottom of the spar to act as stabilizing ballast.

The elements defining the spectral radiometric characteristics of each of the spectrographs are the entrance slit, holographic grating, and cooled CCD detector array (Fig. 2.8). For the blue spectrograph (350 nm to 630 nm), the full-width at half-maximum (FWHM) bandpass of the spectral slit response function centered at any given wavelength is approximately 2 nm, and the 512 element detector array is designed to sample at approximately a 0.6 nm interval. The MOS was designed with such high spectral resolution to support vicarious calibrations of a variety of different satellite ocean color sensors (Appendix A). By measuring *in situ* spectra of $L_u(\lambda,z)$ at this

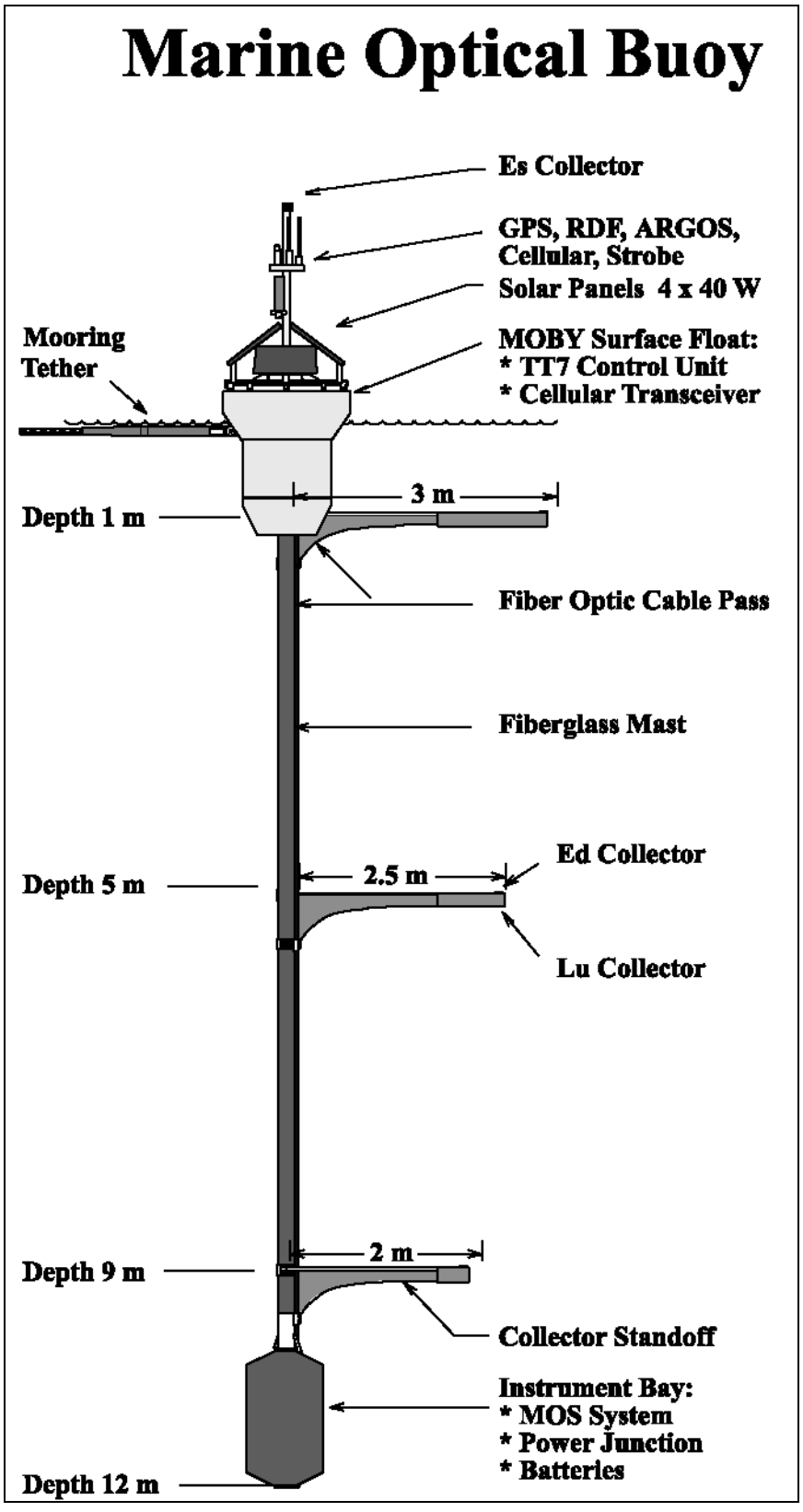

Figure 2.2: The Marine Optical Buoy (MOBY).

resolution, it is practical to compute band-averaged values of $L_{WN}(\lambda)$ that are appropriately weighted for any of these satellite ocean color sensors.

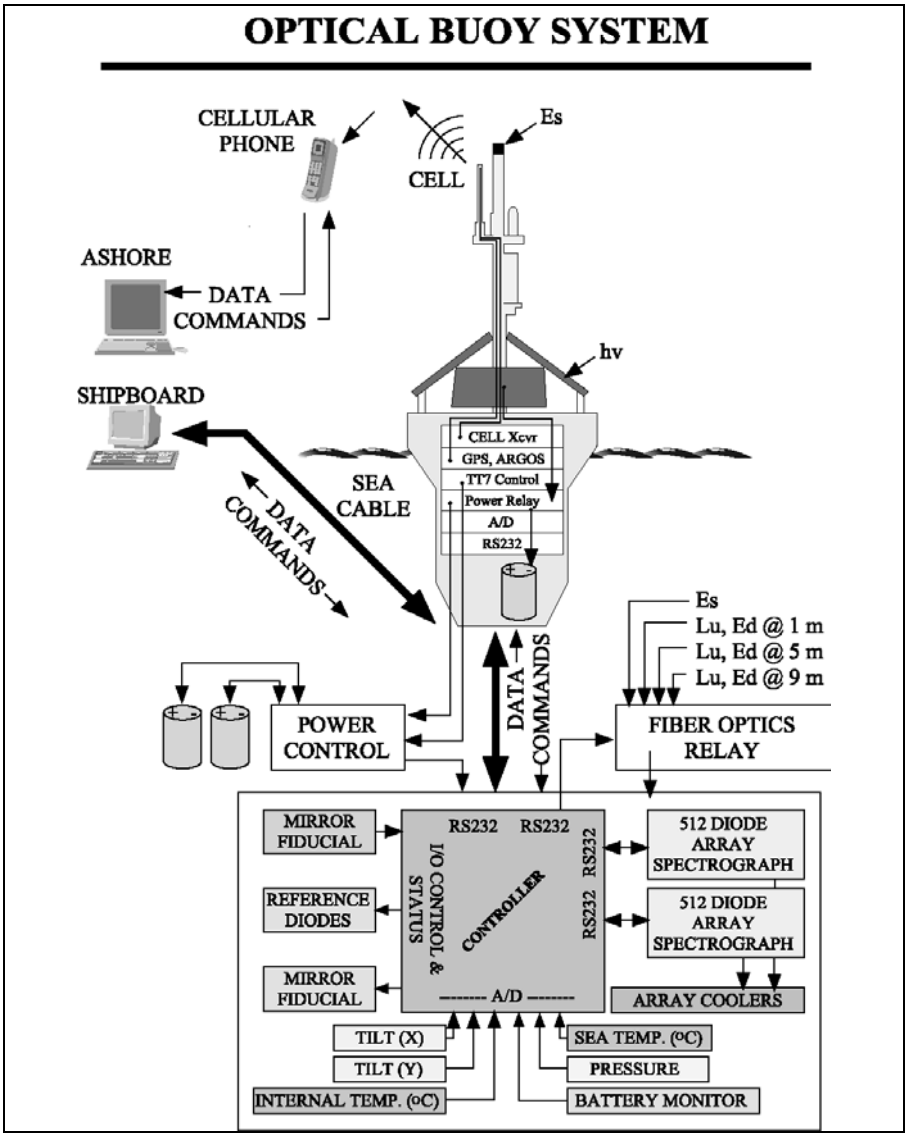

Figure 2.3: A schematic overview of the MOBY system elements.

Ancillary Measurements on MOBY

The principal navigation (latitude and longitude) and UTC (Universal Time, Coordinated) clock reference are determined from the Global Positioning System (GPS) receiver mounted in the MOBY upper instrument bay (Fig. 2.3 and Table 2.2). A secondary navigational position is provided by the System ARGOS transmitter, which is also installed in the upper bay (Fig. 2.3) and provides frequent MOBY position updates as a precaution against losing the buoy should the mooring fail. On two occasions, in fact, the MOBY array did break away from its moorings and was recovered safely thanks to the ARGOS tracking capability. Additional ancillary sensors are installed in the MOS package:

- Internal housing and CCD array temperatures are measured as indicators of performance quality, and may be used in applying radiometric calibration factors to the data.

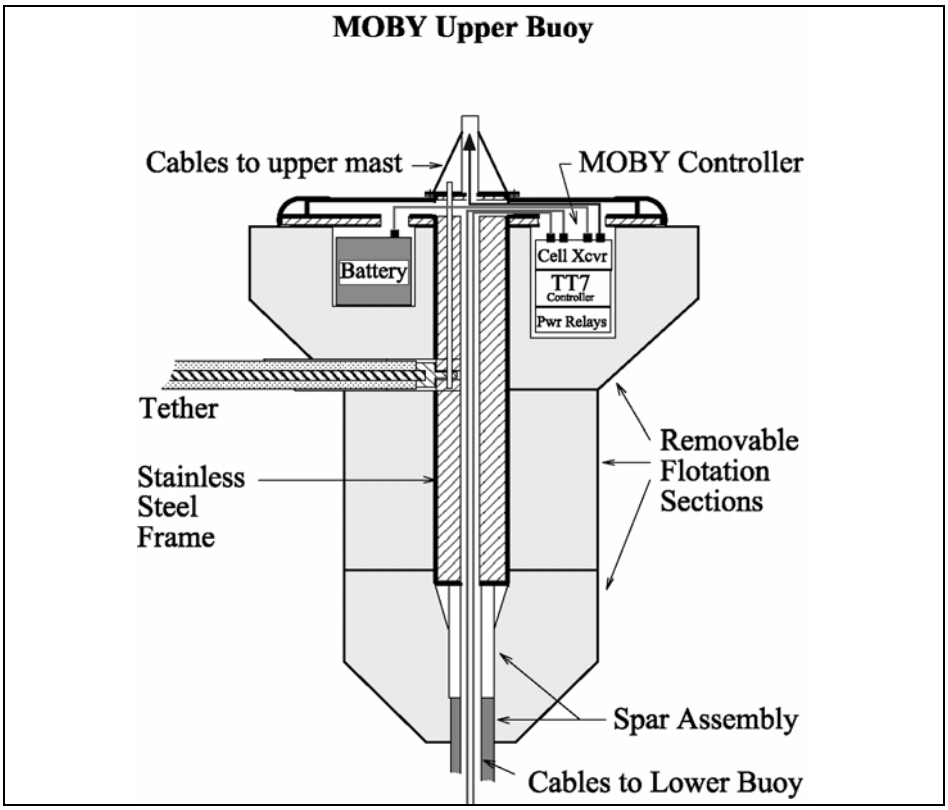

Figure 2.4: The MOBY flotation and upper instrument bay assembly.

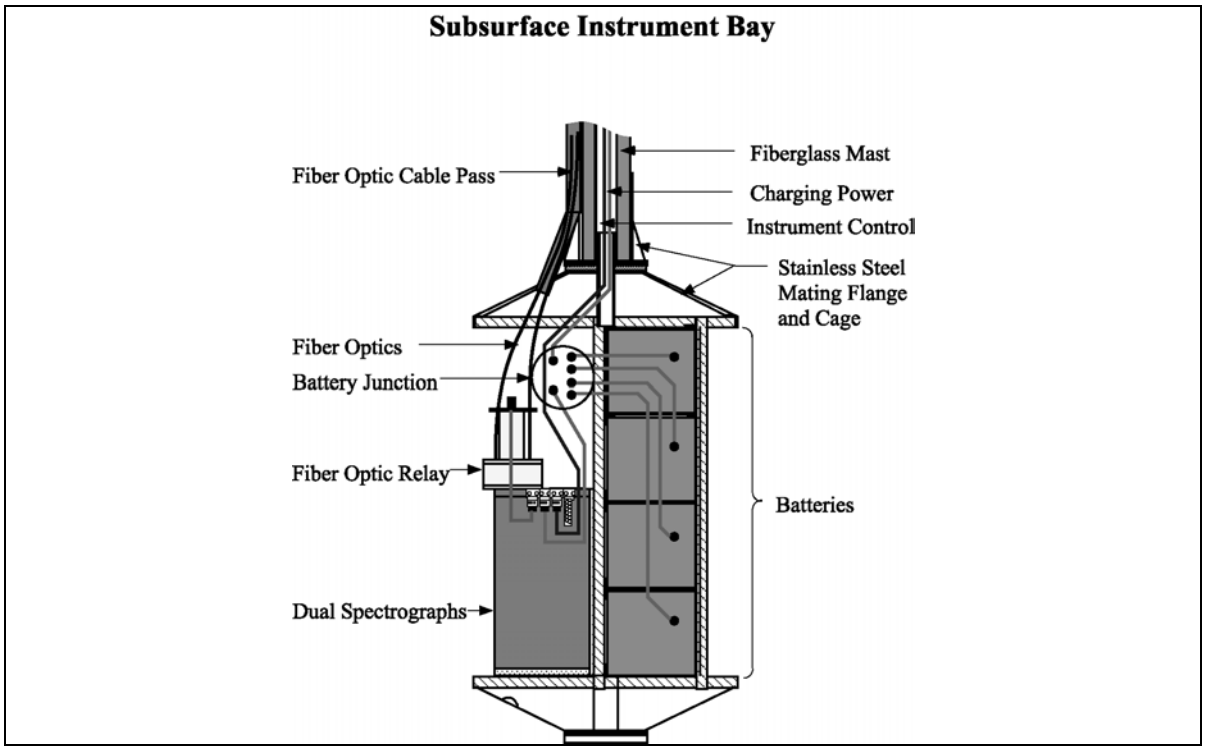

Figure 2.5: A schematic diagram illustrating the mechanical layout of the subsurface instrument and battery bay on MOBY.

- A high precision pressure transducer is installed on the top radiometric arm (Fig. 2.2) to determine depth variations [$z(t)$ - z_P] about its nominal reference depth z_P (fixed by its location on the spar) during each radiometric measurement sequence. A separate temperature sensor monitors the temperature of the pressure transducer, to minimize uncertainties in the depth determinations.
- Tilt sensors within the MOS package are used to determine the 2-axis orientation (pitch and yaw) of the MOBY spar relative to the local vertical. A flux gate compass, also installed within the MOS package, is used to determine the direction (magnetic) in which the radiometric sensor arms extend out from the spar. The relative angle between the spar pointing azimuth and the solar azimuth are used to detect measurement geometries in which the irradiance and radiance collectors may be influenced by shadows, or reflections, from the main MOBY structure.

Mooring Buoy Measurements

Sensors mounted on the mast of the mooring buoy measure wind velocity, surface barometric pressure, air temperature, and relative humidity (Fig. 2.6). Also, near surface sensors on this buoy measure water temperature and conductivity, and chlorophyll *a* fluorescence.

Data Communications

Data from the MOS and other sensors mounted on MOBY are assembled into data records, and annotated with time, latitude and longitude as based on GPS input, by the Tattletale[2] (Model TT7) microcomputer installed in the upper instrument bay (Table 2.2, Fig. 2.3 and Fig. 2.4). Data records are stored on hard disk for download when the MOBY is recovered and replaced at the end of a deployment. The microcomputer also transmits the data records over the cellular phone link to MLML in California. Normally, 99 % of the data are recovered via telemetry. Data from the meteorological sensors on the mooring buoy are similarly processed autonomously by a microcomputer. All data records are stored on hard disk and are downloaded once daily.

2.3 MOBY OPERATIONS AND MEASUREMENT METHODS

Deployment Schedule and Methods

There are two complete MOBY systems, one of which is moored and operational at any given time. The history of MOBY deployments, and key events associated with each, are summarized in Table 2.4. The typical duration of a single mooring deployment is between 3 and 4 months. During this period, the other MOBY is maintained and refurbished and its MOS recalibrated. At approximately monthly intervals during a deployment, the Operations Team visits the MOBY mooring site using a small boat launched from the island of Maui. During these interim visits, divers clean the optical collectors and use a specially designed underwater lamp reference source to check the radiometric stability of the deployed MOS (Sect. 2.4). During these "interim-servicing" cruises, water samples are filtered for phytoplankton pigment analyses, for comparison with pigment concentration determinations using the MOBY radiometric measurements. These pigment concentration comparisons are made to validate the pigment algorithms associated with the various satellite ocean color sensors.

When the time comes to exchange the MOBY systems, the replacement buoy is loaded aboard a research vessel and transported to the mooring site. On arriving at the site, the recalibrated and refurbished replacement MOBY is first deployed and set adrift (Fig. 2.9). Divers release the tether connecting the moored MOBY to the mooring buoy. The replacement buoy is then towed into position by the divers (operating from a support boat) and connected to the mooring. When possible, in-water radiometric measurements are made with both MOBY systems as a final check on the stability of the recovered system. Finally, the recovered MOBY is secured aboard the ship for its return to the MOBY Operations Site in Honolulu. The entire mooring (Fig. 2.6) is replaced at approximately 1-year intervals (Table 2.4). On these occasions, the acoustic release (Fig. 2.6) is activated to free the mooring line and its flotation from its anchor. A new anchor and surface mooring buoy are deployed, and a MOBY is tethered to it.

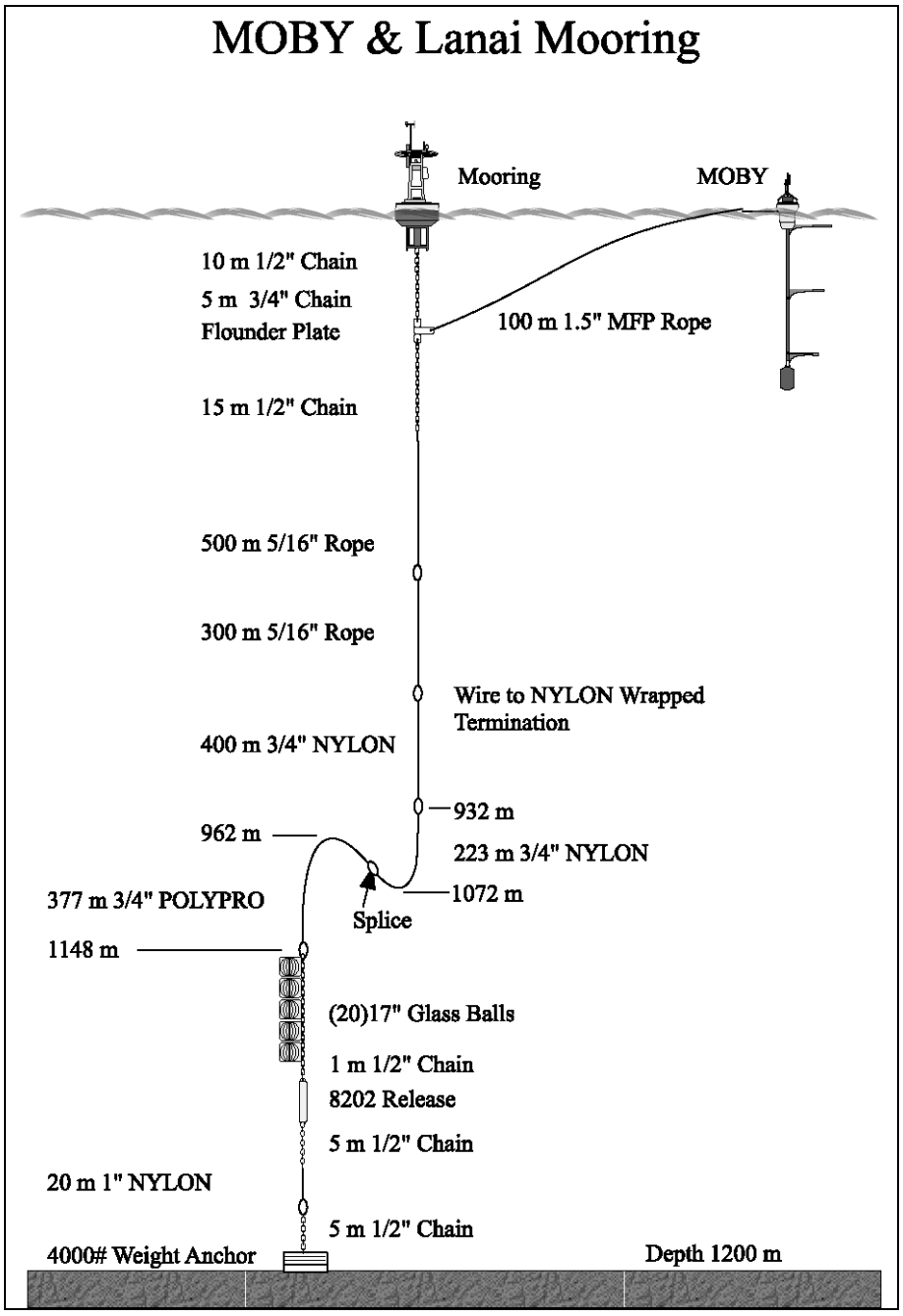

Figure 2.6: The MOBY mooring configuration.

MOCE and Other Validation Shipboard Operations

On some of the MOBY replacement cruises ("L-cruises" in Table 2.1), additional ship time is used to make "Required" and "Highly Desired" radiometric and bio-optical measurements (Vol. I, Chapter 3, Table 3.1), both for radiometric validation of the MOBY and satellite ocean color sensor measurements, and for algorithm development and validation.

Complementing the MOBY project are the MOCE cruises, which are carried out primarily to support vicarious calibration and validation of satellite ocean color sensors. The MOCE team is comprised of scientists from the

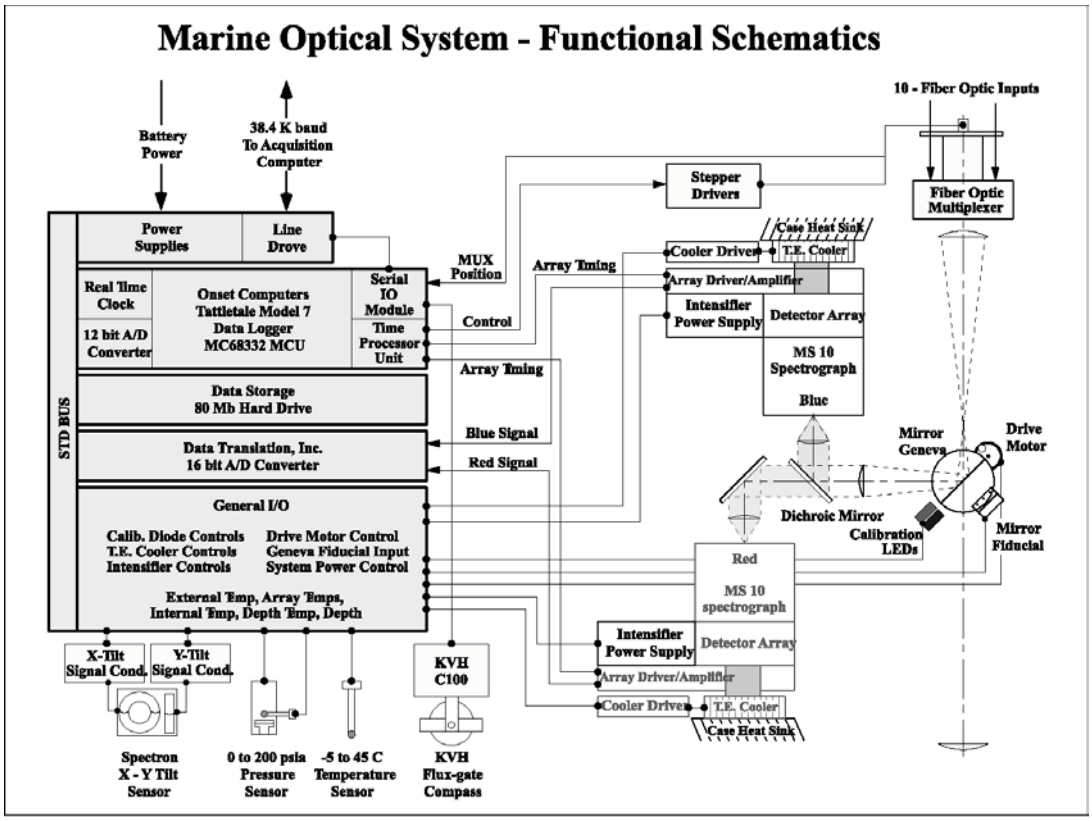

Figure 2.7: A schematic diagram of the MOS functional elements.

National Oceanic and Atmospheric Administration/National Environmental Satellite Data Information Service (NOAA/NESDIS), MLML, San Diego State University, and the University of Miami (Florida). MOCE cruises, which are typically between 10 and 30 days in duration, have been conducted in the general vicinity of the MOBY site and off the west coast of North America (Table 2.1).

Measurements acquired during the MOCE cruises are generally more extensive than those made during the "L-cruises". As an example, measurements made during MOCE-5 are listed in Table 2.5, which includes all of the "Required", nearly all of the "Highly Desired" and some of the "Specialized Measurements" categories of variables listed in Table 3.1 (Vol. I, Chapter 3). Protocols for most of these measurements and analyses conform to those described elsewhere in this document. However, protocols are not provided elsewhere for two of the specialized measurements listed in Table 2.5, "Instrument Self-Shading" and "Particle Size Distribution", nor are measurements of these variables identified in Vol. I, Chapter 3.

The effects of instrument self-shading on upwelling radiance and irradiance measurements are discussed briefly, and provisional protocols (based on Gordon and Ding 1992) for removing self-shading effects from measurements are described in Vol. III, Chapter 2 (Sect. 2.4). Direct measurements of the self-shading phenomenon are made during MOCE cruises (Table 2.5) to test the predictions of Gordon and Ding (1992) and determine relative uncertainties under a variety of ambient illumination conditions. A Fiber Optic Spectrometer (FOS) was developed using two modified American Holographic AH4000 series dual-beam spectrometers, one configured for radiometric measurements spanning the wavelength range from 375 nm to 725 nm at 5 nm resolution, and the other from 600 nm to 1100 nm at 10 nm resolution. The spectrometers are placed in a pressure housing and are coupled by fiber-optic leads to upwelling radiance and downwelling irradiance collectors that are located approximately 1 m away to minimize shading and reflection effects. The upwelling radiance probe is ~5 cm in diameter, and the self-shading effect is varied by attaching discs of increasing diameter to it.

Particle size distributions are measured using a commercial (Spectrex) laser particle counter. Particle counts, binned by size, are determined by measuring the magnitude of reflections from particles in a small working volume

of water illuminated by a Helium-Neon diode (670.8 nm) LASER. The working volume, which is embedded in a 100 ml water sample, and its geometry are defined by the optical elements of the instrument. The water sample is agitated with a magnetic stirrer to keep particles in suspension during the measurements. The protocols used for determining particle size distributions are those provided by the manufacturer of the Spectrex, which claim to resolve particle sizes as small as 1 μm. On the other hand, the assumptions underlying the method are that the individual particles are separated by distances large compared to the wavelength of illumination, and that particle diameters are at least 5 times larger than the wavelength, so that particle reflection is governed by geometric optics. Other investigators have used the Spectrex instrument to measure particle size distributions, but a community consensus has yet to be developed for protocols related to this measurement and its interpretation.

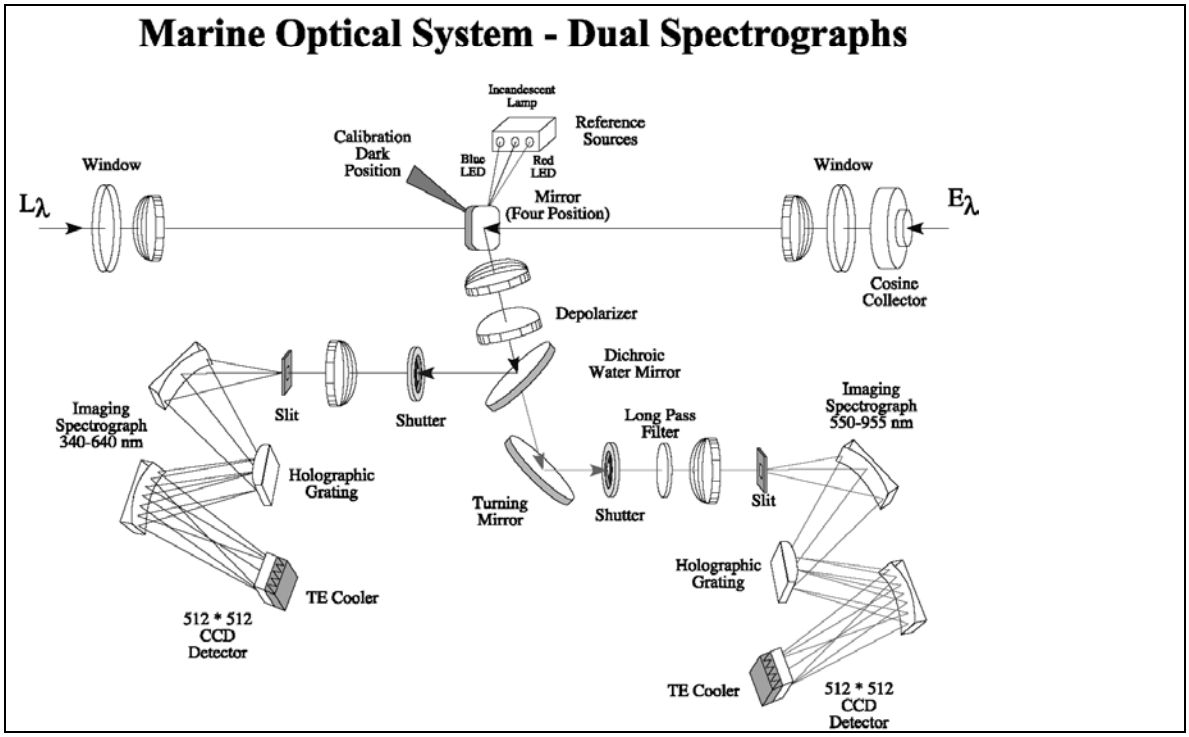

Figure 2.8: A schematic diagram showing the optical design of the MOS spectrographs.

MOBY System Operations Scheduling

MOBY data collection is programmed at the MOBY Operations Site in Honolulu, prior to each deployment. After the buoy has been deployed, any necessary program changes are made using a direct connection to the buoy's on-board computer. The on-board computer is programmed to acquire data during each event when the mooring site is in view of a satellite ocean color sensor. Currently, the MOBY radiometric measurement sequence, described below, is executed twice daily, coincident with the predicted overpasses of SeaWiFS and MODIS.

Radiometric Measurements

The MOS measures radiation input from one $L_u(z,\lambda)$, $E_d(z,\lambda)$ or $E_s(\lambda)$ head at a time. The desired channel is selected by the optical multiplexer. A rotating mirror within the MOS selects alternatively the input from the multiplexer, a dark reference calibration, light emitting diodes (LEDs), or a tungsten halogen incandescent lamp (Table 2.3). Integration times for the radiance collector on the top arm, at 1 m, typically range from 1 s to 4 s for the blue spectrograph and 10 s to 30 s for the red spectrograph. A typical sequence would be to measure $L_u(\lambda,z)$ from a depth, preceded and followed by $E_s(\lambda)$ surface reference spectra and associated dark spectra. Then this sequence is repeated at the 2nd and 3rd depths to complete the profile for $L_u(\lambda,z)$, as summarized in the example of

Figure 2.9: Deployment of a MOBY.

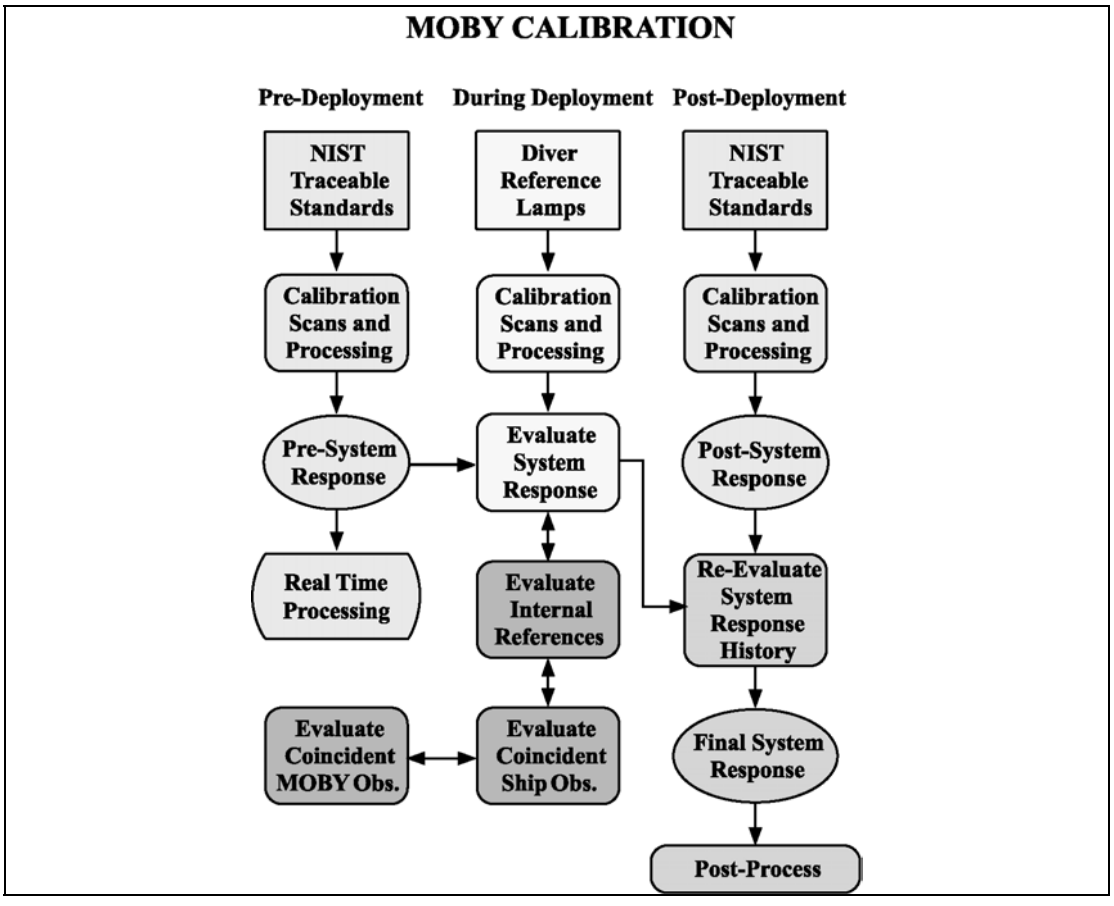

Figure 2.10: MOBY radiometric calibration and system stability check flow chart.

Table 2.6. Note that there are a total of 35 measurements for radiances at the 3 depths, surface irradiance $E_S(\lambda)$ and sensor dark spectra. The 35 measurements are grouped into overlapping subsets of 15 measurements, representing the cycle associated with upwelled radiance measurements at each depth. Not included in the example are measurements from the base of the MOS itself, because these data are not currently used to determine water-leaving radiance. This entire procedure requires between 30 min and 1 hr to complete.

Figure 2.11: The diver-deployed underwater radiometric stability reference unit attached to an upwelling radiance collector on MOBY.

Methods for Mitigating Bio-Fouling

Marine organisms, including algae and barnacles, typically attach themselves to any surface that is immersed in seawater for an extended period. This "bio-fouling" process changes the transmittance of the radiance windows and irradiance cosine diffusers. The radiance windows are placed at the base of copper tubes, and small amounts of bromide are slowly released near the windows throughout the deployment. Both of these substances are poisons for most marine life. It is not practical to use this approach with the irradiance collectors, so a combination of Teflon collector material, copper bezels and less effective anti-fouling compounds is used here. Divers clean the optical collectors and recharge the bromide dispensers at monthly intervals during each deployment.

Ancillary Measurements

Aboard the mooring buoy, the meteorological state variables (wind velocity, surface pressure, air temperature and humidity), sea surface temperature and conductivity, and near-surface *in situ* chlorophyll *a* fluorescence, are sampled as 5 min averages at 15 min intervals, and recorded continuously on the system disk. The data records are downloaded once daily.

Sun Photometer and Sky Radiance Measurements (on Lanai and Oahu)

The AERONET Project at NASA GSFC operates the CIMEL[1] sun photometers on Lanai and Oahu, and retrieves the data, remotely. The aerosol optical thickness and sky radiance distribution data measured at these sites are needed as input to atmospheric correction models when the MOBY water leaving radiances are used for vicarious calibration of the satellite ocean color sensor. The data are archived by, and may be obtained from, the AERONET Project at NASA GSFC. MOBY support personnel visit the photometer sites at monthly intervals to check and clean the instruments.

2.4 CALIBRATION AND QUALITY CONTROL

The MOBY radiometers are characterized and calibrated using procedures that conform to the protocols described in Vol. II, Chapter 3. The unique role of MOBY as a primary, long term, and daily reference for vicarious calibration of satellite ocean color sensors requires radiometric measurements of the highest possible quality, and this in turn places stringent demands on the methods of traceability to NIST radiometric standards. For example, the MOBY team uses exclusively irradiance standards acquired directly from NIST, NIST recalibrates these sources frequently (see below), and NIST investigators validate the team's radiometric sources at annual intervals.

The MOS radiometers are calibrated before and after each deployment, and stability tests are made during deployments using both on-board and diver-deployed sources. These calibrations, tests and comparative measurements are illustrated schematically in Figure 2.10. The special aspects of the MOBY radiometric calibration, characterization and stability test procedures are described in this section.

Radiometric Calibration and Characterization of MOS

The spectral irradiance responsivities of the MOS $E_d(z,\lambda)$ and $E_s(\lambda)$ channels are calibrated using FEL-type lamp standards of spectral irradiance, and the $L_u(z,\lambda)$ channels are calibrated using lamp-illuminated integrating sphere sources. The wavelength calibration is performed using spectral line emission lamps, and every calibration cycle includes a measure of three internal sources (see below). Each instrument, whether for a MOCE or for a MOBY deployment, is calibrated at the support facility site in Honolulu before and after the in-water deployment. The standards of spectral irradiance and radiance are recalibrated every 50 h of operation. The irradiance standards, 1000 W quartz-halogen lamps (model number FEL), are calibrated by NIST. The integrating sphere source radiance standards are calibrated by their manufacturer, Optronic Laboratories, Inc. The MOS irradiance responsivity assignments are NIST-traceable using the NIST-issued FEL lamps. During the MOS irradiance calibration, the lamps are operated at the correct current using a calibrated shunt resistor in series with the lamp. The lamp is operated in an enclosed housing at the same distance and with the same collection area as at NIST (50 cm and 1 cm^2, respectively). A reference mounting plate ensures the alignment of the lamp to the irradiance collector. The validity of this approach was verified by NIST (Mueller *et al.* 1996).

The radiance assignment is NIST-traceable via the commercial standards laboratory's calibration of integrating sphere sources (ISSs). Two ISSs are used: model OL420 and model OL425. They are externally illuminated, with an aperture wheel to vary the radiant output in discrete amounts. However, the two ISS units differ in the designs of their internal baffles, and in the method used by each to continuously vary the output. The ISSs are operated at constant current. The OL425 has, additionally, an internal illuminance monitor detector that is used to relate the output to that during the calibration measurements at Optronic Laboratories. The ISSs are re-lamped by Optronic Laboratories, and calibrated before and after this procedure, so for each sphere and lamp configuration, there is an initial and a final radiometric calibration; to date, only the initial calibration values have been used for the MOBY calibrations.

In addition to the routine calibration of the MOBY radiometric standards, two single-channel, dual-mode radiometers were designed and built by NIST to verify the calibrations of the FELs and ISSs and to monitor their stability at the support facility site in Honolulu. These Standard Lamp Monitors (SLMs) (Clark *et al.* 2001) have interchangeable foreoptics for operation in either radiance or irradiance mode. The narrowband (approximately 10 nm bandwidth) interference filters are centered at 412 nm and 872 nm. During every radiometric calibration at the support site, the SLMs are used to record the output of the radiometric standards. The absolute radiometric

response of the SLMs is determined by measurements at NIST, both during the initial development and subsequently on an interval of 12 months to 18 months.

Finally, site visits by NIST personnel are done at regular intervals, and radiance comparisons are performed. Initially, the SeaWiFS Transfer Radiometer (SXR), a multichannel filter radiometer (Johnson *et al.* 1998) that is calibrated at NIST, was used. At the present time, a later version of the SXR, the Visible Transfer Radiometer (VXR) (Johnson *et al.* 2002) is used, along with a stable, portable, NIST-calibrated ISS, the NIST Portable Radiance Source (NPR) (Brown and Johnson 2002). The VXR and the NPR were developed by NIST in support of the calibration program for the Earth Observing System (EOS) (Butler *et al.* 1999).

MOS Internal Reference Sources

An internal reference system was incorporated into the MOS design to monitor the stability of the radiometric detectors, electronics, and internal optics. These measurements are critical for establishing confidence in the observations acquired during a deployment cycle. One of the viewing positions on the main relay mirror mechanism reflects light from a Spectralon[1] diffuser plate into the blue and red spectrograph optical relays. The diffuser is illuminated in sequence by an incandescent lamp, a blue light emitting diode (LED), and a red LED. The blue and red diodes are centered at 465 nm and 705 nm, respectively, with approximately 100 nm bandwidths. The lamps are run with current controlled circuitry and the temperature of the lamp holder block is monitored. These lamps are observed at the end of each MOBY data acquisition set (Sect. 2.3). Time histories of reference lamp responses for each deployment period show the MOS spectrograph responses to be stable at the 1 % level.

Field Tests of Radiometric Stability Using Diver Deployed Sources

The internal reference lamp and diodes responses (above) do not reflect changes in the throughput of the MOS irradiance and radiance collectors due to bio-fouling. During the nominal three-month duration of a MOBY system deployment period, a team of divers conducts inspections, external reference lamp stability tests, and cleaning monthly. During these maintenance operations, the near-surface components of the moored buoy and MOBY are inspected for damage, deterioration, and bio-fouling. The condition of the buoy is documented with underwater photography. To document these effects on MOBY radiometry, external underwater reference lamp stability baseline measurements are conducted on each irradiance, or radiance, collector immediately after the MOBY is deployed (Fig. 2.11). The underwater reference lamp radiometric stability tests are repeated during each monthly service visit, before and after each collector is cleaned. The reference lamp system is a modified commercial underwater unit using a 35 W incandescent lamp. The lamp is powered by a submersible, 12 V, 6.5 A h battery-pack. Modifications to the commercial lamp system included the addition of constant current circuitry to the battery pack, and construction of lamp housings that fit over the radiance and irradiance collectors to block ambient light, while maintaining a fixed distance between the lamp source and collector. The radiance reference lamp system has a translucent diffuser placed between the lamp and collector window. Laboratory stability tests of the reference lamp systems show the output to be repeatable within 1 % if the battery voltage remains within 25 % of full charge. In the field, batteries are replaced and recharged when voltage decreases to 50 % of full charge.

Examples of the diver reference lamp responses for a few wavelengths at one upwelling radiance collector are illustrated in Fig. 2.12. Data shown at each wavelength represent the difference between the MOS responses on 3 August 2000, when the MOBY was deployed, and the responses before and after cleaning on 4 October 2000. The vertical bars illustrate the standard uncertainty in the diver reference lamp comparisons. Because all the response measurements fall within this uncertainty, the diver lamp response data have not been used to correct for trends during a deployment.

Wavelength Stability Tests Using Fraunhofer Lines

Solar Fraunhofer lines and the atmosphere's oxygen A band absorption near 762 nm are resolved in the MOS $E_S(\lambda)$ spectra. The MOS detector array pixel locations of these lines are used to monitor the wavelength stability of the system throughout each deployment. Within the spectral resolution of the MOS spectrographs, no changes in the locations of any of these bands have occurred since the first MOBY deployment.

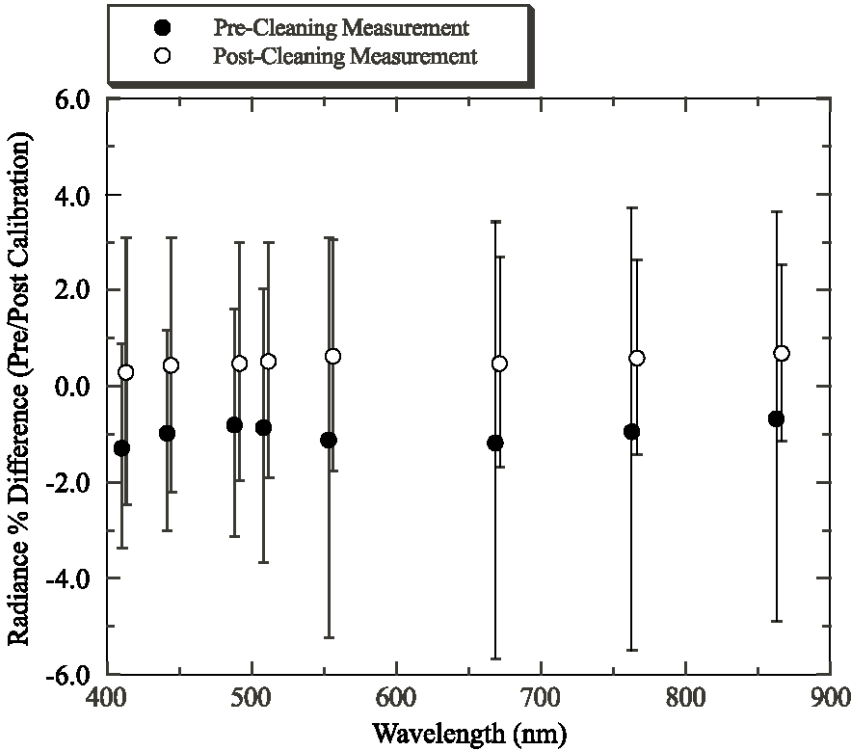

Figure 2.12: An example showing results of diver-deployed underwater radiometric stability source tests for several wavelengths and one radiance collector. The measurements were made immediately before, and after, the diver cleaned the radiance collector. The data are charted as percent differences from the similar test done on the day the buoy was deployed, approximately 2 months earlier.

Stray Light Characterization

A critical issue in ocean color measurements arises because of the large difference in the relative spectral shape of the lamp-illuminated ISS (radiance mode), or the FEL lamp (irradiance mode), when compared to the relative spectral shape of $L_u(z,\lambda)$, or $E_d(z,\lambda)$, measured in the ocean. Radiometric sensors do not have an ideal spectral selectivity, *i.e.*, the response at a wavelength of interest to flux at other wavelengths is small but finite (Vol. II, Chapter 2, Sect. 2.2 and Vol. II, Chapter 3, Sect. 3.4). As a result, measurements at the wavelength of interest include both a component that is proportional to the flux at that wavelength (*e.g.*, the "in-band" component) plus a component that sums the product of the sensor response and the spectrum of flux at wavelengths outside the in-band region. The latter sum, representing the out-of-band component, must be evaluated for all wavelengths for which the detector has finite responsivity. For MOS, the out-of-band response is largely determined by the scattering properties of the grating and unwanted reflections of flux diffracted in second order. We refer to the effect as "stray light".

Stray light considerations for MOS motivated dividing the spectrum into two regions using a dichroic beamsplitter and two spectrographs. As seen by the blue spectrograph, this division results in a better match between the spectral shapes of the FEL-type spectral irradiance sources and $E_d(z,\lambda)$, or the ISSs and $L_u(z,\lambda)$, and minimizes stray light effects in the critical ocean color wavelength bands. At 412 nm and 440 nm, for example, comparisons of $L_u(z,\lambda)$ for MOCE or MOBY deployments agree with measurements using independent filter radiometers to within ±5 %.

The effect of stray light in MOS is most evident in the region of overlap between the two spectrographs, from 545 nm to 650 nm. For the red spectrograph, the decreased transmittance of the dichroic beamsplitter in this region, where it goes from zero to nearly unity transmittance, means that the ratio of the in-band to the out-of-band components is unfavorable. Indeed, for some MOS wavelengths (CCD columns) at the blue side of the red

spectrograph, the recorded signals can be dominated by the out-of-band component. At the present time, the processing algorithms use the results from the blue spectrograph up to 620 nm, and those from the red spectrograph beyond 620 nm. The differences are generally stable in time and depend on depth, another indication that the effect is related to source spectral shape.

To correct for stray light, the function that describes the sensitivity to flux at wavelengths other than the desired wavelength must be determined. This requires a tunable, monochromatic source that fills the entrance pupil of the sensor. Improvements in technology and the recent addition of new facilities at NIST have made it possible to fully characterize sensors such as CCD spectrographs using fully tunable laser-illuminated, integrating sphere sources (Brown, Eppeldauer, and Lykke 2000). The facility is called Spectral Irradiance and Radiance responsivity Calibrations with Uniform Sources (SIRCUS).

A thorough stray light characterization study for the MOBY project was begun in early 2000. Work started on SIRCUS with a MOS bench unit (Habauzit *et al.* 2002), and continued with the full characterization of MOS202 (which is used as a profiler instrument). Measurements are ongoing for the MOBY MOS units. The SIRCUS measurements yield the absolute radiance response of the sensors. Examples of the response of a single column in the blue spectrograph (column 380), and of the red spectrograph (column 277), are shown in Fig. 2.13 and Fig. 2.14 for the MOS profiler. The small peak near 510 nm for the blue spectrograph is caused by flux diffracted in second order and reflected onto the CCD by the grating and the second spherical mirror.

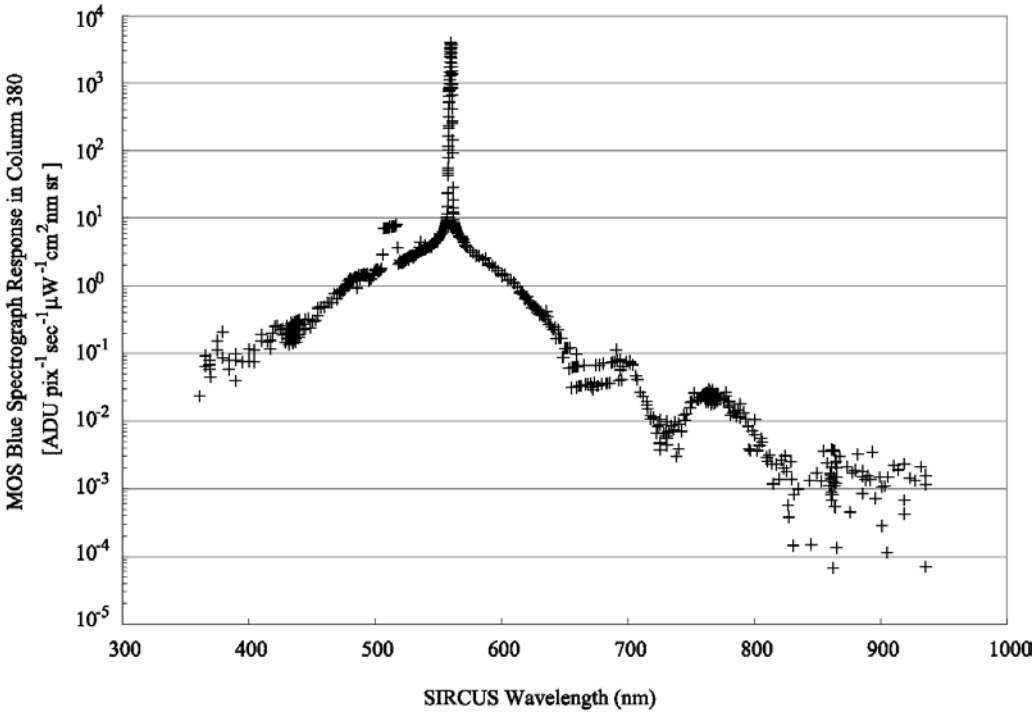

Figure 2.13: An example of the wavelength dependent spectral stray light responsivity of one CCD pixel location (wavelength) for the MOS blue spectrograph.

A stray light correction algorithm was developed that is based on determination of the in-band region for one column on each CCD spectrograph, a description of the shape of the out-of-band response, and a model to account for the effects of the second order "reflection peak" (Brown *et al* 2002). To date, the SIRCUS results for the MOS profiler have been used to implement a preliminary version of the stray light correction algorithm, and test applications to the MOCE5 data sets are extremely encouraging. These preliminary results indicate that stray light affected the MOS Profiler results during MOCE 5 by up to +5 % at 412 nm (the uncorrected radiances are too small) and up to -1.5 % at 546 nm (the uncorrected radiances are too large).

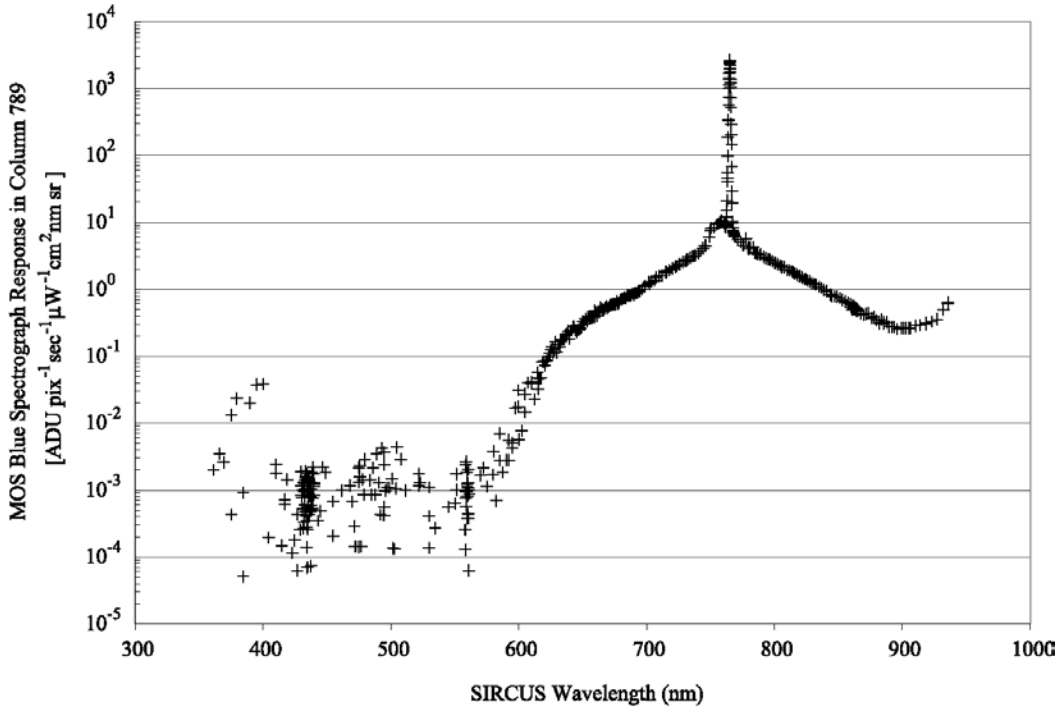

Figure 2.14: Same as Figure 2.13, but for one CCD pixel of the MOS red spectrograph.

Validation of the stray light correction algorithm is accomplished using an ISS that is made to simulate the spectral shape of in-water radiances using colored glass filters. The radiance of this colored source is determined independently by a NIST calibrated double grating monochromator. The results are compared to the corrected and uncorrected MOBY values and used to estimate the uncertainty of the stray-light correction. MOS stray light corrections are discussed in more detail in Chapter 5 of the present Volume.

CIMEL Sun Photometer and Sky Radiance Sensor Calibrations

The CIMEL instruments deployed at the stations on Oahu and Lanai are calibrated and maintained at NASA GSFC by the SIMBIOS Project Office, in collaboration with AERONET Project, following the procedures described in Volume II, Chapter 4.

2.5 DATA ANALYSIS METHODS

As described above in Sect. 2.3, a single MOBY observation comprises a sequence of four to seven spectral radiance and irradiance measurement cycles for optical collectors located at the different depths on the spar (Table 2.6). The portion of the data record for an individual measurement cycle, *e.g.* for the upwelling radiance collector on a MOBY arm at depth z_i, is recorded as 3 arrays of digital counts $C_{Li}(\tau,N_p,z_i,t_m,\lambda)$ [m = 7, 8, 9 in an $L_u(z_i,\lambda)$ cycle of Table 2.6], where t_m is the time of the $m^{\underline{th}}$ measurement and τ is integration time. The "bin factor" N_p is expressed as the number of CCD rows read into the output register during each read step. Preceding and following each set of 3 radiance count arrays $C_{Li}(\tau,z_i,t_m,\lambda)$, the data record for one measurement cycle contains digital count arrays for incident surface irradiance (above water on the MOBY mast) $C_s(\tau_{sm},t_m,N_{pdm},\lambda)$, [m = 2, 3 4 (pre) and m = 12, 13, 14 (post) (Table 2.6)], and the MOS system dark response $D(\tau_{dm},t_m,N_{pdm},\lambda)$, for E_s [m = 1 and 5 (pre)

and m = 11 and 15 (post)] and L_u [m = 6 and 10]. The central time, t_{Li} [or t_{Ei}], associated with a single radiance [or irradiance] measurement cycle (Table 2.6) is calculated as, *e.g.*

$$t_{Li} = \frac{1}{15}\sum_{i=1}^{15} t_i. \tag{2.1}$$

Temporal Averaging

The first step in processing the data is to scale each digital count array to unit integration time and average the individual measurements. Average counts for surface irradiance, normalized to unit integration time and bin factor, are computed as

$$\bar{C}_s\left(t_{Li},\lambda\right) = \frac{1}{6}\sum_{m}\left[\frac{C_s\left(\tau_{s,i},t_m,\lambda\right)}{N_{p,s,i}\tau_{s,i}}\right], m = 2,3,4,12,13,14 \text{ (Table 2.6)} \tag{2.2}$$

Average counts for MOS L_u Dark response, normalized to unit integration time and bin factor, are computed as (L_u cycle indices as in Table 2.6)

$$\bar{D}\left(t_{Li},\lambda\right) = \frac{1}{2}\left[\frac{D\left(\tau_{d,6},t_6,\lambda\right)}{N_{p,d,6}\tau_{d,6}} + \frac{D\left(\tau_{d,10},t_{10},\lambda\right)}{N_{p,d,10}\tau_{d,10}}\right]. \tag{2.3}$$

The 4 E_S Darks for the associated surface reference are averaged similarly. Finally, the average counts for the cycle of upwelled radiance measurements, normalized to unit integration time and bin factor, are computed as

$$\bar{C}_{Li}\left(z_i,t_{Li},\lambda\right) = \frac{1}{3N_p\tau}\sum_{m=7}^{9} C_{Li}\left(\tau,z_i,t_m,\lambda\right). \tag{2.4}$$

With appropriate changes in subscripts (*i.e.* "E*i*" in place of "L*i*"), equations (2.1) through (2.4) apply also to a spectral downwelling irradiance measurement cycle at depth z_i.

System Spectral Response Functions

The MOS system spectral radiance (or irradiance) responsivity functions $R_j(\lambda, \tau)$, for optical collector j and unit integration time (*i.e.* τ = 1), are determined following procedures described in Vol. II, Ch. 3 (Sect. 3.2), with extensions described above in Sect. 2.4. Following the example cycle of M upwelling radiance scans for the MOBY arm at depth z_i, bracketed by surface irradiance and dark response records, incident spectral irradiances $E_S(t_{Li},\lambda)$ [μW cm^{-2}nm^{-1}] and average upwelling spectral radiance $L_u(z_i,t_{Li},\lambda)$ [μW cm^{-2}nm^{-1}sr^{-1}]

$$E_s\left(t_{Li},\lambda\right) = R_{Es}\left(\lambda\right)\left[\bar{C}_s\left(t_{Li},\lambda\right) - \bar{D}\left(t_{Li},\lambda\right)\right], \tag{2.5}$$

and

$$L_u\left(z_i,t_{Li},\lambda\right) = R_{Li}\left(\lambda\right)F_{imm}^{Li}\left(\lambda\right)\left[\bar{C}_{Li}\left(z_i,t_{Li},\lambda\right) - \bar{D}\left(t_{Li},\lambda\right)\right], \tag{2.6}$$

where $F_{imm}^{Li}\left(\lambda\right)$ is the immersion factor for the $i^{\underline{th}}$ radiance collector as determined during the sensor's characterization (Vol. III, Chapter 3, Sect. 3.5 and Sect. 3.4). In equation (2.6), "L*i*" indicates that the subscripted (or superscripted) quantity applies to the spectral radiance collector mounted at depth z_i on the MOBY frame. Equation (2.6), substituting appropriate variables and subscripts, applies also to downwelling spectral irradiance $E_d(z_i,t_{Ei},\lambda)$ [μW cm^{-2}nm^{-1}] measurements using the irradiance collector mounted on MOBY at depth z_i.

Measurement Depths

On MOBY, $L_u(z,\lambda)$ is measured at 4 depths that are rigidly separated at fixed intervals on the buoy. These depths are nominally z_1 = 1 m, z_2 = 5 m, z_3 = 9 m, and z_4 = 2.5 m. The radiance measurement at 2.5 m is not currently used to determine water-leaving radiance. $E_d(z,\lambda)$ is measured only at nominal depths z_1, z_2, and z_3.

K(λ) Analysis

Following the above processing through equation (2.6), the attenuation coefficient for $L_u(z,\lambda)$ is computed from measurements at two discrete depths z_i and z_j as

$$K_L\left(\overline{z}_{ij},\lambda\right)=\frac{1}{z_j-z_i}\ln\left(\frac{L_u\left(z_i,\lambda\right)E_s\left(t_j,\lambda\right)}{L_u\left(z_j,\lambda\right)E_s\left(t_i,\lambda\right)}\right),\ z_j>z_i,\ i=1,2,3,\ j=2,3,4, \tag{2.7}$$

where t_i and t_j are the times of radiance measurements at depths z_i and z_j, respectively. The ratio of incident surface irradiances appears in (2.7) to account for changes in illumination, *e.g.* due to clouds, between the times of the two radiance measurements. The mean depth in the interval between z_i and z_j is

$$\overline{z}_{ij}=\frac{z_i+z_j}{2}. \tag{2.8}$$

The diffuse attenuation coefficient for $E_d(z,\lambda)$ is computed similarly to (2.7) as

$$K_d\left(\overline{z}_{ij},\lambda\right)=\frac{1}{z_j-z_i}\ln\left(\frac{E_d\left(z_i,\lambda\right)E_s\left(t_j,\lambda\right)}{E_d\left(z_j,\lambda\right)E_s\left(t_i,\lambda\right)}\right),\ z_j>z_i,\ i=1,2,\ j=2,3. \tag{2.9}$$

For computing $K_L\left(\overline{z}_{ij},\lambda\right)$ and $K_d\left(\overline{z}_{ij},\lambda\right)$ from data measured with the shipboard MOS instrument, the actual depths z_i are determined to the nearest cm using data from its high precision depth transducer.

Determining $L_W(\lambda)$ by Upward Extrapolation

To determine $L_W(\lambda)$, the measurement of upwelling radiance from a selected depth z_i is propagated to the surface as

$$L_u\left(0^-,\lambda\right)=L_u\left(z_i,\lambda\right)e^{K_L\left(\overline{z}_{ij},\lambda\right)z_i}. \tag{2.10}$$

The depth z_i is selected according to the following hierarchical rules:

1. If the data from the top arm are valid, then that depth is selected.
2. Else, the data from the middle arm, if valid, are selected.
3. Else, the data sequence is rejected entirely.

Water-leaving radiance is calculated by propagating $L_u(0^-,\lambda)$ through the interface as

$$L_W\left(\lambda\right)=\frac{1-\rho}{n^2}L_u\left(0^-,\lambda\right), \tag{2.11}$$

where the upward transmittance through the interface, for nadir viewing radiance, is approximately constant, with value

$$\frac{1-\rho}{n^2}=0.543\,, \tag{2.12}$$

being only weakly dependent on wavelength and insensitive to wind speed (Austin 1974; see also Vol. I, Chapter 2, and Vol. III, Chapters 2 and 4).

Normalized Water-Leaving Radiance

Since the water-leaving radiances are apparent optical properties and are dependent upon the effects of the atmosphere, variations in solar zenith angle θ_o, and the earth-sun distance d, it is necessary to normalize the data to remove these effects for some applications. The normalizing approach used with MOBY water-leaving radiances follows the procedures that were defined by Gordon and Clark (1981) to compute *solar-normalized water leaving radiances* as

$$L_{\mathrm{WN}}(\lambda) = \frac{L_{\mathrm{W}}(\lambda)}{t(\lambda,\theta_{\mathrm{o}})\cos\theta_{\mathrm{o}}\left(\frac{d_{\mathrm{o}}}{d}\right)^2}, \tag{2.13}$$

where d_{o} is the mean earth-sun distance, and $t(\lambda, \theta_{\mathrm{o}})$ is the diffuse atmospheric transmittance computed as

$$t(\lambda,\theta_{\mathrm{o}}) = e^{-\frac{\frac{1}{2}\tau_{\mathrm{R}}(\lambda)+\tau_{\mathrm{O_3}}(\lambda)}{\cos\theta_{\mathrm{o}}}}. \tag{2.14}$$

The Rayleigh optical thickness $\tau_{\mathrm{R}}(\lambda)$ is taken for mean atmospheric pressure (Penndorf 1957), and the ozone optical thickness $\tau_{\mathrm{O_3}}(\lambda)$ is computed for an atmospheric ozone concentration of 350 Dobson units. The ratio of average to actual earth sun distances is approximated as

$$\frac{d_{\mathrm{o}}}{d} = 1 + 0.0167\cos\left[\frac{2\pi(J-3)}{365}\right], \tag{2.15}$$

where J is the sequential day of the year.

The *normalized water-leaving radiances* $L_{\mathrm{WN}}(\lambda)$ computed with Equations (2.13) through (2.15) are still dependent on the bidirectionality of the ocean's reflectance, as determined by the local inherent optical properties of the water and the solar zenith angle θ_{o} (Morel and Gentili 1996). To remove the bidirectional reflectance effects, it is necessary to convert the above $L_{\mathrm{WN}}(\lambda)$ to *exact normalized water-leaving radiance* $L_{\mathrm{WN}}^{\mathrm{ex}}(\lambda)$ following the protocols in Vol III, Chapter 4.

Spectral Band Averaging

The water leaving radiance corresponding to each wavelength band of a satellite ocean color sensor is determined from the MOBY solar-normalized water leaving radiances $L_{\mathrm{WN}}(\lambda)$ as

$$L_{\mathrm{WN}}^{\mathrm{MS}}(\overline{\lambda}_i) = \frac{\int_0^\infty r_{\mathrm{n}}^{S}(\lambda,\overline{\lambda}_i)L_{\mathrm{WN}}(\lambda)\,d\lambda}{\int_0^\infty r_{\mathrm{n}}^{S}(\lambda,\overline{\lambda}_i)\,d\lambda}, \tag{2.16}$$

where the superscripts S and MS denote a particular satellite ocean color sensor and a MOBY derived estimate for that satellite, respectively, $\overline{\lambda}_i$ is the effective wavelength of the i^{th} band of that sensor, and $r_{\mathrm{n}}^{S}(\lambda,\overline{\lambda}_i)$ is the normalized relative spectral response function of that channel. In practice, (2.16) is approximated numerically.

An example MOBY water-leaving radiance spectrum is compared to the shapes of the spectral response function of MODIS ocean bands in Fig. 2.15. Note that $L_{\mathrm{WN}}(\lambda)$ must be transformed to $L_{\mathrm{WN}}^{\mathrm{ex}}(\lambda)$ (Vol. III, Chapter 4) prior to match-up comparisons between MOBY and satellite water-leaving radiances.

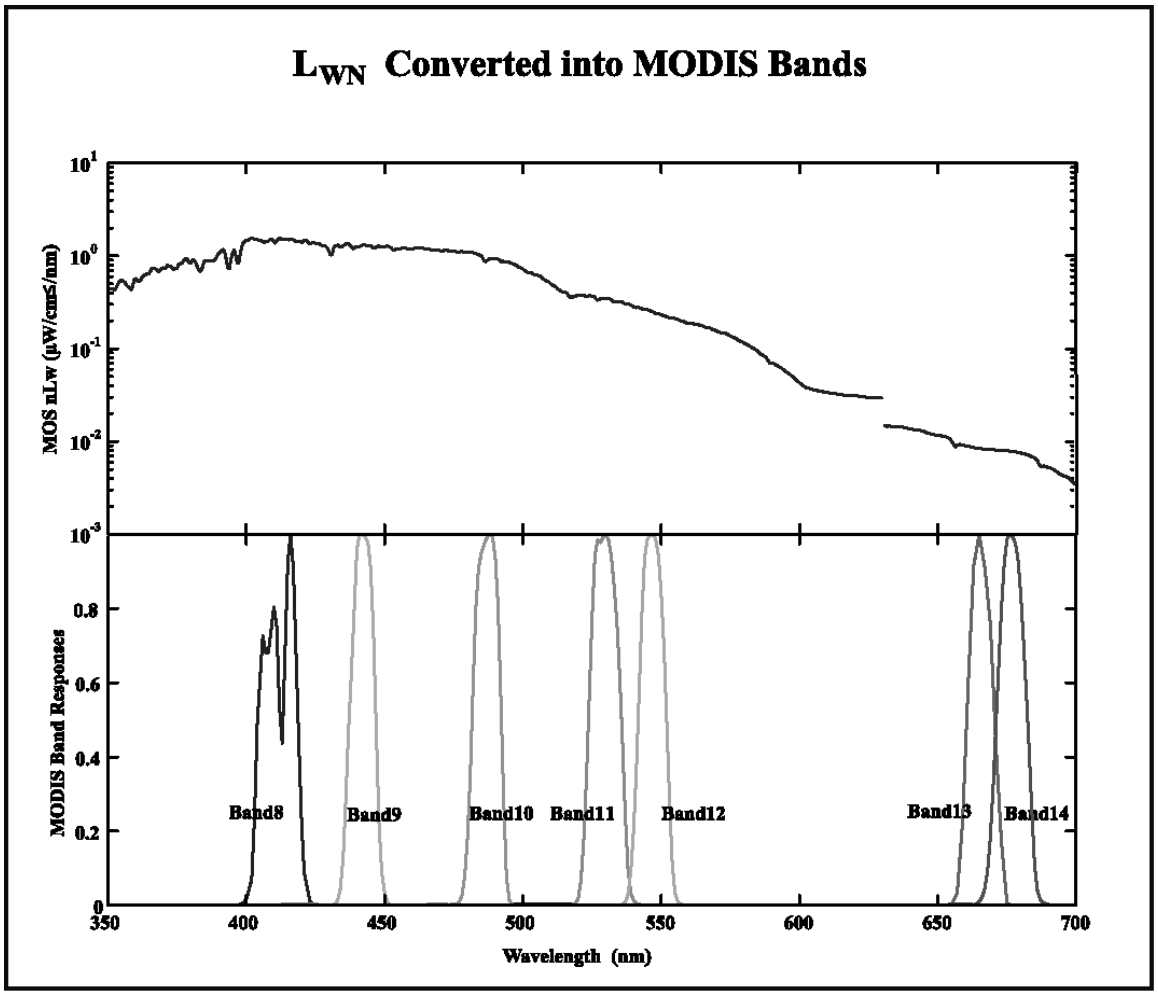

Figure 2.15: Comparison of a normalized water-leaving radiance spectrum measured by MOBY with the spectral band response functions of the MODIS ocean channels. The MOBY radiances have not been corrected for stray light, as is obvious from the large offset between the blue and red spectrographs at 630 nm.

2.6 DATA ARCHIVAL AND RECORDKEEPING

Band averaged water-leaving radiances for SeaWiFS and MODIS are transmitted to the SeaWiFS and SIMBIOS Project Offices, where they are archived in SeaBASS. These data are also transmitted to and archived by the MODIS Team at the University of Miami. All data recorded by the MOBY system and on MOCE and other cruises are archived at MLML in Moss Landing, California and at NOAA NESDIS in Camp Springs, Maryland.

2.7 FUTURE DIRECTIONS

Temperature Characterizations

Although the MOS CCDs are temperature-controlled, the temperatures of the optical components in the spectrographs, the electronics, the MOBY fiber optics, and other system components are subject to environmental conditions. These ancillary instrument temperatures are recorded and archived, but are not used in the present data processing algorithms. Because the ambient temperature and degree of thermal equilibrium depends on the measurement purpose (calibration vs. in-water radiometry) and type of deployment (MOBY vs. MOS), the

radiometric responsivities of MOBY and MOS are being studied as a function of temperature. Various temperature-controlled baths are used, including one large enough for MOS.

Stray Light Characterizations

The MOBY Project includes a suite of instruments, requiring multiple field deployments to address the stray light issues. Once the required data are in hand, the stray light algorithm for all of the required instruments will be optimized. This may require separate model parameters for each input collector on MOBY. Then, the MOCE and MOBY data sets will be reprocessed, leading to an improvement in the accuracy of the derived $L_{WN}(\lambda)$'s that are used for vicarious calibration of MODIS, SeaWiFS, and other ocean color satellite sensors. It is anticipated that the uncertainty in the correction will be about 10 % of the effect, *e.g.* the uncertainty in the corrected values from stray light would be 0.5 % for a 5 % correction.

ACKNOWLEDGMENTS

The NIST efforts are supported by NOAA under contract NA00AANEG0072. Additional support for the NIST participation in this project has been provided under contracts S-41365-F (EOS Project Science Office) and S-64096-E (SeaWiFS Project). The Electro-optics Calibration Coordination Group, U.S. Air Force section, provided funding for SIRCUS (CCG98-439).

REFERENCES

Austin, R.W., 1974: The remote sensing of spectral radiance from below the ocean surface. In: Optical Aspects of Oceanography, N.G. Jerlov and E.S. Nielson, Eds., pp 317-344.

Brown, S.W., G.P. Eppeldauer, and K.R. Lykke, 2000: NIST facility for spectral irradiance and radiance responsivity calibrations with uniform sources. *Metrologia*, **37**, 579-582.

Brown, S.W., and B.C. Johnson, 2002: Development of a portable integrating sphere source for the Earth Observing System's Calibration Validation Program. To appear in *International Journal of Remote Sensing*.

Brown, S.W., C. Habauzit, B.C. Johnson, and K.R. Lykke, 2002: Tunable-laser based calibration of a CCD spectrograph. In preparation.

Butler, *et al*. 1999: J.J. Butler J.J., B.L. Markham, B.C. Johnson, S.W. Brown, H.W. Yoon, R.A.Barnes, S.F. Biggar, E.F. Zalewski, P.R. Spyak, F. Sakuma, and J.W. Cooper, 1999: Radiometric measurement comparisons using transfer radiometers in support of the calibration of NASA's Earth Observing System (EOS) Snesors, in Sensors, Systems, and Next Generation Satellites III, Proc. SPIE Vol. 3870, Ed. P.L. Slater, (Bellingham, Washington: Society of Photo-Optical Instrumentation Engineers), 180-192.

Clark, D.K, H.R. Gordon, K.J. Voss, Y. Ge, W. Broenkow, and C.C. Trees, 1997: Validation of atmospheric corrections over oceans. *J. Geophs. Res*., **102**: 17209-17217.

Clark, D.K., M.E. Feinholz, M.A. Yarbrough, B.C. Johnson, S. W. Brown, Y.-S. Kim, and R.A. Barnes, 2001: Overview of the radiometric calibration of MOBY. *Proc. SPIE, Earth Observing Systems VI*, **4483**, xxx—yyy.

Clark, D.K, H.R. Gordon, K.J. Voss, Y. Ge, W. Broenkow, and C.C. Trees, 1997: Validation of atmospheric corrections over oceans. *J. Geophs. Res*., **102**: 17209-17217.

Evans, R.H. and H.R. Gordon, 1994: Coastal Zone Color Scanner system calibration: a retrospective examination. *J. Geophys. Res.*, **99**:7293-7307.

Fargion, G.S. and J.L. Mueller, 2000: *Ocean Optics Protocols for Satellite Ocean Color Sensor Validation, Revision 2*, NASA TM 2001-209955, NASA Goddard Space Flight Center, Greenbelt, Maryland, 184 pp.

Gordon, H.R., 1981: Reduction of error introduced in the processing of Coastal Zone Color Scanner-type imagery resulting from sensor calibration and solar irradiance uncertainty. *Appl. Opt.*, **20**: 207-210.

Gordon, H.R., 1987: Calibration requirements and methodology for remote sensors viewing the ocean in the visible. *Remote Sens. Environ*., **22**:103-126.

Gordon, H.R., 1988: Ocean color remote sensing systems: radiometric requirements. *Recent Advances in Sensors, Radiometry, and Data Processing for Remote Sensing*, P.N. Slater, Ed., SPIE, **924**: 151-157.

Gordon, H.R., J.W. Brown, O.B. Brown, R.H. Evans, and D.K. Clark, 1983: Nimbus-7 CZCS: reduction of its radiometric sensitivity with time. *Appl. Opt*., **24**:3929-3931.

Gordon, H.R. and D.K. Clark, 1981: Clear water radiances for atmospheric correction of Coastal Zone Color Scanner imagery. *Appl. Opt.*, **20:** 4174-4180.

Gordon, H.R., D.K. Clark, J.W. Brown, O.B. Brown, R.H. Evans, and W.W. Broenkow, 1983: Phytoplankton pigment concentrations in the middle Atlantic bight: comparison of ship determinations and CZCS estimates. *Appl. Opt*. **22:** 20-36.

Gordon, H.R. and K. Ding, 1992: Self shading of in-water optical instruments. *Limnol. Oceanogr*., **37**: 491-500.

Hooker, S.B. and S. Maritorena, 2000: An evaluation of oceanographic radiometers and deployment methodologies. *J. Atmos. Oceanic Technol*. **17**: 811-830.

Habauzit, C., S.W. Brown, K.R. Lykke, B.C. Johnson, M.E. Feinholz, M.A. Yarbrough, and D.K. Clark, 2002: Radiometric characterization and absolute calibration of the Marine Optical System (MOS) bench unit. Submitted to the Journal of Atmospheric and Oceanic Technology.

Johnson, B.C., J.B. Fowler, and C.L. Cromer, 1998: The SeaWiFS Transfer Radiometer (SXR). *NASA Tech. Memo. 1998-206892, Vol. 1*, S.B. Hooker and E.R. Firestone, Eds., NASA Goddard Space Flight Center, Greenbelt, Maryland, 58 pp.

Johnson, B.C., S.W. Brown, G.P. Eppeldauer, and K.R. Lykke, 2002: System-level calibration of a transfer radiometer used to validate EOS radiance scales. To appear in International Journal of Remote Sensing.

Morel, A. and B. Gentili, 1996: Diffuse reflectance of oceanic waters. III. Implication of bidirectionality for the remote-sensing problem. *Applied Optics,* **35**: 4850-4862.

Mueller, J.L. and R.W. Austin, 1992: Ocean Optics Protocols for SeaWiFS Validation. *NASA Tech. Memo. 104566, Vol. 5,* S.B. Hooker and E.R. Firestone, Eds., NASA Goddard Space flight center, Greenbelt, Maryland, 45 pp.

Mueller, J.L. and R.W. Austin, 1995: Ocean Optics Protocols for SeaWiFS Validation, Revision 1. *NASA Tech. Memo. 104566, Vol. **25,*** S.B. Hooker and E.R. Firestone, Eds., NASA Goddard Space flight center, Greenbelt, Maryland, 66 pp.

Mueller, J.L., B.C. Johnson, C.L. Cromer, S.B. Hooker, J.T. McLean, and S.F. Biggar, 1996: The Third SeaWiFS Intercalibration Round-Robin Experiment, SIRREX-3, September 1994. *NASA Tech. Memo 104566, Vol. 34*, S. B. Hooker, E. R. Firestone, and J. G. Acker, Eds., NASA Goddard Space Flight Center, Greenbelt, Maryland, 78 pp.

Penndorf R., 1957: Tables of the refractive index for standard air and the Rayleigh scattering coefficient for the spectral region between 0.2 and 20.0 microns and their application to atmospheric optics, *J. Opt. Soc. Am.*, **47**, 176-182.

Siegel, D.A., M.C. O'Brien, J.C. Sorenson, D.A. Konnoff, E.A. Brody, J.L. Mueller, C.O. Davis, W.J. Rhea, and S.B. Hooker, 1995: Results of the SeaWiFS Data Analysis Round Robin, July 1994 (DARR-94). *NASA Tech Memo. 104566, Vol. **26***, S.B. Hooker and E.R. Firestone, Eds., NASA Goddard Space Flight Center, Greenbelt, Maryland, 58p.

Taylor, B.N., and C.E. Kuyatt, 1994: Guidelines for Evaluating and Expressing the Uncertainty of NIST Measurement Results. *NIST Tech. Note 1297*, U.S. Department of Commerce, National Institute of Standards and Technology, Washington, DC, 20 pp.

Table 2.1: Summary of MOCE data collection cruises. Cruises dedicated to the collection of bio-optical data are indicated with "MOCE". Cruises where data were collected in conjunction with MOBY operations are indicated with "MOBY".

Cruise	Cruise Dates	Cruise Location	No. of Stns	Satellite(s) Supported
MOCE-1	28 Aug-11 Sep 1992	Monterey Bay	7	
MOCE-2	27 Mar-14 Apr 1993	Gulf of California	13	
MOCE-3	27 Oct-15 Nov 1994	Hawaiian Archipelago	16	
MOBY-L14	14-22 Sep 1996	Hawaii-Lanai	6	
MOBY-L15	14-22 Nov 1996	Hawaii-Lanai	5	OCTS Initialization
MOBY-L16	23 -28 Feb 1997	Hawaii-Lanai	8	OCTS Initialization
MOBY-L20	19-27 Jul 1997	Hawaii-Lanai	5	
MOBY-L22	22 Sep-4 Oct 1997	Hawaii-Lanai	7	
MOBY-L25	7-15 Dec 1997	Hawaii-Lanai	3	
MOCE-4	26 Jan-12 Feb 1998	Hawaiian Islands	17	SeaWiFS Initialization
MOBY-L28	30 Mar-1 Apr 1998	Hawaii-Lanai	2	
MOBY-L35	23-26 Jul 1998	Hawaii-Lanai	5	
MOBY-L38	25-30 Oct 1998	Hawaii-Lanai	5	
MOBY-L43	6-11 Feb 1999	Hawaii-Lanai	3	
MOBY-L45	1-6 May 1999	Hawaii-Lanai	4	
MOCE-5	1-21 Oct 1999	Gulf of California	20	
MOBY-L54	10-15 Feb 2000	Hawaii-Lanai	2	
MOCE-6	9-16 Apr 2000	Hawaiian Islands	8	MODIS Initialization-Side A
MOBY-L56	15-19 May 2000	Hawaii-Lanai	3	
MOBY-L59	24 Jul-11 Aug 2000	Hawaii-Lanai	3	MODIS Initialization-Side A
MOCE-7	3-10 Dec 2000	Hawaiian Islands	7	MODIS Initialization-Side B
MOCE-8	28 Feb-9 Mar 2001	Hawaiian Islands	9	MODIS Initialization-Side B
MOBY-L69	1-4 Jun 2001	Hawaiian Islands	2	

Table 2.2a: MOBY Specifications	
Physical Specifications:	
Dimensions D x L (m)	1.7 x 15
Collector standoff length (m)	3.0 max
Weight in air (kg)	955
Height above waterline (m)	3
Reserve buoyancy (kg)	816
Flotation material	Isomer foam
Undamped period (sec)	2.5
Damping	Suspended drag device
Surface float frame	Welded stainless steel (T316L)
Spar	Stainless steel reinforced fiberglass
Instrument Bay	Welded stainless steel (T316L)
Collector standoff depths	Variable

Table 2.2a: MOBY Specifications (Continued)			
Optical:			
Spectrograph	MOS		
MOS optical interface	Fiber optic multiplexer, 10 ports		
Fiber optics	1mm silica/silica		
Fiber optic Interface	O-ring sealed SMAS		
Collectors:			
	E_s:	**E_d:**	**L_u:**
Dimensions	5 cm x 18 cm	5 cm x 17 cm	5 cm x 17 cm
Collector dimensions	3 cm	7 cm	2.8 cm
FOV	Cosine response	Cosine response	Max 5 °
f#	-	-	2
Electrical:			
Power source	4 x 40 W solar panels		
Charge control	Trace C12		
Battery monitoring	Individual monitor and charge control		
Average daily power production (W)	640		
Reserve battery capacity (W)	9600		
Instrument Bay battery type	4 x 200 A h, 12 v, Sealed Marine Gel Cell		
GPS	Raytheon RS112LP		
Argos	Seimac GPSMML		
R.F. beacon/locator strobe	Novatec, RF700C5		
Cellular antenna	Cellwave		
Controller battery type	80 A h, 12 v Sealed Marine Gel Cell		
Controller battery capacity	960		
Buoy power consumption, Sleep (uW)	3		
Buoy power consumption, Active (W)	9.6		
Buoy power consumption, Telemetry mode(W)	42		
Buoy power consumption, Acquisition mode (W)	132		
Surface Buoy Controller:			
Processor	MC68332		
Operating system	MLML Forth		
Modem	Zyxel, U-1496P		
Cellular transceiver	Motorola, S1765A		
Host serial interface	RS232, 9600 baud		
MOS serial interface	RS485, 9600 baud		
Subsurface power controller serial interface	RS485, 19.2k baud		
GPS serial interface	RS232, 4800 baud		
Internal power control	Latching relays		
A/D System:	High resolution	**Low resolution**	
Resolution	16 bit	12 bit	
Gains	1,10,100,500		
Channels	16	4	
Throughput	33 kHz, max	>100 kHz	
Accuracy	0.0024%, max	0.01%	
Subsurface Instrument bay Power Controller			
Operating system	TTBasic		
Status functions	Instrument bay power monitor		
	MOS power monitor		
	Battery charge monitor		
Control functions	Battery charge control		
	MOS power control		

Table 2.2b: MOBY Ancillary measurements

Parameter	Sensor Type	Range	Precision	Accuracy
Surface controller battery voltage (V)	Voltage monitor	0-25	0.006	0.02
Humidity	Monolithic capacitive	0-100 %	0.01%	2%
Case internal temperature (°C)	Thermistor	-10-50	0.05	0.1
Upper arm pressure (depth)	Strain gauge	0-25 meters	1.0 mm	5mm
Controller current (A)	Shunt	0-25	0.04	0.25
Controller battery charge current (A)	Shunt	0-25	0.04	0.25
Solar panel 1 current (A)	Shunt	0-25	0.04	0.25
Solar panel 2 current (A)	Shunt	0-25	0.04	0.25
Solar panel 3 current (A)	Shunt	0-25	0.04	0.25
Solar panel 4 current (A)	Shunt	0-25	0.04	0.25
Subsurface power controller voltage (V)	Voltage monitor	0-25	0.006	0.02
MOS voltage	Voltage monitor	0-25	0.006	0.02
MOS Battery current (A)	Shunt	0-25	0.04	0.25
MOS Battery #1	Voltage monitor	0-25	0.006	0.02
MOS Battery #2	Voltage monitor	0-25	0.006	0.02
MOS Battery #3	Voltage monitor	0-25	0.006	0.02
MOS Battery #4	Voltage monitor	0-25	0.006	0.02

Table 2.3a: MOS Spectrograph Characteristics

Dimensions:	
MOS only, D x L, (mm)	330 x 660
Weight in air (Kg)	64
Weight in sea water (Kg)	4
MOS with profiling rack and battery, D x L, (mm)	673 x787
Weight in air (Kg)	143
Weight in sea water (Kg)	122
Construction	O-ring sealed aluminum
Depth rating (meters)	100
Electrical:	
Profiler Lead-acid battery capacity (W)	600
MOS Power consumption (W)	120 W @ 10.5 – 14.5
Optics:	
Material (windows, lenses)	Fused Silica
Input optics f#	2
Diameter (mm)	43
FOV (deg)	Max 5 °
Input telescope ports	2 (up & down)
Polarization filter (option)	Quartz wedges
Input selection	4 positions
Input mirror settings	Up, Down, Reference, Dark
Spectrographs	2
Spectral separation optics	45° dichroic mirror
Separation wavelength, 50% pass (nm)	635
Full spectral range (nm)	340-955
Spectral resolution (nm)	<1
Polarization sensitivity	<1% (with depolarizing optics option)

Table 2.3a: MOS Spectrograph Characteristics (continued)

Spectrographs:	
Dimensions, L x W x H (mm)	178 x 152 x 100
Type	Offner variant
Construction	Stainless steel (T316) bench Aluminum fixtures
Optics	SiO protected, Al coated glass (Blue) Au coated, black glass (Red)
Grating	Convex holographic
Wavelength Range (nm)	340 - 640 (Blue) 550 - 955 (Red)
Focal length (mm)	100
f#	3.8
Slit dimension (um)	12 (h) * 25 (w) * 40 (t)
Slit material	Electroformed Nickel
Resolution (nm)	0.6 (Blue) / 0.8 (Red)
Bandpass, FWHM, over spectrograph range, (nm)	1.0 - 1.2 (Blue) / 1.28 - 1.5 (red)
Fore optics	Ø25 mm, Cylindrical
Out of band rejection filters	580 nm High Pass (Red)

Table 2.3b: MOS Ancillary Measurements

Parameter	**Sensor Type**	**Range**	**Precision**	**Accuracy**
Mains (Battery) voltage	Voltage monitor	0-25 V	0.006 V	0.02 V
Humidity	Monolithic capacitive	0-100 %	0.01%	2%
Case internal temperature	Thermistor	-10-50°C	0.05	0.1
Water Temperature	Thermistor	-10 to 50 °C	0.005	0.05
Pressure (depth)	Strain gauge	0-200 meters	1.0 cm	4.0 cm
Tilt-X	Electrolytic	±60°	0.0026 °	0.03 °
Tilt-Y	Electrolytic	±60°	0.0026 °	0.03 °
Blue Array Temperature	Thermistor	-50 to 40°C	0.005 °C	0.05 °C
Red Array Temperature	Thermistor	-50 to 40°C	0.005 °C	0.05 °C
Blue Calib diode monitor	Photodiode	NA	15-bit	0.001%
Red Calib diode monitor	Photodiode	NA	15-bit	0.001%
Calib. Source block temp	Thermistor	-10 to 50 °C	0.005	0.05 °C
Coolant Flow	Pelton Wheel	20-2000 ml/min	1.5 ml/min	0.01 ml/min
Depth Sensor Temperature	Thermistor	-10 to 50 °C	0.005	0.05 °C
System Current	Hall effect	0 - 20 A	.01 A	0.05 A
Blue CCD Heater Monitor	Voltage monitor	NA	15-bit	0.001%
Red CCD Heater Monitor	Voltage monitor	NA	15-bit	0.001%
Internal Temperature at TT7	Thermistor	-10-50°C	0.05	0.1
Blue CCD Head Temperature	Thermistor	-10 to 50 °C	0.005	0.05 °C
Red CCD Head Temperature	Thermistor	-10 to 50 °C	0.005	0.05 °C
Heading	Flux gate compass	0 to 360 °	0.1°	0.5 °

Table 2.4: Summary of MOBY Deployment and Interim Servicing Cruises.

Cruise Name	Cruise Dates	Mooring	Diver Cals	MOBY	CIMEL
MOBY-L1	3-7 Oct 93	deployed			
MOBY-L2	6-10 Feb 94			aborted deploy	
MOBY-L3	21-25 Feb 94			deployed	
MOBY-L4	24-29 Mar 94		X		
MOBY-L5	5-9 May 94			check-up	
MOBY-L6	24-27 May 94		cancelled-bad weather		
MOBY-L7	25-30 Jun 94	retrieved		recovered	
MOBY-L8	9-12 Sep 94			testing	
MOBY-L9	8-27 Mar 95			testing	
MOBY-L10	15-30 Aug 95			testing	
MOBY-L11	3-8 Nov 95	deployed			
MOBY-L12	21 Feb-6 Mar 96			testing	
MOBY-L13	24 Jul-15 Aug 96			testing	X
MOBY-L14	14-21 Sep 96			deployed	
MOBY-L15	2-4, 14-22 Nov 96			exchanged	
MOBY-L16	23 Feb-2 Mar 97			recovered	
MOBY-L17	1-17 Apr 97			assembly	
MOBY-L18	9-23 May 97			testing	
MOBY-L19	9-23 Jun 97			testing	
MOBY-L20	19-27 Jul 97			deployed	
MOBY-L21	31-Aug-97		X		
MOBY-L22	22 Sep-4 Oct 97		X		
MOBY-L23	30-31 Oct 97			retrieved/reattached	
MOBY-L24	10-11 Nov 97		X		
MOBY-L25	7-14 Dec 97	exchanged	X	exchanged	
MOBY-L26	13-14 Jan 98		X		
MOBY-L27	9-10 Mar 98		X		
MOBY-L28	29 Mar-2 Apr 98			aborted-bad weather	
MOBY-L29	21-24 Apr 98			exchanged	X
MOBY-L30	4-May-98		cancelled-bad weather		X
MOBY-L31	15-May-98			maintenance	X
MOBY-L32	2-3 Jun 98		X		
MOBY-L33	21-Jun-98			repair	X
MOBY-L34	2-3 Jul 98		X		X
MOBY-L35	22-26 Jul 98			exchanged	

Table 2.4: Summary of MOBY Deployment and Interim Servicing Cruises (Continued)

Cruise Name	Cruise Dates	Mooring	Diver Cals	MOBY	CIMEL
MOBY-L36	25, 28-29 Aug 98		cancelled-bad weather		X
MOBY-L37	17, 19-20 Sep 98		X	maintenance	
MOBY-L38	24-30 Oct 98		X	exchanged	X
MOBY-L39	7-10 Dec 98		X	maintenance	
MOBY-L40	5-Jan-99			maintenance	
MOBY-L41	10-12 Jan 99		X		X
MOBY-L42	21-Jan-99			maintenance	
MOBY-L43	6-11 Feb 99	exchanged	X	exchanged	
MOBY-L44	9-11 Mar 99		X	maintenance	X
MOBY-L45	1-6 May 99		X	exchanged	
MOBY-L46	2-3 Jun 99		X	maintenance	X
MOBY-L47	29 Jun-1 Jul 99		X	maintenance	X
MOBY-L48	29 Jul-1 Aug 99		X	exchanged	
MOBY-L49	5-Sep-99			check-up	
MOBY-L50	10-Oct-99			check-up	
MOBY-L51	15-18 Nov 99		X	exchanged	
MOBY-L52	16-19 Dec 99		X		X
MOBY-L53	25-Jan-00			maintenance	X
MOBY-L54	10-15 Feb 00	exchanged	X	exchanged	
MOBY-L55	29-31 Mar 00		X	maintenance	
MOBY-L56	15-19 May 00		X	exchanged	
MOBY-L57	19 -21 Jun 00		X		X
MOBY-L58	17-19 Jul 00		X		
MOBY-L59	3-6 Aug 00		X	exchanged	
MOBY-L60	12-14 Sep 00		X		X
MOBY-L61	23-Sep-00			maintenance	
MOBY-L62	5-6 Oct 00		X		X
MOBY-L63	9-11 Jan 01		X		X
MOBY-L64	28-Jan-01			maintenance	
MOBY-L65	7-8 Feb 01		X		
MOBY-L66	18-Mar-01			check-up	
MOBY-L67	7-9 Apr 01		X		X
MOBY-L68	22-23 May 01			maintenance	X
MOBY-L69	1-4 Jun 01		X	exchanged	
MOBY-L70	4-6 Jul 01		X	maintenance	X

Table 2.5: *In situ* observations collected during a MOCE cruise in support of vicarious calibration/validation of satellite ocean color systems. Measurement subcategories follow those shown in Vol./ I, Chapter 3, Table 3.1.

MOCE Cruise Data Acquisition	Institution	Instrumentation System
Required Measurements		
Downwelled Irradiance	MLML	MOS, SPMR
Upwelled Radiance	MLML	MOS, SPMR
Incident Irradiance	MLML	SIS, SMSR
Aerosol Optical Depth	NOAA/NESDIS, U of Miami	HHCRM, MicroTops
Phytoplankton Pigment Composition	CHORS	HPLC
Chlorophyll a and Phaeopigment Concentration	CHORS	Fluorometric
Latitude and Longitude	NOAA/NESDIS	Trimble GPS
Date and Time (UTC)	NOAA/NESDIS	Trak
Wind Speed and Direction	NOAA/NESDIS	Young
Surface Barometric Pressure	NOAA/NESDIS	Setra
Air Temperature/Relative Humidity	NOAA/NESDIS	Vaisala
Cloud Cover	NOAA/NESDIS	Sky Camera
Secchi Depth	MLML	Secchi Disk
Highly Desired Measurements		
Beam Attenuation	NOAA/NESDIS	VLST
Beam Attenuation Profiles	MLML	WETLabs C-Star
Particle Absorption	NOAA/NESDIS	Diode Array Spectrophotometer
Dissolved Material (CDOM) Absorption	NOAA/NESDIS	Diode Array Spectrophotometer
Non-Pigmented Particle Absorption	NOAA/NESDIS	Diode Array Spectrophotometer
Phytoplankton Absorption	NOAA/NESDIS	Diode Array Spectrophotometer
Fluorometric Profiles	MLML	Chelsea
Whitecap Conditions	U of Miami	
Conductivity and Temperature Profiles	MLML	SeaBird CTD
Conductivity and Temperature - Alongtrack	NOAA/NESDIS	Falmouth TSG
Specialized Measurements		
Instrument Self-Shading	NOAA/NESDIS	FOS
Upwelled Radiance Distribution	U of Miami	RADS
Particle Size Data	NOAA/NESDIS	Laser Particle Counter
Total Suspended Particulate Matter (TSM)	MLML	
Particulate Organic Carbon/Nitrogen (POC/PON)	MLML	

Table 2.6: An example of a MOBY MOS upwelled radiance measurement cycle. The cumulative index is the order in which measurements are made. The $L_u(z_i,\lambda)$ Cycle Indices group the measurements at depth z_i with bracketing $E_s(\lambda)$ measurements and associated dark measurements; these indices are used in Equations (2.1) through (2.4) to average the individual measurements within each cycle.

Cumulative Index	**Variable Measured**	**Depth z (m)**	$L_u(z_1,\lambda)$ **Cycle Index**	$L_u(z_2,\lambda)$ **Cycle Index**	$L_u(z_3,\lambda)$ **Cycle Index**
1	$E_s(\lambda)$ Dark	--		1	
2 – 4	$E_s(\lambda)$	0^+		2 – 4	
5	$E_s(\lambda)$ Dark	--		5	
6	$L_u(\lambda)$ Dark	--		6	
7 – 9	$L_u(z_2,\lambda)$	5		7 – 9	
10	$L_u(\lambda)$ Dark	--		10	
11	$E_s(\lambda)$ Dark	--	1	11	
12 – 14	$E_s(\lambda)$	0^+	2 – 4	12 – 14	
15	$E_s(\lambda)$ Dark	--	5	15	
16	$L_u(\lambda)$ Dark	--	6		
17 – 19	$L_u(z_1,\lambda)$	1	7 – 9		
20	$L_u(\lambda)$ Dark	--	10		
21	$E_s(\lambda)$ Dark	--	11		1
22 – 24	$E_s(\lambda)$	0^+	12 – 14		2 – 4
25	$E_s(\lambda)$ Dark	--	15		5
26	$L_u(\lambda)$ Dark	--			6
27 – 29	$L_u(z_3,\lambda)$	9			7 – 9
30	$L_u(\lambda)$ Dark	--			10
31	$E_s(\lambda)$ Dark	--			11
32 – 34	$E_s(\lambda)$	0^+			12 – 14
35	$E_s(\lambda)$ Dark	--			15

Chapter 3

Radiometric and Bio-optical Measurements from Moored and Drifting Buoys: Measurement and Data Analysis Protocols

Victor S. Kuwahara[1], P. G. Strutton[1], T. D. Dickey[2], M. R. Abbott[3], R. M. Letelier[3], M. R. Lewis[4], S. McLean[4], F. P. Chavez[1], A. Barnard[5], J. Ruairidh Morrison[6], Ajit Subramaniam[7], Derek Manov[2], Xiaobing Zheng[2] and James L. Mueller[8]

[1]Monterey Bay Aquarium Research Institute, Moss Landing, California
[2]Ocean Physics Lab., University of California, Santa Barbara, California
[3]College of Oceanic and Atmospheric Sciences, Oregon State University, Corvallis, Oregon
[4]Satlantic Inc., Halifax, Nova Scotia, Canada
[5]Bigelow Laboratory for Ocean Sciences, W. Boothbay Harbor, Maine
[6]Woods Hole Oceanographic Institution, Woods Hole, Massachusetts
[7]University of Maryland, College Park, Maryland
[8]Center for Hydro-Optics and Remote Sensing, San Diego State University, California

3.1 INTRODUCTION

No single type of observational platform provides radiometric and other bio-optical measurements at all scales of spatial and temporal variability that are important for research in oceanic primary productivity and regional, or global, carbon cycles, for example (Figure 3.1). Traditional shipboard observations enable detailed regional studies, but provide limited spatial and temporal coverage. Observations from instruments on moored and drifting buoys afford excellent temporal and vertical resolutions, but are limited to Eulerian and Lagrangian spatial contexts, respectively. Ocean color satellites offer excellent spatial and daily-to-weekly coverage, but are limited to clear-sky conditions and cannot account for variations with depth in the water column. In recent years, it has become increasingly clear that the combined data from moorings, drifters, ships and satellites provide a powerful tool for identifying and describing oceanographic processes (Dickey, 1991, 2003). The purpose of this chapter is to provide protocols describing methods for making and applying time-series measurements from moored and drifting buoys in this context.

The deployment and operation of moored and drifting observation platforms has proven to be a successful and reliable means of acquiring oceanographic and meteorological data (Dickey 1991, 2003; Smith *et al*. 1991; Chavez *et al*. 1997). Bio-optical, radiometric and physical time-series measurements, made at high temporal resolution throughout periods of several months duration from moored platforms, provide data describing important episodic and periodic oceanographic processes that are difficult to observe using other methods. Moorings have formed the foundation of several long term ocean monitoring projects, including the Tropical Ocean Global Atmosphere (TOGA) observing system (McPhaden *et al*. 1998), the Hawaii Ocean Time-series (HOT; Karl and Lukas, 1996), and the Bermuda Testbed Mooring (BTM; Dickey *et al*. 1998a, 2001) at the Bermuda Atlantic Time Series (BATS; Siegel *et al*. 2001) site, as well as several ONR and NSF JGOFS funded process studies of one or more years duration, including Biowatt (Dickey *et al*. 1987), Marine Light in the Mixed Layer (Dickey *et al*. 1991), JGOFS/ONR Arabian Sea Experiment (Dickey *et al*., 1998b), JGOFS Equatorial Pacific Study (Foley *et al*., 1998), and the ONR Coastal Mixing and Optics Experiment (Dickey and Williams, 2001). Moored bio-optical arrays were used in the Antarctic Environment Southern Ocean Process Study as part of the U.S. Joint Global Ocean Flux Study (JGOFS) to study mesoscale processes in the Antarctic Polar Front (Abbott *et al*., 2000). Instrumented drifting buoys of many different types have also been used in a variety of field campaigns including the TOGA-TAO project (McPhaden *et al*., 1998), the IronEx cruises (Kudela and Chavez, 1996) and the World Ocean Circulation

Experiment (WOCE; http://www.soc.soton.ac.uk/others/woceipo/index.html). Regional ocean observing systems, such as the Gulf of Maine Ocean Observing System (GoMOOS; www.gomoos.org) are now in operation, or are being planned in the near future with the long-term goal of forming a network of integrated, sustained operational observing systems for the U.S. coastal waters (see Ocean.US web site). Government agencies now recognize the importance of moorings and drifters and plan to implement an integrated ocean observing system incorporating both technologies (www.ocean.us.net).

Moorings carry significant payloads, allowing many many different variables to be measured from each platform. As a result of the large number of instruments and the necessary hardware needed to support a mooring (float, line, glass balls, anchor, acoustic release, etc.), these platforms are relatively expensive to build, deploy, operate and maintain. Drifters, on the other hand, are usually smaller, carry fewer instruments, need much less hardware, and each copy is far less expensive than a typical moored array. In addition, since drifters are designed to track water masses they can quantify the time-dependent evolution of physical and bio-optical properties within particular water mass features. However, large numbers of drifters are needed, and as they are generally not recoverable, they must be considered expendable. Moored instruments, on the other hand, are recovered and reused. Moreover the methods of interpreting mooring data are much better developed. Nevertheless, equivalent ship-based observations are even more expensive than mooring, or drifter, observations. A relatively large number of drifting data buoys can be used to augment high-resolution time-series measured with moored arrays at a few fixed locations, seeking an optimal balance between spatial and temporal coverage (Dickey, 2003).

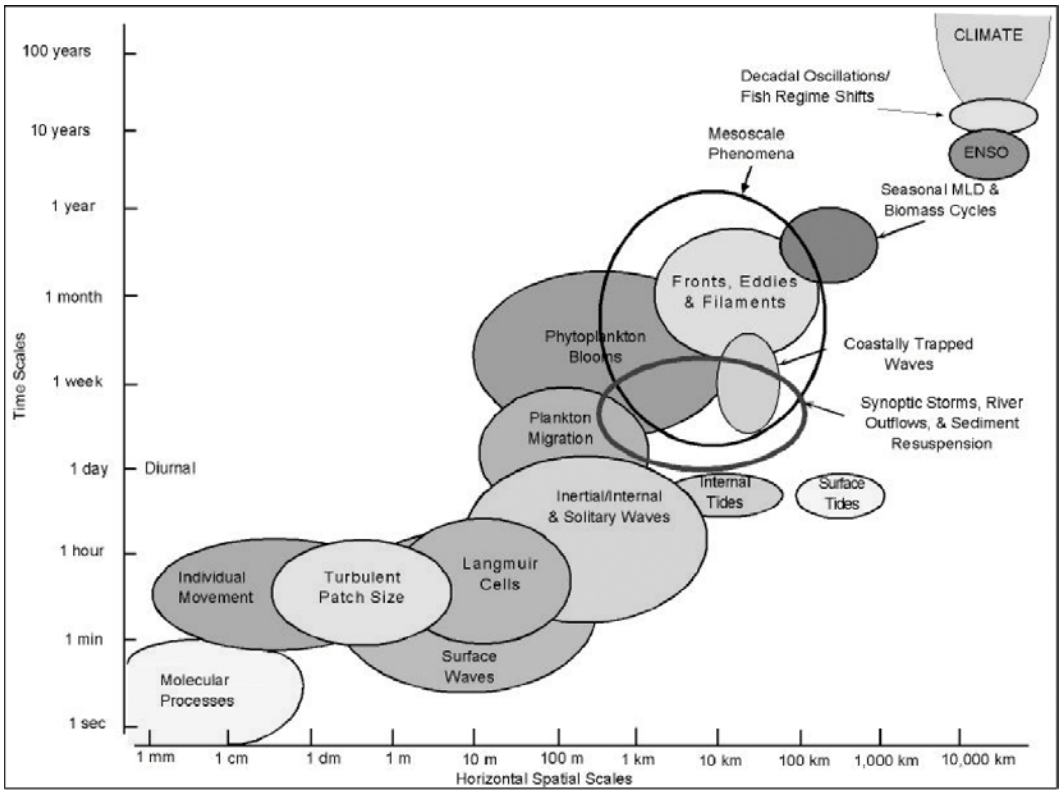

Fig. 3.1: Time-horizontal space scale diagram illustrating several physical and biological processes in ovals. (after Dickey, 2003).

Bio-optical measurements from moored and drifter platforms

The deployment of radiometers, and other bio-optical sensors, on moorings and drifters facilitates bio-optical measurements that transcend the spatial and temporal boundaries of classical shipboard methods (*e.g.* shipboard radiometric profiles) to enhance our understanding of oceanographic processes, particularly biological-physical coupling. Moored arrays observe bio-optical variables and ocean current velocities from an Eulerian perspective, yielding vector transport of bio-optical properties at a fixed point. It was recognized in the initial version of the

Ocean Optics Protocols (Mueller and Austin, 1992) that optical measurements from moorings would provide new insight into optical, oceanographic and biophysical measurements in the field and be important platforms for the validation of SeaWiFS. In particular, optical moorings were recommended as important platforms for the collection of long-term, *in situ* data that could be used, together with satellite ocean color data, for:

- Radiometric validation of SeaWiFS normalized water-leaving radiance. This concept has been implemented in the Moored Optical Buoy observatory off Lanai, Hawaii (Vol. VI, Chapter 2), data from which have been used as the primary reference for vicarious calibration of SeaWIFS and other satellite ocean color sensors (Gordon and Wang, 1994; Clark *et al*. 1997; McClain *et al*. 2000a, 200b).
- Developing and validating algorithms for pigment biomass and phytoplankton primary productivity (Dickey *et al*. 1998a, 2001; Chavez *et al*. 1999).
- Providing long-term, virtually continuous, time series of *in situ* observations characterizing biogeochemical processes in the upper ocean.

Chavez *et al.* (1999) and (Dickey *et al*. 1998a, 2001) expanded these ideas as they relate to combining satellite ocean color time series data with measurements from moored and drifting buoys to obtain regional and global descriptions of biological variability. These applications require the use of *in situ* radiometers, and other bio-optical sensors, for long periods of time to evaluate and correct for inherent satellite under-sampling and degradation of satellite color sensors.

Multi-year deployments of optical moorings and frequent drifter deployments are now realistic as a result of recent technological advances such as in hardware, power sources, and anti-fouling devices (Dickey *et al*. 1998a, 2001; Chavez *et al*. 1997, 2000; Manov *et al*. 2003). In order to assure that radiometric and bio-optical data acquired from various optical moorings meet uniform standards of quality and accuracy, clear and rigorous sampling and data processing methods must be used consistently throughout the community.

The purpose of this chapter is to describe protocols covering:

1. Strategic principles for the location and deployment duration of moored instrument arrays, and for numbers, locations and frequency of deploying instrumented drifting buoys, to augment satellite ocean color imagery and shipboard sampling (or vice versa) in studies of mesoscale and regional scale oceanographic phenomena.
2. State of the art design and fabrication of bio-optical moored and drifting data buoys
3. Methods for maintaining and operating moored instrument arrays, including:
    a. Mooring deployment
    b. Periodic maintenance during deployments and replacement of moorings and instruments.
4. System operation methods, including:
    a. Instrumentation
    b. Bio-fouling avoidance and mitigation
    c. On-board autonomous instrument operations, data acquisition, data storage, sampling schedules, time base methods (*e.g.* GPS on on-board clock), and time synchronization of data records from multiple instruments.
    d. On-board data processing and near-real-time data communications
    e. Platform geo-location, for tracking drifting buoys, and as a safety measure should a mooring come adrift.
5. Methods of data processing, quality control and analysis.
6. Data archival and retrieval.

The chapter concludes with insights into future directions for the design and applications of moored and drifting bio-optical buoys, together with satellite ocean color imagery, in studies of oceanographic biogeochemical phenomena.

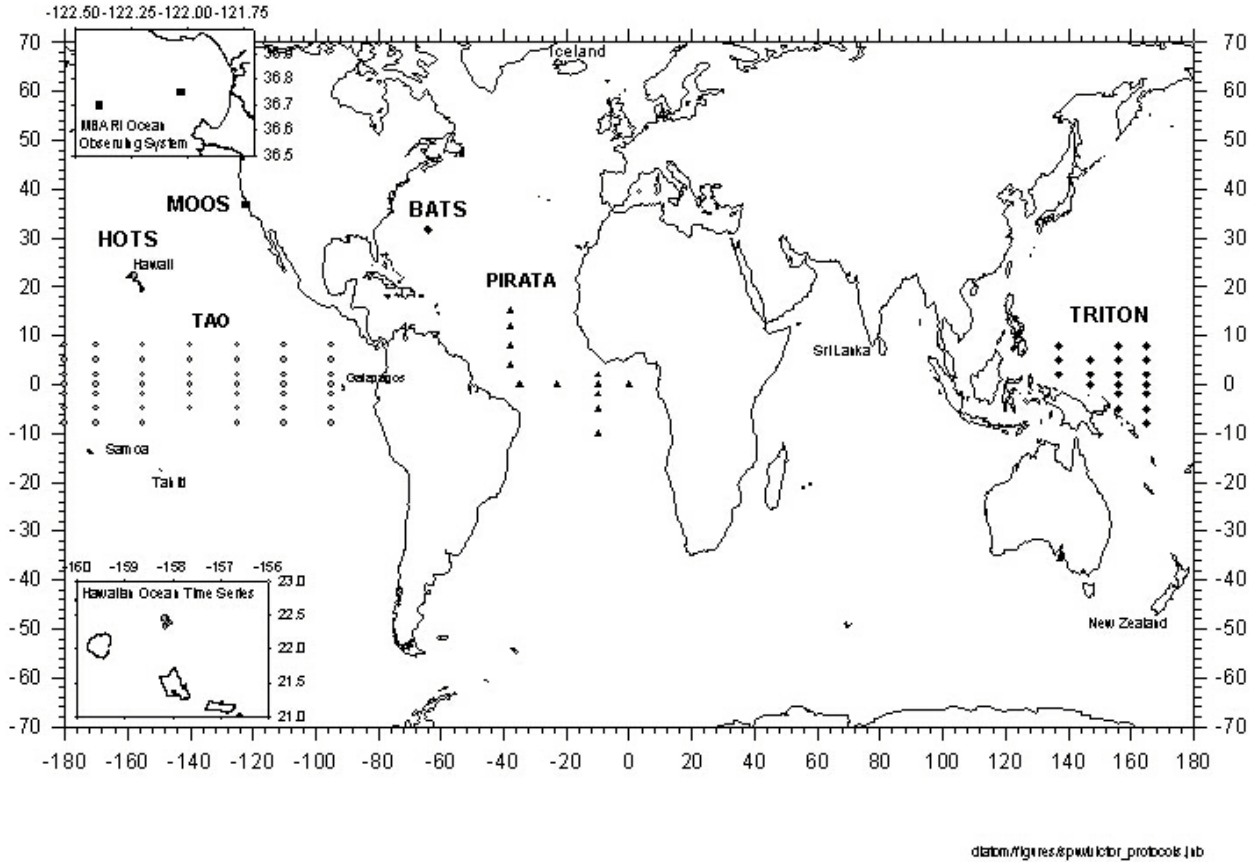

Figure 3.2: Map of selected currently deployed mooring platform projects around the world. Other planned and currently running mooring projects (not shown) can be found in Send *et al*. (2001)

3.2 BIO-OPTICAL MOORING NETWORKS AND DRIFTING BUOY EXPERIMENTS: STRATEGIC PRINCIPLES

The configuration of a mooring, or drifter, is dependent upon the objective and strategy of the respective projects. Ideally, the combination of the two types of instrumented buoys, shipboard oceanographic surveys, and satellite remote sensing measurements will result in a four-dimensional observation system that encompasses time and space scales, ranging from seconds to decades and meters to global proportions, respectively (*e.g.*, Dickey, 1991, 2003; Dickey *et al*., 2003). Careful planning is critical if the desired results, products and benefits are to be realized. The configuration of an ocean observatory must consider the following factors:

- ***Scientific Objectives:*** such as satellite sensor validation, studies of biogeochemical cycling and temporal variability in bio-optical properties of the upper ocean, and biological responses to physical forcing.
- ***Space Scales of Processes:*** water mass formation, transformation, or advection
- ***Time Scales of Processes:*** diurnal, seasonal, episodic, or decadal
- ***Location:*** coastal, equatorial, or central gyre oceanographic regimes
- ***Array Type:*** drifter, single instrumented mooring, or a geographic array of moorings.
- ***Coordination with Other Sampling Methods:*** such as shipboard measurements and satellite remote sensing
- ***Regional Issues and Users Needs:*** Regional ocean observatories may not be strictly science driven. GoMOOS is an excellent example of an observatory maintained to serve the broader public good through

an infrastructure that collects data pertinent to the public, academic, private, and governmental institutions. In the design of future ocean observatories, therefore, a balance must be maintained between scientific objectives and the information needs associated with coastal issues of operational importance to regional institutions, governments, and commercial enterprises.

The purpose and locations (illustrated in Figure 3.2) of some successful moored and drifting projects are described below (organized by types of oceanographic regimes).

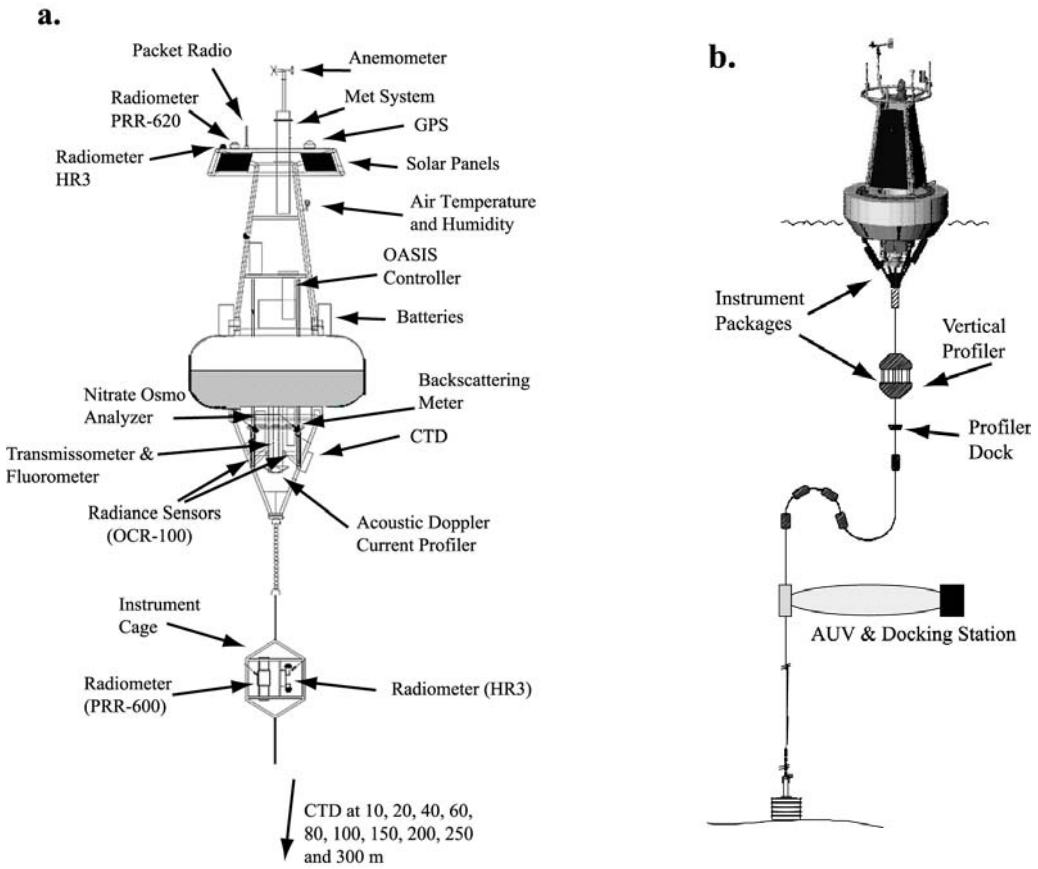

Figure 3.3: (a) Conceptual drawing of the MOOS moorings that are currently deployed. Each mooring is fitted with an assortment of biogeochemical and optical instruments. (b) Conceptual drawing of the new MOOS mooring platform by MBARI. Each buoy houses an assortment of bio-optical instruments in the tower, bridle, and along the harness cable to specific depths. Future moorings will also utilize a custom built vertical profiler and provide AUV docking stations.

Coastal and Continental Shelf Oceanographic Features and Processes

MOOS: The Monterey Bay Aquarium Research Institute (MBARI) has employed advanced mooring platforms in coastal waters for over a decade as part of an ongoing comprehensive Monterey Bay Ocean Observing System (MOOS; Figure 3.3). The main reasons for deploying moorings in coastal settings are to observe the time-series relationship between physical and biological dynamics in upwelling settings, study harmful algal blooms, advance our understanding of the three dimensional carbon cycling process, determine the impact of iron limitation on coastal primary productivity, and serve as a test and development site for new sensors and mooring technology. MOOS utilizes two moorings, located at 36.755°N, 122.025°W (M1) and 36.692°N, 122.390°W (M2), that work together as an array. The MOOS program also includes bi-monthly shipboard oceanographic surveys and routine monitoring of the study region using remote sensing observations. Recently, MBARI has modified the MOOS mooring concept to include satellite based bi-directional communications, event detection and response, as well as

integration and operation with Autonomous Unmanned Vehicles AUV's and automated vertical profilers fitted with optical instruments.

Since 1993, a series of research initiatives, including the ***US GLOBEC North East Pacific*** and ***Coastal Advances in Shelf Transport*** programs, have supported the deployment of a series of subsurface moored radiometers and optical drifters off the Oregon Coast and Northen California (Abbott and Letelier, 1998). The drifters deployed were WOCE Ocean Color Monitor (OCM) Lagrangian drifters, manufactured by METOCEAN Data Systems Ltd. and Satlantic, Inc. These instruments measure the location, sea surface temperature, upwelling radiance at 7 wavebands in the visible (412, 443, 490, 510, 555, and 670 nm (20 nm bandpass); and 683 nm (10 nm bandpass)) and downwelling irradiance at 490 nm (20 nm bandpass). Measurements are made every 90 seconds, averaged over a one hour period, and transmitted to shore-based laboratories via ARGOS. The subsurface moored radiometers are deployed below the first optical depth, between 5 and 10 m depth, and measure downwelling irradiance at the same 7 visible wavebands used in the drifters. All these optical sensors are calibrated by Satlantic, Inc., before deployment.

AVPPO: The Woods Hole Oceanographic Institution has developed a profiling mooring for coastal waters, the Autonomous Vertically Profiling Plankton Observatory (AVPPO). The AVPPO consists of buoyant sampling vehicle and a trawl-resistant bottom-mounted enclosure, which holds a winch, the vehicle (when not sampling), batteries, and controller. Three sampling systems are present on the vehicle: a video plankton recorder, a CTD with accessory sensors, and a suite of bio-optical sensors including Satlantic OCI-200 and OCR-200 spectral radiometers and a WetLabs ac-9 dual path absorption and attenuation meter. At preprogrammed times the vehicle is released, floats to the surface, and is then winched back into the enclosure with power and data connection maintained through the winch cable. Communication to shore is possible through a bottom cable and nearby surface telemetry buoy, equipped with a mobile modem, giving the capability for near-real time data transmission and interactive sampling control.

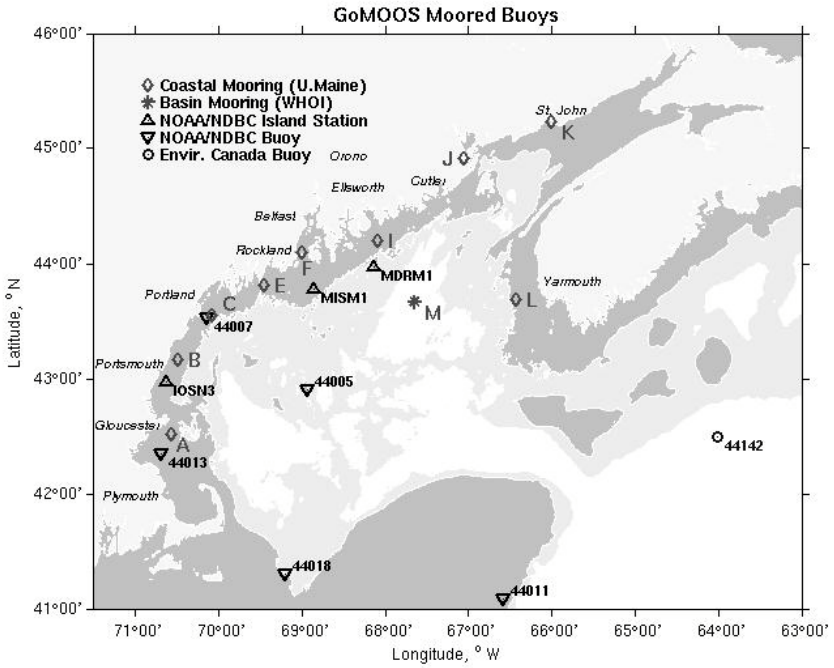

Figure 3.4: Locations of the GoMOOS moorings in the Gulf of Maine. For exact locations see http://gyre.umeoce.maine.edu/GoMoos/gommrg.phtml.

GoMOOS: The Gulf of Maine Ocean Observing System was initiated in late 2000, with the first deployment of the entire mooring array completed in July 2001. GoMOOS was initiated as an opterational observatory, serving as a benchmark for other user-driven ocean observing systems. The primary obective of GoMOOS is to provide the

infrastructure for collecting sustained, long-term observations of the Gulf of Maine region. The backbone of the GoMOOS is the mooring program. Ten mooring are located throughout the Gulf of Maine (Fig. 3.4; see www.gomoos.org for exact locations); one in the deep basin, 4 along the shelf waters, and 6 located in nearshore environments. The standard suite of measurements on each mooring includes metereologic and hydrologic conditions (Fig. AHB2). Four of the GoMOOS moorings also have instrumentation to measure the bio-optical conditions. The GoMOOS program also includes a series of CODAR stations to map the surface currents over the entire Gulf of Maine, circulation and wave modeling programs, as well as utilizing NASA and NOAA remote sensing time series (ocean color, sea surface temperature, winds).

CMO and PRIMER: The interdisciplinary oceanographic programs known as Coastal Mixing and Optics (CMO), Shelfbreak PRIMER (not an acronym), and Synthetic Aperture Sonar (SAS) PRIMER conducted a number of coordinated field experiments in the vicinity of the New England continental shelf over the period from September 1995 to August 1997 (Dickey and Williams, 2001; see www.opl.ucsb.edu). CMO focused on physical, bio-optical, and sedimentary processes on the continental shelf, while the Shelfbreak PRIMER investigated physical processes over the shelf and slope and their influence on sound transmission onto the shelf. The experiment utilized several different observing platforms enabling measurements over space scales from centimeters in the vertical to tens of kilometers in the horizontal and time scales from minutes to the annual cycle. The results of the experiment have led to improved understanding of inter-relationships and couplings among physical, bio-optical, sedimentary, and acoustical properties and processes. Two hurricanes passed near the study site enabling novel research concerning the physical and bio-optical effects of intense atmospheric forcing. Internal solitary waves and their relation to bio-optical events was another highlighted study area.

HyCODE: The Hyperspectral Coastal Ocean Dynamics Experiment (HyCODE) was an Office of Naval Research (ONR) sponsored five-year interdisciplinary program (see www.opl.ucsb.edu). HyCODE field experiments were located off the coast of New Jersey at the Long-term Ecological Observatory site in 15 m water depth (LEO-15), on the west Florida Shelf as part of the ONR Ecology of Harmful Algal Blooms (EcoHAB) program, and in the Bahamas near Lee Stocking Island as part of the ONR Coastal Benthic Optical Processes (CoBOP) program. The main objective of the HyCODE program was to develop an understanding of the diverse processes that control inherent optical properties (IOP) and apparent optical properties (AOP) in the coastal ocean by use of hyperspectral imagery. Platforms included moorings, ships, gliders, AUVs, and aircraft, most of which were equipped with hyperspectral instrumentation. Basic research was centered on the investigation of the impact of relatively small-scale physical, biological, and chemical processes on near-surface spectral IOP and AOP. Some of the processes under investigation for the HyCODE project include advection of optically important material, phytoplankton growth and loss, bubble injection, sediment resuspension, fronts, and internal waves. Applied research focuses on the development and validation of hyperspectral ocean color algorithms. Moorings were used to provide high temporal resolution bio-optical (*i.e.* IOP and AOP) and physical data sets. These experiments were designed to sample the maximum possible number of matched *in situ* IOP and AOP observations for calibrating, groundtruthing, and relating subsurface optical properties (algorithm development) to satellite data, and to develop, test, and validate optical models and high-resolution interdisciplinary models of the coastal ocean.

MEPS: The Marine Environmental Prediction System (MEPS) is a network of moored buoys in Lunenburg Bay, Canada (see www.phys.ocean.dal.ca/programs/cmep/cmep.html). MEPS is part of the CMEP (Centre for Marine Environmental Prediction), a initiative led by Dalhousie University and funded through the Canadian Foundation for Innovation. MEPS consists of three heavily instrumented buoys, a real-time, high speed broadband communications network, and a modeling and analysis system for transforming sensor data into information that can be visualized by a broad range of system users. The buoy network provides data from AOP, acoustic, physical and meteorological sensors to monitor the biological variability and transport of sedimements within Lunenburg Bay. The system is designed to provide both high temporal, spatial and vertical resolution of processes within Lunenburg Bay. This combination of a wide range of sensors and flexible data acquisition system with a large power system and high bandwidth wireless telemetry make this system ideal for validating remote sensing data in the coastal zone.

Equatorial Oceanographic and Air-Sea Interaction Processes

TOGA TAO/TRITON: The Tropical Ocean-Global Atmosphere (TOGA) observing system consists of ~70 moored platforms along the equatorial Pacific to observe oscillations associated with the El Nino and Southern Oscillation (ENSO). These ENSO specific moorings cover the entire equatorial Pacific from 95°W across the date line to 165°E, from 8°N to 8°S. Recently the project name was changed to the Tropical Atmosphere Ocean/Triangle

Trans-Ocean Buoy Network (TAO/TRITON) array to recognize the introduction of TRITON mooring array (http://www.jamstec.go.jp/jamstec/TRITON/) of buoys in the western Pacific by the Japan Marine Science and Technology Center (JAMSTEC); these moorings replaced 12 ATLAS buoys along 137°E, 147°E, and 156°E in 1999.

EqPac: The first moored bio-optical measurements in the equatorial Pacific (0^o, 140^o W) were conducted by the UCSB (formerly USC) during JGOFS in 1991-1993 (Foley *et al*., 1998). More recently, two selected ATLAS buoys in the equatorial Pacific were modified by MBARI to accommodate robust instrument packages for open-ocean bio-optical and biogeochemical measurements as part of SIMBIOS ocean color validation (Figure 3.5). The designs of the two moorings, commonly referred to by MBARI as EP1 (0°, 155°W) and EP2 (2°S, 170°W), are TAO ATLAS buoys modified to host optical and chemical instruments with the objectives:

1. To obtain near real-time moored bio-optical measurements, including L_{WN}, at two locations in the equatorial Pacific for calibration-validation of satellite ocean color sensors.
2. To obtain optical profiles at up to 30 stations per year in the equatorial Pacific, including derivation of L_{WN}, for calibration-validation of satellite ocean color sensors.
3. To use hyperspectral optical data from Monterey Bay and the equatorial Pacific, in conjunction with *in situ* biogeochemical sampling and satellite data, to contribute to bio-optical algorithm development.
4. To determine the spatio-temporal variability in phytoplankton biomass, primary production, carbon dioxide and nutrient distributions, as a result of physical perturbations.

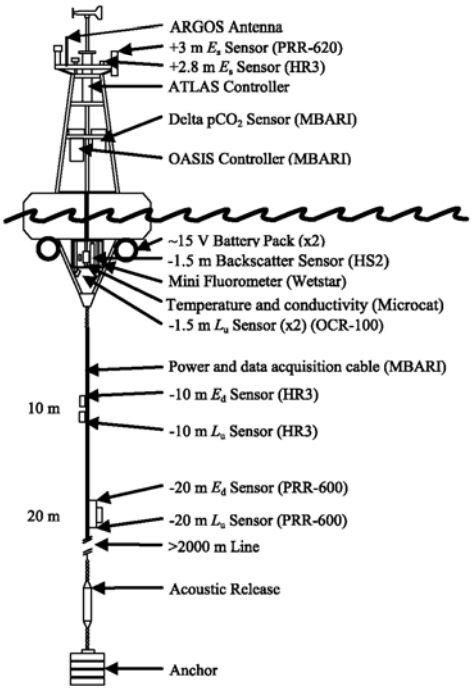

Figure 3.5 Conceptual drawing of the modified ATLAS mooring platform located in the equatorial Pacific (EP1: 0°, 155°W, EP2: 2°S, 170°W). Each optical mooring is equipped with radiance and irradiance sensors, and other equipments labeled above.

PIRATA: The project PIRATA (Pilot Research Moored Array in the Tropical Atlantic) maintains a string of moorings in the Equatorial Atlantic Ocean that is equivalent to the Pacific TAO array (Servain *et al*. 1998). PIRATA is a multinational pilot experiment in operational oceanography, with the participation of Brazil, France and the USA. The PIRATA network consists of 12 ATLAS moorings, extending along the equator and two meridional lines. This geographic configuration is designed to monitor persistently strong wind forcing over the

western Equatorial Atlantic basin, together with seasonal-to-interannual variability in SST in the central and eastern basins. The meridional arrays cover the regions of high SST variability associated with the SST dipole mode. A set of spectroradiometers and fluorometers have been deployed at the *Lambada* mooring (8N, 38W) in the PIRATA array to add a biogeochemical component to the program and to study the effect of the Amazon River/North Equatorial Counter Current, tropical instability vortices, the effect of dust on phytoplankton productivity and carbon cycling in this region. This bio-optical mooring addresses the following three specific objectives:

1. Provide high temporal resolution (6 times daily) in-situ spectroradiometric measurements to fill missing satellite measurements due to dust, clouds, and gaps due to satellite orbit patterns, sun glint avoidance and tilt maneuvers.
2. Use the in-situ measurements to evaluate atmospheric correction algorithms by comparing the in-situ and satellite derived normalized water leaving radiance estimates.
3. Use the combination of the chlorophyll concentrations derived from the in-situ spectroradiometric measurements and fluorometric measurements to study both temporally short events, such as tropical instability waves and the effect of aeolian dust deposition on marine productivity (including the time lag between dust deposition and increased chlorophyll biomass), as well as long-term trends in primary production and biogeochemical cycles in this region.

***JGOFS EQPAC Drifter Studies*:** The first deployment of a drifting buoy with high precision optics (McLean and Lewis, 1991) was carried out in 1994, in association with the JGOFS Equatorial Pacific Process Study. The drifters were air-launched from a NASA P-3 low altitude aircraft, which was carrying out remote sensing support of the seagoing mission. The buoy was a modified Compact Meteorological and Oceanographic Drifter (CMOD) manufactured by MetOcean Data Systems. A seven channel (450, 492, 532, 562, 656, 683, 700 nm) downlooking radiance sensor (Satlantic) was deployed on the buoy approximately 0.5 meters below the sea-surface and a single uplooking irradiance sensor (490 nm) was deployed on the extendable mast above the surface. Raw data was communicated via the ARGOS system. Radiances were propagated to and through the sea-surface using empirical algorithms for spectral attenuation, and normalized by the spectral downwelling irradiance inferred from the measured value at 490 nm and a model for spectral sun and sky irradiance. Two buoys were successfully deployed during this experiment and operated for several months. The resulting normalized water-leaving radiances were used to estimate chlorophyll concentrations. Based on these data, several novel syntheses resulted, ranging from a means to integrate shipboard estimates of primary production and grazing over the larger scale (Landry *et al*., 1997), and an improved understanding of the role of tropical instability waves in the production dynamics of this region (Foley *et al*., 1997). These first drifting buoys were the predecessors for subsequent optical deployments on several platforms, notably the surface WOCE/OCM drifters used extensively by Oregon State University (Abbott and Letelier, 1998).

Oceanographic Processes in Oligotrophic Water Masses

BATS/BTM: The Bermuda Testbed Mooring (BTM) was first deployed in 1994 and continues in operation today (Dickey *et al*., 1998b, 2001a). High frequency, long-term data measured by the BTM instruments are used for studies and models of upper ocean biogeochemistry and physics, to develop and test new multi-disciplinary sensors and systems, and to provide validation data for satellite ocean color imagers including SeaWiFS. The complementary Bermuda Atlantic Time-series Study (BATS) was established in 1988 as part of the U.S. JGOFS program, to characterize, quantify, and understand processes in the Sargasso Sea that control ocean biogeochemistry, especially carbon, on seasonal to decadal time scales. BATS ship sampling is done monthly and every two weeks during the springtime. Ship-based bio-optical profiles (sampling in concert with BATS) and remotely-sensed ocean color data have been obtained at the BATS site (Fig. 3.2) since 1992 by the Bermuda Bio-Optics Program (BBOP; Siegel *et al*. 2001). BTM measurements were an important addition as processes with time scales of less than a few weeks (*e.g.*, eddies, wind-events, and transient blooms) cannot be resolved with monthly or bi-weekly shipboard observations. The BTM program has tested and utilized a broad range of autonomous sampling sensors and systems. These include new measurements of pCO2, dissolved oxygen, nitrate, trace elements (*e.g.*, iron and lead), several spectral inherent and apparent bio-optical properties, ^{14}C for primary production, and currents (Dickey *et al*., 1998a, 2001). Several bio-optical systems designed to measure IOP and AOP have been tested using the BTM (Figure 3.6). The bio-optical instuments (placed on the surface buoy and at 2 to 4 different depths) are used to determine relevant remote sensing parameters such as remote sensing reflectance (*e.g.*, Dickey *et al*., 2001; Zheng *et al*., 2002, 2003). The depths are optimally selected to enable extrapolation of subsurface radiance to the

surface. An advantage of mooring validation is the high number of match-up data for satellite calibrations (data are collected regardless of cloud cover as well).

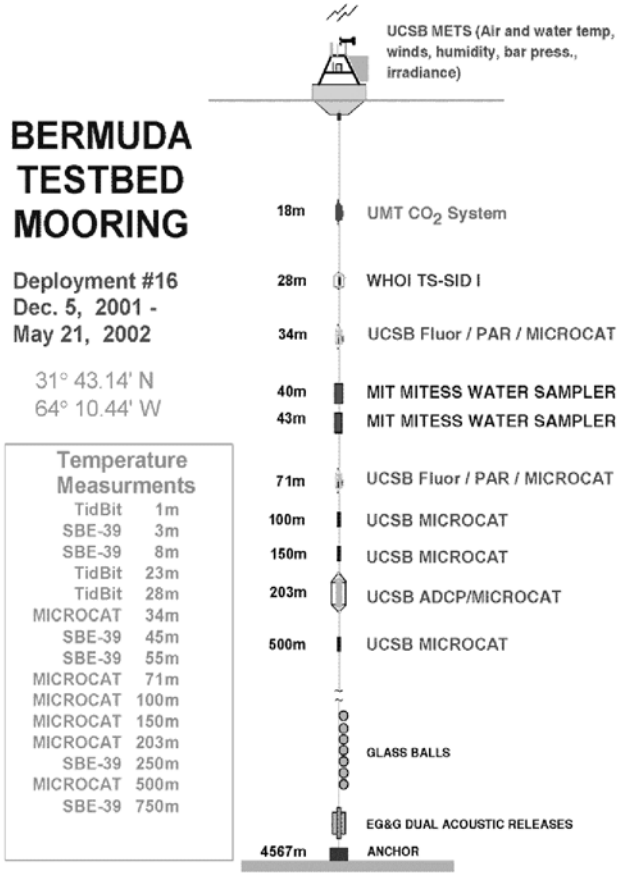

Fig. 3.6. Schematic illustration of the Bermuda Testbed Mooring (BTM), showing an example of the taut-wire mooring, surface buoy, and instrument locations.

HOT: The Hawaii Ocean Time-series (HOT) program was initiated in 1988 in parallel with the BATS program program. The HOT measurements are conducted at the oligotrophic Station ALOHA (22^{o}-45'N, 158 ^{o}-00'W) site north of Oahu. HOT's main objective is to obtain a long time-series of physical and biogeochemical observations in the North Pacific subtropical gyre to:

- document and understand seasonal and interannual variability of water masses, develop climatologies of physical and chemical variables,
- document and understand seasonal and interannual variability in primary production, new production and particle export from the surface ocean,
- quantify time-varying concentrations of carbon dioxide, and
- study the ecology of a subtropical gyre.

HOT's core measurements were selected to provide a data set to improve existing C-N-P biogeochemical models. Selected data trends related to the intensification of N and P cycles, changes in microbial community structure and the role of high frequency physical events have been documented. An interdisciplinary instrumented mooring was deployed at the HOT site in 1996, and continued in operation until about 2000 (Letelier *et al*., 2000). The mooring experiment, dubbed HALE ALOHA (Hawaii Air-sea Listening Experiment; Hale is also a Hawaiian word translated "at the house of") initially included meteorological, physical, optical and chemical sensors. Additional instruments,

including two water samplers designed for trace metal and nutrient analyses (Ed Boyle, MIT; Pers. Comm.), current meters, conductivity-temperature (CT) sensors, and a cellular phone for daily data transmission and instrument interrogation, were added during the HALE ALOHA-II experiment. Since that time, the mooring has been recovered and redeployed a total of five more times, and the mooring instrument configuration has remained more, or less, the same. The data collected by this deep-sea mooring facility are critical to the detection and understanding of the mesoscale processes hypothesized to be the dominant causes of biogeochemical variability in this subtropical gyre habitat. The recently funded NOPP MOSEAN program (www.opl.ucsb.edu) will deploy a new HALE ALOHA mooring, quite similar to the BTM, near the HOT site as well as a shallow water mooring in Santa Barbara Channel off California. Data collected by the deep-sea mooring are essential for detection and understanding of the mesoscale processes that contribute significantly to biogeochemical variability in this subtropical gyre habitat.

The Southern Ocean

The Antarctic Polar Front is a complex set of meandering jets, which appear to support enhanced primary productivity. The U.S. Joint Global Ocean Flux Study (JGOFS) conducted a series of survey and process studies in part to study the processes regulating primary productivity in this high nutrient, low chlorophyll (HNLC) region. Abbott *et al*. (2001) deployed a set of surface velocity drifters, some of which were equipped with bio-optical sensors, to study the temporal and spatial scales of biological and physical processes in the Antarctic Polar Frontal Zone (APFZ). There were two primary sets of deployments: November 1997 before the spring bloom and January 1998 after the spring bloom. The November deployment revealed a strong spring bloom, although it decreased over time, persisted at somewhat higher values throughout the drifter deployment than the bloom observed at a fixed moored optical array. In late spring when incoming solar radiation began to increase, the vertical motions associated with the meanders strongly affected the accumulation of phytoplankton biomass, primarily through their impact on light availability. Weaker meandering was observed in the January deployment, and chlorophyll values remained relatively constant. As the bloom began to decay, it appears that nutrient availability became more important in regulating phytoplankton photosynthesis. Some of the drifters in the November deployment were deployed in coherent clusters, thus allowing us to calculate vertical velocities associated with the meanders. Estimates of fluorescence/chlorophyll suggest that areas of upwelling and downwelling alternately decrease and increase photosynthetic stress, perhaps as a result of changes in the availability of iron or light during the formation of the bloom.

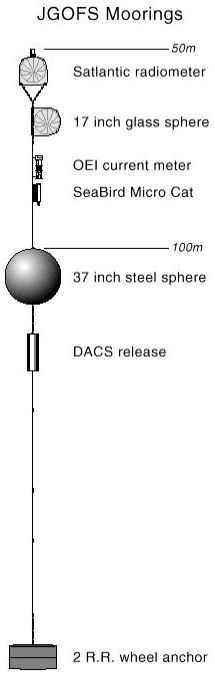

Figure 3.7: A subsurface moored bio-optical instrument array

deployed during Southern Ocean JGOFS (Abbot *et al*. 2000).

As part of the Southern Ocean JGOFS program, 12 subsurface optical moorings were deployed in a grid formation to study the mesoscale variability around 60.5°S, 170.0°W, between October 1997 and March 1998. Each mooring was a bottom-tethered mooring extending from the sea floor to 50 m below the sea surface (Fig. 3.7). Attached to each of these moorings was an irradiance sensor head that measured downwelling irradiance at seven wavebands in the visible from a depth of 50 m (Abbott *et al*. 2000). In addition, an array of physical and optical drifters was deployed within the Antarctic Polar Front zone to study the dynamics of the water masses meandering along this front (Abbott *et al*. 2001). Previously, optical drifter deployments had been successful in sampling eddies off the Antarctic peninsula (Letelier *et al*. 1997).

California Current System Drifter Studies

Abbott and Letelier (1998) used data from bio-optical drifters deployed in the California Current. to estimate the decorrelation time scales (a measure of persistence) for chlorophyll (as estimated from radiance ratios) and for sun-stimulated fluorescence/chlorophyll (as a proxy for photosynthetic rate). These scales were significantly different in the nearshore zone (<200km from shore) while they were nearly identical in the offshore zone (>400km from shore. This implies that the ability to harvest light (as indicated by chlorophyll content) was not in balance with the ability to use light (as indicated by fluorescence/chlorophyll) in the nearshore zone. The similarity of the decorrelation time scales in the offshore zone suggest that the phytoplankton was more nearly in equilibrium. Abbott and Letelier (1998) also noted that physical time scales (as indicated by sea surface temperature) were nearly the same as the biological time scales in the nearshore zone but were significantly longer in the offshore zone. The short time scales (2 days) in the nearshore zone is consistent with variable upwelling and with previous observations of strong correlations between temperature and phytoplankton chlorophyll. In the offshore zone, physical processes affecting SST and chlorophyll are different, and there was little correlation between the two. Thus bio-optical drifters can be used to study the relative roles of physical and physiological processes in governing the spatial patterns ofphytoplankton. Similar drifter deployments have been made as part of the Global Ecosystem Dynamics (GLOBEC) Northeast Pacific Program off the Oregon coast in 2000 and 2002.

3.3 MOORING AND DRIFTER ARRAY CONFIGURATIONS

Optical moorings designed for long-term deployments at open ocean sites must be capable of maintaining the integrity of optical and other measurements while the instruments are unattended for prolonged periods of time. Details of traditional mooring engineering concepts, theories and hardware configurations can be found in Berteaux (1991). Successful early examples of multiple-task optical moorings were the Multivariable Moored System (MVMS; Dickey *et al*. 1991, 1993) and the Bio-optical Moored System (BOMS; Smith *et al*. 1991). Optical drifters can be designed for short or long term deployments, as recoverable, or disposable, in coordination with various oceanographic sampling methods.

Moored Surface Buoys

Moored buoys generally have similar design configurations consisting of a tower, flotation buoy, bridle, mooring line, acoustic release, and anchor (Table 3.1). The TOGA array, for example, uses both the Profile Telemetry of Upper Ocean Currents design (PROTEUS; McPhaden *et al*., 1991) and the Autonomous Temperature Line Acquisition System (ATLAS) buoys designed by NOAA/PMEL (Milburn and McClain 1986). The PROTEUS and ATLAS frames are essentially similar in design (Figures 3.3 and 3.5). The ATLAS buoy employs a 2.3 m diameter toroid, fabricated with fiberglass over a foam core, a simple aluminum tower (+4.9 m) and a stainless steel bridle capable of holding a stainless-steel instrument cage. Each mooring platform is equipped with a low-cost ATLAS wind and thermistor chain array (Hayes *et al*. 1991). Two of the ATLAS buoys in the equatorial Pacific (M1 and M2, see above) were modified to host optical and chemical instruments. Currently deployed MOOS moorings are also of a PROTEUS design, modified to accommodate an instrument controller, solar panels, an elevator assembly for mounting near-surface sensors, and instrument cages for additional sensors at 0, 10 and 20 m depth. The elevators allow service of sensors, which are subject to substantial bio-fouling, at monthly intervals. The

stainless steel cages at 10 and 20 m protect the instruments. The new MOOS moorings are welded from aluminum utilizing a Surlyn discus buoy.

Table 3.1: Characteristics of moored bio-optical buoys, selected as examples from instrumented mooring networks covering the oceanographic regimes illustrated in Figure 3.1.

PROJECT:	MOOS M1 & M2	TAO/TRITON EP1	TAO/TRITON EP2	PIRATA Lambaba	HOT: HALE ALOHA	MEPS	BATS BTM
INSTITUTION:	MBARI	MBARI	MBARI	Multinational	UH	Dalhousie University	UCSB
LOCATION:	36.76°N, 122.02°W 36.69°N, 122.39°W	0°N, 155°W	2°S, 170°W	8°N, 38°W	22.75°N,158°W	Lunenburg Bay, Canada	31.7°N,64.2°W
DEPTH (m)	2000 to ~4000 m	>2000	>2000		4750	20 m	4600
BUOY TYPE:	PROTEUS	ATLAS	ATLAS	ATLAS	Guardian	Surlyn discus	WHOI/UCSB
Diameter (m)	2.5	2.3	2.3	2.3	3	1.2m	3
Height (m)	5.5	4.9	4.9	4.9	~5?	4	5
MOORING TYPE:	Semi-Slack Reverse Catenary	Taut Wire	Taut Wire	Taut Wire	Semi-Taut Wire	Semi-Taut Bi-moor	Semi-Taut Wire
POWER	Solar Panels & Batteries	Battery Pack	Battery Pack	Battery Pack	Solar Panel & Batteries	Solar Panels & Batteries	Battery Pack
DEPLOYMENT DURATION*	1 Month	1 Year	1 Year	???	1 Month	6-12 months	6 Months
CONTROLLER/ DATA-LOGGER	OASIS (MBARI)	OASIS & ATLAS	OASIS & ATLAS	STORE-X	Multiple Data Loggers	DACNet	Multiple Data Loggers
ON-BOARD DATA STORAGE	Yes	Yes	Yes	Yes	Yes	Yes	Yes
NEAR REAL-TIME TELECOMM	RF and Satellite Comms.	ARGOS	ARGOS	ARGOS	None	High speed broadband wireless	Inductive Link, Acoustic & ARGOS Telemetry
PLATFORM NAVIGATION	GPS	ARGOS	ARGOS	ARGOS	ARGOS	GPS	ARGOS
FIGURE:	3.3	3.5	3.5			3.9 & 3.10	3.6 &3.8
* Nominal operating service life between refurbishment/replacement visits.							

A newly designed buoy was developed jointly by UCSB and WHOI to accommodate a variety of interdisciplinary sensors and systems (Figure 3.8). Some of the technical features of the new buoy include: reduced size for safer ship operations, removable instrumentation well, upgraded tower, improved and removable bridal, and overall total weight reduction. The buoy is equipped for satellite data telemetry, using ARGOS at present, and an Iridium system will be added in May 2003. The expected lifetime of the new buoy is about 10 years. The new buoy was deployed at the BTM site in September 2002, and another of this design is currently under construction to replace the present HALE-ALOHA (see above).

Fig. 3.8: Photograph of the newly designed and recently deployed interdisciplinary BTM surface buoy (www.opl.ucsb.edu).

The MEPS buoys are 1.2m Surlyn discus buoys. These house the DACNet computer system, wireless telemetry system, batteries and solar panels. The AOP sensors are deployed on a secondary surface-tracking package with a 33cm float to minimize shading. This small float is suspended within a triangular guard frame 9m on a side. The AOP package consists of a hyperspectral Es, a hyperspectral Lu sensor (at 40cm), and a chain of four, four channel irradiance sensors placed at 2, 4, 8, and 12m below the small surface float. The system also includes two ADVs (acoustic doppler velocimeters) and an ADCP (acoustic doppler current profiler) on a bottom-mounted frame. Power and real-time telemetry are connected via special Kevlar electromechanical cables to the main discus buoy. To avoid tangling of cables and the various packages, both the surface tracking AOPs and the main discus bouy are bi-moored to train wheels at the bottom. A schematic of the system configuration is shown in Figure 3.9. A photo of one of the buoy systems deployed is shown in Figure 3.10.

Another buoy package in common use is the HyperTSRB, a tethered buoy often deployed for vicarious calibration of remote sensing platforms. This system was originally developed for the ONR CoBOP and HyCODE programs to measure hyperspectral reflectance near the ocean surface. A typical configuration uses an in-air hyperspectral irradiance sensor to measure incident irradiance and a hyperspectral radiance sensor to measure upwelled radiance 50 cm below the surface. The buoy hull uses a 33 cm diameter flotation collar to keep the radiometers at the surface. Eight of these systems were used as calibration/validation references for the hyperspectral NRL PHILLS airborne imager during both HyCODE and CoBOP experiments. More recent configurations also utilize a multichannel chain of four irradiance radiometers below the surface (typically at 2, 4, 8 and 16m) for computing the diffuse attenuation coefficient. This type of configuration is used as part of MEPS. Other autonomous coastal monitoring systems have used these sensors as well, using the STOR-X and a cellular phone for data telemetry.

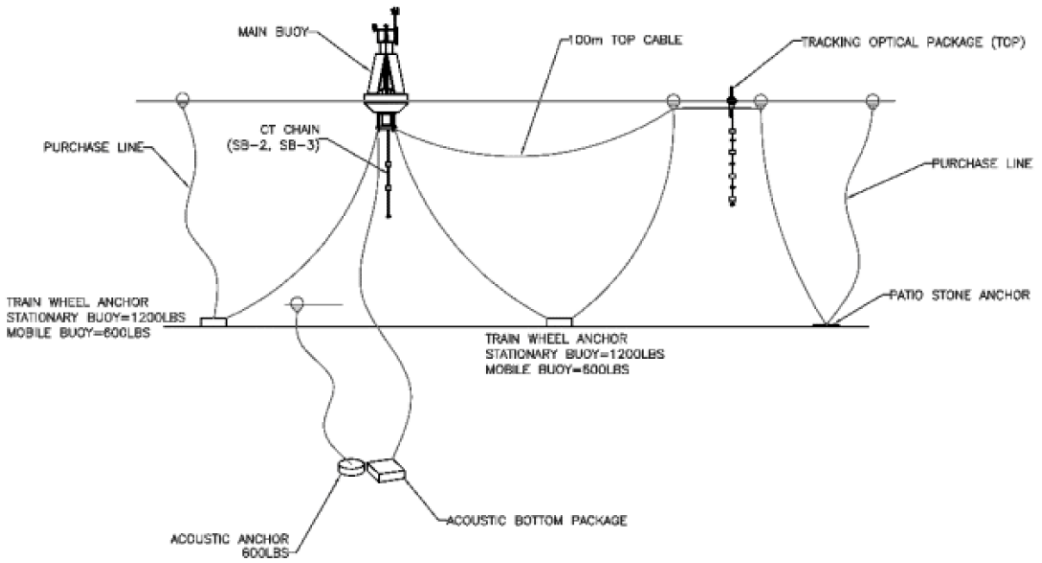
MAIN BUOY
100m TOP CABLE
TRACKING OPTICAL PACKAGE (TOP)
PURCHASE LINE
CT CHAIN
(SB-2, SB-3)
PURCHASE LINE
TRAIN WHEEL ANCHOR
STATIONARY BUOY=1200LBS
MOBILE BUOY=600LBS
PATIO STONE ANCHOR
TRAIN WHEEL ANCHOR
STATIONARY BUOY=1200LBS
MOBILE BUOY=600LBS
ACOUSTIC BOTTOM PACKAGE
ACOUSTIC ANCHOR
600LBS

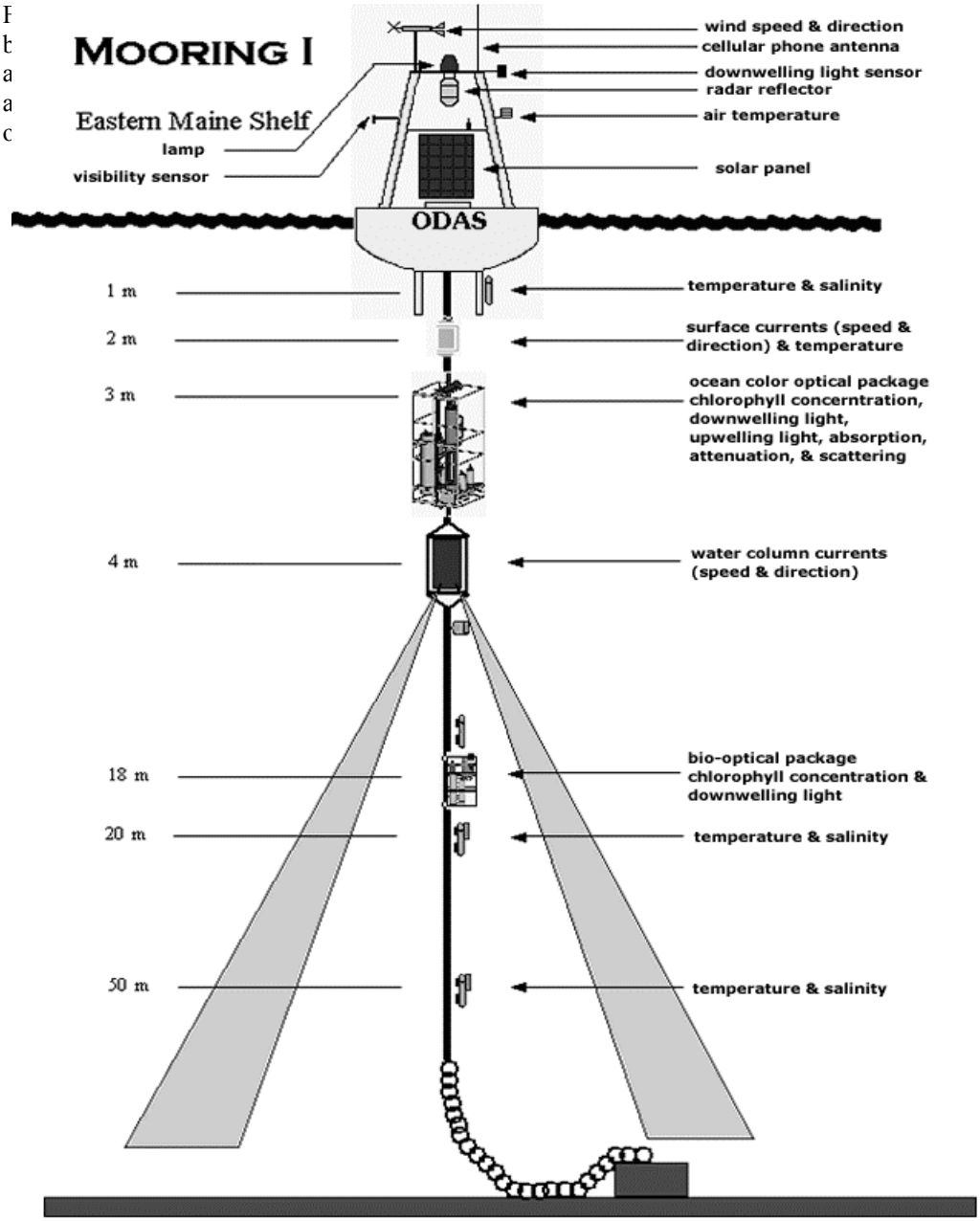
MOORING I
Eastern Maine Shelf
lamp
visibility sensor
wind speed & direction
cellular phone antenna
downwelling light sensor
radar reflector
air temperature
solar panel
ODAS
1 m
temperature & salinity
2 m
surface currents (speed & direction) & temperature
3 m
ocean color optical package
chlorophyll concerntration,
downwelling light,
upwelling light, absorption,
attenuation, & scattering
4 m
water column currents
(speed & direction)
18 m
bio-optical package
chlorophyll concentration &
downwelling light
20 m
temperature & salinity
50 m
temperature & salinity

Figure 3.11: Conceptual drawing of the "Ocean Color" GoMOOS moorings that have bio-optical instrumentation for use in ocean color remote sensing validation/calibration. The right panel shows the above water irradiance sensor mounted on the buoy, the ocean color bio-optical instrumentation package mounted at 3m, and the small optics package mounted on the mooring at 18 m (from top to bottom).

Buoys are usually moored using either a taut, or slack, wire design, although the recent introduction of wires with more spring offers advantages of both designs. Wire types include:

- ***Taut-Wire Surface Moorings***: For the ATLAS systems used in the TAO, TRITON and PIRATA mooring networks, the upper 500 m of the mooring utilizes a jacketed 1.27 cm non-rotating (nilspin). This segment is followed by an eight-strand plaited nylon line (1.9 cm) extending to just above the ocean bottom, where an acoustic release couples it to a ~2000 kg railroad wheel anchor. Taut-line moorings, with a nominal scope of 0.985 (ratio of mooring line length to water depth) are used in water depths greater than 1800 m to ensure that the upper section of the mooring is nearly vertical. More detailed information on the ATLAS taut-wire mooring design is available on-line at (http://www.pmel.noaa.gov/tao).
- ***Slack-Wire Moorings:*** The TAO slack-line moorings have a scope of 1.35, due to either shallow bathymetry, or severe current regimes. GoMOOS moorings are slack-wire moorings, with a scope of ~ 1.32, using 80 m of wire and 100 m of chain, anchored by 3 railroad wheels (Fig. 3.11). In these cases, the upper portion of the mooring is kept close to vertical (but less so than with taut-line moorings) by using a reverse catenary design. The reverse catenary design allows the capabilities of being stretched under tension while utilizing traditional catenary concepts through a semi-slack method. Although taut-line moorings maintain subsurface sensor locations at or near desired depths, surface instruments may be subjected to stronger forces from waves and currents. The slack-line moorings provide greater flexibility in the upper water column, which may help reduce these forces.
- ***Semi-slack/taut Wire Mooring:*** MOOS moorings are on 'semi-slack' S shaped tethers with a 1.20% scope. The BTM and HALE ALOHA 3 m diameter buoy platforms have been previously configured as semi-slack moorings. However, the new configurartions will be an inverse catenary design to reduce stress on all mooring components..

Subsurface Moorings

Subsurface moorings tested off Hawaii and used in the Southern Ocean during JGOFS (Fig. 3.7) are designed to minimize the vertical motion of radiometers derived from wave action and to remove the shading effect of a surface buoy and wiring. The mooring hardware includes two glass spheres and one large steel sphere. The 17" glass sphere beneath the sensor head was used to limit the range of tilt of the sensors. Note, however, that the mooring design allows vertical and horizontal movement of the sensors with variations in currents.

Profiling Moorings

Profiling optical moorings generally consist of a buoyant instrumented vehicle and a bottom-mounted enclosure housing a winch, controller and batteries if used autonomously. Profiles are achieved by paying out a tether which can also allow communications between the controller and instruments on the vehicle. Communications with a shore-based server, for example with a cell phone modem, allows data transmission and periodic updating of mission parameters such as profiling frequencies and minimum profile depth. Surface detachment of the profiling vehicle from the tether can facilitate instrument maintenance without recovery of the whole system.

Drifting Buoy Configurations

Drifting buoys have been deployed with AOP sensors in various configurations, most notably the ship-launched or air-launched CMOD type (McLean and Lewis, 1991), and the more common WOCE/OCM type, both manufactured by MetOcean Data Systems Limited. Both systems have surface tracking in-water multichannel radiance radiometers, and a single channel above water irradiance sensor (490 nm) and telemeter data back to the user via the ARGOS system. Due to bandwidth restrictions, the systems report an hourly average of radiometric measurements sampled every 90 seconds. Typically (latitude dependent) 12 data collections are reported to the user per day.

The CMOD type utilized a gas cartridge inflatable float around an 11cm diameter hull containing batteries, computer system and an ARGOS transmitter. At the base of the hull a seven channel radiance sensor (OCR-100) provided a nadir view of the light field at a depth of 50cm. At the top of the ARGOS antenna mast, a single channel (490 nm) irradiance sensor provided a reference for ambient solar radiation. A conical cloth drogue and base weight provided platform stability.

The WOCE type drifter uses a standard 35cm fiberglass hull with batteries, computer and ARGOS transmitter (Fig. 3.12). In the WOCE type buoys, a 1m diameter holey sock drogue located about 10m below the buoy is used to significantly improve water current tracking capabilities. A seven channel radiance sensor (OCR-100) is placed on the bottom of the hull, offset and angled ten degrees off nadir to avoid interference from the drogue. A single channel (490 nm) irradiance sensor is located on top of the hull. Since the irradiance sensor is very close to the water surface, it may become submerged, thus a submergence sensor is used to avoid collecting surface irradiance when the sensor is below the surface. In experiments off the Oregon Coast, the typical lifetime for these drifters was 3 - 7 months, although some failed immediately upon, or shortly after, deployment, and one lasted for 10 months. During the Southern Ocean Iron Enrichment Experiment (SOFeX) in 2002, several WOCE drifters were deployed by OSU, in coordination with deployments of a more heavily instrumented recoverable drifter by MBARI (Fig. 3.12 and Table 3.2).

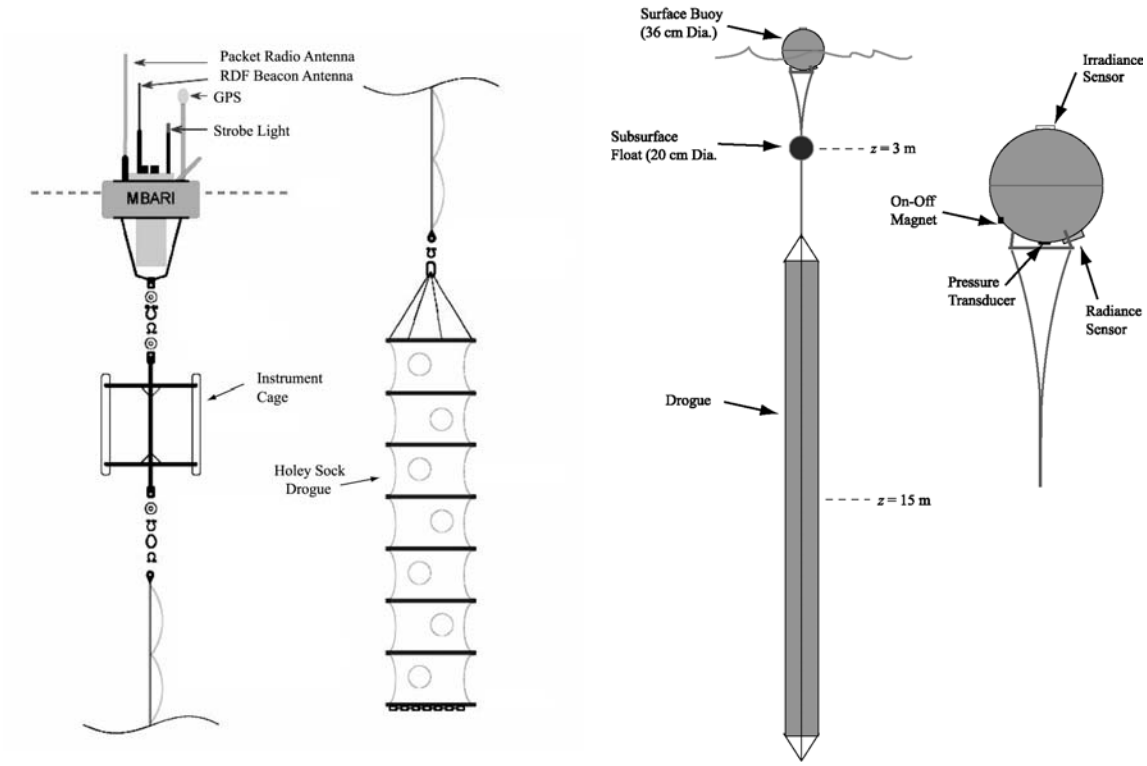

Fig. 3.12: Configurations of drifters that were used during SOFeX 2002. The panel on the left schematically shows the configuration of the "short term" MBARI drifter, while the panel on the right shows the configuration of the "one-use" OSU/WOCE drifter.

3.4 MEASUREMENT METHODS AND INSTRUMENTATION

Many of the variables described as required and highly desired in Volume I, Chapter 3 (Table 3.1) can be measured using arrays of instruments mounted on buoys[3], either moored or free-drifting. The protocols covering instrument performance characteristics, and related characterization and calibration methods, for radiometers (Volume II, Chapters 2 and 3), IOP instruments (Volume IV, Chapters 2, 3 and 5), *in situ* chlorophyll a fluorometers (Volume V, Chapter 3), and instruments for ancillary measurements such as Conductivity-Temperature-Depth (CTD), wind speed and direction, and barometric pressure (Volume II, Chapter 1) are fully applicable to the use of such instruments on buoys. These topics will not be repeated here. On the other hand, while methods for making these measurements from buoys have much in common with the corresponding shipboard measurement methods for radiometry (Volume III, Chapter 2), IOP (Volume IV), and ancillary measurements (Volume I, Chapter 4), the protocols for measurement methods on buoys must take account of special factors:

1. All measurements must take place autonomously, without real-time hands-on operator intervention.
2. Automated measurements must be reduced to digital (or less-often analog) form, and either transmitted via a telecommunications link to a base laboratory, and/or stored on board for retrieval when the buoy is visited for maintenance, or recovery, at time intervals typically ranging from weeks to months. Especially in the case of free-drifting buoys, which are often treated as expendable and are not routinely recovered, the data must be retrieved over typically low-bandwidth telecommunications links (such as ARGOS); therefore, data retrieved in this way must usually be processed on-board and only limited data, *e.g.* temporal averages and standard deviations, are transmitted.
3. Although special buoy designs permit continuous profile measurements of some variables over depth in the water column, more typical buoy configurations are instrumented to make time series measurements only at the surface and a few discrete depths.

Table 3.2 Characteristics of drifting bio-optical buoys, selected as examples from the experimental projects discussed in the text.

PROJECT:	**SOFeX**	**JGOFS EQPAC**	**SOFeX**
INSTITUTION:	MBARI	Dalhousie University	OSU
LOCATION:	Southern Ocean	Equatorial Pacific	Southern Ocean
DEPTH (m)	>2000	>2000	>2000
BUOY TYPE:	Toroid Float & Payload "Can"	CMOD (A size sonobuoy)	WOCE (sphere)
Diameter (m)	1	.33	0.35
Height (m)*	1	.6	< 0.3
DROGUE:	Holey Sock	cloth cone and base weight	WOCE type**
POWER	Batteries	Batteries	Batteries
DEPLOYMENT DURATION***	2 Weeks (recovered)	3-6 Months(expendable)	6 Months (expendable)
CONTROLLER/ DATA-LOGGER	OASIS (MBARI)	MetOcean	???
ON-BOARD DATA STORAGE	Yes	No	No
TELECOMM	RF Packet Radio	ARGOS	ARGOS
PLATFORM	GPS	ARGOS	GPS & ARGOS?

[3] An instrumented buoy that is tethered to a ship, tower, or shore facility, and is actively attended by an operator during use, is simply a particular instrument deployment mechanism used in shipboard (or equivalent platform) measurements. The protocols for this type of buoy and instrument configuration are those applicable to any other shipboard measurement method, and they do not fall within the context of this chapter.

NAVIGATION			
FIGURE:	3.12	3.12	3.7B
* Above waterline. ** A 12 m long fabric tube, 40 cm in diameter, suspended below a subsurface float at –3 m, which was in turn connected to the surface float using an elastic tether to isolate the drogue from surface wave motion. *** Nominal operating service life between refurbishment/replacement visits.			

4. Radiometric field measurement methods designed to minimize platform shading and reflection artifacts are needed for autonomous measurements on buoys. The more successful methods used for shading avoidance in operator attended measurements from ships, *i.e.* free-fall profiling (Volume III, Chapter 2), are not readily applied to radiometric measurements on moorings and drifters. The unusual MOBY platform (Volume VI, Chapter 2) is an example of a buoy and instrument configuration designed specifically to address this problem, but it would be neither affordable, nor practical, to replicate such a configuration in the vast majority of projects where bio-optical buoys are appropriately deployed (Section 3.2 above).

5. Unattended instruments on buoys are either immersed in water, or exposed to the atmosphere, continuously for periods of weeks to months without opportunity to clean optical windows, or other exposed sensor surfaces. In this situation, the performance of buoy instrumentation is subject to progressive degradation due to marine organism growth on sensors in water (biofouling), or salt, dust and/or bird dung deposition in air.

The remainder of this section describes methods for acquiring reliable measurements under the constraining conditions described above (see also the related methods in Vol. VI, Chapter 2, as applied to the more specialized MOBY observatory). The discussion emphasizes the mounting and integration of radiometric, optical, fluorescence, meteorological, CTD, and other sensors under the control of an on-board microcomputer, pre-processing and storage of the data measured by those sensors, and near-real-time transmission of selected data values to ships, or laboratories ashore. Essential characteristics of instrument arrays are summarized in Tables 3.3 and 3.4, respectively, for moored and drifting buoy examples. Specific commercial[4] and custom instruments listed by model, or name, in Tables 3.3 and 3.4 are briefly described below.

Instrument Control and Data Acquisition

A critical aspect of any mooring or drifter platform is its instrument controller and its ability to perform in harsh environments. The system controller must be configured to communicate with instruments, operate electromechanical devices (*e.g.* shutter mechanisms), store measured data and metadata (*e.g.* GPS time, latitude and longitude), preprocess measurements and transmit the resulting parameters to a ship or laboratory. Generically, a system controller consists of a microcomputer interfaced to an array of instruments, the buoy's power source (batteries and/or solar cells), and sometimes a telecommunications link. Many of the instruments used on buoys have some sort of internal microcomputer, operate semi-autonomously to acquire data scans, store the data internally, perhaps average scans over a specified time interval, and transmit digital data to the controller; the instrument controller interfaces to these digital-format instruments using either multiple single channel interfaces (*e.g.* serial RS232), or a network protocol interface (*e.g.* serial RS485 or parallel IEEE-488). Other instruments may produce an analog output, in which event the controller's microcomputer must also be interfaced to one or more analog-to-digital (A-to-D) converters; for most such applications, it is necessary to calibrate the A-to-D converter by recording it's digital responses to known voltage inputs. In other controller-instrument configurations, analog devices may be connected to A-to-D ports of a digital instrument, *e.g.* a CTD, and communicated to the controller as part of its data frame.

Recent development of smaller Ethernet devices has allowed the creation of Local Area Network on moorings, which can provide easy communications between both individual system controllers and serial output from instruments. For example a controller may be physically separated from instruments connected to an Ethernet RS-

[4] Certain commercial equipment, instruments, or materials are identified in this document to foster understanding. Such identification does not imply recommendation or endorsement by the National Aeronautics and Space Administration, nor does it imply that the materials or equipment identified are necessarily the best available for the purpose.

232 hub. In another variant developed by UCSB for the BTM, self-contained, battery operated data acquisition systems at three depths combine acoustic telemetry with ARGOS satellite data telemetry for near real-time data transmission.

The systems used on the GoMOOS bio-optical moorings are a blend of the examples described above. Each GoMOOS mooring is controlled by a Campbell Scientific CR10X control system. The Campbell system controls the power and sampling for all of the metereological sensors, the current (Aanderra and RDI ADCP) and hydrographic (SeaBird SBE37 and SBE16 temperature and conductivity) sensors, as well as the wave sensor. The Campbell system also controls the mooring to shore transmissions of the data, which are mainly done using hourly cellular phone communications. Most moorings also utilize GOES transmissions as a backup method to transmit data to shore in case of cellular phone problems. Because of limitations of the Campbell data logger in terms of storage space and data resolution, it was necessary to utilize a separate data logger to collect, store and pre-process the bio-optical data. The data logger was developed with WETLabs for implementation on the GoMOOS moorings. The data logger has a microprocessor and firmware to control the power and sampling to 4 externally connected sensors. The data logger has 4 serial (RS232) input ports, one RS232 output port and a power port that can be connected to a battery power supply. The GoMOOS implementation of the data logger firmware controls the sampling period and power to each of the 4 serial input ports. The GoMOOS optics data logger can either be set up to run in autonomous mode, or can be controlled externally via RS232 communications. The optics data logger records all of the raw data onto an on board flash disk for later retrieval and processing. The data logger is programmed to average each of the input data streams from each instrument, and outputs the averages and diagnostics to the output RS232 serial port.

Table 3.3 (Part 1 of 2): Radiometric, bio-optical and ancillary measurements and instruments on selected moored bio-optical buoys; see Table 3.1 and Figures 3.1 and 3.2 for information on the location, buoy type and mooring configuration of each.

Moored Buoy Array:		**MOOS**	**TAO (EP1 & EP2)**		**PIRATA (Lambaba)**
Variable	**Sensor**	**z (m)**	***z* (m)**	***z* (m)**	***z* (m)**
$E_s(\lambda)$	PRR-620	~ +4	+3		+3
	HR3	~ +4	+2.8		
	MiniSpec-I			+0.5	
	OCR504 ICSA				
$E_d(z, \lambda)$	PRR-600	-10, -20	-20		
	HR3	-10, -20	-10		
	OCI100				
	OCI200				
	OCR504 ICSW			-2,-4,-8,-12	
$L_u(z, \lambda)$	PRR-600	-10, -20	-20		
	HR3	-10, -20	-10	2	
	OCR100	-1.5	-1.5		-3.6, -9.6
	OCR200				
	MiniSpec-R			-0.5	
	OCR507 R10W				
$E_u(z, \lambda)$	PRR-600	-10, -20	-20		
	HR3	-10, -20	-10		
Chl *a* Fluorescence	WETStar	-1.5	-1.5		-9, 40
	DFLS				
	HS2	-1.5	-1.5		
$b_b(z,\lambda)$	HS-2, 4 or 6	-1.5	-1.5		
	VSF				
$c(z,\lambda)$	ac9	-1.5	---		

Water Temp. (^{o}C) & Conductivity	SBE/CT	-1.5,-10,-20,-40, -60,-80,-100,-150, -200,-250,-300	-1.5*	-2,-4,-6,-12	3 CT & 10 T in the interval -0 m to -500 m.
Surface Wave Spectrum	Accelerometer				
Current Velocity	ADCP	-5 to -75 m in 4 m bins	*	-20 (Sontek)	
Wind Velocity	Anemometer	+5.5	+5	+4	+5
Air Temperature (^{o}C)	Thermistor	+3	*	+4	+5
Relative Humidity	Hygrometer?	+3	*	+4	+5
ΔpCO_2	Custom (MBARI)	+1.5	+2		
* See Hayes *et al*. 1991 for a description of the TAO ATLAS core measurements and instrumentation.					

Table 3.3 (Part 2 of 2): Radiometric, bio-optical and ancillary measurements and instruments on selected moored bio-optical buoys; see Table 3.1 and Figures 3.1 and 3.2 for information on the location, buoy type and mooring configuration of each.

Moored Buoy Array:		**GoMOOS**	**HOT (HALE-ALOHA)**	**BATS (BTM)**
Variable	**Sensor**	***z* (m)**	***z* (m)**	***z* (m)**
$E_s(\lambda)$	***PRR-620***			
	HR3			
	OCR507 ICSA	+3.4		
	OCI200			+3
$E_d(z, \lambda)$	PRR-600			
	HR3			
	OCI100			
	OCI200		-25	-15, -35
	OCR504 ICSW	-3, -18		
$L_u(z, \lambda)$	PRR-600			
	HR3			
	OCR100			
	OCR200			-15, -35
	OCR507 R10W	-3		
$E_u(z, \lambda)$	PRR-600		(MER2020)	
	HR3			
Chl *a* Fluorescence	**WETStar**			-34, -71, -100
	DFLS	-3.4, -18.2		
	HS2			
$b_b(z,\lambda)$	HS-2, 4 or 6			
	VSF	-3.4		
$c(z,\lambda)$	ac9	-3.4		
Water Temp. (^{o}C) & Conductivity	**SBE/CT**	-1, -2 (T only),-10,-50	-50,-120,-180 -410,-475,-540, -560,-650,-785	-34, -45, -55, -71, -100, -150, -200, -250, -500, -750
Surface Wave Spectrum	Accelerometer	0		
Current Velocity	ADCP	-10 m to -80 m in 4 m bins		

	Aandaraa RCM9	-2		-200
Wind Velocity	Anemometer	+4		+5
Air Temperature (^oC)	Thermistor	+3		+5
Relative Humidity	Hygrometer?			
Visibility	**Aandaraa 3544**	+32		
ΔpCO_2	**Custom** (MBARI)			+5 (MBARI, YSI, LODCY, Tufts & SAMI
* See Hayes *et al*. 1991 for a description of the TAO ATLAS core measurements and instrumentation.				

Table 3.4: Radiometric, bio-optical and ancillary measurements and instruments on selected examples of drifting bio-optical buoys used in oceanographic experiments.

Project (Institution)		**JGOFS EQPAC (Dalhousie)**	**SOFeX (MBARI)**	**SOFeX (OSU)**
Variable	**Sensor**	**z (m)**	**z (m)**	***z* (m)**
$E_s(\lambda)$	***ED-100*** (490 NM)	+1	+0.5	+0.25
$L_u(z, \lambda)$	OCR100	-0.5	-2.5	-0.2
Chl *a* Fluorescence	HS2		-2.5	
$b_b(z,\lambda)$	HS2		-2.5	
Water Temp. (^oC) & Conductivity	**SBE/CT**	-.05	-2.5	-0.2 (SST only)
Dissolved O_2	SBE		-2.5	
Nitrate	ISUS (MBARI)		-2.5	
CO_2	Licor GasHound (LI-800)		+0.5 and –2.5	
Barometric pressure		+1		
Air Temp (^oC)		+1		

The STOR-X (used on PIRATA) is a commercial data acquisition system designed for data storage and telemetry of up to five serial (RS-232) inputs. The system operates a preprogrammed user schedule, switches sensor power, acquires data from the various sensors, and stores the time tagged data onto a solid-state flash disk. The system can also be programmed to process and transmit data on ARGOS (as in PIRATA), cellular phone systems and broadband telemetry systems such as Freewave.

The data acquisition system used on MEPS is DACNet, which is a complete mooring management system capable of multinode operation. DACNet typically consists of three main components, a PC104 computer system on each buoy node, a wireless telemetry system, and a shore based central server. The MEPS configuration of DACNet has three buoy nodes located within 6km of a shore station. Each buoy node has 12 high-speed (up to 115kbps) serial (RS-232) inputs, some of which were connected to serial instrument networks. In the initial deployment MEPS had 18 individual sensors connected to each node collecting approximately 3MB of data in 20 minutes of data collection each hour. This data was stored on a 1GB microdrive in each buoy and transmitted via a wireless telemetry system at up to 11Mbps back to the central server. Each buoy has four 85W solar panels charging a 250Ah battery pack which is sufficient to serve a peak load of 40W for 20 minutes each hour, 24 hours a day. Guest ports on each buoy allow for the easy addition of new sensors and the ability to allow visiting scientists to connect sensors into the system, while device drivers are remotely loaded via the central server over the internet. User access to the system for configuation control and maintanence is via web browser using secure HTTP. Data

access is via FTP and SMTP interfaces. Data is provided in raw native format with time tags appended to each frame for later data processing by CMEP. The system has the capability to allow direct user connection to any sensor on the platform over the internet, via using TCP/IP facility within DACNet, which is useful for remote sensor configuration, sensor testing, and special measurement sequences.

DACNet will also be used in the MERIS cal/val buoy, BOUSSOLE, to be deployed at the DYFAMED site the Ligurian Sea. This system is operated by CNRS/INSU in Villefranche Sur Mer, France. On the BOUSSOLE buoy, data is stored on disk and downloaded via high-speed wireless telemetry during periodic cruises to the area. System parameters and a limited amount of processed AOP data are sent back to CNRS via an ARGOS transmitter

Radiometric Measurement Methods

Above-water incident spectral irradiance $E_s(\lambda)$, and in-water downwelling and upwelling spectral irradiance $E_d(z,\lambda)$ and $E_u(z,\lambda)$, and upwelling spectral radiance $L_u(z,\lambda,\theta',\phi)$, are often measured using arrays of radiometers mounted on moored or drifting buoys. The notation here follows the definitions of Volume I, Chapter 2, where z is depth in m, λ is wavelength in nm, and (θ',ϕ) are the nadir and azimuth angles of the in-water directional radiance measurement. The directional nature of the in-water radiance field becomes critical when measured $L_u(z,\lambda,\theta',\phi)$ field data are used to determine *normalized water-leaving radiance* $L_{WN}(\lambda)$ and exact normalized water-leaving radiance $L_{WN}^{ex}(\lambda)$ (Section 3.6 below and Volume III, Chapter 4).

Radiometric measurements are typically acquired for relatively brief sampling periods at preprogrammed intervals during each day. The number and duration of radiometric measurement samples scheduled in a buoys instrument controller program is based on factors including diurnal variability in incident radiation, productivity and other light-sensitive biological processes, scheduled ocean color satellite overpasses, and the buoy's electrical power management plan for the particular deployment. Examples of radiometric sampling schedules for particular buoy experiments are described below in Section 3.5, in addition to the following general guidelines:

- In a single radiometric measurement sequence, measurements should be recorded for 10 to 15 minutes to allow averaging over variations in incident irradiance (due to clouds) and in-water radiometric variations resulting from surface waves.
- In addition to daylight measurement sequences, it is recommended to acquire a dark measurement sequence near local midnight.

In most of the instrument configurations listed as examples in Tables 3.3 and 3.4, radiometric collectors (either individual radiometers, or collector optics connected via a fiber-optic lead to a remotely located radiometer) are mounted at one or more fixed depths in the water column. The $E_s(\lambda)$ sensor is typically mounted on the buoy superstructure, while $E_d(z,\lambda)$ and $E_u(z,\lambda)$ sensors are typically mounted on the mooring cable at one or more depths, and are often combined with a nadir-viewing $L_u(z,\lambda)$ sensor at each depth.

The depths at which radiometers are mounted in a fixed array depend on the particular buoy and the diffuse attenuation coefficient typical of the water masses the buoy is expected to observe. For many small drifting buoys, instruments are mounted directly on the buoy to measure only $E_s(\lambda)$ and $L_u(z,\lambda)$, with the hull mounted radiance sensor at a depth $z \cong 1$ m. When additional wire-mounted radiometers are included in the array, they should be deployed at depths spaced to approximately determine the diffuse attenuation coefficient $K(\lambda_{ref}) = \dfrac{\int_{0^-}^{z_{90}} K_d(z,\lambda_{ref})\,dz}{z_{90}}$ averaged over the first attenuation length z_{90} for a selected reference wavelength λ_{ref}. When $\lambda_{ref} = 490$ nm, $K(\lambda_{ref})$ is the diffuse attenuation coefficient determined from satellite ocean color data (Austin and Petzold 1981), and $z_{90} = K(490)^{-1}$ m is the depth from which 90% of the radiance contributing to $L_{WN}(490)$ originates by backscattering. Note that z_{90} is a function of wavelength, and that 490 nm is often used as a reference wavelength because it is the wavelength of maximum transparency in oligotrophic and mesotrophic water

masses. The median $K_{\mathrm{med}}(490)$ and maximum $K_{\max}(490)$ expected to be sampled during a particular buoy deployment can be estimated from satellite ocean color images, combined with radiometric profiles from previous research cruises and optical buoy deployments in that water mass regime. Given that information, a reasonable guideline for $K_{\mathrm{med}}(490) \le 0.1\ \mathrm{m}^{-1}$ situations would be to place a single wire-mounted set of $E_{\mathrm{d}}(z,\lambda)$ and $L_{\mathrm{u}}(z,\lambda)$ at a depth midway between the minimum and median values of z_{90}, *i.e.* at $\hat{z}_{90} = \left[\dfrac{K_{\mathrm{med}}(490) + K_{\max}(490)}{2}\right]^{-1}$ m , and if available, a second such radiometer package could be mounted at $\dfrac{\hat{z}_{90}}{2}$ m .

The approach used on the GoMOOS moorings, for example, is to place the $E_{\mathrm{d}}(z,\lambda)$ sensors at the surface and at the yearly averaged 90% light level depth (for the 490 nm wavelength), typically 3 m and 18 m for the nearshore coastal moorings, and 5 m and 30 m for the more oligotrophic, deep basin moorings. The GoMOOS moored arrays have only have one $L_{\mathrm{u}}(z,\lambda)$ sensor placed at 3m, a depth as near as to the surface as the mooring configuration will allow, and to minimize the effects of shadowing.

Platform shading effects on wire-mounted $E_{\mathrm{d}}(z,\lambda)$ and $E_{\mathrm{u}}(z,\lambda)$ ***spectral irradiance*** sensors are similar to the ship shadow effects discussed in Volume III, Chapter 2 (Section 2.2), but are considerably reduced by the much smaller size of a buoy, compared to a ship.

Upwelling radiance sensors may be mounted either on the underside of a buoy hull, to measure $L_{\mathrm{u}}(z,\lambda,\theta',\phi)$ at a depth $z \cong 1$ m , and/or on a mooring cable at fixed depths (often paired with a downwelling irradiance sensor) to measure $L_{\mathrm{u}}(z,\lambda)$ in a nadir-viewing geometry.

- ***Platform shading effects for wire-mounted radiance sensors*** are directly analogous to ship shadow (and reflection) effects, again mitigated by the relatively small size of a buoy Volume III, Chapter 2 (Section 2.2). For the larger buoys $(r \ge 0.5\ \mathrm{m})$, at least, the uncertainties associated with platform shading for a wire-mounted measurement configuration are better understood, and more widely accepted within the ocean color community, than are those associated with hull-mounted configurations.
- For a ***hull-mounted radiance sensor, the shadows and reflections*** due to a buoy hull are more directly analogous to the instrument self-shading case for a sensor radius equal to half the buoy hull diameter. When a nadir-viewing radiometer is mounted in the center of a buoy hull, the instrument self-shading correction protocol (Volume III, Chapter 2. Section 2.4) based on Gordon and Ding (1992) is directly applicable. The correction will be large in even clear, Case I water masses, however, and shading will significantly increase the uncertainty of water-leaving radiances derived from such measurements. In an attempt to reduce shading, some investigators have mounted radiance sensors near the edge of the buoy hull, and in some cases have pointed the radiometer radially away from the buoy center at a nadir angle $\theta' > 0$. In either of these cases, a modified self-shading correction algorithm must be devised, and validated to correct for platform shading and to determine the uncertainty of the resulting water-leaving radiance.
- For ***profiling moorings***, shading of downwelling radiometers is often not an issue. This may not the case for upwelling sensors where engineering considerations may dictate a profiling package having a fairly large diameter.

Perhaps the most significant factor distinguishing subsurface radiometric measurements using buoy arrays from similar shipboard measurements is ***biofouling*** due to growth of marine organism on optical collectors and windows during prolonged, unattended deployments.

Historically, anti-fouling chemical compounds were applied to optical surfaces in an attempt to prevent microbial growth and settlement of larvae of sessile invertebrates. The results of this chemical approach were typically unsatisfactory. In some recorded cases, biofouling was actually enhanced when chemical anti-fouling compounds provided a rougher surface for organism attachments (McLean *et al.* 1997). In general, the toxicity and limited retention time of antifouling compounds was proved to be undesirable.

A copper shutter mechanism was developed to protect optical sensors from exposure except intermittently, when the shutter is opened to expose the windows/collectors for brief periods while measurements are made (Chavez *et al.,* 2000; Manov *et al*., 2003). The buoy's instrument controller, as part of the programmed measurement schedule, activates the shutter mechanism. In the TOGA/TRITON, MOOS, and some other examples described in Tables 3.3 and 3.4, such a copper shutter device is used to protect the subsurface radiometers from fouling. UCSB OPL and WETLabs, Inc. have designed non-contact servo controlled copper-shuttered devices for radiometers and other bio-optical sensors (Manov *et al*., 2003). This new battery-powered shuttered system uses a commercial high torque servo with dual ball bearings and metal gears (Figure 3.13). A copper plate is attached to the servo arm through a waterproof dynamic o-ring seal. The copper shutter is kept closed over the sensor's optical elements until a measurement is required. Several minutes of data are collected, and then the copper plate is swung back over the sensor to keep the optical elements protected from biofouling between measurement intervals. The OPL/WETLabs, Inc. battery-operated shutter system is self-contained and flexible, and is designed to be easily interfaced and integrated into a complete data logging system.

Fig. 3.13. Examples of optical instruments equipped with copper shutter mechanisms to protect the optical windows from bio-fouling. A new instrument is shown in the upper panels with its shutter closed (left) and open (right). The lower panel shows biofouling organisms covering a different instrument, except for its copper shutter, upon recovery from a moored deployment.

The radiometric windows/collectors on MOBY, although continuously exposed to the water, are surrounded by a copper bezel. The optical surfaces are cleaned monthly by divers, who also document the in-water radiometric responsivities of the system using a portable, underwater lamp source (Vol. VI, Chapter 2).

Profiling moorings can allow cleaning of radiometers by deploying the profiler to the surface where the windows/collectors can be cleaned in-water. Ship-board and shore-based maintenance may also be possible if the profiling vehicle can be detached from the tether.

Radiometers

The buoy instrumentation arrays listed as examples in Tables 3.3 and 3.4 incorporate a variety of commercially available radiometers, listed by the manufacturers model nomenclature. The wavelength characteristics of these sensors comply with those specified in Volume II, Chapter 2 (Table 2.1), and all comply with the other performance characteristics specified Volume II, Chapter 2. Several of the irradiance sensors may be configured to measure irradiance either in air, *i.e.* $E_S(\lambda)$, or in water, *i.e.* $E_d(z, \lambda)$ or $E_u(z, \lambda)$. The reader is referred to Vol. II, Chapter 3, Sects. 3.5 and 3.7 for more information on irradiance immersion factors and cosine response functions in water and air.

The filter radiometers appearing in Tables 3.3 and 3.4 are the:

- **OCR-100:** A 7-channel analog spectral radiance sensor manufactured by Satlantic, Inc.
- **OCR-200:** A 7-channel analog spectral radiance sensor manufactured by Satlantic, Inc.
- **OCI-200:** A 7-channel spectral irradiance radiometer, counterpart to the **OCR-200**, also manufactured by Satlantic, Inc. The cosine collectors on this instrument – a separate one is used at each wavelength - may be ordered to measure spectral irradiance either in air [*i.e.* $E_S(\lambda)$], or in water [*i.e.* $E_d(z, \lambda)$ or $E_u(z, \lambda)$].
- **OCR-504/507:** A 4 or 7 channel digital spectral irradiance or radiance sensor manufactured by Satlantic Inc. The cosine collectors on this instrument – a separate one is used at each wavelength - may be ordered to measure spectral irradiance either in air [*i.e.* Es(l)], or in water [*i.e.* Ed(z, l) or Eu(z, l)].
- **ED-100:** A single-channel (usually 490 nm) radiometer manufactured by Satlantic, Inc. and configured to measure $E_S(490)$ in air.
- **PRR-600:** A filter radiometer manufactured by Biospherical Instruments, Inc., configured to measure $E_d(z, \lambda)$ and $L_u(z, \lambda)$ in water at 7 wavelengths.
- **PRR-620:** A filter radiometer manufactured by Biospherical Instruments, Inc., configured to measure $E_S(\lambda)$ in air at 7 wavelengths.
- **MER-2020A:** A filter radiometer manufactured by Biospherical Instruments, Inc., configured to measure $E_d(z, \lambda)$ and $L_u(z, \lambda)$ in water at 8 wavelengths.

Also used with moored and drifting buoys are two commercially available hyperspectral radiometers, both of which are based on miniature fiber-optic monochromators:

- **HR-3**: The HydroRad-3 manufactured by HobiLabs, Inc. In the examples given in this chapter, the HR-3 is configured with collector optics to measure $E_S(\lambda)$, $E_d(z, \lambda)$ and $L_u(z, \lambda)$ from 400 to 700 nm, with approximately 2 nm resolution in each variable.
- **MiniSpec**: A series of Satlantic hyperspectral radiometers configured to measure irradiance (**MiniSpec I**) $E_S(\lambda)$ or $E_d(z, \lambda)$, and radiance (**MiniSpec R**) $L_u(z, \lambda)$, from 350 nm to 800 nm with a spectral resolution of approximately 10 nm, sampled at 3.3 nm intervals.

Inherent Optical Properties Measurement Methods

Some buoy instrument arrays incorporate sensors to measure inherent optical properties (IOP): the volume beam attenuation coefficient $c(z,\lambda)$, the volume absorption coefficient $a(z,\lambda)$, and the backscattering coefficient $b_b(z,\lambda)$, as defined in Volume I, Chapter 2 (Section 2.4). Given these IOP measurements, the volume scattering coefficient may be calculated as $b(z,\lambda) = c(z,\lambda) - a(z,\lambda)$.

IOP sensors often used on buoys (Tables 3.3 and 3.4) include the:

- **AC9**: An instrument manufactured by WETLabs, Inc. that may be used to measure the absorption coefficient, using a reflecting tube to capture forward-scattered photons, and beam attenuation at 9 wavelengths. Water must be pumped through the enclosed optical paths of this instrument. The instrument

is calibrated against optically pure water, and the derived absorption and beam attenuation coefficients are $a(z,\lambda)-a_w(z,\lambda)$ and $c(z,\lambda)-c_w(z,\lambda)$, respectively (Volume IV, Chapters 2 and 3).

- **HYDROSCAT-N** (**HS-N**): A "backscattering meter" manufactured by HOBILABS, that measures a weighted integral of the volume scattering function (VSF) $\overline{\beta}(\overline{\lambda},\overline{\Psi};c)$ at a central scattering angle of $\overline{\Psi}=140°$, at N wavelengths. The backscattering coefficient $b_b(z,\lambda)$,is then determined using a model relating it to $\overline{\beta}(\overline{\lambda},140°;c)$ (Volume IV, Chapter 5). Alternatively, one of the N channels may be configured to measure chlorophyll a fluorescence, rather than backscattering. On the MOOS buoy, for example, a hull-mounted HS-2 is used to determine $b_b(z,532)$ and chlorophyll a fluorescence at a depth of approximately 1.5 m.
- **VSF**: A device similar to the HS-N, but which measures $\overline{\beta}(\overline{\lambda},\overline{\Psi};c)$ at 3 centroid angles, $\overline{\Psi}=100°,\ 120°$ and $150°$, at a single wavelength, and determines $b_b(z,\lambda)$ using a model of the VSF that is different from that used with the HS-N (Volume IV, Chapter 5).

Protocols describing methods for measuring these variables, including laboratory and field calibrations of instruments and quality control measures, are described in Volume IV, Chapters 2, 3 and 5 for $c(z,\lambda)$, $a(z,\lambda)$ and $b_b(z,\lambda)$, respectively. As with radiometry, the measurement protocols for IOP instruments on buoys differ from shipboard protocols in that they are usually placed at fixed depths, they are subject to biofouling during lengthy deployments, and the instrument cleaning and field calibrations recommended for shipboard use can only be carried out before and after the deployment. Profiling moorings may mitigate bio-fouling problems by "storing" the instrument package in the dark at a depth below the euphotic zone.

Manov *et al*. (2003) review methods for reducing biofouling of IOP, as well as AOP, sensors. In particular, they (OPL UCSB) have developed An anti-foulant copper tubing flow-through system was developed by USCB OPL for the ac-9 and HiSTAR (100-wavelength ac-meter) (Figure 3.14), for closed path flow-through fluorometers (WET Labs, Inc. WETStar) and transmissometers (WET Labs, Inc. C-Stars). The copper tubing systems were tested on a mooring, at depths of 5, 11, and 20 m, during the Hyperspectral Coastal Ocean Dynamics Experiment (HyCODE) in productive inland waters off New Jersey, U.S.A (Chang *et al*., 2002). One-half inch copper tubing was utilized to connect the intakes of the ac-9 to a pump. Between one-hour measurement cycles, copper from the tubing was allowed to leach into the water contained in the tubes of the instrumentation system. Prior to taking the absorption and attenuation measurements, the pump was run on for 10 seconds to clear the system of the leached copper and to pump non-contaminated water into the intake port for sampling. The pump was then left on during the 70 s measurement period. Stainless steel screen filters were used to remove large particles, *e.g.*, seaweed, macroorganisms, and large detritus, from the sensor elements. Separate pumped water systems were utilized for the plumbing the WETStars and C-Stars. One-quarter inch copper tubing was utilized to fit the two instruments together and to a pump. Isolation of the copper by Tygon tubing (black tubing is used to reduce ambient light levels) was made in order to avoid dissimilar metal corrosion effects with the sensors pressure cases, mounting brackets, and the stainless steel instrumentation cage. Manov *et al*. (2003) concluded that copper-tubing based systems provide biofouling protection superior to that achieved with chemically-based methods.

It is recommended to deploy one set of IOP sensors in the near-surface layer at a depth centered between those at which radiometers are placed to determine $K(\lambda)$ and $L_{WN}(\lambda)$ (see above). If additional IOP sensors are deployed in an array, the usual practice is to distribute them to optically characterize the water column throughout the euphotic zone.

These guidelines are appropriate, though perhaps difficult to adhere to in practice. The GoMOOS moorings, for example, deploy one set of IOP sensors at 3.5 m depth. This IOP package includes:

- Three WETLabs VSF (440, 530, and 650 nm) volume scattering meters are integrated with a VSF3S controller that controls the sampling period for each of the 3 sensors, and collates the data from all 3 sensors into a single output stream to the buoy's DH4 data logger, where sample period averages are formed. Each VSF sensor has a small copper shutter that covers the optical sensing area when not in operation, and rotates out of the way during the measurement period. The copper shutter sits about 1-2 mm above the optical face. Copper foil tape is also wrapped around the outside of the sensor to deter growth.

- One WETLabs ac9 absorption and beam attenuation meter is used to measure $a(\lambda)$ and $c(\lambda)$. Short lengths of copper pipe added to the the intake and outflow ends of the flow-through tubing (Fig. 3.14). The copper pipe sections provide a toxic barrier on each end of the flow tube system to prevent biological organisms from entering the flow tube area when the pump is off between sampling periods. This system yields approximately 2-3 months protection before effects of biofouling begin to become apparent in the data record. Bromide, or bleach, leaching methods are not used, because these reactive materials may etch of the quartz window surfaces during a several month deployment.

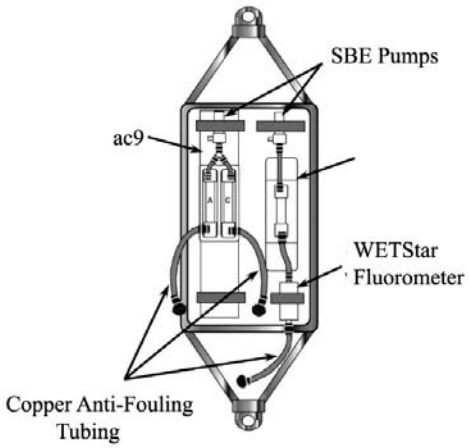

Fig. 3.14: Schematic diagram showing a bio-optical package with copper tubing used to protect the flow-through optical instruments from bio-fouling (after Manov 2003).

Methods for Other Measurements

The MBARI-ISUS (Johnson and Coletti, 2002) is a new system for the optical determination of nitrate concentrations *in situ* without the use of reagents. The system has been successfully deployed on a number of buoys (MOOS-M1, TAO, and SOFeX). ISUS uses UV spectroscopic techniques to provide a measure of nitrate in a 1 cm path length cell in approximately one second. ISUS provides a real time nitrate concentration (in analog and digital formats) and optionally, a full UV absorption spectrum from 200-400nm. Real time nitrate concentrations are accurate to 2mM with a precision of 0.05mM. For moored systems, a novel antifouling chamber has been developed by MBARI using a perforated copper tube and Nitex filter cloth over the probe.

Validation Using Shipboard Measurements

During any recovery, deployment, or servicing of optical moorings or drifters, it is strongly recommended that shipboard bio-optical and radiometric profiles of the water column be measured for comparison with the concurrent buoy measurements. The appropriate measurements are those listed in Vol. I, Chapter 3, Table 3.1, where the protocols covering each measurement are provided in the volumes and chapters indicated in Table 3.2, of Volume I, Chapter 3. Examples of data sets used for this purpose are described in Dickey *et al*. (2001). In the present context, the shipboard radiometric profile measurements made just after a drifting or moored buoy's radiometers are placed in the water, and just before they are recovered, provide invaluable information on the extent of biofouling during a deployment and the quality of water-leaving radiances and diffuse attenuation derived from the buoy measurements. A similar suite of samples are collected off the Oregon Coast when optical drifters are deployed. In addition, a calibrated Tethered Spectral Radiometer Buoy (Satlantic Inc.) is used to collect optical data in the vicinity of the drifters for comparative purposes.

It is also useful to acquire i*n situ* fluorometric chlorophyll *a* before or after radiometric profiles and optical mooring or drifter deployments. Samples to determine the chlorophyll-specific absorption coefficient (a^*) are also

important near optical mooring locations. Recently, strong emphasis has been placed on determining other pigments by means of HPLC analysis to confirm the fluorometric chlorophyll *a* and phaeopigment measurements (Volume V, Chapter 3) and to quantify the influence that other pigments may have on remote sensing data quality.

During MOOS and BTM mooring recovery/maintenance/deployments for example, CTD rosette casts are made to measure physical and biological water column attributes and primary productivity studies, and radiometric profiles are measured. During equatorial Pacific mooring visits a SeaWiFS Profiling Multi-channel Radiometer (SPMR) profiles are measured and various water samples are collected for measurements of pigments concentration (Vol. V, Chapters 2 and 3) and absorption on filters (Vol. IV, Chapter 4).

3.5 DATA BUOY OPERATIONS AND MEASUREMENT METHODS

Upon determining the objective, location, configuration and instrumentation of the mooring or drifter platform, the specific measurement and operation methods, logistics, and shipboard support must be determined.

Deployment/recovery schedules and methods

Deployment and recovery schedules for moorings and drifters will vary dependent upon the selected location, available power supply, and at which expected rates of bio-fouling may significantly degrade sensor performance. For example, MOOS moorings in Monterey Bay take advantage of maintenance visits every 3-4 weeks (sometimes by divers) to maintain the instrument integrity, check for bio-fouling, and replace power supply. The moorings undergo yearly recovery and deployments (turn-arounds) but have bi-annual instrument and OASIS controller swap-outs dependent upon status. Each buoy, tower, and bridle (annotated with serial numbers) is checked for any faults caused from corrosion and documented accordingly. The moorings are built in a staging area at MBARI and undergo rigorous testing before being deployed from the R/V Pt. Sur.

In the GoMOOS project, each mooring is on a 6-month duty cycle, during which time servicing or maintenance is performed on an as needed basis only. This is mainly due to programmatic cost limitations. Each mooring, buoy and associated instruments are completely replaced approximately every 6 months, depending on weather and ship scheduling. Thus, the operational goal of GoMOOS is deployments of 6 months without (or minimal) servicing. In terms of the optical sensors, the 6 month duty cycle is too long for most of the instrumentation due to the effects of biofouling. In our analysis, the above water downwelling irradiance sensor, the chlorophyll fluorometers, and the VSF sensors performance over 6 months is acceptable, and most of the effects of biofouling can be removed or minimized using post-processing procedures and pre- and post-calibrations. However, the ac9 and the in water radiometric sensors do suffer from biofouling that is very difficult to account for using post-recovery processing procedures. We feel that once an effective copper shutter system is developed, the in water irradiance and radiance sensors will be able to collect data over the 6 month duty cycle with only minimal effects of biofouling. The ac9, however, is in need of further anti-biofouling prevention above the copper pipe tubing system we use. The main problem we are having is with the organic film that builds up over the first 2 months of deployment on the optical surfaces. Originally we had proposed to GoMOOS to have divers service the optical systems every 2-3 months, by retrieving the optical packages off of the mooring, and then cleaning and calibrating the sensors before returning them to the mooring system. In fact all of our in water optical packages can easily be removed from the mooring chain without having to retrieve the entire mooring (using a set of strongbacks and clamping systems) or interrupt the hourly mooring sampling schedule (using under water protective cable connectors). However, again, due to GoMOOS programmatic cost limitations, this proposed servicing of the optical sensors was cut from the program.

In remote locations such as in the equatorial Pacific, TAO mooring visits may only occur every 3-6 months with annual turnarounds. Therefore, those moorings are designed to stay completely operational for one year without visits. As a result of the schedule and deck space aboard the *R/V Ka'imimoana*, the buoys are built, tested, and deployed sometimes within a 24 hour time period. Prior to leaving port, all mooring hardware is checked for integrity and serial numbers are carefully documented before deployment. Immediately following deployment, ARGOS data transmission is verified and deployment locations are documented.

At the HOT/HALE ALOHA and BATS/BTM sites, monthly[5] visits are made to the mooring location during regularly scheduled HOT cruises. After a thorough evaluation of biofouling and other considerations, it was determined an optimal duty cycle for the mooring (4-6 months).

Drifters are generally deployed from ships, although some drifting bio-optical buoys are designed to be deployed from aircraft.

Instrument Controllers, Data Recording, and Telemetry Scheduling

A critical aspect of any mooring or drifter platform is its instrument controller and its ability to perform in harsh environments (Section 3.4 above). The system must be configured to communicate with instruments, store and transmit data. The availability of power is dependent on platform design and frequency of visit or deployment duration, which in turn structures the controller to operate at higher or lower sampling frequencies.

The equatorial Pacific, (EqPac) instrument controller and instruments are powered by two battery packs as described in a previous section. The power consumption to sampling rate of all instruments is calculated so that the instruments can be functional for a year. Typically, the OASIS controller commands optical instruments to measure irradiance and radiance at 15 min intervals from 6 am to 6 pm. At each 15 min sampling interval the anti-fouling shutters (Chavez *et al*., 2000) on the subsurface radiometer open for approximately 30 seconds and the radiometer samples for 20 seconds. Data obtained between 10:00 and 14:00 local are averaged to provide representative daily readings, and are then processed to obtain bio-optical parameters. In addition to the measurements during daylight hours, dark readings (00:00 local) are also recorded to provide a zero offset and information on the status of the radiometers. All of the data are stored on a hard drive within the OASIS controller and daily noon readings of selected instruments are transmitted via one-way ARGOS. The total data for ~6 months is ~3 Mb of memory.

GoMOOS: The programmatic goals of GoMOOS are to provide hourly, near-real time data of all oceanic and metereologic conditions from 10 mooring locations, with each mooring having a 6 month duty cycle before replacement of the entire mooring. Each mooring has two 12V Glassmat (gel cell) batteries, and 4 solar panels, which provide power to the main buoy controller (Campbell Scientific CR10X), the cellular phone, and all instruments with the exception of the deep optics package at 18 m, which is powered by a twenty-four 9V lithium battery pack. Hourly sampling is done in "burst" mode, sampling between 20 seconds to 10 minutes depending on the instrument. The hourly sampling intervals for each instrument were selected based on trade-offs between power usage, disk storage space, and temporal resolution. Each hourly sample period is initiated 10 minutes before the top of each hour and ends at 10 minutes after the top of the hour. During this period, each instrument is powered, collects data, and reports the average data to the main data logger (Campbell system). Note that each instrument may have a slightly different sampling interval. Almost all of the raw resolution data is stored by the main data logger system, or stored by the individual sensors for later retrieval. All of the optics systems data loggers store the raw resolution data on a resident flash disk (64 or 192 MB). Transmission of the averaged hourly data samples from all instruments (including diagnostic information such as position, battery voltage, etc) is initiated between 12 and 25 minutes after the top of each hour, with each buoy calling in at a different time frame. The main mode of data transmission to shore is via cellular phone to a shore based modem.

At HOT/HALE-ALOHA and BATS/BTM sites, optical parameters are sampled at 20 min intervals and recorded to a data logger (Letelier *et al*., 2000), and are telemetered to shore via satellite.

As another example, all instruments on the MBARI SOFeX drifter were connected to the logger/controller unit, which was a customized version of the OASIS system (Chavez *et al.,* 1997). The OASIS internal power supply (28 D-cell alkaline batteries) provided power to the controller unit itself and to all of the instruments except the ISUS and GasHound (Table 3.4), which were powered by internal batteries. Sampling frequencies of the instruments were selected to provide the best trade-off between temporal resolution and length of deployment, since battery life (as opposed to fouling) was the most important variable governing deployment duration. In addition to measuring biological, physical and chemical properties of the surface waters, the other major purpose of the drifters was to provide a Lagrangian framework for ship navigation around the Fe fertilized patch. Consequently, GPS data were acquired, and radio connections attempted every 5 min – these two processes were the largest drain on the batteries. Data from all other instruments were collected at hourly intervals. At the temperatures of the Southern Ocean, battery life was significantly shortened, and with the sampling frequencies just described, each drifter could be

[5] The interval between visits to the HALE-ALOHA mooring is likely to increase to 3 months in the near future.

deployed for at most 2 weeks before the package was recovered and new batteries installed. All data were stored in memory (RAM) and transmitted via packet radio to the supporting ship when it was in range (~5 Km to 10 Km depending on sea state). In contrast to equatorial mooring applications, no hard drive was included in this configuration of the OASIS.

The unique nature and increased vulnerability of profiling moorings can necessitate specialized logic on the part of the controller. Two way communications with a shore-based server allows the updating of mission and scheduling files. Amongst other parameters mission files can determine profile speed, the systems activated, and the minimum profile depth. Increasing the minimum profile depth is an effective method to prevent instrument damage during bad weather. Inclement conditions may also be detected, for example, from the vertical motion of profiling vehicle and/or the wave height from bottom a mounted pressure sensor, and subsequently acted on by the controller. A default, or safe, mission program to be used by the controller in the absence of shore communication may be advantageous. In common with other type of moorings a low-power standby mode can be entered between activity periods. An example of a simple control sequence upon waking is:

1. establish communications with the shore station to check for updated mission or scheduling files,
2. perform the profile, and stream some data in real-time,
3. preprocess the profile data for telemetry, and
4. transmit this data to the shore station.

3.6 DATA ANALYSIS AND QUALITY CONTROL METHODS

As described above, the data recorded by an array of sensors mounted on a buoy are retrieved either remotely via a telecommunications link, or by directly downloading it when the buoy is visited for service or retrieval. As with methods of measurement and instrument deployment (Sect. 3.4 above), many aspect of data processing, analysis and quality control are already covered by protocols specified for similar shipboard measurements. Radiometric characterization and calibration requirements and conversion of sensor counts to irradiance and radiance units must follow the protocols described in Volume II (Chapters 2 and 3) and Volume III (Chapter 2), with adjustments to account for:

1. in-water spectral irradiance and radiance measurements at only 1 to 3 depths in the water column,
2. prolonged sensor operation for weeks to months without hands-on stability checks and cleaning, and
3. bio-fouling of submerged optical surfaces, and contamination of above-water sensors by deposition of dust, salt and/or bird droppings.

Similarly, IOP sensors are calibrated, and the data processed, analyzed and checked for quality, following the protocols described in Volume IV, with adjustments for the special circumstances applicable to sensors deployed on buoys.

The following subsections describe recommended methods for handling *Above-Water Spectral Irradiance Data*, *In-Water Radiometric Data*, *Absorption and Beam Attenuation Data*, *Backscattering Data*, and *Chlorophyll a Fluorescence Data*, respectively. The contents of each subsection describe procedures for ***Data Processing***, ***Data Analysis*** and ***Quality Control***, in that order. In general terms:

- "***Data Processing***" covers conversion of sensor response counts to engineering and scientific measurement units, including adjustments for pre- and post-deployment sensor calibration results.
- "***Data Analysis***" covers methods for determining derived quantities such as, for example, water-leaving radiance, diffuse attenuation coefficients, volume scattering coefficients and backscattering.
- "***Quality Control***" describes methods for analyzing the time series of each measurement, together with derived quantities, for internal consistency, symptoms of instrument failure, symptoms of biofouling, consistency with other on-board measurement channels and/or sensors, and consistency with external information (*e.g.* SeaWiFS water-leaving radiance spectra comparisons with measured upwelled radiance spectra).

Above-Water Spectral Irradiance

A radiometer mounted above the water surface (Tables 3.3 and 3.4) is frequently used to measure incident spectral irradiance $E_S(\lambda,t)$ at one or more wavelengths λ, at times *t* programmed into a particular buoy's Instrument Controller (Sects. 3.4 and 3.5).

Data Processing steps, which may be implemented either in a buoy's Instrument Controller, or retrospectively applied to data downloaded when a buoy is visited for maintenance, or retrieved, include:

1. Dark counts, obtained by averaging data scans obtained at local midnight, are first subtracted from each channel.
2. The radiometer's spectral irradiance responsivity calibration factors are applied to convert dark-corrected counts in each channel into spectral irradiance units $\left[\mu W\ cm^{-2} nm^{-1}\right]$. The calibration factors are obtained from pre-deployment responsivity calibrations, in air, using characterization methods consistent with protocols described in Vol. II, Chapter 3 (Section 3.2). The detailed algorithms by which these coefficients are applied are provided by the instrument manufacturer; these may, or may not, include adjustments for detector temperature (if measured internally in the instrument). In some cases, it may be appropriate to adjust the responsivity calibration coefficients to account for differences observed in pre- and post-deployment calibrations; such adjustments must be approached with extreme caution, however, as changes in detector sensitivity are not necessarily linear over time.
3. It may be necessary, or desirable, to average $E_S(\lambda,t)$ observations over a period of minutes-to-hours, and to transmit (or store) only the temporal average $\overline{E}_S(\lambda,\overline{t})$.

Data Analysis:

1. The time series of spectral irradiance incident above the sea surface $E_d(0^+,\lambda,t) \equiv E_S(\lambda,t)$ is obtained directly from the calibrated data.
2. To obtain downwelled spectral irradiance just beneath the water surface $E_d(0^-,\lambda,t)$ it is necessary to account for not only the downward transmission of $E_d(0^+,\lambda,t)$ across the interface, but also the downward reflectance at the interface of upwelled spectral irradiance $E_u(0^-,\lambda,t)$. The reader is referred to Vol. I, Chapter 2 (Sect. 2.7)and Vol. III, Chapter 4 (Sects. 4.2, 4.4 and 4.6). From Vol. III, Chapter 4, in particular, equation (4.11) gives the relationship $E_d(0^-,\lambda) \cong E_d(0^+,\lambda)\dfrac{1-\overline{\rho}}{1-\overline{r}R(0^-,\lambda)}$, and the related discussion gives $\overline{\rho} \cong 0.043 \pm 0.02$, $\overline{r} \cong 0.48$, and $0 < R(0^-,\lambda) \le 0.1$. Combining this information for clear sky conditions and Case I waters, a useful approximation may be obtained as

$$E_d(0^-,\lambda,t) \cong 0.98 E_S(\lambda,t). \qquad (3.1)$$

Quality Control:

1. Inspect the time-series of raw data in each channel of the radiometer for bad data points (*e.g.* obvious dropouts), instrument failure, power failure, and symptoms of salt or other depositions on the irradiance collector.
2. Calculate time series of normalized irradiance spectra $\hat{E}_S(\lambda,t) = \dfrac{E_S(\lambda,t)}{E_S(\lambda_{REF},t)}$ and test whether the shape of the spectrum, as defined by the relative magnitudes of normalized irradiance at all wavelengths, fall within limits defined by clear sky, partly cloudy and overcast models of incident daylight. This is sometimes termed a "rank-order" test between ratios for different wavelengths within a given spectral measurement at time *t*.

3. Compare the magnitudes of measured $E_S(\lambda,t)$ to clear-sky model estimates $\tilde{E}_S(\lambda,t)$ (*e.g.* Frouin *et al*. 1989, Gregg and Carder 1990) calculated for the solar zenith angle at each time *t*. Reject as suspect any measurements exceeding the threshold

$$E_S(\lambda,t) > 1.25\tilde{E}_S(\lambda,t). \quad (3.2)$$

The factor 1.25 allows measured spectral irradiances to moderately exceed calculated clear sky irradiances due to reflections from scattered clouds. Although larger $E_S(\lambda,t)$ values (up to factor of 3) may occur under some cloud conditions (*e.g.* scattered cumulus), these large values are intermittent and will not persist over the averaging periods usually applied to buoy measurements.

4. Combining the previous two steps, the shape of each $\hat{E}_S(\lambda,t)$ spectrum should be consistent with its magnitudes relative to the clear-sky model. In other words, if the magnitudes of $E_S(\lambda,t)$ indicate clear-sky conditions, then the spectral shape should fall off significantly with increasing wavelength. And conversely, if relatively low $E_S(\lambda,t)$ magnitudes suggest overcast conditions, the shape of the spectrum should be relatively flat and not decrease strongly with wavelength.

5. Examine the $E_S(\lambda,t)$ time series for consistency with the seasonal cycle of incident solar irradiance throughout the period of the deployment.

6. If $E_S(\lambda,t)$ is measured at 6 or more wavelengths consistent with the specifications of Volume II, Chapter 2 (Table 2.1), it should be possible to compute an estimate of Photosynthetically Available Radiation (PAR) at each time *t*. As a further quality control measure, these PAR estimates may be compared to independently measured PAR (if a PAR sensor is mounted on the buoy) and/or to regional PAR estimates modeled using cloud imagery measured using radiometers on geostationary satellites (*e.g*. Frouin *et al*. 1989).

In-Water Radiometric Data

Radiometers are mounted underwater on moored and drifting buoys, in a variety of configurations, to measure time series of upwelled spectral radiance $L_u(z,\lambda,t)$, downwelled spectral irradiance $E_d(z,\lambda,t)$, and less often, upwelled spectral irradiance $E_u(z,\lambda,t)$ (Sect. 3.4; Tables 3.3 and 3.4).

Data Processing: The initial steps in processing data from underwater radiometers are the same as for the above-water spectral irradiance:

1. Dark counts, from local midnight scans, are subtracted from each the data for radiometric channel.
2. Responsivity calibration factors determined in air are applied to convert radiance sensor counts to spectral radiance $\left[\mu W\ cm^{-2} nm^{-1} sr^{-1}\right]$ and irradiance sensor counts to spectral irradiance $\left[\mu W\ cm^{-2} nm^{-1}\right]$ units. The above comments regarding $E_S(\lambda,t)$ calibrations apply here also.
3. Calibrated radiances in each radiance sensor channel are multiplied by radiance immersion factors to determine $L_u(z,\lambda,t)$, and calibrated downwelled and upwelled irradiances are multiplied by irradiance immersion factors to determine $E_d(z,\lambda,t)$ and $E_u(z,\lambda,t)$, respectively. The immersion factors for radiance are calculated based on the refractive index of the radiometer's window material, and immersion factors for spectral irradiance sensors must be determined experimentally, following the protocols described in Volume II, Chapter 3 (Sect. 3.5). The instrument manufacturer ordinarily provides these factors, but frequently, only "representative values" for a "collector class" are listed. As pointed out in in Volume II, Chapter 3 (Sect. 3.5), immersion factors may vary up to 8 % between irradiance sensors of the same design and material specifications. To comply with these protocols, therefore, an investigator must ensure that the immersion factors for each in-water irradiance instrument have been experimentally characterized.

4. As with $E_S(\lambda,t)$, it is often necessary, or desirable, to average individual $L_u(z,\lambda,t)$ and $E_d(z,\lambda,t)$ measurements over periods of minutes, or hours. If so, clearly the averaging interval for the in-water and above water data must be the same. Averaging should be applied with caution, if at all, *in situ*ations where bio-optical conditions (*e.g.* chlorophyll a concentration) at the measurement site may be expected to vary significantly during the averaging period. When chlorophyll a variability during the averaging period is large, *Chl* determined using, *e.g.*, $\frac{\overline{L}_u(0^-,443,\overline{t})}{\overline{L}_u(0^-,555,\overline{t})}$ in a remote sensing algorithm is always an underestimate of the mean chlorophyll a concentration. This is a well-known, direct consequence of the nonlinear relationship between remote sensing reflectance and absorption in seawater.

Data Analysis: methods are described to determine diffuse attenuation coefficients, water-leaving radiance, normalized water-leaving radiance, and remote sensing parameters including chlorophyll concentration *Chl*. The methods applicable to data from a particular buoy are determined by the available combination of measurements. Small, expendable drifters often carry only a single radiance sensor (*e.g.* a 7 wavelength Satlantic OCR-100) mounted beneath the buoy's hull (or flotation collar) at a depth $z_o \sim 1$ m (for example the OSU SOFeX drifter illustrated in Figure 3.12). The MOOS (Fig. 3.3) and ARGOS (Fig. 3.5) moored arrays, on the other hand, combine an $L_u(z,\lambda,t)$ sensor (OCR-100) mounted immediately beneath the buoy hull with paired $L_u(z,\lambda,t)$ and $E_d(z,\lambda,t)$ sensors at 10 m and 20 m depths. The GoMOOS optical moorings have paired Lu and Ed sensors at 3m, and an Ed sensor at 18m. Somewhat different data analysis schemes are possible with data from each of these and other radiometer configurations on a buoy. Zheng *et al*. (2002, 2003) describe procedures for the BTM data sets. In general, the uncertainty of derived quantities will be both lower and better understood for configurations with radiometers at several depths. Many of these uncertainties are not as important with profiling moorings, where virtually continuous profiles may be obtained and analysed using the methods of Vol. III, Chapter 2.

1. ***Diffuse Attenuation Coefficients*** $K_d(z,\lambda)$ for $E_d(z,\lambda)$ and $K_L(z,\lambda)$ for $L_u(z,\lambda)$ may be determined directly either from radiometric measurements at two depths (z_i,z_j), $j>i$, or modeled, from ratios $\frac{L_W(\lambda_m)}{L_W(\lambda_n)}$ using remote sensing algorithms, as average values $\overline{K}(\lambda)$ (denoted also as, *e.g.*, *K490* or *K520*, for wavelengths of 490 nm or 520 nm).

    a. $K490(t)$ and $\overline{K}(\lambda,t)$ from water-leaving radiance ratios: Assuming that $\frac{L_u(z_o,\lambda_1,t)}{L_u(z_o,\lambda_2,t)} \cong \frac{L_W(\lambda_1,t)}{L_W(\lambda_2,t)}$, ratios of upwelled radiance from a radiometer mounted under the buoy at a depth $z_o \sim 1$ m may be directly substituted into satellite remote sensing algorithms to determine ***Chl*** concentration [mg m^{-3}] (*e.g.* O'Reilly *et al*. 2000, Strutton *et al*. 2001) and ***K490*** [m^{-1}] (*e.g.* Austin and Petzold 1981). The remote sensing parameter $K490(t) \equiv \overline{K}(490,t)$ is the diffuse attenuation coefficient at 490 nm averaged over the first attenuation depth, *i.e.* the depth where $E_d(z,490,t)$ is 37 % of $E_d(0^-,490,t)$. Given $\overline{K}(490)$, the empirical algorithm and coefficient tables of Austin and Petzold (1986) may be used to determine $\overline{K}(\lambda)$ at other wavelengths. Morel (1988) provides an alternative algorithm for determining $\overline{K}(\lambda)$ from remote sensing *Chl*.

    b. $K_d(\overline{z}_{01},\lambda,1)$ from $E_S(\lambda,t)$ and $E_d(z_1,\lambda,t)$: Given irradiances measured by radiometers located above the surface and at depth z_1 [m], $E_d(0^-,\lambda,t)$ is determined from $E_S(\lambda,t)$ using

equation (3.1), and the diffuse attenuation coefficient averaged from the surface to z_1 is calculated as

$$K_{\mathrm{d}}\left(\overline{z}_{01},\lambda,t\right)=\frac{1}{z_1}\ln\left[\frac{E_{\mathrm{d}}\left(0^{-},\lambda,t\right)}{E_{\mathrm{d}}\left(z_1,\lambda,t\right)}\right], \tag{3.3}$$

where $\overline{z}_{01}=\frac{z_1}{2}$.

c. $K_{\mathrm{d}}\left(\overline{z}_{\mathrm{ij}},\lambda,t\right)$ from $E_{\mathrm{d}}\left(z_i,\lambda,t\right)$ and $E_{\mathrm{d}}\left(z_j,\lambda,t\right)$,: Given two underwater downwelled irradiance sensors at depths $z_j>z_i$, the diffuse attenuation coefficient averaged over that depth interval is given by

$$K_{\mathrm{d}}\left(\overline{z}_{\mathrm{ij}},\lambda,t\right)=\frac{1}{z_j-z_i}\ln\left[\frac{E_{\mathrm{d}}\left(z_i,\lambda,t\right)}{E_{\mathrm{d}}\left(z_j,\lambda,t\right)}\right], \tag{3.4}$$

where $\overline{z}_{ij}=\frac{z_i+z_j}{2}$.

d. $K_{\mathrm{L}}\left(\overline{z}_{\mathrm{ij}},\lambda,t\right)$ from $L_{\mathrm{u}}\left(z_i,\lambda,t\right)$ and $L_{\mathrm{u}}\left(z_j,\lambda,t\right)$,: Given two underwater upwelled radiance sensors at depths $z_j>z_i$, the diffuse attenuation coefficient averaged over that depth interval is given by

$$K_{\mathrm{L}}\left(\overline{z}_{\mathrm{ij}},\lambda,t\right)=\frac{1}{z_j-z_i}\ln\left[\frac{L_{\mathrm{u}}\left(z_i,\lambda,t\right)}{L_{\mathrm{u}}\left(z_j,\lambda,t\right)}\right], \tag{3.5}$$

where $\overline{z}_{ij}=\frac{z_i+z_j}{2}$.

In principle, the uncertainties of the diffuse attenuation coefficients determined using (3.4) and (3.5) should be better than that from (3.3), and the uncertainty associated with any of those 3 methods should be better than the estimates of $\overline{K}\left(\lambda,t\right)$ modeled using ratios of upwelled radiance measured just below the sea surface. If the measurement combination from a particular buoy is sufficient, it is recommended that diffuse attenuation coefficients be calculated for comparison and quality control purposes.

2. ***Water-Leaving Radiance*** $L_{\mathrm{W}}\left(\lambda,t\right)$ is determined by extrapolating upwelled radiance measured at depth *z* to the surface as

$$L_{\mathrm{u}}\left(0^{-},\lambda,t\right)=L_{\mathrm{u}}\left(z,\lambda,t\right)e^{\overline{K}_{\mathrm{L}}\left(z,\lambda,t\right)z}, \tag{3.6}$$

where $\overline{K}_{\mathrm{L}}\left(z_i,\lambda\right)\equiv\frac{1}{z_i}\int_0^{z_i}K_{\mathrm{L}}\left(z,\lambda\right)dz$. Upwelled radiance is then propagated upward through the interface as $L_{\mathrm{W}}\left(\lambda,\theta,\phi\right)=\frac{1-\rho\left(\theta',\theta;W\right)}{n^2}L_{\mathrm{W}}\left(0^{-},\lambda,\theta',\phi\right)$, for general viewing angles $\theta'>0$ [see Vol. I, Chapter 2, (Sect. 2.5) and Vol. III, Chapter 4,][6]. If only nadir-viewing geometry is considered, then the surface reflectance term becomes independent of wind speed *W*, and the upward transmittance term is constant at $\frac{1-\rho\left(0,0;W\right)}{n^2}=0.543$ (Austin 1974), and water-leaving radiance is calculated as

[6] Note that $\rho\left(\theta',\theta;W\right)$ is reflectance for a wind-roughened sea surface, and not the Fresnel reflectance.

$$L_{\mathrm{W}}(\lambda,t) = 0.543 L_{\mathrm{u}}\left(0^{-},\lambda,t\right). \tag{3.7}$$

Given only discrete radiometric measurements, $\overline{K}_{\mathrm{L}}\left(z_i,\lambda\right)$ must be estimated as some combination of the methods 1a) through 1d), described above, for determining the diffuse attenuation coefficient. Some possible approaches are:

a. If upwelled radiance is measured using two wire-mounted radiometers at depths $z_2 > z_1$, for example, $K_{\mathrm{L}}\left(\overline{z}_{12},\lambda,t\right)$ may be calculated with (3.5) for the interval between the two depths. [Combining radiance measurements in this way between hull-mounted and wire-mounted radiometers, *i.e.* to determine $K_{\mathrm{L}}\left(\overline{z}_{01},\lambda,t\right)$, may be less straightforward if the buoy diameter is large and/or the measurement at z_{O} is not nadir-viewing] In clear oligotrophic water masses, it may be reasonable to assume optical homogeneity from the surface to depth z_2, or that $\overline{K}_{\mathrm{L}}\left(z_1,\lambda,t\right) \cong K_{\mathrm{L}}\left(\overline{z}_{12},\lambda,t\right)$. Other approximations must be considered if there is reason to believe that optical properties vary strongly in the layer above depth z_2.

b. If upwelled radiance is measured at only one depth, whether using a hull-mounted or wire-mounted radiometer, and downwelled irradiance is measured at one or more depths, it can usually be assumed that $K_{\mathrm{L}}\left(z,\lambda\right) \approx K_{\mathrm{d}}\left(z,\lambda\right)$ within approximately 5 % (Kirk 1994). Then, $\overline{K}_{\mathrm{L}}\left(z_i,\lambda\right)$ may be determined using some combination of (3.3) and (3.4).

c. If upwelled radiance is measured only at depth z_{o}, just beneath the buoy hull, then there is no choice but to assume that $\overline{K}_{\mathrm{L}}\left(z,\lambda\right) \approx \overline{K}\left(\lambda\right)$ and apply remote sensing algorithms such as those cited above under 1a).

3. ***Normalized Water-Leaving Radiance*** $L_{\mathrm{WN}}\left(\lambda,t\right)$ is calculated from $L_{\mathrm{W}}\left(\lambda,t\right)$ following the definition of (Gordon and Clark 1981)[7] as

$$L_{\mathrm{WN}}\left(\lambda,t\right) = L_{\mathrm{W}}\left(\lambda,t\right)\frac{\overline{F}_{\mathrm{o}}\left(\lambda\right)}{E_{\mathrm{S}}\left(\lambda,t\right)}, \tag{3.8}$$

where $\overline{F}_{\mathrm{o}}\left(\lambda\right)$ is mean extraterrestrial solar irradiance (Neckle and Labs 1984) [see also Vol. I, Chapter 2, equation (2.55) in and Vol. III, Chapter 4 (Sect. 4.1)]. If reliable measurements of $E_{\mathrm{S}}\left(\lambda,t\right)$ are available, they are substituted directly in (3.8). Otherwise, incident surface irradiance may be approximated either as the modeled clear-sky irradiance $\tilde{E}_{\mathrm{S}}\left(\lambda,t\right)$ (*e.g.* Frouin *et al*. 1989, Gregg and Carder 1990) calculated for the solar zenith angle θ_{o} at time *t*, or more simply as

$$\tilde{E}_{\mathrm{S}}\left(\lambda,t\right) = \overline{F}_{\mathrm{o}}\left(\lambda\right) t_{\mathrm{atm}}\left(\lambda,\theta_{\mathrm{o}}\right)\cos\theta_{\mathrm{o}}\left(\frac{\mathrm{d}_{\mathrm{o}}}{d}\right)^{2}, \tag{3.9}$$

where at time *t*, $t_{\mathrm{atm}}\left(\lambda,\theta_{\mathrm{o}}\right)$ is the diffuse transmission of the atmosphere, and d_{o} and *d* are the mean and actual earth-sun differences, respectively. Finally, $L_{\mathrm{WN}}\left(\lambda,t\right)$ must be converted to Exact Normalized Water-Leaving Radiance by the methods described in Vol. III, Chapter 4.

4. ***Ocean Color Remote Sensing Parameters, Chl*** – chlorophyll a concentration in mg m^{-3} – and ***K490*** – the diffuse attenuation coefficient in m^{-1} averaged over the first e-folding attenuation depth - are

[7] Gordon *et al*. (1988) introduced a variant definition of Normalized Water-Leaving Radiance that included an adjustment for the downward Fresnel transmittance of incident direct solar flux into the ocean. Although this approximation has the correct sign, its magnitude is not correct for a real ocean surface (even under calm conditions). Therefore, the Gordon *et al*. (1988) definition is not used, because it is inconsistent with the definition of Exact Normalized Water-Leaving Radiance (Vol. III, Chapter 4), which correctly accounts for downward irradiance transmittance through the sea surface.

calculated from ratios of either water-leaving radiance at different wavelengths, or more directly from ratios of near-surface measurements of upwelled spectral radiance (*e.g.* Sutton *et al*. 2001). Algorithms for calculating these parameters are cited in item 1a) above, as part of the discussion of methods to determine diffuse attenuation coefficient.

Quality Control:

1. Inspect the time-series of raw data in each radiometric channel for bad data points (*e.g.* obvious dropouts), instrument failure, power failure, and symptoms of biofouling.

2. Calculate time series of normalized spectra $\hat{E}_{\mathrm{d}}\left(z_i,\lambda,t\right)=\dfrac{E_{\mathrm{d}}\left(z_i,\lambda,t\right)}{E_{\mathrm{d}}\left(z_i,\lambda_{\mathrm{REF}},t\right)}$, $\hat{L}_{\mathrm{u}}\left(z_i,\lambda,t\right)=\dfrac{L_{\mathrm{u}}\left(z_i,\lambda,t\right)}{L_{\mathrm{u}}\left(z_i,\lambda_{\mathrm{REF}},t\right)}$ and $\hat{L}_{\mathrm{W}}\left(\lambda,t\right)=\dfrac{L_{\mathrm{W}}\left(\lambda,t\right)}{L_{\mathrm{W}}\left(\lambda_{\mathrm{REF}},t\right)}$. Test whether

   a. The shapes of these spectra should be consistent with those of normalized spectra from previous deployments in the site, and from earlier in the current deployment.

   b. The shapes of $\hat{L}_{\mathrm{W}}\left(\lambda,t\right)$ spectra should be consistent with similar spectra of wavelength ratios in time-series of water-leaving radiances determined from SeaWiFS, MODIS, and other ocean color satellites.

   c. Following Abbott and Letelier (1998), set $\lambda_{\mathrm{ref}}=555$ nm and use $\hat{L}_{\mathrm{u}}\left(z,683,t\right)$ and $\hat{E}_{\mathrm{d}}\left(z,683,t\right)$ to test for biofouling. In theory, if chlorophyll bearing organisms aggregate on or near the radiometer's window (or collector), the transmittance of the window (or collector) at 555 nm would be severely decreased while chlorophyll fluorescence on or near the surface would continue to provide a significant signal. Abbott and Letelier (1998) suggest that biofouling is indicated when either ratio exceeds 0.1, a value appropriate for clear oligotrophic water masses. In very productive coastal water masses, a threshold of 0.5 may be more appropriate. A regional threshold may be established by comparing the $\hat{L}_{\mathrm{u}}\left(z,683,t\right)$ and $\hat{E}_{\mathrm{d}}\left(z,683,t\right)$ (555 nm reference) ratio history during each deployment to the extent of biofouling observed when the sensor is recovered.

3. Compare absolute values of water-leaving radiances derived from the buoy measurements with those determined from SeaWiFS and other satellite ocean color sensors. These comparisons are best done in a time-series mode to detect outliers, and divergences indicating the onset and growth of biofouling organisms on the optical surface. Caution must be used in this method if the *in situ* data are collected in regions that are characterized by Case 2 water types with high concentrations of colored dissolved and particulate organic matter, relative to to phytoplankton pigment concentration. Moreover, the atmospheric correction procedure used by SeaWiFS, and other ocean color sensors, may underestimate the normalized water leaving radiance estimates in Case 2 waters.

4. Examine diffuse attenuation coefficients calculated from the data

   a. Check whether $K_{\mathrm{d}}\left(z,\lambda\right)\geq a_{\mathrm{w}}\left(\lambda\right)$, where $a_{\mathrm{w}}\left(\lambda\right)$ is the spectral volume absorption coefficient of pure water [Vol. I, Chapter 2 (Sect. 2.5) and references cited therein]. If $0<\left[a_{\mathrm{w}}\left(\lambda\right)-K\left(\lambda\right)\right]\leq 0.005$ m^{-1}, flag the data as suspect, but if $\left[a_{\mathrm{w}}\left(\lambda\right)-K\left(\lambda\right)\right]>0.005$ m^{-1} the diffuse attenuation coefficients are clearly bad data. If such conditions persist, it is likely that one of the radiometric channels used to determine the diffuse attenuation coefficient has either failed, or has experienced significant biofouling. In MBARI's experience in the equatorial Pacific, less than 5% of the calculated data fail this test, and this percentage should be less in mesotrophic or eutrophic waters. Measurements not meeting this criterion usually occur during extremely cloudy or overcast days, and are possibly result from unresolved incident irradiance variability during the 4-hour period over which the data are averaged.

b. When the data permit, compare diffuse attenuation coefficients calculated by the different methods outlined above to determine internal offsets and uncertainties in the data set. These comparisons can also be used, in time series mode, to detect the onset and extent of biofouling in different radiometers. Fig. 3.15, shows time series of $K_{\mathrm{d}}\left(\overline{z}_{0i},490,t\right)$ for a 5 month MOOS buoy deployment in Monterey Bay. The three time series were computed using equation (3.3) with surface values determined from $E_{\mathrm{S}}\left(\lambda,t\right)$ in (3.1) and $E_{\mathrm{d}}\left(z_i,\lambda,t\right)$ for $z_1 = 10$ m (top curve), $z_2 = 20$ m (bottom curve), and $z_3 = 30$ m (middle curve). After approximately 2 months, the 3 curves diverge in a manner that cannot be explained by optical stratification of the water column, offering strong evidence of progressive biofouling of the radiometers at 10 m and 30 m.

c. When $K_{\mathrm{d}}\left(\overline{z}_{ij},\lambda,t\right)$ is determined from in-water measurements alone, *i.e.* independently from $E_{\mathrm{S}}\left(\lambda\right)$, measures of internal consistency between in-water and the above-water radiometer may be calculated as the unbiased percent differences

$$\Delta_{0k}\left(\lambda,t\right) = 100\left|\frac{E_{\mathrm{d}}\left(z_k,\lambda,t\right)e^{-K_{\mathrm{d}}\left(\overline{z}_{0k},\lambda,t\right)z_k} - E_{\mathrm{d}}\left(0^-,\lambda,t\right)}{E_{\mathrm{d}}\left(0^-,\lambda,t\right)}\right| \%, \tag{3.10}$$

where $k = i$ or j, and $E_{\mathrm{d}}\left(0^-,\lambda,t\right)$ is calculated using $E_{\mathrm{S}}\left(\lambda,t\right)$ in equation (3.1). If running means and standard deviations of $\Delta_{0i}\left(\lambda,t\right)$ and $\Delta_{0j}\left(\lambda,t\right)$ are calculated over a suitable averaging period - perhaps 2 weeks - the comparative time series may be used to provide additional diagnostic indications of instrument degradation and biofouling.

5. *Chl* and *K490* derived from ratios of water-leaving radiance should agree with the parameters determined from satellite ocean color data within approximately 35 % and 20 %, respectively. Fig. 3.16 illustrates an example time series of *Chl* derived from the MBARI radiometers on the EP1 TAO mooring compared with *Chl* derived from SeaWiFS data and with chlorophyll a concentration from shipboard samples.

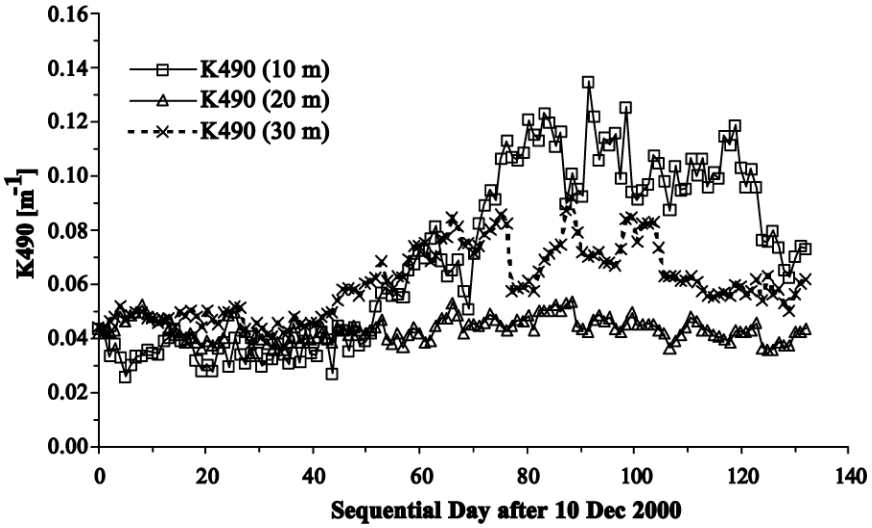

Fig. 3.15: An example of biofouling symptoms, as evidenced by the divergences in K490 over different depth intervals, beginning midway through a 135 day time series of radiometric measurements on a mooring in Monterey Bay, CA.

IOP Data

Protocols for data analysis and quality control of beam attenuation and absorption coefficients are described in Vol. IV, Chapters 2 and 3, respectively. Protocols for determining the backscattering coefficient $b_b(\lambda)$ from measurements of the volume scattering function at one or more scattering angles are described in Vol. IV, Chapter 5.

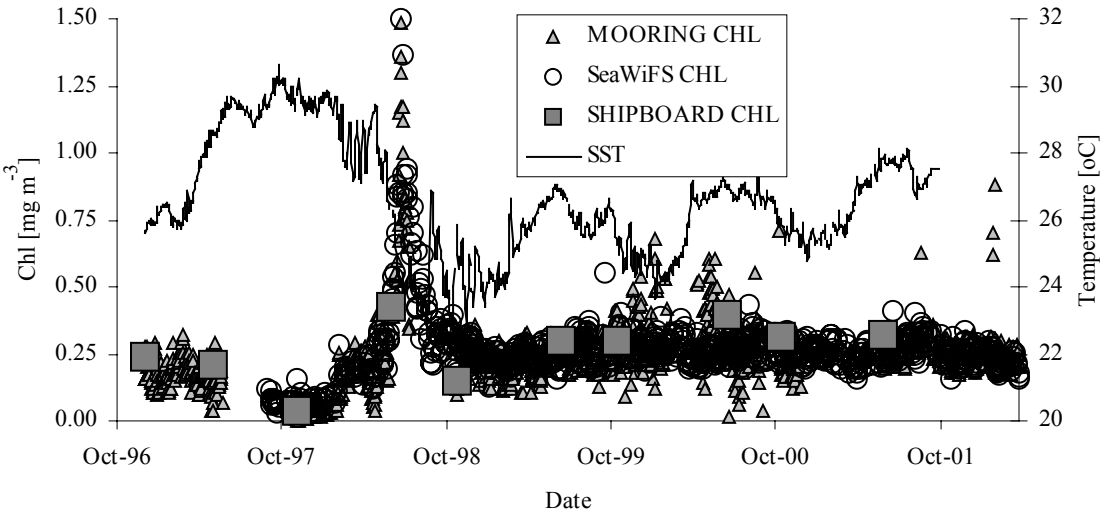

Fig. 3.16: Time series of chlorophyll concentrations derived from MBARI optical instruments, calculated from two depths (surface and 20 m depth) on the TAO mooring at EP1 (0°,155°W). For comparison, SeaWiFS derived *Chl* and *in situ* shipboard chlorophyll *a* concentration measurements for the mooring location are also plotted.

Chlorophyll a Fluorescence Data

The GoMOOS moorings use the WETLabs Inc digital ECO shuttered fluorometer (DFLS) series for all chlorophyll fluorescence measurements (Table 3.3). This instrument is low power, stable, and has a copper shutter to prevent biofouling. The sensor is wrapped in copper foil tape as an additional prevention measure. The epoxy facing of the DFLS prevents calibrating the instrument against a chlorophyll standard dissolved in acetone. Therefore, the GoMOOS project calibrates the DFLS sensors against a dilution series of a monoculture of phytoplankton (*T. pseudonana*) *in vitro*, the chlorophyll a concentration of which is measured using the protocols of Vol. V, Chapter 2. The fluorometer responses are fit to a linear regression equation as a model for converting the data to chlorophyll concentration. Each DFLS is additionally characterized for stability (using a pure water standard) and for temperature dependence using a controlled water bath. All sensors are calibrated against a dilution series of phytoplankton and for the pure water offset before and after each deployment.

Data Processing

1. Temperature correction of the linear regression offset is applied based on the *in situ* water temperature and the results of the temperature characterization.
2. Average digital counts reported to shore are converted to chlorophyll concentration units (mg l-1) based on the linear regression equation from the calibration.
3. Upon recovery of the mooring, the entire raw data record is analyzed again. For each hourly sampling period, the raw digital counts are are filtered using a 1.5 standard deviation filter and then steps 1 and 2 are repeated.

Data Analysis

1. Upon recovery of the mooring, the DFLS is recalibrated against pure water and 0.2 micron filtered seawater to check for instrument drift and for biofouling of the optical face. If significant instrument drift or biofouling is detected, a linear correction is applied to the temporal data to account for these effects based on the pre- and post-calibrations against the phytoplankton dilutions.
2. The fluorometric chlorophyll concentration values are compared to Morel's chlorophyll estimates using $K_d(z,\lambda)$ values calculated from the downwelling irradiance data (see above). Comparisons are only made between the average night time fluorometric chlorophyll data and the day time $K_d(z,\lambda)$ values in order to minimize the influence of fluorescence quenching of the fluorometric data. Note that in many of the GoMOOS mooring locations, the surface fluorometric chlorophyll data time series show a strong diurnal response, with high chlorophyll values at night and the lowest values at local noon due to fluorescence quenching.

Quality Control

1. The data are inspected to ensure that all values fall between minimum and maximum limits derived from the DFLS calibrations. Any data point that is outside of these limits is flagged as questionable data.
2. The entire raw data set of chlorophyll fluorometric data is analyzed after recovery of the mooring and corrections are applied based on the pre- and post-calibrations of the DFLS sensor.

3.7 RECORDKEEPING AND DATA ARCHIVAL

Logs and supporting documentation

The configuration of a mooring or drifter design and instrumentation can change continuously due to various upgrades between deployments. Therefore, concise documentation of deployment, maintenance, recovery and any changes to instruments should be clearly recorded in both hard and soft copy format. Serial numbers should be issued to each part of a mooring or drifter to determine the life span of the hardware from eventual corrosion. Instrument serial numbers and calibration files must also be carefully documented and stored. Examples of deployment reports for respective projects covered in this chapter can be found at

- MOOS: http://www.mbari.org/bog/MOOS/mooringlog.html
- TAO/TRITON (optical platforms only): http://bog.shore.mbari.org/~bog/eqpac_log.txt
- BTM: http://www.opl.ucsb.edu
- HOT: http://hahana.soest.hawaii.edu/hot/hale-aloha/instruments.html
- OSU Drifters and moorings: http://picasso.coas.oregonstate.edu/ORSOO
- GoMOOS: http://gyre.umeoce.maine.edu/GoMoos/gominfo.php

Data Archival

Data archiving and methods also vary with projects. For example, MBARI maintains an extensive mooring data archive in NetCDF format. All of the data from high frequency raw to averaged quality controlled data is stored in internal databases. Data access to the public is limited to the quality controlled data. The various projects described in this chapter offer websites with limited access to there respective data as follows

- MOOS: http://www.mbari.org/oasis/
- TAO/TRITON: http://www.pmel.noaa.gov/tao/jsdisplay/
- PIRATA: http://www.pmel.noaa.gov/tao/data_deliv/deliv-pir.html
- EQPAC: http://bog.shore.mbari.org/~bog/oasis.html
- BTM: http://www.opl.ucsb.edu

- HOT: http://hahana.soest.hawaii.edu/hot/hale-aloha/ha.html
- OSU http://picasso.coas.oregonstate.edu/ORSOO
- AVPPO: http://seabass.gsfc.nasa.gov/j

REFERENCES

Abbott, M. R., J. G. Richman, R. M. Letelier, and J. S. Bartlett, 2000: The spring bloom in the Antarctic Polar Frontal Zone as observed from a mesoscale array of bio-optical sensors, Deep-Sea Research II, 47, 3285-3314.

Abbott, M.R., J.G. Richman, J.S. Nahorniak, and B.S. Barksdale, 2001, Meanders in the Antarctic Polar Frontal Zone and their impact on phytoplankton, Deep-Sea Res. II, 48, 3891-3912.

Abbott, M. R. and Letelier, R. M., 1998: Decorrelation scales of chlorophyll as observed from bio-optical drifters in the California Current, Deep-Sea Research II, 45, 1639-1667.

Austin, R.W., 1974: The remote sensing of spectral radiance from below the ocean surface. In: Optical Aspects of Oceanography, N.G. Jerlov and E.S. Nielson, Eds., pp317-344.

Austin, R.W. and T.J. Petzold, 1981: The determination of the diffuse attenuation coefficient of sea water using the Coastal Zone Color Scanner. Oceanography from Space, J.F.R. Gower, Ed., Plenum Press, 239-256.

Austin, R.W. and T.J. Petzold, 1986. Spectral dependence of the diffuse attenuation coefficient of light in ocean waters. *Opt. Eng.*, **25(3):** 471-479.

Berteaux, H. O., 1991: Purposes and Types of Buoy Systems, In: H. O. Berteaux (ed.), *Coastal and Oceanic Buoy Engineering*, Williams S. Sullwold Publishing, Taunton, Massachusetts.

Chang, G.C., T.D. Dickey, O. Schofield, A.D. Weidemann, E. Boss, W.S. Pegau, M. Moline, and S.M. Glenn, 2002, Nearshore physical processes and bio-optical properties in the New York Bight, *J. Geophys. Res.*, **107(C9):** 3133.

Chavez, F. P., J. T. Pennington, R. Herlien, H. Jannasch, G. Thurmond, and G. E. Friederich, 1997: Moorings and drifters for real-time interdisciplinary oceanography, *J. of Atmos. and Oceanic Tech.*, **14:** 1199-1211.

Chavez, F.P., Strutton, P.G., Friederich, G.E., Feely, R.A., Feldman, G.C., Foley, D.G., McPhaden, M.J., 1999: Biological and chemical response of the equatorial Pacific Ocean to the 1997-98 El Niño, *Science*, **286:** 2126-2131.

Chavez, F. P., Wright, D., Herlien, R., Kelley, M., Shane, F., and Strutton, P. G., 2000: A Device for Protecting Moored Spectrophotometers from Biofouling, *J. of Atmos. and Oceanic Tech.*, **17:** 215-219.

Dickey, T. D., 1991: The Emergence of Concurrent High-Resolution Physical and Bio-optical Measurements in the Upper Ocean and their Applications. *Rev. of Geophys*., **29:** 383-413

Dickey, T. D., 1995: Bermuda Testbed Mooring Program, *Bull. of Am. Met. Soc.*, **76:** 584.

Dickey, T., 2001, Inherent optical properties and irradiance, *Encyclopedia of Ocean Sciences*, J.H. Steele, S.A. Thorpe, and K.K. Turekian (Eds.), Academic Press, Orlando, pp1313-1323.

Dickey, T., 2003, Future ocean observations for interdisciplinary data assimilation models, *J. Mar. Sys.* In press.

Dickey, T. D., Douglas, R. H., Manov, D., Bogucki, D., Walker, P. C., and Petrelis, P., 1993: An Experimental in Two-Way Communication with a Multivariable Moored System in Coastal Waters, *J. of Atmos. and Oceanic Tech.*, **10,** 637-644.

Dickey, T., D. Frye, H. Jannasch, E. Boyle, D. Manov, D. Sigurdson, J. McNeil, M. Stramska, A. Michaels, N. Nelson, D. Siegel, G. Chang, J. Wu, and A. Knap, 1998, Initial results from the Bermuda Testbed Mooring Program, *Deep-Sea Res. I*, **45:** 771-794.

Dickey, T., T. Granata, J. Marra, C. Langdon, J. Wiggert, Z. Chai-Jochner, M. Hamilton, J. Vazquez, M. Stramska, R. Bidigare, and D. Siegel, 1993, Seasonal variability of bio-optical and physical properties in the Sargasso Sea, *J. Geophys. Res.*, **98:** 865-898.

Dickey, T., J. Marra, T. Granata, C. Langdon, M. Hamilton, J. Wiggert, D. Siegel, and A. Bratkovich, 1991, Concurrent high resolution bio-optical and physical time series observations in the Sargasso Sea during the spring of 1987, *J. Geophys. Res*., **96:** 8643-8663.

Dickey, T., J. Marra, D.E. Sigurdson, R.A. Weller, C.S. Kinkade, S.E. Zedler, J.D. Wiggert, and C. Langdon, 1998, Seasonal variability of bio-optical and physical properties in the Arabian Sea: October 1994 - October 1995, *Deep-Sea Res. II*, **45:** 2001-2025.

Dickey, T., J. Marra, M. Stramska, C. Langdon, T. Granata, R. Weller, A. Plueddemann, and J. Yoder, 1994, Bio-optical and physical variability in the sub-arctic North Atlantic Ocean during the spring of 1989, *J. Geophys. Res.*, **99:** 22,541-22,556.

Dickey, T.D. and A.J. Williams III, 2001, Interdisciplinary ocean process studies on the New England shelf, *J. Geophys. Res*., **106:** 9427-9434.

Dickey, T., S. Zedler, D. Frye, H. Jannasch, D. Manov, D. Sigurdson, J.D. McNeil, L. Dobeck, X. Yu, T. Gilboy, C. Bravo, S.C. Doney, D.A. Siegel, and N. Nelson, 2001, Physical and biogeochemical variability from hours to years at the Bermuda Testbed Mooring site: June 1994 - March 1998, *Deep-Sea Res. II*, **48:** 2105-2131.

Foley, D.G., T.D. Dickey, M.J. McPhaden, R.R. Bidigare, M.R. Lewis, R.T Barber, S.T. Lindley, C. Garside, D.V. Manov, and J.D. McNeil, 1997, Longwaves and primary production in the central equatorial Pacific at 0^{o}, 140^{o}W, *Deep-Sea Res. II*, **44:** 1801-1826.

Friederich, G. E., P. G. Brewer, R. Herlien, F. P. Chavez, 1995: Measurements of sea surface partial pressure of CO2 from a moored buoy, *Deep-Sea Res. II*, **42:** 1175-1186.

Frouin, R., D. W. Lingner, C. Gautier, K. S. Baker, R. C. Smith, 1989: A simple analytical formula to compute clear sky total and photosynthetically available solar irradianceat the ocean surface, *J. of Geophys. Res*., **94:** 9731-9742.

Gordon, H. R., O. B. Brown, R. H. Evans, R. H., J. W Brown, R. C. Smith, K. S. Baker, and D. K. Clark, 1988: A Semianalytic Radiance Model of Ocean Color, *J. of Geophys. Res*., **93:** 10909-10924.

Gordon, H. R., and M. Wang, 1994: Retrieval of water-leaving radiance and aerosol optical thickness over the oceans with SeaWiFS: A preliminary algorithm, *Appl. Opt.*, **33**: 443-452.

Gregg, W.W. and K.L. Carder, 1990: A simple spectral solar irradiance model for cloudless maritime atmospheres, *Limnol. Oceanogr.*, **35(8):** 1657-1675.

Griffiths, G., R. Davis, C. Eriksen, D. Frye, P. Marchand, T. Dickey, and R. Weller, 2001, Towards new platform technology for sustained observations, *Observing the Ocean for Climate in the 21st Century*, C.J. Koblinsky and N.R. Smith (Eds.), GODAE, Bureau of Meteorology, Australia, Melbourue, Australia, pp324-338.

Hayes, S. P., L. J. Mangum, J. Picaut, A. Sumi, and K. Takeuchi, 1991: TOGA-TAO: A moored array for real-time measurements in the tropical Pacific Ocean. *Bull. of Amer. Meteorol. Soc.*, **72,** 339-347.

Johnson, K.S. and Coletti, L.J., 2003: *In situ* ultraviolet spectrophotometry for high resolution and long term monitoring of nitrate, bromide and bisulfide in the ocean. *Deep-Sea Research II.*, **49:** 1219-1305.

Karl, D. M. and Lukas, R., 1996: Hawaii Ocean Time-series (HOT) program: Background, rationale, and field implementation, *Deep-Sea Res. II*, **43:** 129-156.

Kirk, J. T. O., 1994: *Light and Photosynthesis in Aquatic Ecosystems*, Cambridge University Press, New York,. 509 pp

Kudela, R. M. and F. P. Chavez, 1996: Bio-optical properties in relation to an algal bloom caused by iron enrichment in the Equatorial Pacific, *Geophys. Res. Letters*, **23:** 3751-3754.

Landry, M.R., R.T. Barber, R.R. Bidigare, F. Chai, K.H. Coale, H.G. Dam, M.R. Lewis, S.T. Lindley, J.J. McCarthy, M.R. Roman, D.K. Stoecker, P.G. Verity, and J.R. White. 1997. Iron and grazing constraints on primary production in the central equatorial Pacific: An EQPAC synthesis. *Limnol. Oceanogr*., **42:** 405-418.

Letelier, R.M., M.R. Abbott, and D.M. Karl. 1997, Chlorophyll natural fluorescence response to upwelling events in the Southern Ocean. *Geophys. Res. Letters*, **24(4):** 409-412.

Letelier, R.M., D.M. Karl, M.R. Abbott, P. Flament, M.H. Freilich, R. Lukas, and P.T. Strub, 2000, Role of late winter mesoscale events in the biogeochemical variability of the upper water column of the North Pacific Subtropical Gyre, *J. Geophys. Res.*, **105:** 28,723-28,740.

Manov, D., G. Chang, and T. Dickey, 2003, Methods for reducing biofouling on moored optical sensors, *J. Atmos. Ocean. Tech*., in press.

McLean, S.D. and M.R. Lewis. 1991. An expendable spectral radiometer drifter system (ESR). *IEEE Oceans '91 Proceedings*.

McLean, S., Schofield, B., Zibordi, G., Lewis, M., Hooker, S., and Weidemann, A., 1997: Field evaluation of anti-biofouling compounds on optical instrumentation. In: Ackleson, S. G., Frouin, R. (Eds.), *Ocean Optics XIII*, Proc. SPIE, Bellingham, WA, vol. 2963, pp. 708-713.

McPhaden, M. J., Hansen, D. V., and Richardson, P. L., 1991: A Comparison of Ship Drift, Drifting Buoy, and Current Meter Mooring Velocities in the Pacific South Equatorial Current, *J. Geophys. Res.*, **96:** 775-782.

McPhaden, M. J., A. J. Busalacchi, R. Cheney, J. R. Donguy, K. S. Gage, D. Halpern, M. Ji, G. Meyers, G. T. Mitchum, P. P. Niiler, J. Picaut, R. W. Reynolds, N. Smith, and K. Takeuchi, 1998: The tropical ocean global atmosphere observing system: A decade of progress, *J. Geophys. Res.*, **103:** 14169-14240.

Milburn, H. B., and P D. McLain, 1986: ATLAS: A Low cost satellite data telemetry mooring developed for NOAA's Climate Research Mission, Proceedings from MTS Marine Data Systems International Symposium, Institute of Electrical and Electronics Engineering/Marine Technology Society, New Orleans.

Morel, A., 1988: Optical modeling of the upper ocean in relation to its biogenous content (Case I Waters), *J. Geophys. Res.*, **93,** 10749-10768.

Mueller, J. L. and R. W. Austin, 1992: Ocean Optics Protocols for SeaWiFS Validation, SeaWiFS Tech. Report Series, NASA Technical Memorandum 104566, Vol. 5, Goddard Space Flight Center, Geenbelt, MD, 43pp.

Neckel, H. and D. Labs, 1984. The solar radiation between 3300 and 12500A. *Solar Physics*. **90:** 205-258.

Niiler, P. P., A. S. Sybrandy, K. Bi, P. M. Poulain, and D. Bitterman, 1995: Measurements of the water-following capability of holey-sock and TRISTAR drifters, *Deep-Sea Res. I*, **42:** 1951-1964.

O'Reilly *et al*., 2000: NASA Technical Memorandum 2000–206892, Volume 11 SeaWiFS Postlaunch Technical Report Series, Volume 11, SeaWiFS Postlaunch Calibration and Validation Analyses, Part 3.

Send, U., B. Weller, S. Cunningham, C. Eriksen, T. Dickey, M. Kawabe, R. Lukas, M. McCartney, and S. Osterhus, 2001: Oceanographic time-series observatories, In: C.J. Koblinsky and N. R. Smith (Eds), Observing the Ocean in the 21st Century, GODAE Project Office and Bureau of Meteorology, Melbourne.

Servain, J., A. J. Busalacchi, M. J. McPhaden, A. D. Moura, G. Reverdin, M. Vianna, and S. E. Zebiak, (1998). A Pilot Research Moored Array in the Tropical Atlantic (PIRATA). *Bull. Am. Meteorol. Soc*., **79:** 2019-2031.

Siegel, D. A., D. M. Karl, and A. F. Michaels, 2001: Interpretations of biogeochemical processes from the US JGOFS Bermuda and Hawaii time-series sites, *Deep Sea Res. II*: *Topical Studies in Oceanography*, **48:** 1403-1404.

Smith, R. C., K. J. Watersand, K. S. Baker, 1991: Optical Variability and Pigment Biomass in the Sargasso Sea as Determined Using Deep-Sea Optical Mooring Data, *J. Geophys. Res.*, **96:** 8665-8686.

Strutton, P. G., J. P. Ryan, and F. P. Chavez, 2001: Enhanced chlorophyll associated with tropical instability waves in the equatorial Pacific, *Geophys. Res. Letters*, **28:** 2005-2008.

Strutton, P. G. and F. P. Chavez, In preparation, Merging observations from satellites, moorings and ships to quantify scales of biological-physical coupling in the equatorial Pacific, In: L. Seuront and P.G. Strutton (Eds.), *Handbook of scaling methods in aquatic ecology: Measurement, analysis and simulation*, CRC Press, Boca Raton, FL.

Zheng, X., T. Dickey, and G. Chang, 2002, Variability of the downwelling diffuse attenuation coefficient with consideration of inelastic scattering, *Appl. Opt.*, **41(30)**: 6477-6488.

Chapter 4

Ocean Color Radiometry from Aircraft: I. Low Altitude Measurements from Light Aircraft

Gordana Lazin[1], Lawrence W. Harding, Jr.[2], and Scott McLean[1]

[1]*Satlantic Inc., Halifax, Nova Scotia, Canada*

[2]*University of Maryland, Center for Environmental Science, Cambridge, Maryland*

4.1 INTRODUCTION

Low altitude, passive remote sensing of ocean color from aircraft spans nearly three decades and has used a variety of sensors. The Multichannel Ocean Color Sensor (MOCS) was first used in field experiments in 1980-82. MOCS measured spectral radiances in twenty contiguous 15-nm wide bands from 400 to 700 nm. Early applications of a spectral curvature ocean color algorithm for chlorophyll *a* concentration, *Chl* [mg m^{-3}], used data from MOCS along the East coast of the US over a six-year period (Grew, 1981; Campbell & Esaias, 1983). The spectral curvature algorithm (Sect. 4.4 below) was applied in real-time without calibration to estimate *Chl*. MOCS was operated with the Airborne Oceanographic Lidar (AOL) that combined active and passive radiometry and produced independent estimates of *Chl*. Study sites for the comparisons included shelf waters of the western Atlantic Ocean, Chesapeake Bay, Nantucket Shoals, and warm-core Gulf Stream rings. MOCS- and AOL-derived chl-a and in-situ measurements of chl-a from ships showed good agreement.

The successful retrieval of *Chl* using MOCS data and the spectral curvature algorithm led to the development of a small and relatively simple ocean color instrument, the Ocean Data Acquisition System (ODAS) in the mid-1980s, supported by NASA and NOAA. Following on the findings of Grew (1981) and Campbell and Esaias (1983) using equally spaced bands around MOCS band 7, ODAS was designed with three bands in the blue-green region of the visible spectrum at 460, 490, and 520 nm. The instrument was specifically designed for missions on light aircraft, an attribute rare, or absent, in previous ocean color instruments. The goal was to enable repeat coverage with high spatial resolution on affordable, relatively slow flying platforms, thus to move from demonstration to operational mode in acquiring remotely sensed data on *Chl* in estuarine and coastal waters. The ODAS nadir-viewing radiance sensor was designed to collect data along a line-of-flight at a sampling rate of 10 Hz. It was equipped with Loran-C for onboard navigation and was usually flown together with an infrared temperature sensor (PRT-5 or Heimann instruments) to sample sea surface temperature (*SST*) concurrently with ocean color measurements. The early uses of ODAS were in waters of the middle Atlantic bight, and it subsequently received heavy use from 1989-96 in Chesapeake Bay as part of the Chesapeake Bay Remote Sensing Program (CBRSP – http://www.cbrsp.org). Nearly 150 flights were conducted with ODAS to study seasonal and inter-annual variability of phytoplankton biomass and primary productivity in the Bay.

4.2 MEASUREMENT METHODS

Key operational attributes of ODAS flights were low altitude (150 m), low speed (100 knots = 50 m s^{-1}), and schedules timed to avoid high sun angles (flights conducted at 08:30 – 10:30 h and 14:30 – 16:30 h local time), high

wind speeds (>7 m s^{-1}) and variable cloud cover. Frequent coordination with shipboard sampling yielded a validation data set spanning a period of six years and covering a wide range of hydrographic conditions.

The routine use of passive remote sensing of ocean color from aircraft continues in a variety of locations, including Chesapeake Bay, Albemarle-Pamlico Sound in North Carolina, the middle Atlantic Bight, and several coastal sites in East Asia. These programs now use commercial sensors[8] mounted on light aircraft and helicopters. The SeaWiFS Aircraft Simulator (SAS) manufactured by Satlantic, Inc., of Halifax, Nova Scotia is used by a number of these programs. CBRSP, for example, currently flies routinely a SAS III, a 13-band radiometer, to continue the 1989-present time-series for Chesapeake Bay. This generation of sensors is nadir-viewing, simple to operate, uses GPS for navigation, and records data to a PC. Survey flights using single- or twin-engine aircraft are conducted in clear-sky conditions, to the extent possible, at 150 m altitude using single- or twin-engine aircraft.

The surface glint (sun and sky glint) is determined largely by observation geometry and solar zenith angle. The amount of sun-glint entering the sensor is affected by wind speed and orientation of the sensor relative to the sun. The sky-glint contribution increases radically with increasing observation nadir angle θ, and off-nadir viewing measurements in a direction near the solar azimuth will be totally saturated by sun glint., Practical arrangements for mounting ocean color radiometers on aircraft often make it difficult to adjust observation angles relative to the sun, and therefore, a nadir viewing angle (θ = 0) is the preferred - or at least the default - pointing direction for these instruments. Sun-glint may be reduced, or avoided, by choosing an appropriate time to make remote sensing observations, *i.e.*, by collecting data only when solar zenith angles are greater than 30° (Bukata *et al*. 1995). The probability of seeing the direct sun-glint can be estimated from the Cox and Munk model (1954) as a function of wind speed and solar zenith angle. If possible, a radiometer should be mounted on top of the aircraft to measure zenith sky radiance $L_{\mathrm{sky}}(\lambda,\pi)$, and/or global incident irradiance at flight level, to aid in glint removal and normalization of the nadir radiance measurements. Methods for correcting airborne nadir-viewing radiance measurements for sun and sky glint are presented below in Sect. 4.3.

4.3 RADIOMETRIC CORRECTION METHODS FOR AIRBORNE OCEAN COLOR RADIANCE MEASUREMENTS

The total radiance L_t sensed at altitude h Km by a radiometer pointed at the sea surface contains contributions from atmospheric scattering, and surface reflection, in addition to the desired water-leaving radiance. It may be partitioned and expressed as a sum

$$L_t(\lambda,\theta,\phi,\theta_o;h) = L_P(\lambda,\theta,\phi,\theta_o;h) + t(\lambda,\theta;h)\left[L_G^{sun}(\lambda,\theta,\phi,\theta_o) + L_G^{sky}(\lambda,\theta,\phi,\theta_o) + L_W(\lambda,\theta,\phi,\theta_o)\right] \quad (4.1)$$

where (θ,ϕ) are the viewing nadir and azimuth angle (relative to the sun), respectively, θ_o is solar zenith angle, t is atmospheric transmittance from the surface to altitude h, L_P is atmospheric path radiance, L_W is water-leaving radiance, and L_G^{sun} and L_G^{sky} are surface sun and sky glint, respectively. The first problem connected with the atmospheric correction of data remotely sensed at different altitudes is the definition and evaluation of the absorption and scattering processes due to atmospheric constituents as a function of flight altitude. The second problem involves surface glint correction.

Atmospheric Attenuation

The atmospheric attenuation by absorption and scattering is defined through the optical thickness of atmospheric constituents (permanent gases, aerosols, ozone and water vapor). The optical thickness $\tau(\lambda,h)$ of the atmospheric layer between the sensor at altitude h and the sea surface is expressed as the sum of individual optical

[8] Certain commercial equipment, instruments, or materials are identified in this document to foster understanding. Such identification does not imply recommendation or endorsement by the National Aeronautics and Space Administration, nor does it imply that the materials or equipment identified are necessarily the best available for the purpose.

thicknesses of air molecules $\tau_R(\lambda,h)$ (Rayleigh optical thickness), aerosols $\tau_A(\lambda,h)$, water vapor $\tau_W(\lambda,h)$ and ozone $\tau_{O_3}(\lambda,h)$, *i.e.*

$$\tau(\lambda,h)=\tau_R(\lambda,h)+\tau_A(\lambda,h)+\tau_W(\lambda,h)+\tau_{O_3}(\lambda,h). \tag{4.2}$$

The total transmittance of the atmospheric layer between the sensor and the sea surface is then computed as

$$t(\lambda,\theta;h)=\exp\left[-\frac{\tau(\lambda,h)}{\cos\theta}\right]. \tag{4.3}$$

The parameterization of optical thickness as a function of altitude for permanent gases, ozone and water vapor, in terms of meteorological parameters (temperature, due point temperature, relative humidity, ozone concentration) can be found in Guzzi *et al*. (1987), Zibordi *et al*. (1990a,b) and references within. In contrast, the aerosol optical thickness cannot be parameterized because the aerosol is highly variable in time and space, and is, in general, unknown in remote sensing experiments. Aerosol optical thickness can be evaluated either from models (Shettle and Fenn 1979), or deduced from the remote sensing data itself as an unknown during iteration procedures of a correction algorithm (Guzzi *et al*. 1987, Zibordi and Maracci 1988, Zibordi *et al*.1990), or by direct measurements (Maracci and Zibordi 1990).

Atmospheric Path Radiance

Path radiance $L_P(\lambda,\theta,\phi,\theta_o;h)$ can be partitioned into the sum of independent contributions due to molecular scattering, called Rayleigh radiance $L_R(\lambda,\theta,\phi,\theta_o;h)$, and scattering by aerosols, called aerosol radiance $L_A(\lambda,\theta,\phi,\theta_o;h)$, *i.e.*

$$L_P(\lambda,\theta,\phi,\theta_o;h)=L_R(\lambda,\theta,\phi,\theta_o;h)+L_A(\lambda,\theta,\phi,\theta_o;h). \tag{4.4}$$

The partitioning in the form of (4.4) assumes that the single scattering approximation can be applied with no interaction between scattering by air molecules and aerosols (Gordon 1978). This assumption is especially reasonable at measurement altitudes $h\le 1$ Km.

Rayleigh scattering is wavelength dependent and varies in proportion to λ^{-4}. The Rayleigh path radiance originating in the atmosphere below the sensor at altitude *h* can be written as (Bukata *et al*. 1995, Guzzi *et al*. 1987)

$$L_R(\lambda,\theta,\phi,\theta_o;h)=\frac{E_{sun}(\lambda;h)t(\lambda,\theta;h)}{\cos\theta}\frac{\tau_R(\lambda,h)P_R(\psi)}{4\pi}, \tag{4.5}$$

where $E_{sun}(\lambda;h)$ is direct solar irradiance incident at altitude *h*, $\psi=\psi(\theta,\phi,\theta_o)$ is the scattering angle [see Vol. I, Ch. 2, equation (2.5)], and $P_R(\psi)$ is the Rayleigh scattering phase function, giving the angular distribution of scattered energy (normalized to 4π),[9]

$$P_R(\psi)=\frac{3(1+\cos^2\psi)}{4}. \tag{4.6}$$

The atmospheric molecular optical thickness $\tau_R(\lambda,h)$, as a function of flight altitude, can be obtained approximately through relations proposed by Van Stokkom and Guzzi (1984)

$$\tau_R(\lambda,h)=0.0088H_R(h)\lambda^{-4.15+0.2\lambda}, \tag{4.7}$$

[9] The molecular scattering phase functions for air and water are the same, neglecting the depolarization properties of the two media. Compare (4.6) to equation (2.29) in Vol. I, Chapter 2, where the molecular scattering phase function for pure water is denoted $\tilde{\beta}_w(\psi)$. The standard practice in the ocean optics community is to normalize the integral of the molecular phase function to unity, whereas the practice in the atmospheric community is to normalize it to 4π. Thus, $\tilde{\beta}_w(\psi)=\frac{P_R(\psi)}{4\pi}$.

where λ is in μm, h is in Km, and the funtion $H_R(\lambda)$ is

$$H_R(h) = 1 - \exp\left(-0.1188h - 0.0011h^2\right). \tag{4.8}$$

In contrast to Rayleigh scattering, aerosol scattering is only weakly wavelength dependent, especially when the particle size is large relative to the wavelength (McCartney 1976). The aerosol path radiance can be written as

$$L_A(\lambda,\theta,\phi,\theta_o;h) = \frac{E_{sun}(\lambda;h)t(\lambda,\theta;h)}{\cos\theta}\frac{\varpi_A(\lambda)\tau_A(\lambda,h)P_A(\psi)}{4\pi}, \tag{4.9}$$

where $\varpi_A(\lambda)$ is the single scattering albedo [Vol. I, Ch. 2, equation (2.26)] for aerosols, and $P_A(\psi)$ is the aerosol phase function. The optical properties of aerosols [τ_A, ϖ_A and $P_A(\psi)$] are determined by the size, shape, complex refractive index and concentration of aerosol particles in the intervening atmospheric layer; they can be estimated from the models for aerosol extinction in a marine boundary layer using relative humidity (Shettle and Fenn 1979; Wong 1998; Winter 1994). A convenient, approximate analytic representation of the aerosol phase function is a two-term Henyey-Greenstein function, using parameters for marine aerosol proposed by Gordon *et al*. (1983). The estimation of aerosol scattering remains the largest uncertainty in the remote sensing of ocean color from space (Gordon 1978).

Surface Glint

Sun-glint outliers that are present in the data should be removed by filtering of the high-frequency records before any averaging is performed. The outliers are identified by the concurrent increase (often to saturation) of signals in all bands. A common sun-glint filter entails rejection of outliers that fall 1.5 standard deviation above the mean value of a chosen data segment (Mueller and Austin 1995; Harding *et al*. 1992; Lazin 1998).

To the present, two methods for sky-glint correction have been applied to low altitude airborne radiometric data. In the first method, sky glint is computed using sea surface reflectance $\rho(\theta;W)$, where W is wind speed in m s^{-1}, and incident sky radiance $L_{sky}(\lambda,\pi-\theta,\phi)$. For a sensor looking at nadir, sky glint is computed as

$$L_G^{sky}(\lambda) = \rho(0;W)L_{sky}(\lambda,\pi), \tag{4.10}$$

where $L_{sky}(\lambda,\pi)$ is zenith sky radiance. As elsewhere in this protocol document, the omission of explicit (θ,ϕ) dependence indicates nadir-viewing geometry. The dependence of surface reflectance $\rho(\theta;W)$ on wind speed W, sky radiance distribution, and solar zenith angle was modeled by Mobley (1999) for shipboard observations (Vol III, Ch. 3), but this approach has not been used in airborne applications. For nadir viewing geometry, at any rate, surface reflectance $\rho(\theta;W)$ is essentially independent of wind speed W (Austin 1974; see also Vol. III, Ch.4). Some researchers have used Fresnel reflectance for vertical incidence of 0.021 (Hoge *et al*. 1987). Ideally the zenith sky radiance should be measured because the prediction of its magnitude and spectral distribution from the models (Harrison and Combes 1988) is difficult and may have large uncertainties.

The second method assumes that the sky glint is proportional to the diffuse sky irradiance $E_{sky}(\lambda;h)$ (Bukata *et al*. 1995, Lazin 1998) and can be expressed as

$$L_G^{sky}(\lambda) = f_1(\theta_o;W)E_{sky}(\lambda;h), \tag{4.11}$$

where the factor f_1 depends on sky conditions, solar zenith angle θ_o, and wind speed W. For Case I water where the water leaving radiance at a red, or near-infrared, wavelength λ_o is approximately zero, the factor f_1 can be computed as

$$f_1 = \frac{L_t'(\lambda_o)}{E_{sky}(\lambda_o;h)t(\lambda_o;h)}, \tag{4.12}$$

where $L_t'(\lambda_o)$ is the total radiance corrected for the atmospheric effects. For low flying aircraft, where atmospheric effects can be assumed to be negligible, it was found that f_1 has approximately a constant value of 0.0087 (Lazin *et al*. 1996).

The diffuse sky irradiance $E_{\text{sky}}(\lambda;h)$ for clear skies can be easily predicted from measured global downwelling irradiance $E_{\text{S}}(\lambda;h)$ and the ratio of diffuse $\hat{E}_{\text{sky}}(\lambda)$ to global irradiance $\hat{E}_{\text{S}}(\lambda)$ obtained from a clear sky model (Gregg and Carder 1990, Bird and Riordan 1986) as

$$E_{\text{sky}}(\lambda;h) = \frac{\hat{E}_{\text{sky}}(\lambda)}{\hat{E}_{\text{S}}(\lambda)} E_{\text{S}}(\lambda;h). \tag{4.13}$$

The input parameters in the clear sky models are solar zenith angle, ozone scale height and meteorological data (pressure, temperature, dew point temperature, relative humidity, wind speed, visibility) that, ideally, should be measured on board the aircraft. The ozone scale height can be estimated from climatological, or satellite, data for that region.

Water-Leaving Radiance from Low-Altitude Radiance Measurements

In the case of flight altitudes 150-300 m, and typical clear sky/low wind conditions the radiance scattered by aerosol is usually an order of magnitude less than the signal measured on the aircraft and therefore can be neglected. Additionally, the aerosol scattering has very little wavelength dependence and would not greatly affect the spectral distribution of the signal. On the contrary, Rayleigh scattering contributes more in the blue part of the spectrum and therefore cannot be neglected even for low flight altitudes. The transmittance of the atmospheric layer between the sensor and the sea surface is usually close to 1 and for the altitudes up to 300 m the intervening atmospheric layer can be considered transparent (Lazin 1998). In that case the remote sensing equation simplifies to the following form

$$L_{\text{t}}(\lambda;h) = L_{\text{R}}(\lambda,\theta_{\text{o}};h) + L_{\text{G}}^{\text{sun}}(\lambda,\theta_{\text{o}}) + L_{\text{G}}^{\text{sky}}(\lambda,\theta_{\text{o}}) + L_{\text{w}}(\lambda,\theta_{\text{o}};h), \tag{4.14}$$

where the Rayleigh contribution is computed using equations (4.5) through (4.8), the sun-glint outliers are filtered out, and the sky glint is computed by one of the methods described in the previous subsection.

4.4 CHLOROPHYLL a DETERMINATION

Water-Leaving Radiance Ratio Algorithms

If corrected water-leaving radiances are determined, via equation (4.14), from airborne radiance measurements at appropriate wavelengths, their ratios may be used in SeaWiFS, MODIS or other satellite ocean color remote sensing algorithms to determine *Chl* and/or the diffuse attenuation coefficient *K490*. Reviews of available algorithms of these types are beyond the scope of this protocol document.

Spectral Curvature Algorithm

A detailed description of the theoretical basis for the spectral curvature algorithm was given by Campbell and Esaias (1983), including a summary of the advantages over radiance ratio algorithms in several respects. The algorithm removes, or lessens, much of the "extraneous variation" (solar zenith, atmospheric transmittance) in remote sensing data collected at low altitude.

"Spectral Curvature" is characterized by the inflection ratio $G(\lambda_1,\lambda_2,\lambda_3)$ determined from the triplet of spectral radiances $\left[L(\lambda_1), L(\lambda_2), L(\lambda_3)\right]$ as

$$G(\lambda_1,\lambda_2,\lambda_3) = \frac{L(\lambda_2)^2}{L(\lambda_1)L(\lambda_3)} \tag{4.15}$$

where $\lambda_1 < \lambda_2 < \lambda_3$ and ideally $\lambda_2 = \frac{\lambda_1 + \lambda_3}{2}$.

The form of the spectral curvature algorithm for chlorophyll *a* concentration *Chl* is

$$\log_{10} Chl = a + b \bullet \log_{10} G(\lambda_1,\lambda_2,\lambda_3), \tag{4.16}$$

where the coefficients a and b are depend on aircraft altitude, the specific type of radiance measurement used in (4.15), and the wavelengths of the measurements. The algorithm is relatively insensitive to other variables such as solar elevation (Campbell and Esaias 1983).

4.5 DISCUSSION

Grew (1981) substituted raw spectral data (instrument outputs in digital counts) to compute inflection ratios $G(\lambda_1,\lambda_2,\lambda_3)$ [Eq. (4.15)], for three fixed MOCS channels having between-band wavelength intervals of 30 nm. Campbell and Esaias (1983) reported significant differences in inflection ratio spectra for "greener" and more turbid waters related to mixtures of absorbing and scattering materials. The presence and abundance of *Chl* dramatically influenced the spectrum, as shown in their Fig. 1 for blue water and in green water normalized to the blue water spectrum in their Fig. 2. The effect of *Chl* on the inflection ratio was very pronounced at MOCS band 12, centered at 568 nm, but Grew reported a more reliable indicator of *Chl* was the inflection ratio of MOCS band 7, centered at 490 nm.

Chl recoveries from ODAS data used calibrated total radiances $L_t(\lambda)$ from the three bands in a spectral curvature algorithm, as per MOCS. Raw counts were substituted into the curvature algorithm to generate a preliminary, real-time *Chl* output during each flight. The coefficients, of the algorithm were derived by regression analysis of 120 matched pairs of ODAS derived $G(460,490,520)$ curvature parameters (inflection ratios) and in-situ chlorophyll *a* measurements; the two data types were considered "matched" if the measurements were made within 24 h of one another in locations separated by no more than 0.01^o Latitude and 0.005^o Longitude. These samples were acquired, in 1990-95, from the EPA Chesapeake Bay Program monitoring cruises, spanning the entire main stem of the Bay and a range of *Chl* concentrations from less than 1 mg m^{-3} to more than 50 mg m^{-3}. The ODAS program is described in several publications (*e.g.*, Harding *et al*. 1992a, 1994, 1995).

To date, the accuracy of water-leaving radiance obtained from low-flying aircraft has not been properly assessed. In one study (Lazin 1998) the agreement between L_w computed from airborne data using E_{sky} for sky-glint correction, and the L_w measured in-situ by tethered radiometric buoy during overflights, was within 15 %, and the ratio of remote sensing reflectances agreed within 3.4% for clear sky conditions. If no corrections were applied to those data, the differences in estimated L_w were 40-130%, and in remote sensing reflectance ratios up to 34 %. It was also found that the ratio $\frac{R_{RS}(490;h)}{R_{RS}(555;h)}=\frac{L_t(490;h)E_S(555;h)}{E_S(490;h)L_t(555;h)}$ agreed better with *in situ* remote sensing reflectance ratios if no correction was applied to the airborne radiances, whereas ratios utilizing bands at 412 nm, and 443 nm showed significant improvement after correction, because of increased Rayleigh scattering effects at these shorter wavelengths. For overcast conditions large disagreements in L_w and R_{RS} ratios were observed regardless of corrections, suggesting that accurate airborne ocean color radiometric measurements are very difficult to obtain under overcast skies.

REFERENCES

Austin, R.W., 1974: The remote sensing of spectral radiance from below the ocean surface. In: Optical Aspects of Oceanography, N.G. Jerlov and E.S. Nielson, Eds., pp 317-344.

Bird,R.E., Riordan, C., "Simple solar spectral model for direct and diffuse irradiance on horizontal and tilted planes at Earth's surface for cloudless atmospheres", J. Climatol. Appl. Meteorol. Soc. 25: 87-97, 1986

Bukata, R.P., Jerome, J.H., Bruton, J.E., "Particulate concentrations in lake St. Clair as recorded by shipborne multispectral optical monitoring system", Remote Sens. Envir., 25, 201-229, 1988

Bukata, P.B., Jerome, H.J., Kondrattyev, K.Y., Pozdnyakov, D.V., Optical properties and remote sensing of inland and coastal waters, CRC Press, Boca Raton, 1995

Campbell, J.C, Esaias, W.E., "Basis for spectral curvature algorithms in remote sensing of chlorophyll", Appl. Optics, 22, 1084-1093, 1983

Cox, C, Munk, W., "Statistics of the sea surface derived from sun glitter", J. Marine Res. 13, 198-277, 1954

Gordon, H.R., "Removal of atmospheric effect from satellite imagery of the oceans", Appl. Opt. 17, 1631, 1978

Gordon, H.R., Clark, D.K., Brown, J. W., Brown, O.B., Evans R.H., Broenkow, W.W., "Phytoplankton pigment concentration in the Middle Atlantic Bight: comparison of ship determination and CZCS estimates", Appl. Optics 22, 20-36, 1983

Gregg, W.W., Carder, K.L., "A simple spectral solar irradiance model for cloudless maritime atmospheres", Limnol. Oceanogr. 35, 1657-1675, 1990

Grew, G.W., "Real-time test of MOCS algorithm during Superflux 1980", NASA Publ. CP-2188, 301 p.

Guzzi, R., Rizzi, R., Zibordi, G., "Atmospheric correction of data measured by a flying platform over the sea: elements of a model and its experimental validation", Appl. Opt. 26, 3043-3051, 1987

Harding, L.W., Itsweire, E.C., Esaias, W.E., "Determination of phytoplankton chlorophyll concentrations in the Chesapeake Bay with aircraft remote sensing", Remote Sens. Environ., 40, 79-100, 1992

Harding, L.W., Itsweire, E.C., Esaias, W.E., "Estimates of phytoplankton biomass in Chesapeake Bay from aircraft remote sensing of chlorophyll concentrations, 1989-92", Remote Sens. Environ., 49, 41-56, 1994

Harding, L.W., Itsweire, E.C., Esaias, W.E., "Algorithm development for recovering chlorophyll concentrations in the Chesapeake Bay using aircraft remote sensing", Photogramm. Eng. Rem. Sens., 61, 177-185, 1995

Harrison, A.W., Combes, C.A., "Angular distribution of clear sky short wavelength radiance", Solar Energy, 40, 57-63,1988

Hoge, F.E., Wright, C.W., Swift, R.N., "Radiance ratio algorithm wavelengths for remote oceanic chlorophyll determination", Appl. Opt. 26, 2082-2093, 1987

Lazin, G., Davis, R.F., Ciotti, A.M., and Lewis, M.R., "Ocean color measurements from low flying aircraft: Atmospheric and surface glint correction", Ocean optics XIII proceeding, SPIE, 703-707, 1996

Lazin, G, Correction methods for low altitude remote sensing of ocean color, M.Sc. Thesis, Dalhousie University, Halifax, 1998

Maracci, G., Zibordi, G., "Atmospheric optical thickness from '2p radiometer' data", Int. J. Remote Sensing, 10: 1957-1961, 1990

McCartney, E.J., Optics of the atmosphere, Wiley, New York, 1976

Mueller, J.L., Austin, R.W., "Ocean optics protocol for SeaWiFS validation, revision 1", SeaWiFS Technical Report Series, NASA Technical Memorandum 104566, Vol. 25, 1995

Mobley, C.D., Estimation of the remote sensing reflectance from above-surface measurements, Appl.Opt. 38, 7442-7455, 1999

Shettle, E.P., Fenn, R.W., "Models for aerosols of the lower atmosphere and the effect of the humidity variations on their optical properties" Air Force Geophysics laboratory, Hanscomb AFB, MA 01731, AFGL-TR-79-0214, 1979

Van Stokkom, H. T. C., Guzzi, R., "Atmospheric spectral attenuation of airborne remote-sensing data: Comparison between experimental and theoretical approach", Int. J. Remote Sensing 5, 925-938, 1984

Winter, B., Light scattering by a sea salt aerosol layer, M.Sc. Thesis, Dalhousie University, Halifax, 1994

Wong, J., "Radiative Impact of Atmospheric Aerosols and Clouds", PhD Thesis, Dalhousie University, Halifax, 1998

Zibordi, G., Maracci, G., "Determination of atmospheric turbidity from remotely-sensed data", Int. J. Remote Sensing 9, 1881-1894, 1988

Zibordi, G., Maracci, G., Schlittenhardt, "Ocean colour analysis in coastal waters by airborne sensors", Int. J. Remote Sensing 11, 705-725, 1990a

Zibordi, G., Parmiggiani, F., Alberotanza, L., "Application of aircraft multispectral scanner data to algae mapping over the Venice lagoon", Remote. Sens. Environ. 34, 49-54, 1990b

Chapter 5

Stray-Light Correction of the Marine Optical Buoy

Steven W. Brown[1], B. Carol Johnson[1], Stephanie J. Flora[2], Michael E. Feinholz[2], Mark A. Yarbrough[2], Robert A. Barnes[3], Yong Sung Kim[4], Keith R. Lykke[1], and Dennis K. Clark[5]

[1]*Optical Technology Division, National Institute of Standards and Technology, Gaithersburg, Maryland*

[2]*Moss Landing Marine Laboratories, Moss Landing, California*

[3]*Science Applications International Corporation, Beltsville, Maryland*

[4] *Data Systems Technologies, Inc., Rockville, Maryland*

[5]*National Oceanic and Atmospheric Administration, National Environmental Satellite Data and Information Service, Camp Springs, Maryland*

5.1 INTRODUCTION

In ocean-color remote sensing, approximately 90 % of the flux at the sensor originates from atmospheric scattering, with the water-leaving radiance contributing the remaining 10 % of the total flux. Consequently, errors in the measured top-of-the atmosphere radiance are magnified a factor of 10 in the determination of water-leaving radiance. Proper characterization of the atmosphere is thus a critical part of the analysis of ocean-color remote sensing data. It has always been necessary to calibrate the ocean-color satellite sensor vicariously, using *in situ*, ground-based results, independent of the status of the pre-flight radiometric calibration or the utility of on-board calibration strategies (Gordon 1998). Because the atmosphere contributes significantly to the measured flux at the instrument sensor, both the instrument and the atmospheric correction algorithm are simultaneously calibrated vicariously.

The Marine Optical Buoy (MOBY) (Clark *et al*. 1997; Clark *et al*. 2002a; Clark *et al*. 2002b), deployed in support of the Earth Observing System (EOS) since 1996, serves as the primary calibration station for a variety of ocean-color satellite instruments, including the Sea-viewing Wide Field-of-view Sensor (SeaWiFS) (Barnes *et al*. 2000), the Moderate Resolution Imaging Spectroradiometer (MODIS) (Esaias *et al*. 1998), the Japanese Ocean Color Temperature Scanner (OCTS) (Isaacman *et al*. 1999), and the French Polarization and Directionality of the Earth's Reflectances (POLDER) (Deschamps *et al*. 1994). MOBY is located off the coast of Lanai, Hawaii. The site was selected to simplify the application of the atmospheric correction algorithms (Clark *et al*. 1997). Vicarious calibration using MOBY data allows for a thorough comparison and merger of ocean-color data from these multiple sensors (Wang *et al*. 2002).

MOBY uses an instrument known as the Marine Optical System (MOS) to detect radiation over the spectral range from 350 nm to 955 nm. The MOS system contains two single-grating spectrographs, a blue spectrograph (BSG) to measure light in the near ultraviolet and visible from 340 nm to 640 nm and a red spectrograph (RSG) to measure light in the red and near infrared from 550 nm to 955 nm (Clark *et al*. 2002a; Clark *et al*. 2002b). MOS resides in the MOBY instrument bay located at the bottom of the buoy. It is connected by optical fibers to radiance and irradiance ports on the three MOBY arms (denoted Top, Mid, and Bot), located at different ocean depths (typically 1.5 m, 5 m and 9 m), as well as to a surface irradiance port. MOBY measures upwelling radiance, L_u, as well as the down-welling irradiance, E_d. A fiber-optic multiplexer in the MOBY instrument bay selects which spectrum is acquired by MOS. As described in Clark *et al*. (2002b), these data are used to determine the water-leaving radiance, L_w.

MOBY buoys are typically deployed for 3 months to 4 months, then retrieved for servicing and repair. Deployments are numbered sequentially. One MOS instrument, MOS204, is used for even-buoy deployments while a separate instrument, MOS205, is used for odd deployments. The buoys are calibrated before and after deployment using sources traceable to radiometric standards maintained at the National Institute of Standards and Technology (NIST) (Clark *et al*. 2002a). During a deployment, the buoy's radiometric stability is checked using on-board

calibration sources and monthly lamp calibrations by divers (Clark *et al*. 2002a). The MOBY radiometric standards are monitored during the year using two single-channel filter radiometers, called Standard Lamp Monitor (SLM) radiometers, with filter channels at 412 nm and 870 nm. They are calibrated at NIST on a regular basis. In addition, transfer-standard artifacts are deployed from NIST to the MOBY field laboratory on a yearly basis to validate the calibration protocols and assess the accuracy and stability of the MOBY spectral radiance sources.

The generally stated uncertainty goal for ocean-color radiometry is 5 % ($k = 1$) for L_w, which results in an uncertainty of 35 % for chlorophyll-*a* (Hooker *et al*. 1993). This requirement for high accuracy places stringent demands on the uncertainties in water-leaving radiance measurements with MOBY. The uncertainties of MOBY measurements of water-leaving radiance L_w — without accounting for the effects of stray light — are estimated to be in the range from 4 % to 8 % ($k = 1$) (Clark *et al*. 2002a).

Spectrographs are imaging systems with dispersive elements and multi-element detectors that enable simultaneous acquisition of an entire spectrum over some finite spectral width. There are intrinsic limitations in the background signal originating from radiation scattered from imperfections in the optical elements in the instrument. This unwanted background radiation, called stray light, while small — on the order of 0.01 % or less of the incident spectral radiance in a single grating spectrograph — can give rise to unforeseen errors, often much larger than anticipated, when the spectral distribution of a source being measured differs significantly from the spectral distribution of the calibration source. Such a situation is routinely encountered in oceanographic measurements, where instruments are calibrated against incandescent sources with a peak radiance in the short-wave infrared (~1000 nm) and subsequently measure the radiance of the ocean, which peaks in the blue spectral region (~450 nm) (Fig. 5.1). Consequently, stray light, if not properly accounted for, can have a significant effect in ocean-color research (Clark *et al*. 2002a).

Measurements with the two spectrographs in the MOS systems can be compared in the spectral interval from about 580 nm to 630 nm. In this spectral range the two spectrographs give different values for L_u or E_d at a common wavelength. In Fig. 5.2, L_u is shown for the Top (Top), Middle (Mid) and Bottom (Bot) MOBY arms. The difference in the measured radiance in the overlap region is a function of depth, increasing for deeper-lying MOBY arms. While the signal is small in this region (approximately 1 % of the peak radiance), the lack of agreement in the overlap region and particularly its dependence on the spectral distribution of the upwelling radiance are possible manifestations of stray light in the system.

To look for stray light in MOS, the response of the two spectrographs in the MOS205 system to monochromatic laser excitation was measured. In this experiment, lasers were directed into an integrating sphere and the radiance was measured with each MOBY arm. For monochromatic radiation, the entrance slit is spatially imaged on the detector. Ideally, no radiation falls on detector elements outside the image. In practice, the image is modified by scattered light within the spectrograph and every element in the array can in principle have a finite response to this monochromatic radiation. Results for the two spectrographs are shown in Fig. 5.3. The spectra are similar for both spectrographs. There are three components to the image: a strong, sharp peak corresponding to the image of the spectrograph entrance slit on the CCD; a broad, peaked structure around the slit image; and a non-zero constant component. These three components are similar to specular, haze and diffuse components of reflectance. The specular component corresponds to the properly imaged radiation; the haze and diffuse components arise from light scattered in the spectrograph, principally from the grating. These two components are analogous to the spectral out-of-band features commonly observed in a filter radiometer.

In certain spectral regions, additional features are observed in the CCD response. From physical examination of the spectrographs, the additional peaks are associated with a higher order diffraction peak from the grating. Optical ray-trace modeling of the system confirms this hypothesis. Representative MOBY images showing this reflection peak in the system response are given in Fig. 5.4. Note, for example, the secondary reflection peak centered about pixel 160 (pixel 725) for light imaged onto pixel 195 (pixel 760) for the BSG (RSG).

This scattered light causes unknown but potentially significant errors in the measured up-welling radiance. Consequently, the MOS instrument was characterized for its stray-light response and the results incorporated into an algorithm that was developed to correct its measurements for stray light. In Section 5.2, we describe the iterative approach used to correct a MOS spectrum for stray light. The derivation of the instrument's stray-light parameters is described in Section 5.3 and applied to MOBY data sets in Section 5.4.

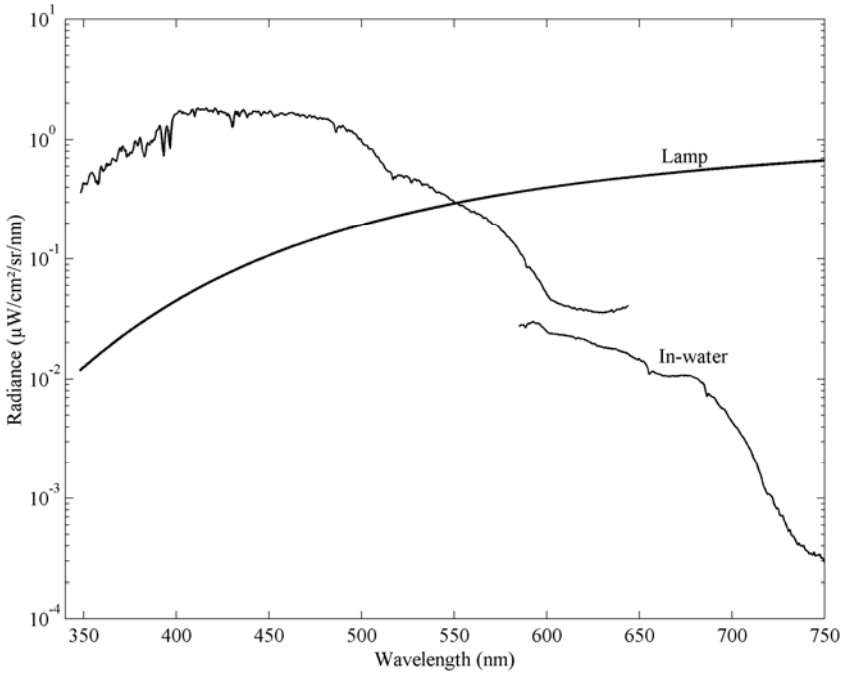

Figure 5.1. Typical spectral radiances of a lamp-based calibration source and in-water, up-welling radiance at the MOBY site.

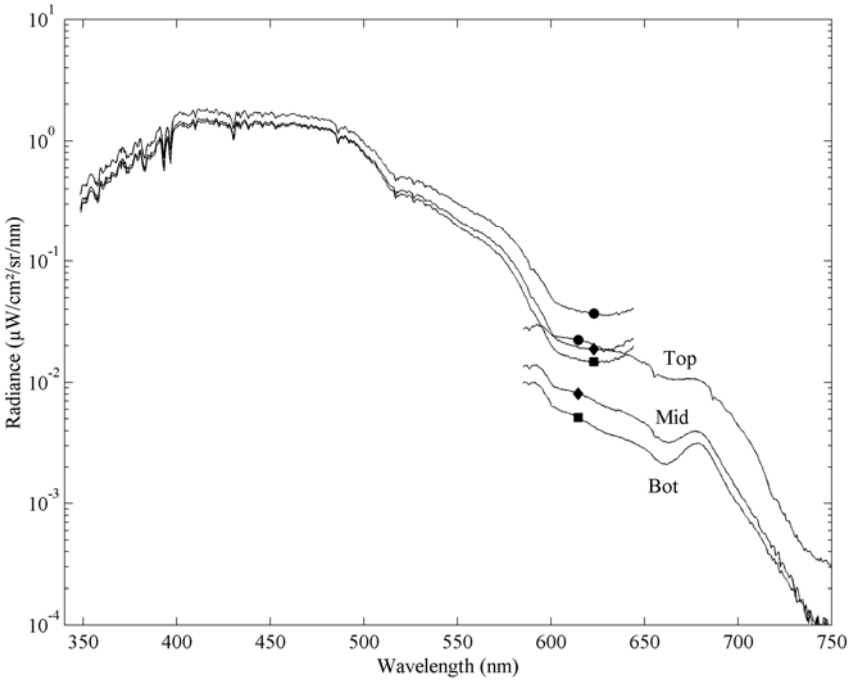

Figure 5.2. MOBY L_u (typical) for the three MOBY arms showing the lack of agreement in the overlap region where both spectrographs make measurements.

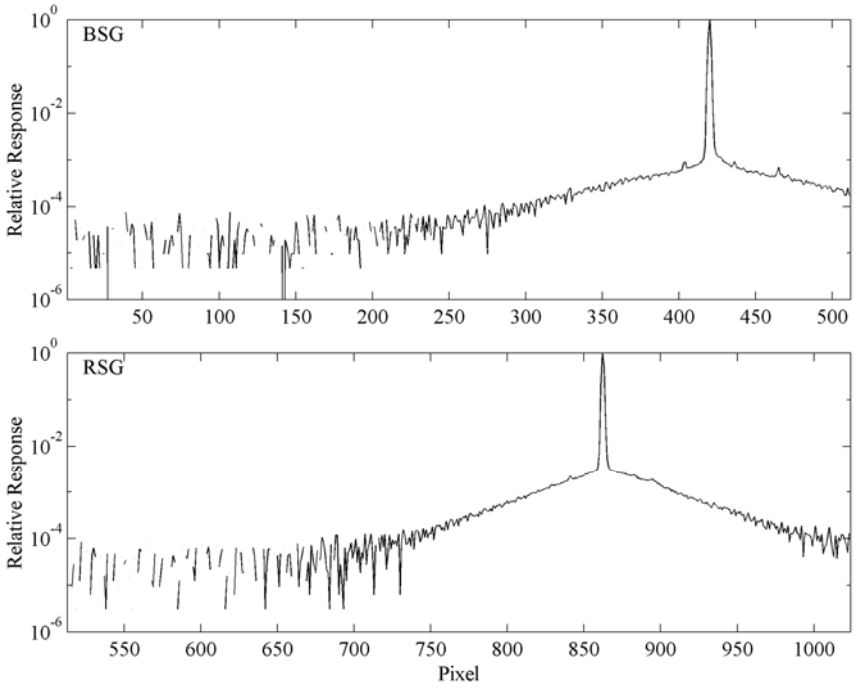

Figure 5.3. MOS205 response to monochromatic excitation.

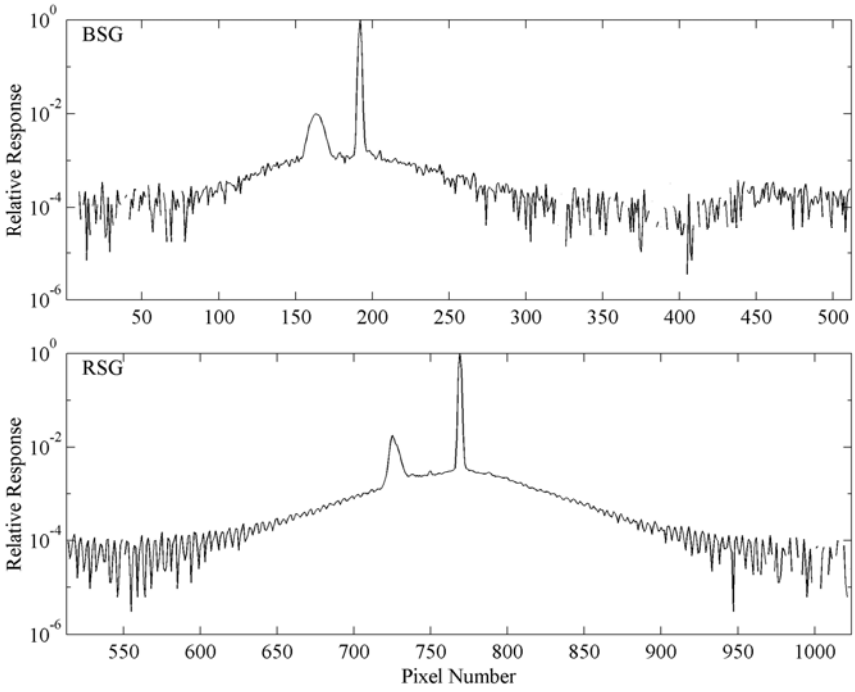

Figure 5.4. MOS205 response to monochromatic excitation showing reflection peaks.

5.2 STRAY-LIGHT CORRECTION ALGORITHM

Each MOS spectrograph uses a 512 by 512 element CCD array to detect incident radiation. When acquiring an image, the signals from the central 384 pixels in each column are averaged and a 512-element array is generated from each spectrograph. The total signal from element *i* of a MOS CCD is given by the equation

$$S_i = \int r_i(\lambda) L(\lambda) d\lambda \qquad (5.1)$$

where $r_i(\lambda)$ is the spectral responsivity of element *i* and $L(\lambda)$ is the spectral radiance of the source being measured. Note that $r_i(\lambda)$ is the spectral responsivity of element *i* when considered as part of the spectrograph and includes effects such as grating diffraction efficiency and mirror losses.

For monochromatic radiation, an image of the entrance slit is formed on the detector. Expressed as a function of wavelength rather than array element, this normalized spatial image function is known as the instrument's slit-scatter function $\sigma_i(\lambda_i - \lambda)$ (Kostkowski 1979), with the 'exit slit' in this case determined by the array element's spatial width and λ_i is the wavelength of element *i*'s maximum responsivity. There is a fixed relationship between the excitation wavelength and the position of the image on the array. As the wavelength changes, the spatial image moves across the array.

Knowing this relationship enables us to determine the fraction of incident light at some wavelength that is scattered onto a particular element. For example, for the wavelength λ_{ex} in Fig. 5.3, 0.01 % of the light imaged on element 420 (BSG) is scattered onto element 300. Assuming each element in the detector array has the same average spectral responsivity, the signal from element 300 to radiation at wavelength λ_{ex} is 0.01 % of the signal from element 420.

Following Kostkowski (Kostkowski 1979), the total responsivity of element *i* can be approximated by the product of the slit-scattering function and the maximum responsivity of each array element $\bar{r}_i(\lambda_i)$ (Fig. 5.5)

$$r_i(\lambda) = \bar{r}_i(\lambda_i)\,\sigma_i(\lambda_i - \lambda)\,. \tag{5.2}$$

Knowing the slit-scatter function, we have a set of 512 coupled equations

$$S_i = \bar{r}_i(\lambda_i)\int \sigma_i(\lambda_i - \lambda)\,L(\lambda)\,d\lambda \tag{5.3}$$

that can be directly solved for either $\bar{r}_i(\lambda_i)$ or $L(\lambda)$ (provided the other variable is known) using a generalized least-squares approach (Shumaker 1979). Approximate inverse solutions using Singular-Value-Decomposition (SVD) of the applicable matrices are robust and should be directly applicable to this system (Mueller 2002). We used a simpler, more intuitive, iterative approach utilizing the inherently discrete nature of the CCD response. Separating Eq. (5.1) into an in-band (*ib*) and an out-of-band (*oob*) component and assuming that the source radiance is approximately constant over the in-band spectral width, Eq. (5.1) can be written as

$$S_i = \int_{ib} r_i(\lambda)\,L(\lambda)d\lambda + \int_{oob} r_i(\lambda)\,L(\lambda)d\lambda = L(\lambda_i)R_i(\lambda_i) + \bar{r}_i(\lambda_i)\int_{oob}\sigma_i(\lambda_i - \lambda)\,L(\lambda)d\lambda\,, \tag{5.4}$$

where λ_i is the wavelength corresponding to the peak responsivity of element *i*, $L(\lambda_i)$ is the source radiance at λ_i, and $R_i(\lambda_i)$ is the integrated in-band responsivity of element *i*

$$R_i(\lambda_i) = \bar{r}_i(\lambda_i)\int_{ib}\sigma_i(\lambda_i - \lambda)\,d\lambda\,. \tag{5.5}$$

Measuring a calibration source of known spectral radiance, $L_c(\lambda)$, and solving for $R_i(\lambda_i)$ in Eq. (5.4), the integrated in-band responsivity of pixel *i* can be written

$$R_i(\lambda_i) = \frac{S_i}{L_c(\lambda_i)} - \frac{\bar{r}_i(\lambda_i)}{L_c(\lambda_i)}\int_{oob}\sigma_i(\lambda_i - \lambda)\,L_c(\lambda)\,d\lambda\,. \tag{5.6}$$

The second term on the right hand side of Eq. (5.6) is the stray-light contribution to the total responsivity. Utilizing the discrete nature of the spectrograph detector array and substituting Eq. (5.5) for $\bar{r}_i(\lambda_i)$, a recursion relation is developed for $R_i(\lambda_i)$

$$R_i^{(n)}(\lambda_i) = \frac{S_i}{L_c(\lambda_i)} - \frac{1}{L_c(\lambda_i)\int_{ib}\sigma_i(\lambda_i - \lambda)\,d\lambda}\sum_{oob} R_j^{(n\text{-}1)}(\lambda_j)\,\sigma_i(\lambda_i - \lambda_j)\,L_c(\lambda_j)\,\Delta\lambda\,, \tag{5.7}$$

where $\Delta\lambda$ is the pixel-to-pixel wavelength spacing and *j* extends over all 512 elements of the array. The original input values to the responsivity are the signals divided by the radiance of the calibration source

$$R_i^{(0)}(\lambda_i) = \frac{S_i}{L_c(\lambda_i)}\,. \tag{5.8}$$

Following the above discussion, the radiance of a source with an unknown spectral distribution can also be corrected for stray light. In this case, the relation is given by the expression

$$L^{(n)}(\lambda_i) = \frac{S_i}{R_i(\lambda_i)} - \frac{1}{R_i(\lambda_i)\int_{ib}\sigma_i(\lambda_i - \lambda)\,d\lambda}\cdot\sum_{oob} R_j(\lambda_j)\,\sigma_i(\lambda_i - \lambda_j)\,L^{(n-1)}(\lambda_j)\,\Delta\lambda\,, \tag{5.9}$$

where

$$L^{(0)}(\lambda_i) = \frac{S_i}{R_i(\lambda_i)}\,. \tag{5.10}$$

Note that the stray-light corrected responsivity must be used. A stable solution, with changes less than 0.1 %, is reached after 4 to 5 iterations. The solution is robust and insensitive to small variations in the input parameters.

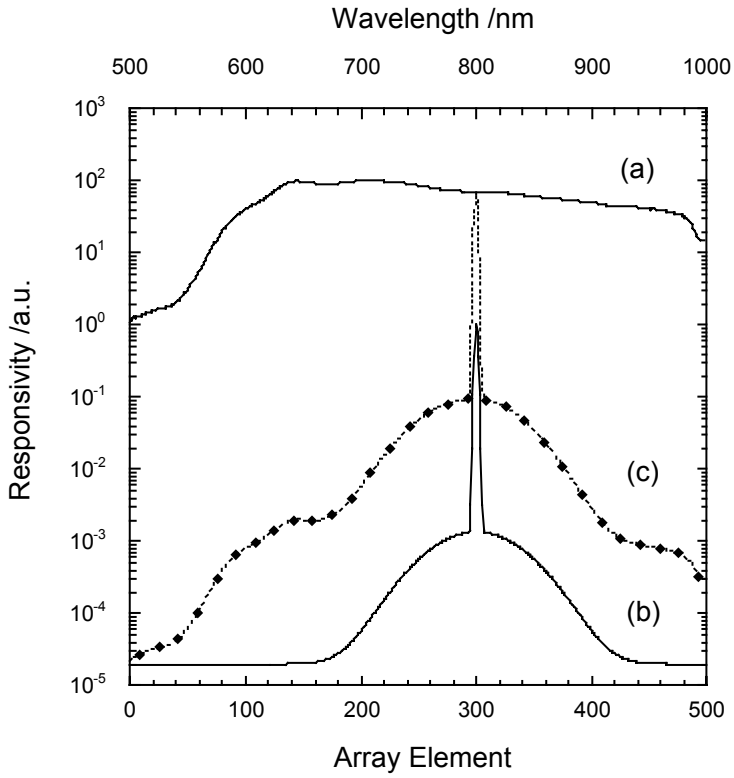

Figure 5.5. **(a)** A spectrograph's absolute spectral responsivity, $\bar{r}(\lambda)$. **(b)** Slit-scatter function for element 300, $\sigma_{300}(\lambda_{300} - \lambda)$. **(c)** Absolute spectral responsivity of element 300.

5.3 DERIVATION OF MOBY SLC MODEL PARAMETERS

There are a total of 3 MOS instruments actively used by the MOBY project. MOS202 is a stand-alone system, known as the MOS Profiler. It is a ship-board instrument used for bio-optical algorithm development and validation and is not directly associated with the MOBY buoy. MOS204 is used as the sensor in even-buoy MOBY deployments; MOS205 is used in odd-buoy deployments. In principle, model slit-scatter parameters need to be independently developed for each MOS and for each MOBY deployment, with separate factors for each MOBY arm, each port (E_d or L_u), for the top E_s port and for the bottom MOS port.

Examination of the system response to monochromatic excitation showed that the different arms (both *E* and *L*) within an individual buoy had the same slit-scatter function. The normalized responses of the MOBY top, middle and bottom arms with MOS205 to monochromatic excitation are shown in Figs. 5.6 and 5.7. Measurements also confirmed that the slit-scatter function remained the same before and after deployment for a particular buoy as well as from buoy to buoy for a particular MOS system. However, the slit-scatter function differs between MOS instruments (Fig. 5.8). Therefore, we only needed to derive model slit-scatter function parameters for a single port on a single MOBY arm for a particular MOS. The results were then extended to every MOBY arm, both L_u and E_d ports, and the E_s collector for a particular MOS system. Radiation entering the MOS directly from the bottom radiance port is imaged differently (Fig. 5.9) onto the CCD array. Consequently, the slit-scatter function parameters for the bottom MOS port on MOBY are considered separately and are not addressed in this work.

Experimental

In a spectroradiometer equipped with a single element detector, the dispersive element, *e.g.* the grating, is rotated while the detector is fixed. The center wavelength of the radiation imaged on the exit slit is a function of the angle of rotation of the grating. The instrument's slit-scatter function can be determined using a single fixed wavelength source and changing the wavelength of the radiation centered on the exit slit by rotating the grating in small steps.

In a spectrograph, the grating is fixed and the spectral selection determined by the image of the entrance slit onto a reference plane where the multi-element sensor is placed as well as the size of the individual elements in the sensor array. In this case, if we want to determine the system's spectral response over some finite spectral range, we need a tunable, monochromatic excitation system. NIST recently established a tunable-laser-based radiometric calibration facility for Spectral Irradiance and Radiance responsivity Calibrations using Uniform Sources, known as SIRCUS (Brown *et al*. 2000). In the SIRCUS facility, tunable, monochromatic, high-power lasers are fiber coupled into an integrating sphere, producing a nearly Lambertian, monochromatic source that overfills the entrance pupil of imaging systems such as MOS. The radiance of the source is determined at any wavelength by an irradiance standard detector, which is in turn directly traceable to primary radiometric standards maintained at NIST. A bench prototype of the MOS system was characterized and calibrated in this facility (Habauzit *et al*. 2003). The results demonstrated the validity of the stray-light correction approach.

The imaging onto the MOS CCDs in MOBY is slightly different than in the MOS system itself (Fig. 5.9). Consequently, a piece-wise characterization approach would not work and the entire MOBY system had to be characterized. Because of the logistical problems associated with transporting an object as large as MOBY to NIST and to the SIRCUS facility, as well as time constraints imposed by the operational protocols developed for MOBY, it was necessary to characterize and calibrate the buoys *in situ* at the calibration facility at the University of Hawaii Marine Center, Honolulu, Hawaii.

A fiber-coupled, laser-based integrating sphere source (ISS), similar to the radiance source in the SIRCUS facility, was developed for use at the MOBY field site. The system consisted of a 532 nm Nd:Vanadate laser pumping a Ti:sapphire laser for tunable radiation from 700 nm to 1000 nm or a dye laser with Rhodamine6G dye for tunable radiation from 565 nm to 615 nm. The Ti:sapphire laser was modified to enable intra-cavity doubling with doubled output from 410 nm to 440 nm. An etalon was placed in the laser cavity to ensure that the output was narrow-band (<0.01 nm). Fixed-frequency HeNe, Argon ion, and diode lasers were used for additional characterization at discrete wavelengths.

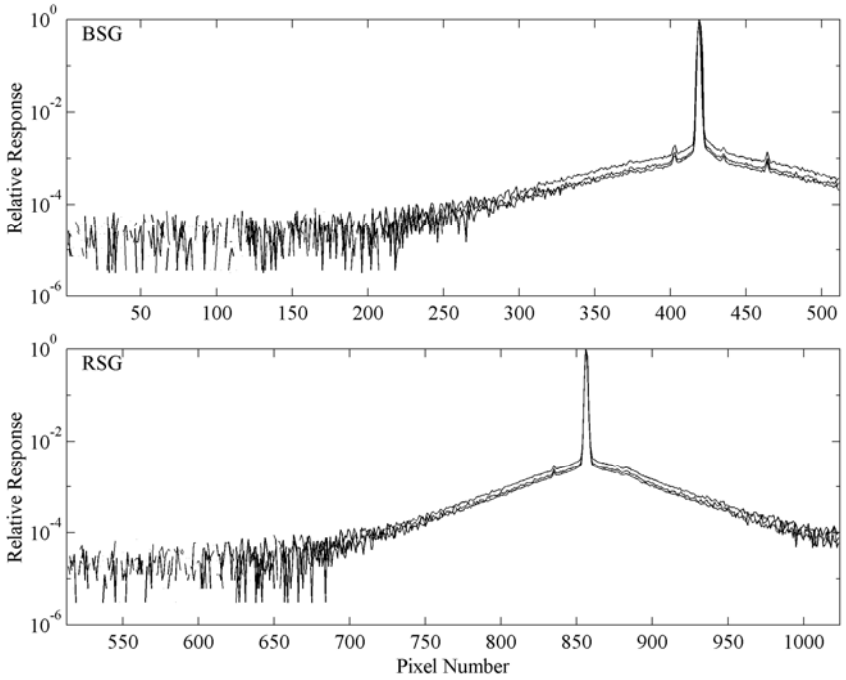

Figure 5.6. Normalized MOS205 response to monochromatic excitation from the top, middle and bottom arms (radiance collector) of MOBY219.

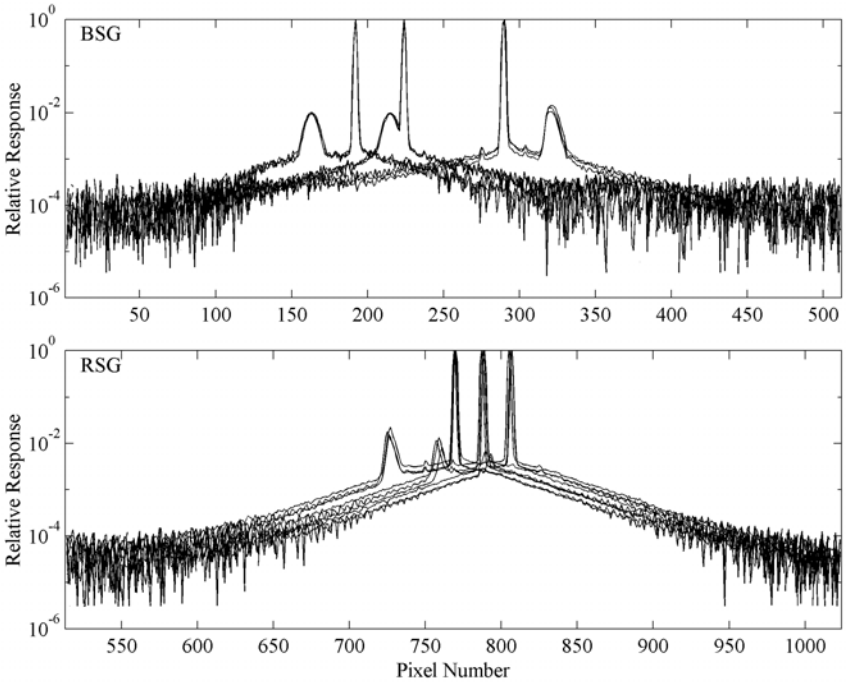

Figure 5.7 Normalized MOS205/MOBY219 response to monochromatic excitation from the three arms showing reflection peaks.

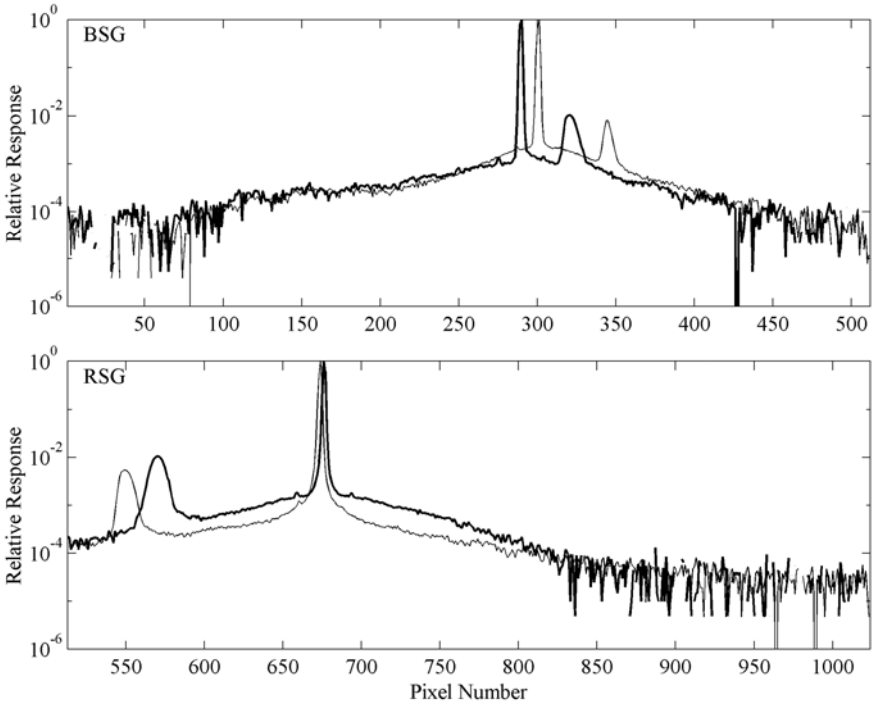

Figure 5.8. Comparison of MOS204/MOBY218 (light solid line) and MOS205/MOBY219 (dark solid line) radiance ports' response to monochromatic excitation.

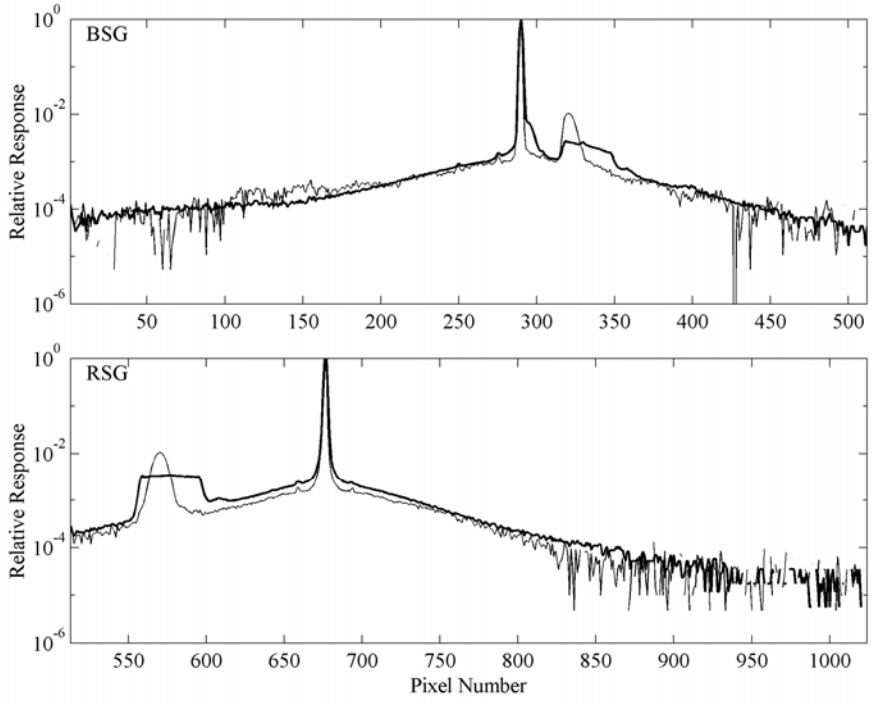

Figure 5.9. Comparison of MOBY radiance arm (light solid line) and MOS (dark solid line) response to monochromatic excitation.

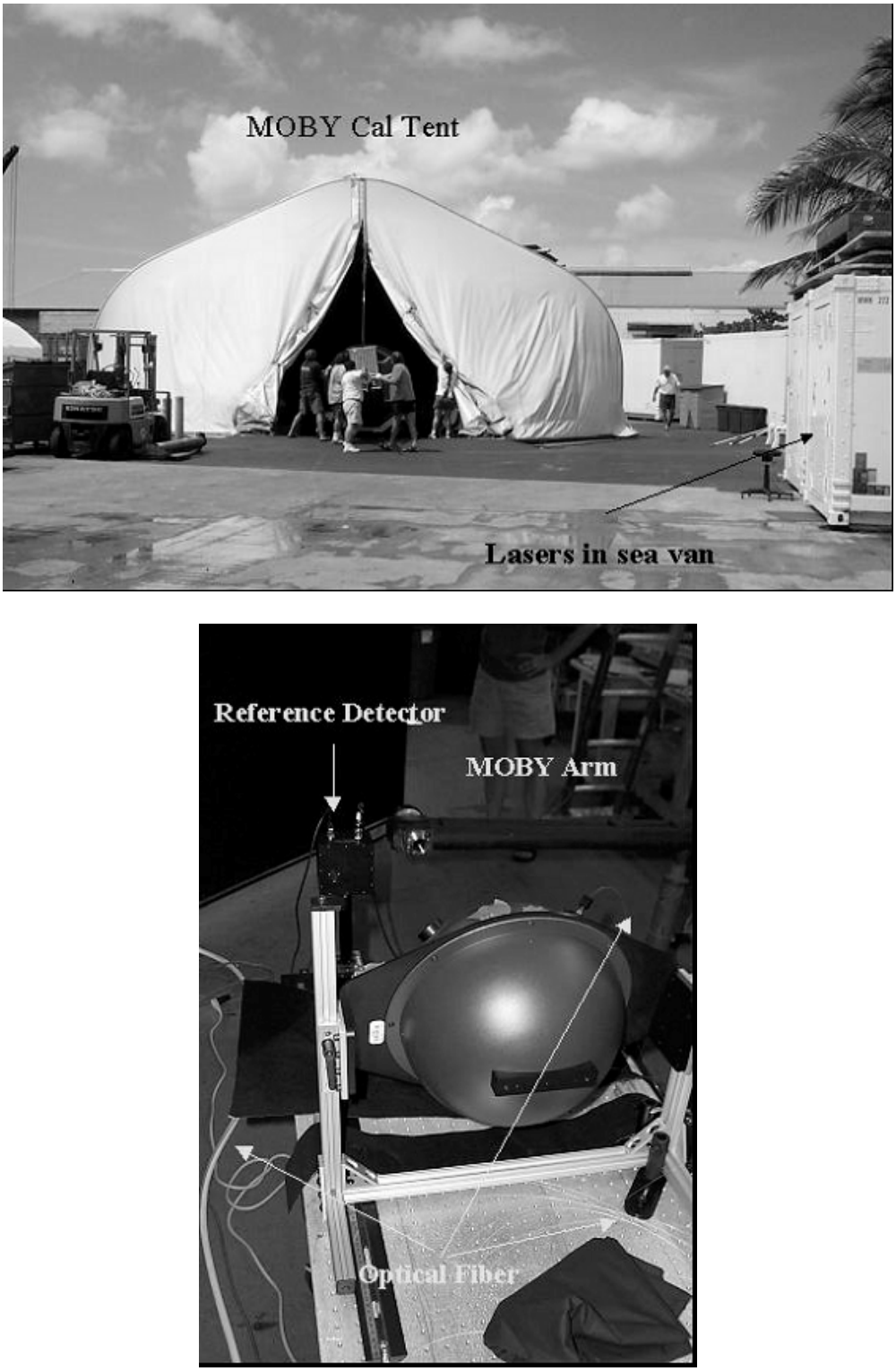

Figure 5.10: Schematic of experimental setup at the MOBY field site at the University of Hawaii Marine Center, Honolulu, Hawaii. (a) Exterior setup showing location of lasers and calibration tent. (b) experimental setup in the calibration tent for measuring the ISS radiance with a collector on the middle MOBY arm.

The output from the lasers was sent into a laser power-controller/stabilizer to reduce power fluctuations in the beam. Portions of the beam were also sent into a wavemeter to determine the wavelength of the laser radiation and into a Fabry-Perot spectrum analyzer so that the mode structure of the laser output could be monitored. The lasers were kept in an air-conditioned sea van and radiation was fiber-coupled into an integrating sphere in the MOBY tent. A portion of the optical fiber was placed in an ultrasonic bath to reduce effects of speckle in the measurement of the output of the ISS. From the sea van, the optical fiber was placed in a garden hose for protection and through an electrical conduit to the MOBY tent. The experimental setup is shown in Fig. 5.10.

The sphere radiance was determined using a calibrated irradiance transfer-standard radiometer. The radiometer is a six-element silicon-transmission trap detector (Eppeldauer and Lynch 2000). It was calibrated for spectral-power responsivity by comparison against a cryogenic radiometer and was equipped with a precision aperture of known area. The sphere radiance is given by the ratio of the measured signal to the trap responsivity times a geometrical flux transfer constant G_D

$$L_{\text{Sphere}} = \frac{S_{\text{Trap}}}{R_{\text{Trap}} * G_D}, \tag{5.11}$$

with G_D given by

$$G_D = \left(\frac{A_1 * A_2}{Z^2}\right)\left(1 + \frac{r_1^2 + r_2^2}{Z^4}\right) \tag{5.12}$$

where we have $Z^2 = r_1^2 + r_2^2 + d^2$, A_1 (r_1) is the sphere exit port area (radius), A_2 (r_2) is the trap aperture area (radius), and d is the distance between the two apertures.

The sphere was equipped with a silicon monitor photodiode. During MOBY measurements, the monitor was calibrated for the sphere radiance over a spectral range of interest using the reference standard trap detector, and then MOBY measurements were made. The monitor signal was recorded for each MOBY measurement.

Communication was established between the laser sea van and the MOBY tent using walkie-talkies or a marine band radio. It was important to properly couple the laser radiation into the optical fiber. During this alignment process, the monitor signal was continuously displayed on a computer in the MOBY tent. Coupling of the laser light into the fiber was adjusted, and the effect on the monitor signal was noted. The laser was properly coupled into the fiber when the monitor signal was maximized. The monitor signal was displayed on a computer screen in the calibration tent. Using commercially available software, the screen was also displayed on a computer in the sea van to simplify the fiber alignment process.

Slit-scatter parameters were determined for the BSG and the RSG coupled to the MOBY arms. To properly model the slit-scatter function (SSF) for the stray-light correction (SLC) algorithm we need the following parameters: (a) the single pixel in-band area; (b) a fit to the OOB slit-scatter function; (c) model for the reflection peaks and (d) model for additional light scatted onto the BSG CCD from radiation in the spectral range from 640 nm to 690 nm. In the following subsections, the basic steps undertaken to derive model parameters for the slit-scatter function are outlined for MOS205/MOBY 219 middle arm L_u port for the BSG and RSG, respectively.

MOS205/MOBY219 BSG in-band area

The stray-light correction terms on the right hand side of Eqs. (5.7) and (5.9) are divided by the normalized in-band area, N. N is given by Eq. 3.3, where the integration is over a 'suitably defined' in-band area

$$N = \int_{ib} \sigma(\lambda_i - \lambda)\, d\lambda . \tag{5.13}$$

To determine the in-band area, the laser output was changed in small increments (0.1 nm to 0.2 nm) from 590 nm to 600 nm and an image was acquired at each wavelength. The raw data (ADU/pixel/s) were divided by the sphere radiance, then normalized to a pixel's maximum responsivity. The wavelength of each pixel's maximum responsivity was subtracted, leaving each pixel's normalized responsivity, centered about a relative wavelength of 0 nm, for three adjacent pixels, P420-P422. Fig. 5.11 shows the normalized in-band responsivity of these pixels. Numerically integrating the line shapes gives in-band areas for the three pixels that agree to within 1%. Changing the limits of integration from ± 4 nm to ± 6 nm changed the areas by less than 0.2 %. Fitting to an analytical function also gave results in agreement with the numerical integration. The in-band area and associated relative

standard uncertainty are listed in Table 5.1. In-band scans were repeated over the range from 420 nm to 430 nm to determine the spectral dependence of the bandwidth. No dependence was observed.

Table 5.1. Values and uncertainties in the slit-scatter function derived uncertainties for MOS205/MOBY219 Lu middle arm.

Parameter	Variable	MOS205/MOBY BSG	Uncertainty [%]	MOS205/MOBY RSG	Uncertainty [%]
Normalization	N	0.985	1	1.137	1
Bandwidth	bw	0.5805	0.25	0.8047	0.25
OOB SSF	m_1	0.1142	2	0.164	2
	m_2	113.17	2	90.42	2
	m_3	1.125e-5	25	1.5e-5	25
Reflection Peak Position	l_o	92.485	0.25	343.0125	0.25
	l_1	0.6108	0.25	0.5859	0.25
Reflection Peak Area (P<100)	a_1	0.02599	3	0.0279	3
	a_2	295.0	3	713.997	3
	a_3	33.0	3	25.4843	3
Area (P>100)	b_1	0.02599	3		
	b_2	346.2642	3		
	b_3	13.2884	3		
Off CCD Amplitude	ScaleFactor	0.14	10	NOP	
Reflection Peak Dispersion	c_1	0.6108	0.25	0.5859	0.25

MOS205/MOBY219 BSG out-of-band slit-scatter function component

In modeling the slit-scatter function, we are considering the normalized relative response of the array to monochromatic excitation. To determine the out-of-band (OOB) component of the slit-scatter function, the laser excitation wavelength was fixed at the peak of the response of one of the in-band pixels and a number of images were acquired and averaged. The OOB slit-scatter function is shown in Fig. 5.12. The spectrum, with the center ± 5 pixels masked, was fit to a double exponential of the form

$$y = m_1 \exp\left(-2\left|x - x_0\right|\right) / m_2\right) + m_3 , \tag{5.14}$$

where x = column number and x_o is the column number with the peak response to the excitation wavelength, and the m_i's are constants determined from the fit. The fit is shown by the solid line in Fig. 5.12, and fit parameters are listed in Table 5.1. Note that there is an apparent 2-pixel shift in the center pixel between the imaged peak (centered at column 419) and the fit peak (x_o = 421). This shift is ignored in the model of the slit-scatter function.

MOS205/MOBY219 BSG Reflection peaks

The amount of light scattered onto the CCD in this reflection peak is significant. It is therefore necessary to include a model for these peaks in the general model for the slit-scatter function. For the model, we want to know what fraction of the incident light imaged onto some pixel is measured by the pixel under consideration. The modeling is complicated by the fact that the reflection peak area is a strong function of position and the rate at which it moves across the CCD with changing wavelength differs from the primary image.

To model the incident light scattered onto a particular pixel, we first need the relationship between the reflection peak position and the excitation peak position. This relationship, shown in Fig. 5.13, was fit to a linear regression, given by the solid line in the figure. Values are given in Table 5.1.

To calculate the fraction of the incident light that is in the reflection peak, we want to compare the integrated areas of the reflection peaks to the areas of the fundamental peak. The primary peaks in the data set are first

normalized to 1. The relative reflection peak data, plotted as a function of separation from the primary image (in pixels), are shown in Fig. 5.14. There is a large variance in both the amplitude and the total area under each reflection peak, but we need to consider that not all excitation wavelengths were centered on a pixel's response, so the reflection peaks may not be properly normalized to a pixel's peak response. Consequently, it was necessary to correct the amplitude of the reflection peaks in Fig. 5.14 for the excitation offset.

The in-band data set was fit to a Gaussian distribution given by

$$y = p_o + p_1 \exp\left(-\frac{1}{2}\left(\frac{x - p_2}{p_3} \right)^2 \right), \tag{5.15}$$

where the p_i's are constants determined from the fit.

We get a reasonable fit, shown in Fig. 5.15, though the area is slightly underestimated because the fit does not represent the right-hand shoulder well. The calculated area from the Gaussian fit agrees with the numerically integrated value to within 1 %. In Eq. (5.15), p_1 is the amplitude; p_2 is the center or offset; and p_3 is the width. To correct the excitation peak, we fit the primary image for the reflection peak data set to a Gaussian lineshape with a fixed width determined by the in-band fit. Note that to obtain the proper width for the fitting routine, it is necessary to convert the width from wavelength to pixel by dividing the width (nm) determined by the fit in Fig. 5.15 by the pixel-to-pixel spacing of the BSG (0.58 nm/pixel).

With the width fixed, we are only concerned with the amplitude determination (or the value of p_1) in Eq. 3.4. Each primary image peak was fit to Eq. (5.15), and results are summarized in Table 5.1. Corrections as large as 26 % are applied to the reflectance peak amplitude data set. Note that there is often a small shift in the peak position as well. The shift is less than 0.5 pixels and is not included in the modeled reflection peak position.

The corrected, normalized reflection peak data set is shown in Fig. 5.16. The 440 nm data set had an additional correction applied to make the haze component similar to the other data sets. One possible explanation for the apparent increase in scattered light is a wavelength-instability problem with the 440 nm diode laser used to acquire the spectrum. This would broaden the primary image and lead to an overestimation of the reflection peak amplitude in the modeled slit-scatter function.

For the slit-scatter function model, we are interested in the fraction of the in-band radiation scattered into the reflection peak. The amplitude-corrected reflection peaks are fit to Gaussian line shapes, giving the reflection peak area as a function of excitation wavelength or peak pixel. The reflection peak area as a function of position is shown in Fig. 5.17. The solid line is the fit to the data using Eq. (5.16) for pixels greater than 100 and Eq. (5.17) for pixels less than 100; *i.e.*

$$y = a_1 / (1 + (x / a_2)^{a_3}) \text{ , and} \tag{5.16}$$

$$y = b_1 / (1 + ((350 - x) / b_2)^{b_3}) \text{ .} \tag{5.17}$$

where x refers to the pixel under consideration.

The area must be further corrected for the increased rate at which the reflection peak moves through a particular pixel compared with the primary image. The primary image moves at a rate of approximately 0.58 nm/pixel while the reflection peak's dispersion is 0.35 nm/pixel. This will be discussed further, in subsections to follow, with regard to the red spectrograph.

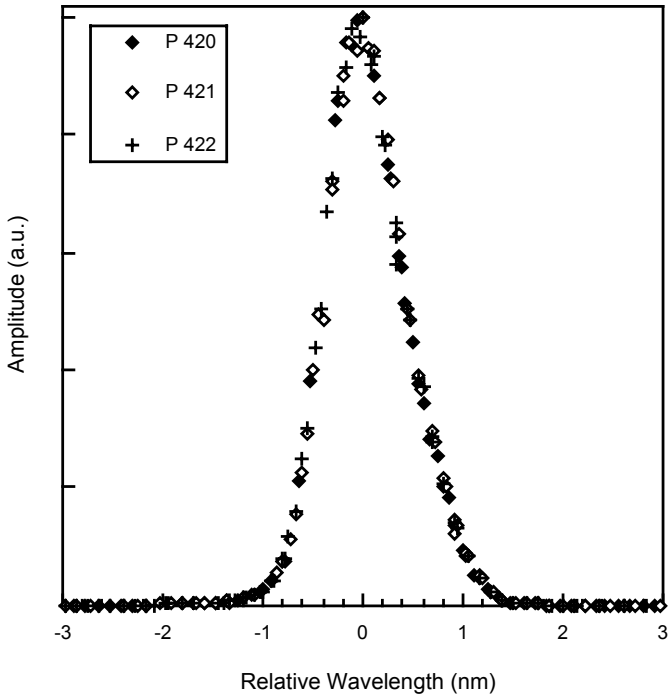

Figure 5.11: Normalized, center-wavelength-subtracted responsivity of BSG pixels 420, 421 and 422.

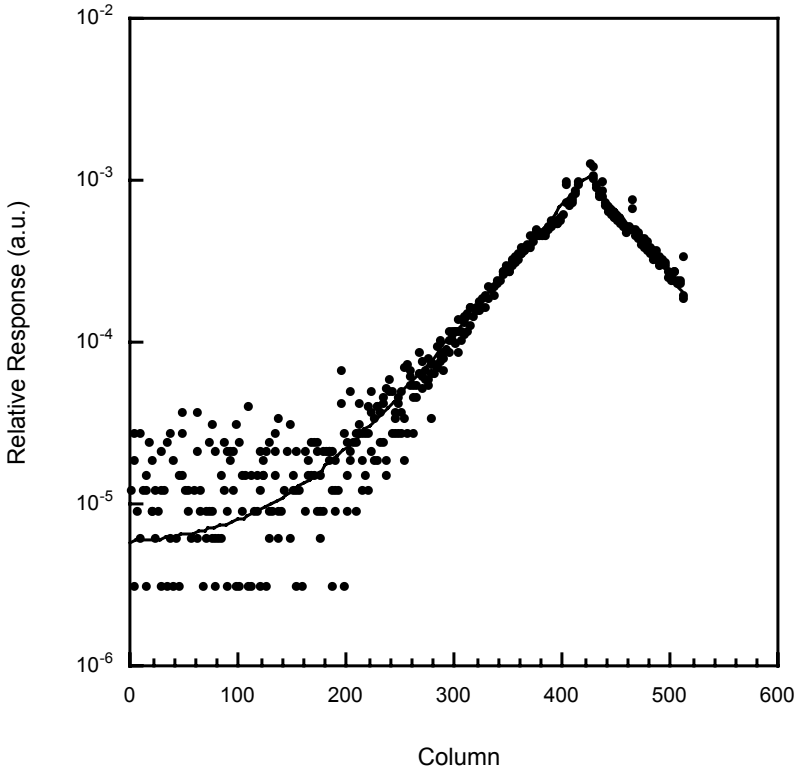

Figure 5.12: MOS205 BSG out-of-band slit-scatter function.

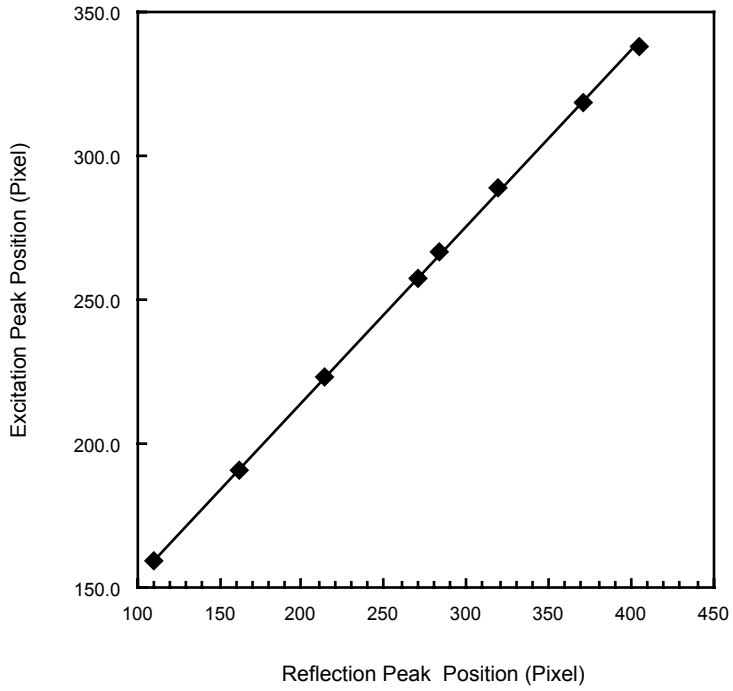

Figure 5.13: Location of the MOS205 BSG primary image versus the position of the reflection peak, with the solid line a fit to the data.

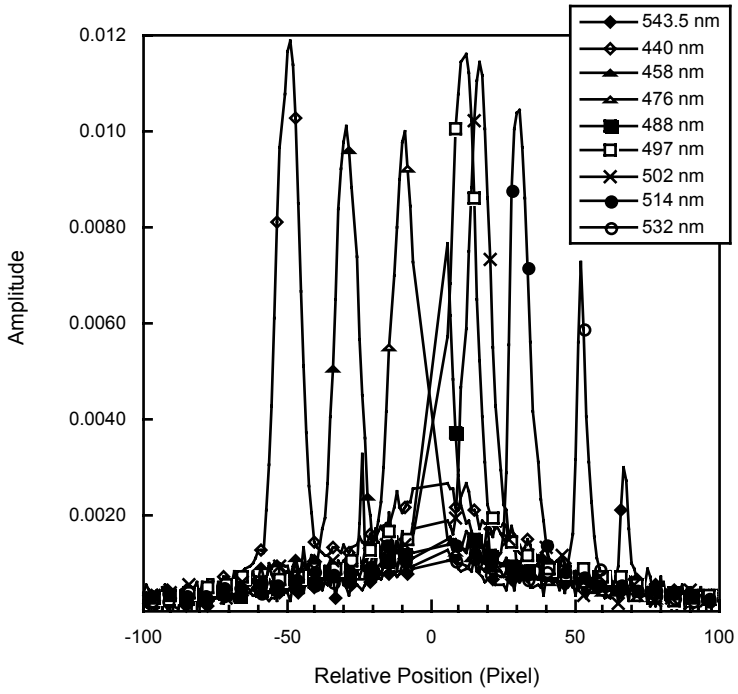

Figure 5.14: MOS205/MOBY219 L_uMid BSG reflection peak data set, uncorrected for the amplitude of the excitation peak

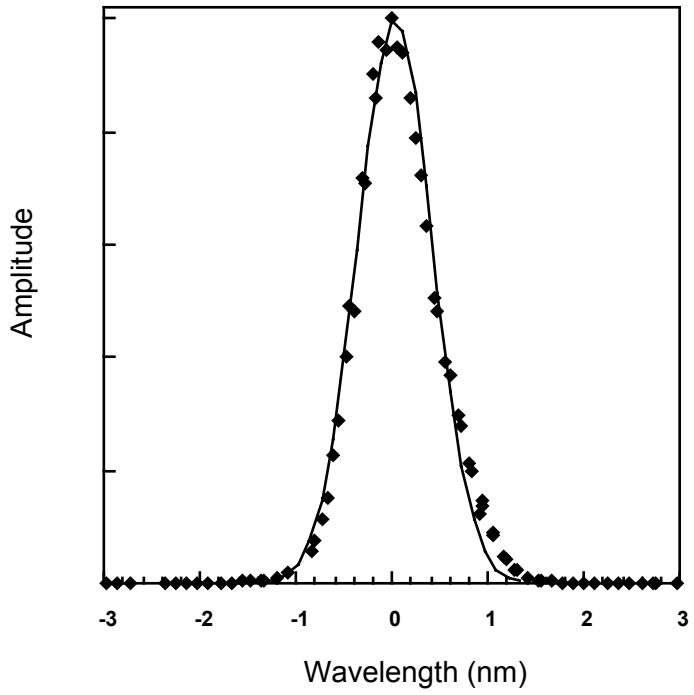

Figure 5.15: Gaussian fit to the MOS205/MOBY219 BSG in-band data set.

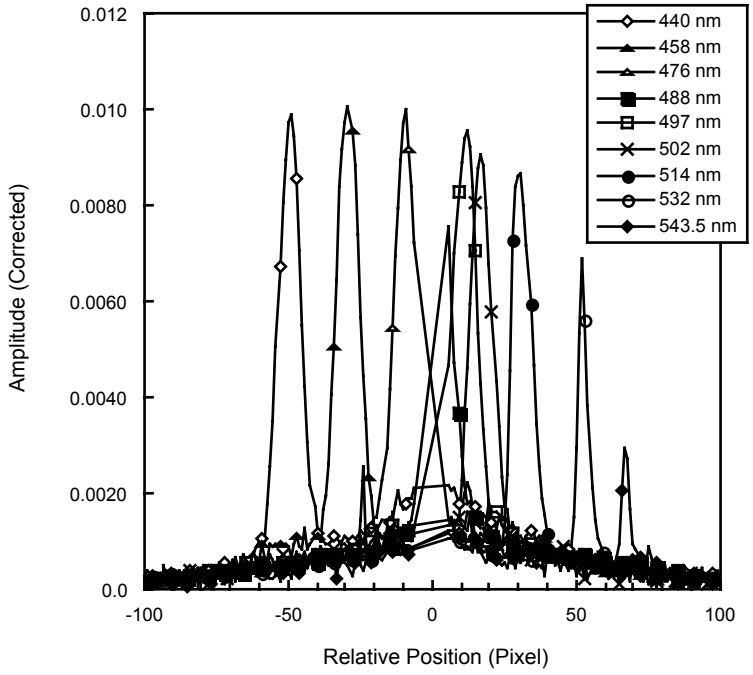

Figure 5.16: MOS205/MOBY219 LuMid BSG reflection peak data set, corrected for the amplitude of the excitation peak.

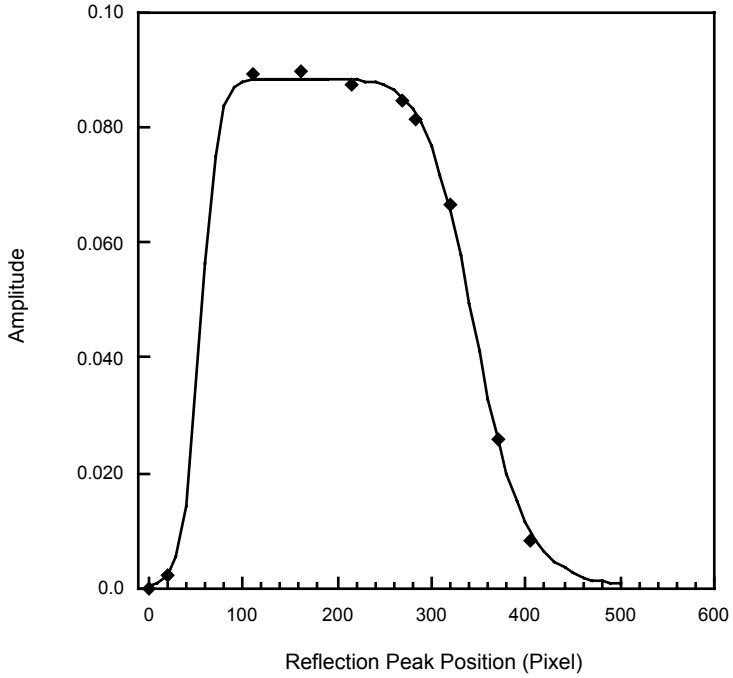

Figure 5.17: Reflection peak area as a function of position; the solid line is a fit to the data.

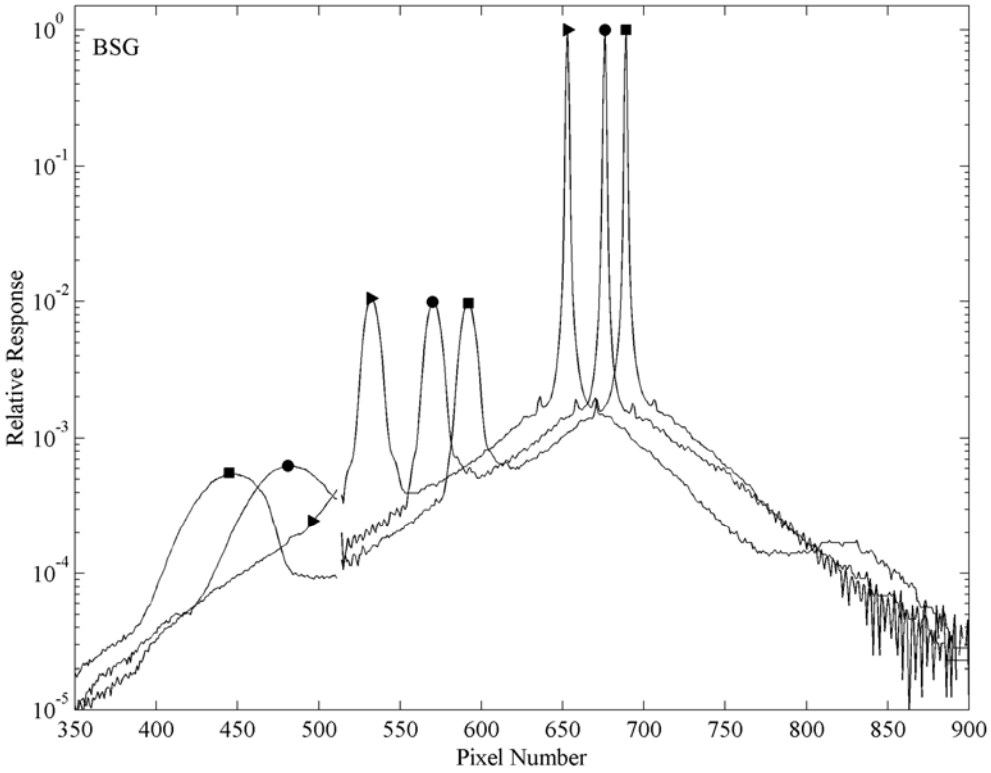

Figure 5.18: Response of BSG pixels 400 to 511 and full RSG response for discrete laser excitation in the range from 640 nm to 690 nm.

M205/MOBY219 BSG Off-CCD Scattering

There is additional scattering onto the right edge of the CCD from light not directly imaged onto it. In Fig. 5.18, we show the responsivity of pixels 400 to 511 for the BSG from discrete laser excitation in the range from 640 nm to 690 nm. Tunable lasers in the 640 nm to 690 nm spectral range were not available during the field measurements and we do not have enough spectral data to directly model BSG stray light effects in this range. Consequently, the magnitude of this contribution was empirically fit to validation source data sets (discussed in Section 5) by including a quadratic term in the BSG slit-scatter function in the overlap region (pixels 400 to 511).

MOS205/MOBY219 Red Spectrograph (RSG)

The same set of model slit-scatter parameters was determined for the MOS205/MOBY219 RSG, with the exception of the off CCD term. Flux transmitted through the dichroic beamsplitter, incident on the RSG, falls off rapidly below 600 nm. Essentially no light below 550 nm is incident on the CCD, so a term to account for off-CCD scattering is not included in the RSG model slit-scatter function.

MOS205/M219RSG in-band area

Images were acquired as the excitation wavelength was tuned in small steps over the spectral range from 740 nm to 750 nm. The in-band areas of three adjacent pixels P756, P757, and P758, shown in Fig. 5.19, were determined. The areas agreed to within 0.25 %; changing the limits of integration from ± 4 nm to ± 6 nm changed the in-band area less than 0.2 %. The in-band area and uncertainty are listed in Table 5.1.

MOS205/M219 LuMid RSG OOB Slit-scatter Function

The peak-normalized OOB slit-scatter function, along with the double-exponential fit to the data [Eq. (5.13)] are shown in Fig. 5.20. Note that the reflection peak was masked for this fit as well as the in-band ± 5 center pixels. There is a 0.6 pixel offset from center between the image and the fit. This small offset is ignored in the model. Parameters are listed in Table 5.1.

MOS205/M219 LuMid RSG Reflection peaks

Images were acquired for excitation wavelengths ranging from 640 nm to 800 nm. A linear fit to the relationship between the reflection peak and the excitation peak positions is shown by the solid line in Fig. 5.21. Next the central peaks were fit to a Gaussian lineshape, with a width determined from the in-band scan. As with the BSG, these data are used to properly normalize the reflection peak amplitude. For the RSG, the dispersion is 0.804 nm/pixel. Uncorrected and corrected reflection peak data sets are shown in Figs. 5.22 and 5.23. Note that there is an apparent increase in the amplitude of the reflection peak for the first 3 wavelengths, where diode lasers were used for excitation. As with the BSG 440 nm data set, it may be a consequence of the multi-mode spectral output of the diode lasers used for this spectral region.

The amplitude-corrected reflection peaks are fit to Gaussian functions with a linear offset, giving the reflection peak area as a function of excitation peak pixel. The areas are again corrected for the rate at which the reflection peak moves through a particular pixel. For example, consider the RSG fine scans around 740 nm. In this spectral region, a reflectance peak is observed around 700 nm (pixel 702), as shown in Fig. 5.24. As the excitation is scanned in small steps, the response of pixel 702 can be measured and compared with the spectral width of the reflection peak in Fig. 5.24. Fig. 5.25(a) shows the reflection peak observed for 740.3 nm excitation, while Fig. 5.25(b) shows the spectral response of pixel P702. Both are plotted in wavelength scale using a dispersion of 0.804 nm/pixel for Fig. 5.25(a). Note the reduction in the width of the P702 reflection peak with respect to the reflection peak image from monochromatic excitation. This apparent reduction occurs because of the difference in the spectral dispersion of the primary and reflection peak images, and must be taken into account in the model of the reflection peak amplitude.

The final results are graphically illustrated in Fig. 5.26 with the fit to Eq. (5.16) shown by the solid line. Fit parameters are listed in Table 5.1.

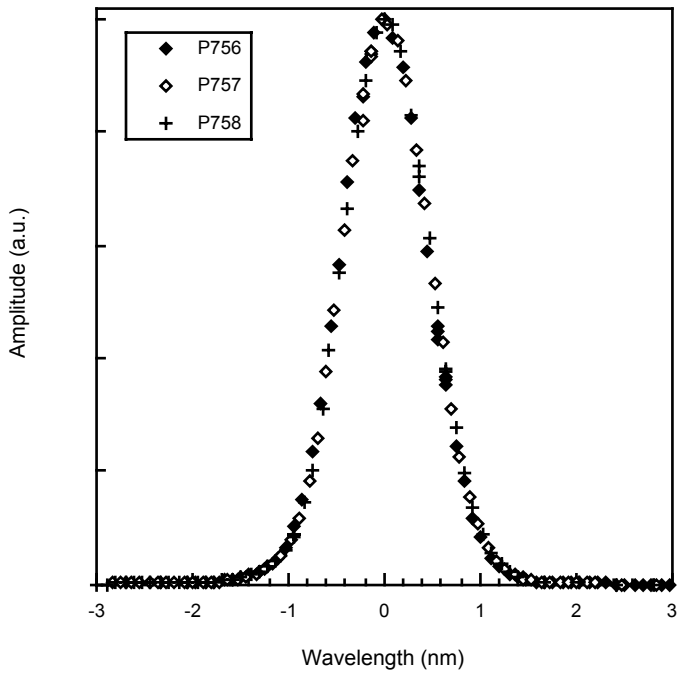

Figure 5.19: Center-wavelength subtracted, peak normalized, MOS205/MOBY219 RSG in-band scans for pixels 756,757, and 758.

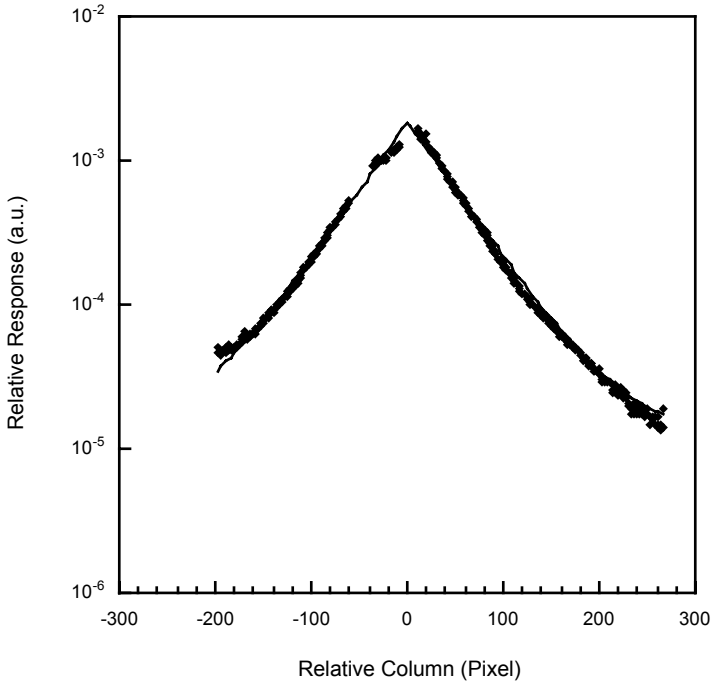

Figure 5.20: Peak normalized MOS205/MOBY219 RSG out-of-band slit-scatter function.

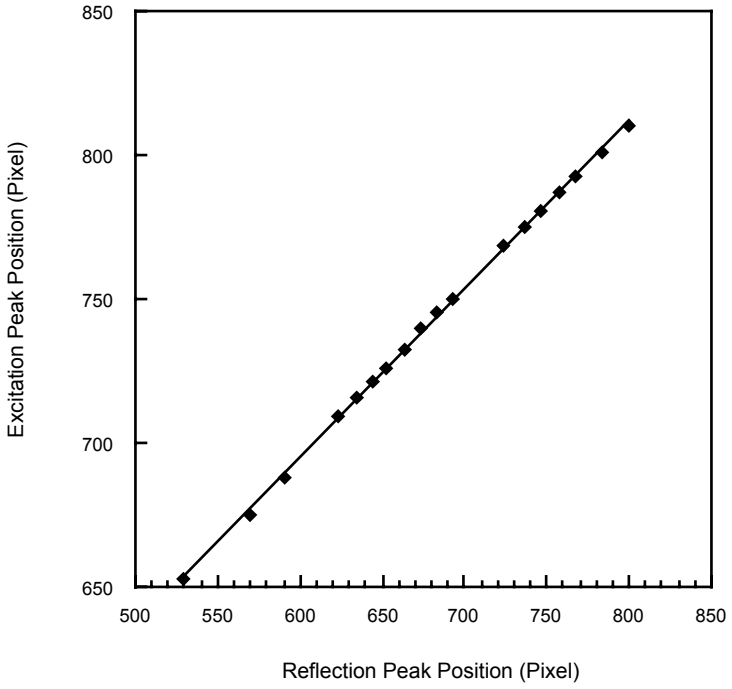

Figure 5.21: MOS205/MOBY219 excitation peak position as a function of reflection peak position.

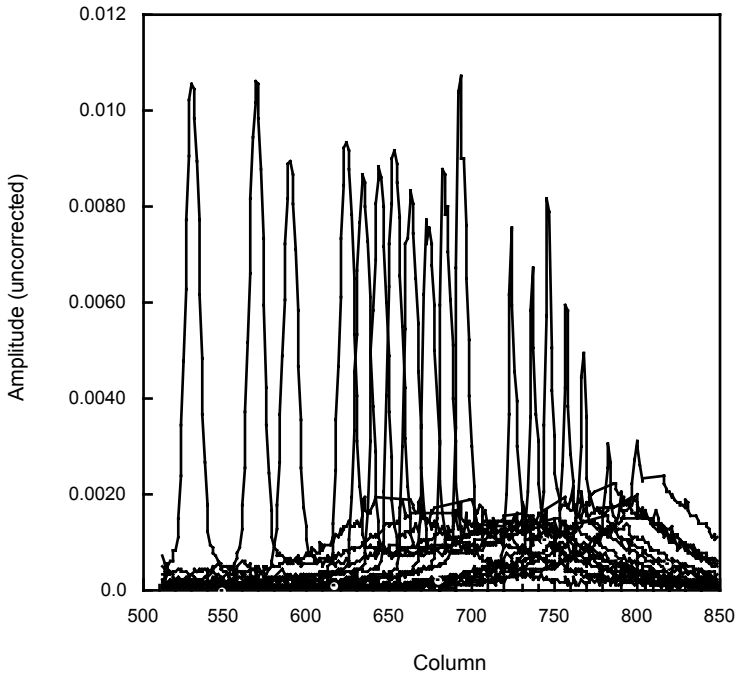

Figure 5.22: MOS205/MOBY219 uncorrected reflection peak data set.

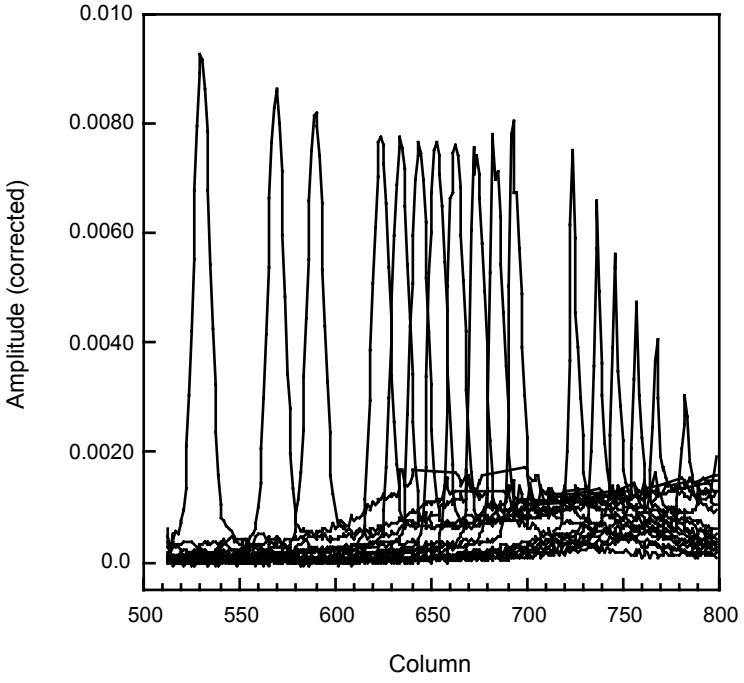

Figure 5.23: MOS205/MOBY219 corrected reflection peak data set.

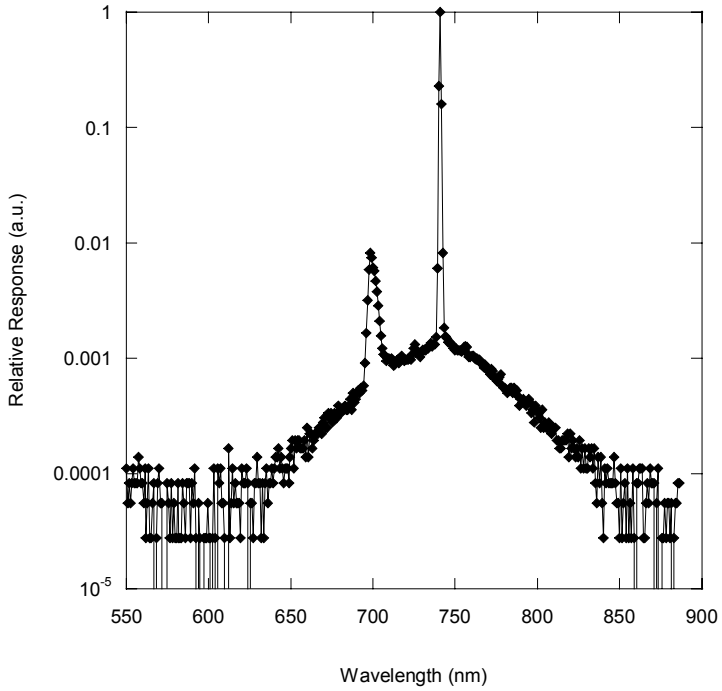

Figure 5.24: Relative RSG response to monochromatic excitation at 740.3 nm.

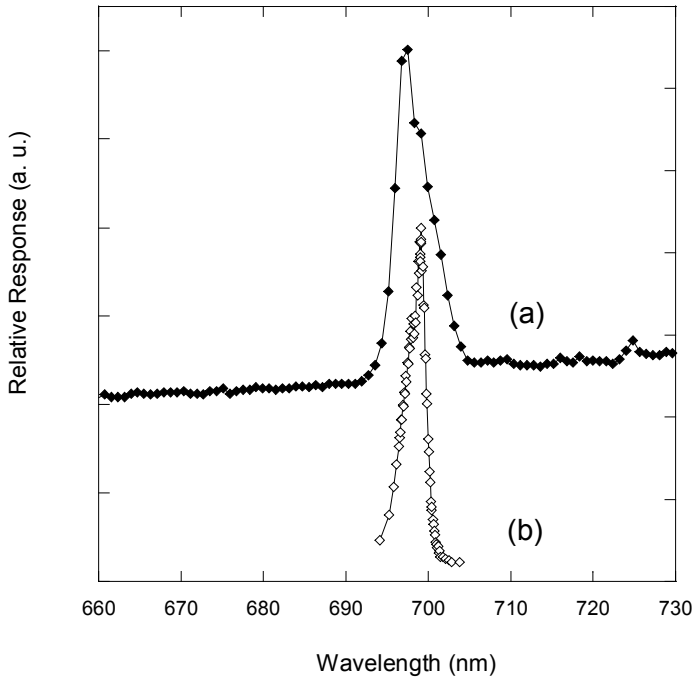

Figure 5.25: (a) Reflection peak for RSG response to monochromatic excitation at 740.3 nm. (b) Response of pixel 702 as the excitation wavelength is changed from 695 nm to 705 nm.

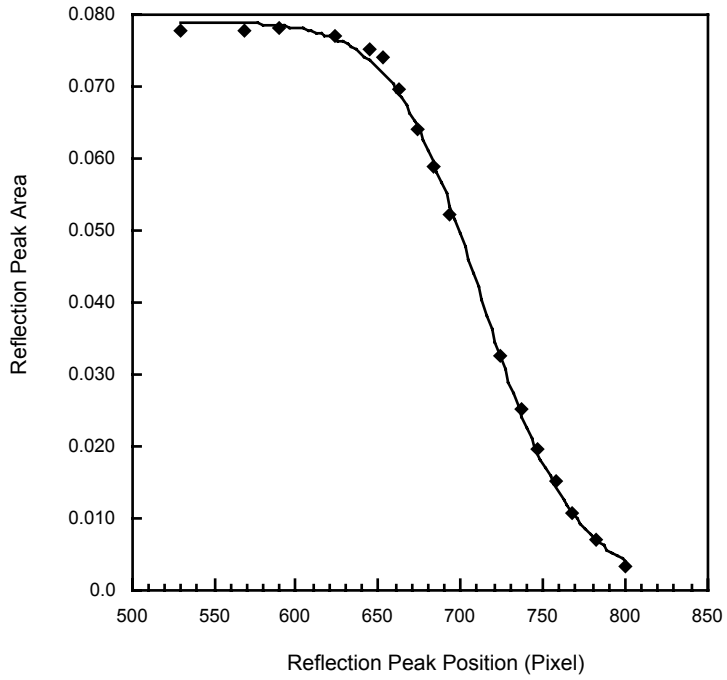

Figure 5.26: MOS205/MOBY219 reflection peak amplitude as a function of reflection peak position.

5.4 STRAY-LIGHT CORRECTION OF MOBY

The parameters developed in Section 5.3 for MOS205/MOBY219 were incorporated into the stray-light correction algorithm described in Section 5.2. The algorithm was used to correct MOBY calibration and in-water data sets. MOBY was calibrated using a lamp-illuminated integrating sphere calibrated for spectral radiance. The iterative stray-light correction procedure described in Section 5.2 [Eq. (5.7)] was applied to the measured signal. Iterations were repeated until a stable solution was reached; a solution that changed by less than 0.1 % from the previous iteration was considered stable. Typically, a stable solution was reached after 4 to 5 iterations. The uncorrected responsivity and the stray-light corrected responsivities are shown in Fig. 5.27. In Fig. 5.28, the ratio of the corrected responsivity to the uncorrected responsivity is shown. Stray-light is responsible for approximately 10 % of the signal over much of the spectral range, increasing rapidly below 400 nm for the BSG, and below 640 nm for the RSG. The rectangular increase in the corrected over uncorrected ratio (reduction in stray-light) for the BSG near 500 nm occurs in the region where the reflection peak coincides with the primary image.

Using the stray-light-corrected responsivities, MOBY up-welling radiance data are corrected using Eq. (5.9). Uncorrected and corrected radiance measured by each arm is shown in Fig. 5.29, and the ratio of uncorrected to corrected up-welling radiance in Fig. 5.30. Note the dramatic improvement in the agreement between the two spectrographs in their overlap region in the stray-light-corrected results. There is also a significant increase in the measured up-welling radiance below 400 nm.

MOBY is used to vicariously calibrate SeaWiFS by providing measurements of water-leaving radiance. The water-leaving radiance is determined from the up-welling radiance according to Clark (Clark *et al*. 2002a; Clark *et al*. 2002b). The water-leaving radiance was calculated for stray-light-corrected and uncorrected data sets. The correction factor — or ratio of corrected to uncorrected water-leaving radiance — is shown in Fig. 5.31. We again see a strong increase in the corrected water-leaving radiance below 400 nm, reaching a value of approximately 40 % for 360 nm radiation. The corrected water-leaving radiance is less than the uncorrected values for wavelengths longer than 500 nm. The decrease rises to approximately 20 % for the BSG beyond 600 nm.

Band-integrated stray-light-correction factors for water-leaving radiance for the SeaWiFS bands are listed in Table 5.2. The correction factors range from +8.5 % for Band 1 to –2.5 % for Band 4.

Table 5.2. Band-integrated stray-light-correction factors for water-leaving radiance in the SeaWiFS bands.

SeaWiFS Band	Ratio Corrected/Uncorrected L_w
1	1.085
2	1.033
3	1.012
4	0.976
5	0.979
6	1.014

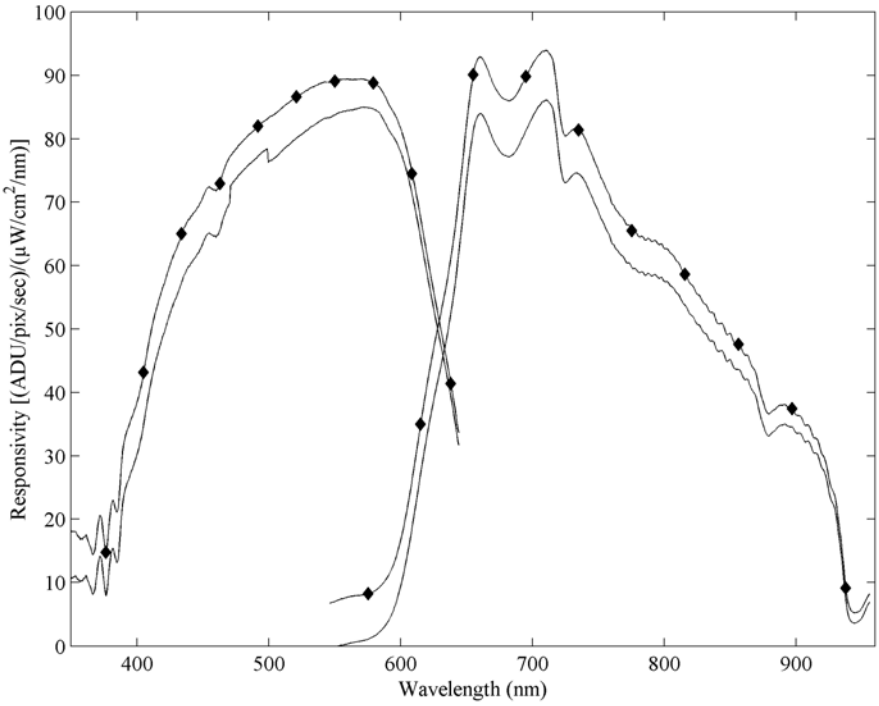

Figure 5.27: Uncorrected (diamonds) and stray-light-corrected (solid line) responsivity of MOS205/MOBY219 radiance arms.

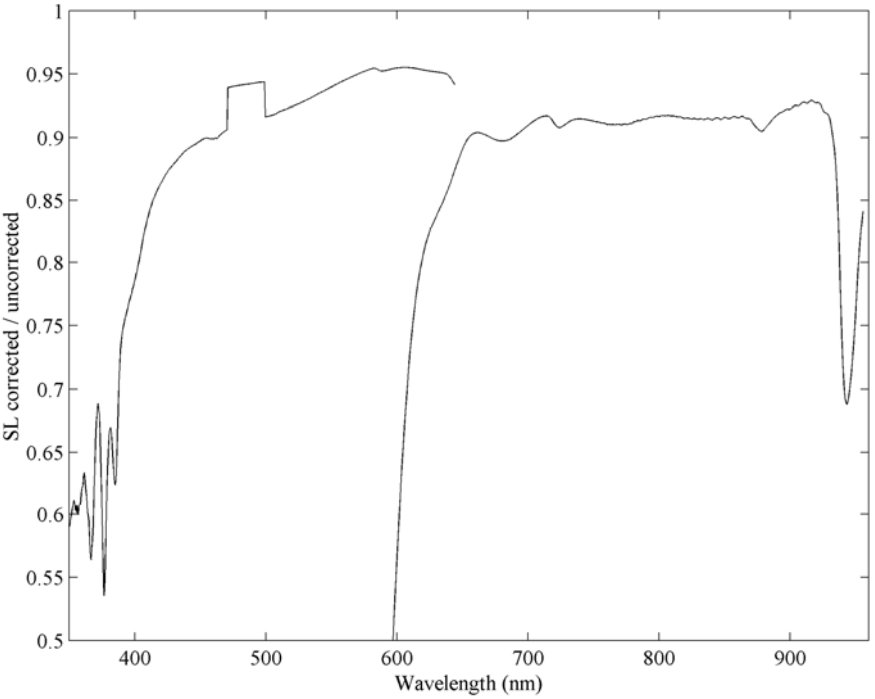

Figure 5.28: Ratio of the MOS205/MOBY219 L_uMid radiance arm corrected responsivity to the uncorrected responsivity.

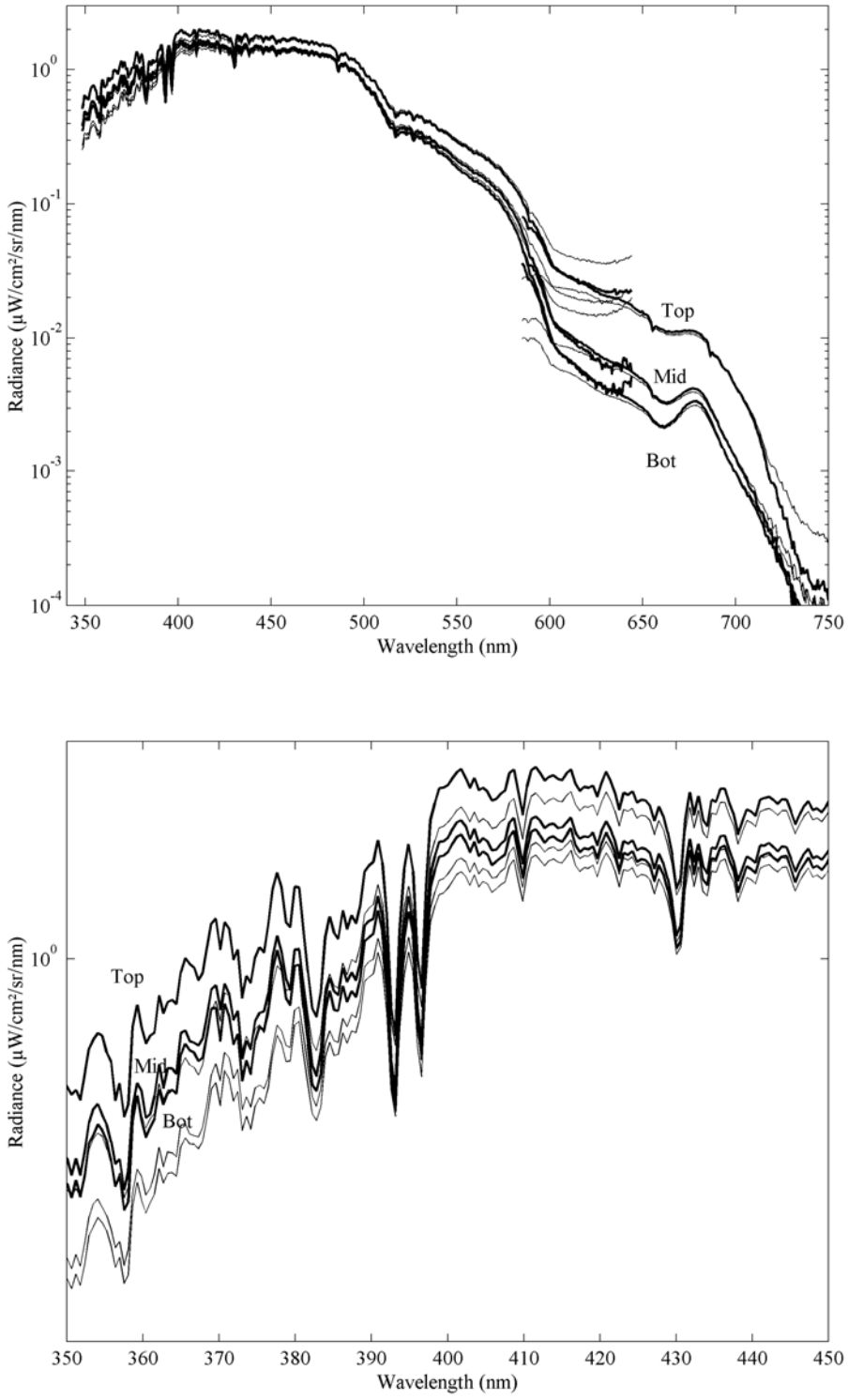

Figure 5.29: Uncorrected (thin solid line) and corrected (thick solid line) up-welling radiance measured by each MOS205/MOBY219 arm. (Bottom panel) Expanded view in the UV region.

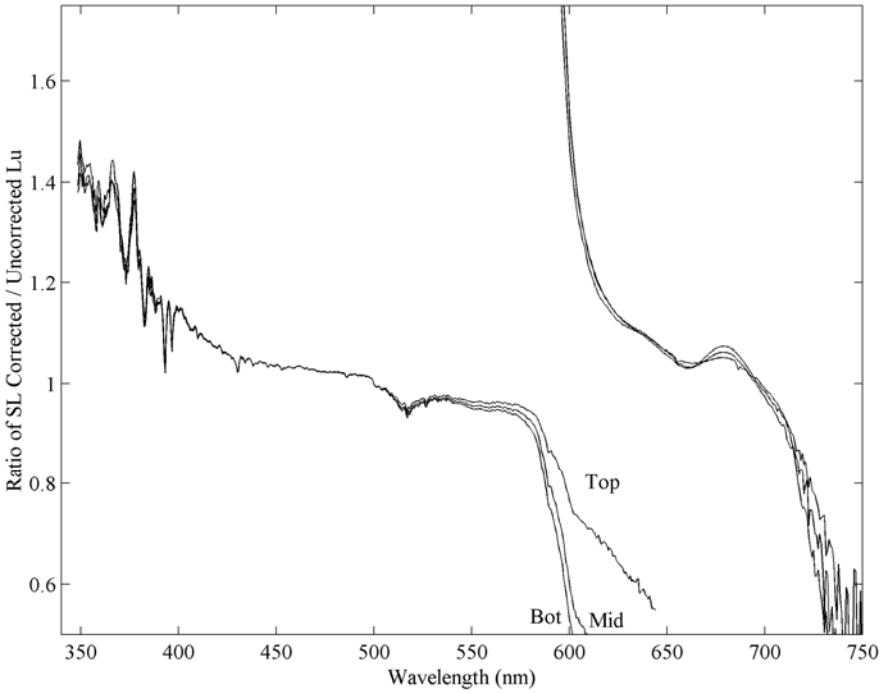

Figure 5.30: Ratio of corrected to uncorrected up-welling radiance L_u measured by each MOS205/MOBY219 arm.

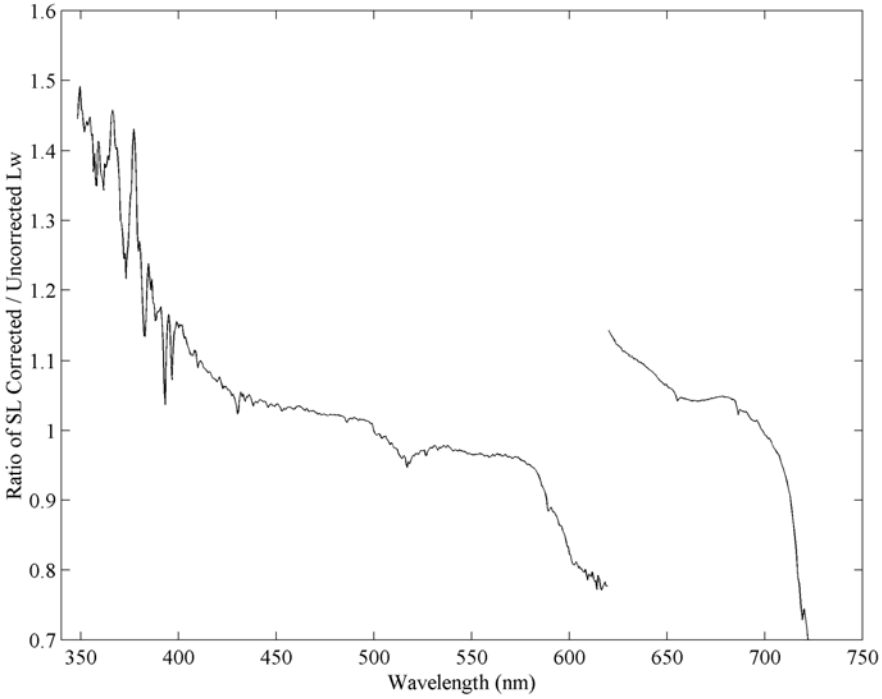

Figure 5.31: Ratio of stray-light-corrected to uncorrected water-leaving radiance L_W measured by MOS205/MOBY219.

5.5 ALGORITHM VALIDATION

To validate the stray-light correction model, a Colored Source (CS) was developed. Different relative spectral distributions were realized using glass and interference filters and a lamp-illuminated integrating sphere source. The spectral radiance for the CS configurations was determined separately using a calibrated spectroradiometer. The SLC algorithm was validated by comparing the corrected spectral radiances from measurements with MOBY to the known CS spectral radiances.

A lamp-illuminated integrating sphere source, model OL420 from Optronic Laboratories,[10] was used for the CS. Briefly, it is a 20.32 cm diameter, externally illuminated sphere that is coated with barium sulfate. The exit aperture is 5.72 cm in diameter and the entrance aperture is orientated 90° with respect to the exit aperture. Quartz windows on both apertures protect the sphere from contamination. A monitor detector, fitted with a photopic filter, is mounted in the wall of the sphere and its output voltage is recorded during operation.

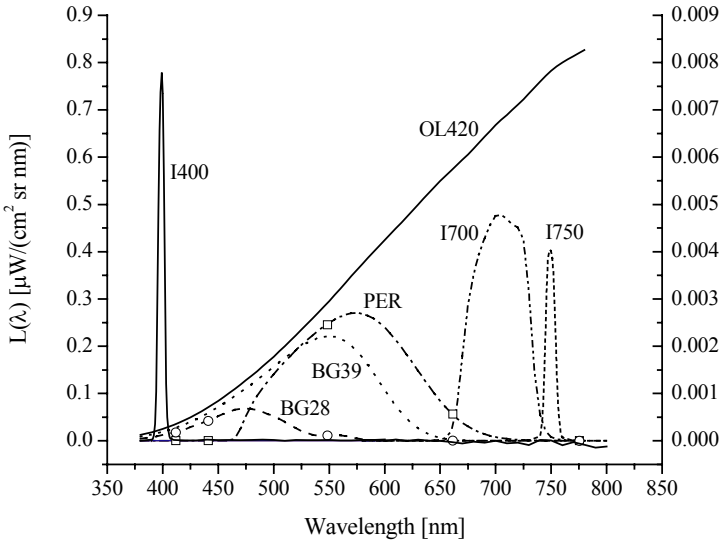

Figure 5.32: Spectral radiance of the OL420 Colored Source with different filters. The radiance of the CS with the I400 nm interference filter, which is a very low level, is shown on the right-hand axis. VXR measurements of the CS are given by the open symbols.

For the CS, we utilized the filter slide that is located between the lamp and the entrance aperture. Six CS configurations were possible, with each filter in a corresponding filter slide for ease of use and minimization of contamination through handling. Three colored glass filters were used: Schott BG28 and BG39[11], and CVI[12] PER filter, producing blue, turquoise and photopic (green) spectral distributions. Three interference filters were used, centered at 400 nm, 700 nm, and 750 nm, with full-width half-maximum (FWHM) bandwidths of 10 nm, 45 nm and 10 nm, respectively.

[10] Certain commercial equipment, instruments, or materials are identified in this paper to foster understanding. Such identification does not imply recommendation or endorsement by the National Institute of Standards and Technology, nor does it imply that the materials or equipment identified are necessarily the best available for the purpose.
[11] Schott Glass Corporation (www.us.schott.com).
[12] CVI Laser Corporation, Albuquerque, NM.

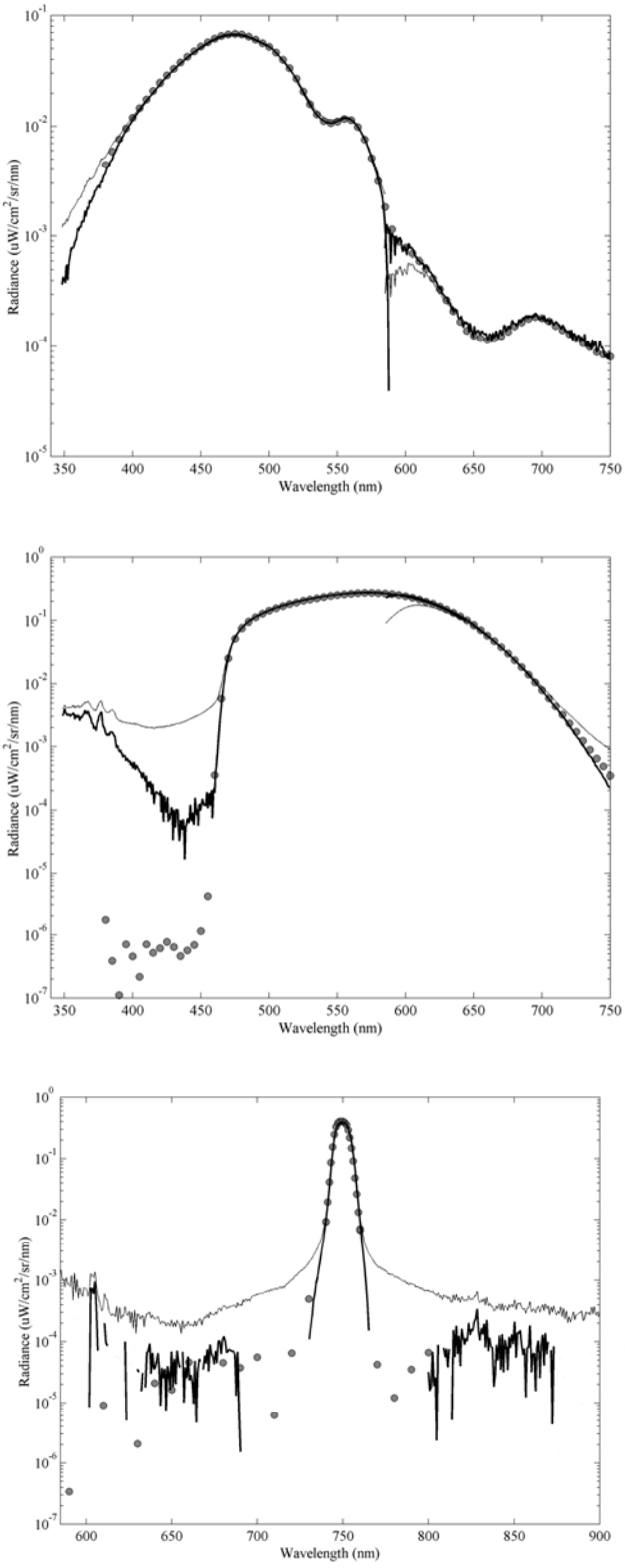

Figure 5.33: Uncorrected (thin line) and stray-light-corrected (dark line) and 'true' (gray circles) measured radiance of the Colored Source with (a) BG28, (b) PER, and (c) I750 filters.

The OL420 was calibrated for spectral radiance on the NIST Facility for Spectroradiometric Calibrations (FASCAL) (Walker *et al*. 1987) in March 2001. The spectral radiances for the PER, BG28, and BG39 configurations of the CS were determined at NIST in May 2001 using a reference spectroradiometer. The instrument is a double-grating, scanning monochromator (Brown and Ohno 1999). It has been fully characterized, with a stray-light factor of less than 10^{-6}. For the CS calibration, the bandpass was set to 5 nm FWHM and a wavelength step of 5 nm was used. For determinations of the CS spectral radiances, the unfiltered OL420 was used to calibrate the scanning monochromator. Typical spectral radiances for the six configurations are shown in Fig. 5.32. The reference spectroradiometer is not a field instrument, and was not transported to the MOBY field site.

During the field deployments, the EOS/NIST Visible Transfer Radiometer (VXR) was used to verify the CS spectral radiances. The VXR is a six-channel filter radiometer (Butler *et al*. 1999), and comparison to the reference spectroradiometer results could only be done where the VXR filter channels coincided with measurable output for the CS configurations. The agreement with the PER was -0.8 % at 548 nm and +1.9 % at 661 nm; with the BG28, it was -3 % at 441 nm and -0.7 % at 548 nm, where negative values indicate the VXR values were lower than the reference spectroradiometer. The VXR results are shown as symbols in Fig. 5.32.

The CS was measured by the radiance ports on the upper or middle buoy arms. The results for the source BG28, PER, and I750 filters are shown in Fig. 5.33. The spectral radiances derived using MOBY are shown with and without correction for stray light along with the spectral radiances for the CS configurations determined using the reference spectroradiometer. Within the in-band spectral regions, the corrected MOBY values agree with the CS spectral radiances to within 5 %.

The out-of-band regions are an important test of the stray-light-correction algorithm. The BG28 configuration decreases by an order of magnitude in the crossover region between the BSG and the RSG, similar to the behavior seen in MOBY waters [see Fig. 5.33(a)]. For this configuration, the correction algorithm was sensitive to the parameters for the off-CCD scattering, resulting in under- or over-correction in the overlap region. We determined the off-CCD parameters by minimizing the differences between the two spectrographs for the BG28 configuration.

Figure 5.33(a) shows that MOBY overestimates the spectral radiance as the wavelength decreases if not corrected for effects arising from stray light. The PER configuration, shown in Fig. 5.33(b), is an excellent test of the ability of the SLC algorithm for the shorter measurement wavelengths in the BSG. The spectral radiance in the region below 450 nm for the PER configuration decreases by more than 10^{-6} compared to the maximum value. Uncorrected, the MOBY values are discrepant by more than three decades in this spectral region. With correction for stray light, the agreement is improved substantially.

The inability to correct at the shortest wavelengths, below 400 nm, is understood in terms of the low system responsivity in this spectral region.

A test of the algorithm for the RSG is shown in Fig. 5.33(c) using the I750 interference filter (peak transmittance at 750 nm). In the out-of-band region, the uncorrected MOBY values are discrepant by a factor of 10 to 100, but the corrected values are in good agreement.

5.6 UNCERTAINTIES

A Monte Carlo approach was used to estimate the uncertainties in the stray-light-correction factors for MOBY up-welling and water-leaving radiance measurements. Model slit-scatter function parameters were input into the stray-light correction algorithm using mean values given in Table 5.1 and a random normal distribution with uncertainties given in Table 5.3. Uncertainties are approximately a factor of 2 larger than those given in Table 5.1 to account for possible additional uncertainties in the model parameters arising from changing environmental conditions and other unknown factors. The full stray-light correction algorithm - correcting both the responsivity and the in-water data - was run 100 times for a typical in-water spectrum and mean correction factors and uncertainties calculated. Typical results for the BSG are shown in Fig. 5.34 for MOS205/MOBY219 LuTop. Both the correction factor and the associated relative uncertainty is less than 1 % over the spectral range from 420 nm to 590 nm and both increase rapidly below 400 nm and above 600 nm, rising to approximately 8 % at the ends of the array: 360 nm and 640 nm, respectively.

Similarly, the uncertainty in the stray-light-correction factor for derived water-leaving radiance was determined, as shown in Fig. 5.35. The uncertainty in Lw is larger than the uncertainty in Lu, with a 14 % uncertainty in the stray-light-correction factor at 360 nm. In Table 5.4, the relative uncertainties in the band-averaged mean stray-light-correction factors are given for SeaWiFS bands.

Table 5.3: Uncertainties in slit-scatter function model parameters used in Monte Carlo simulations of MOS205 measurements.

Parameter	BSG Uncertainty [%]	RSG Uncertainty [%]
Normalization	2	2
OOB SSF		
	m_1	
5		3
3		
	m_2	
5		4
3		
	m_3	
25		5
25		
Reflection Peak Amplitude P<100		
		6
	a_1	
5		
5		

Table 5.4: Relative combined standard uncertainties in the band-averaged L_w stray-light-correction factor for SeaWiFS bands.

SeaWiFS Band	Ratio Corrected/Uncorrected L_W Uncertainty [%]
1	1.085
2	0.83
2	1.033
3	1.012
3	0.15
4	0.976
3	0.21
5	0.979
25	0.58
6	1.014
NOP	

a_2

5

5

a_3

5

5

Amplitude (P>100)

a_2

5

5

a_3

5

5

Off CCD Amplitude

10

NOP

5.7 DISCUSSION

The SeaWiFS band-averaged water-leaving radiance stray-light-correction factors measured by MOBY during a two-month deployment (M220) is shown in Fig. 5.36. In Figs. 5.37 and 5.38, the corrected/uncorrected SeaWiFS band-averaged ratios are shown for 4 years of deployments. Each grouping in the figure is a separate deployment. The correction factors have been stable over the entire deployment sequence, implying that the MOBY imaging and the MOS slit-scatter functions, along with the ocean-color, have remained stable over this time frame. The only exception was for the first three deployments of the MOS204 sensor (even buoys, Fig. 5.38), when the Band 1 correction factor was 2 % higher than for the other deployments. For these three deployments, low hydroxyl (OH) optical fiber was used to couple the radiance heads to the instrument bay. This fiber transmitted less light than the other fibers in the blue spectral region, in particular below 400 nm. For these three deployments, then, the relative stray-light contribution to the total signal in the blue spectral region was larger than for subsequent buoys, resulting in the larger Band 1 stray-light-correction factor for these buoys. The observed radiometric stability of the MOBY systems enables us to correct previous deployments for stray light with confidence.

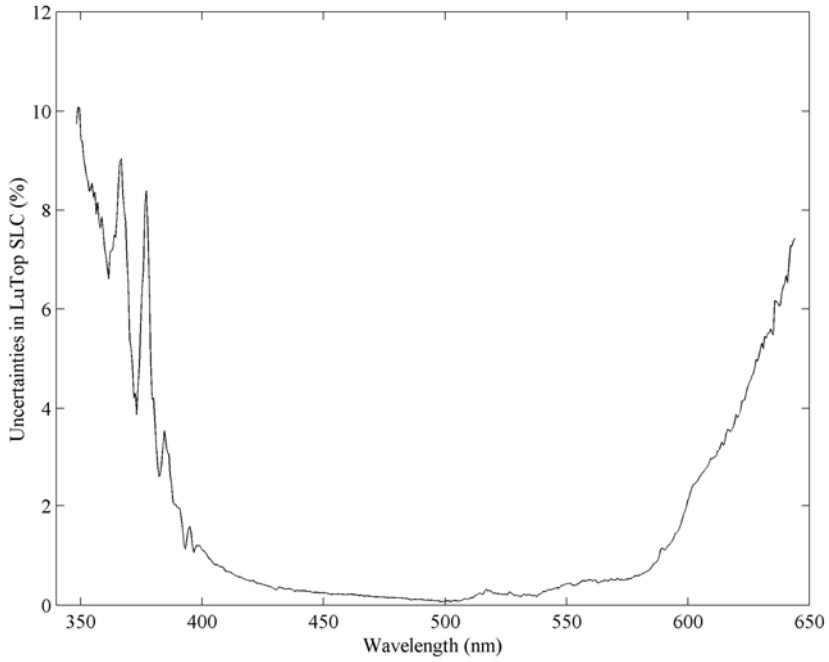

Figure 5.34: Uncertainty in L_u stray-light correction amplitude from Monte Carlo simulation.

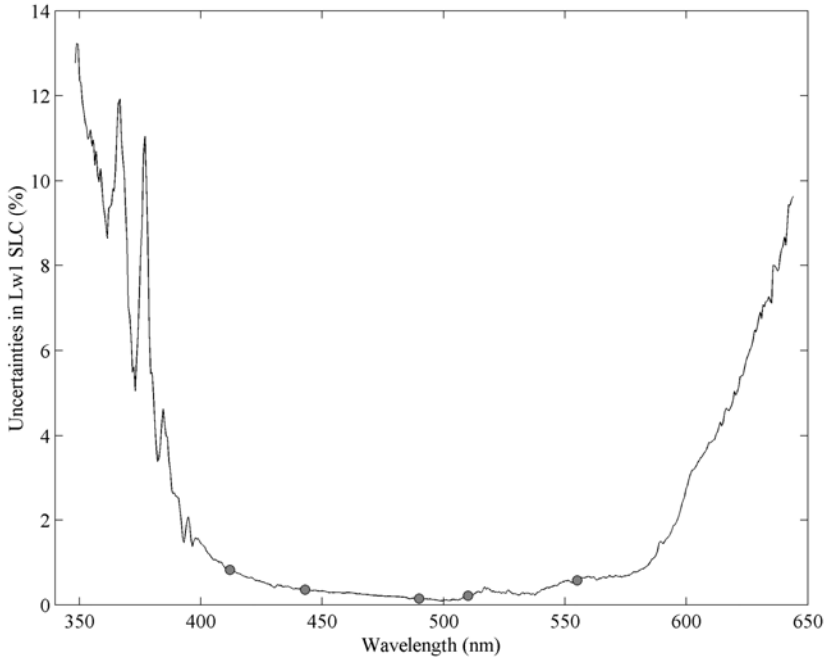

5.35: Uncertainty in L_w stray-light correction amplitude from Monte Carlo simulation. Grey circles represent band-center wavelengths of SeaWiFs bands.

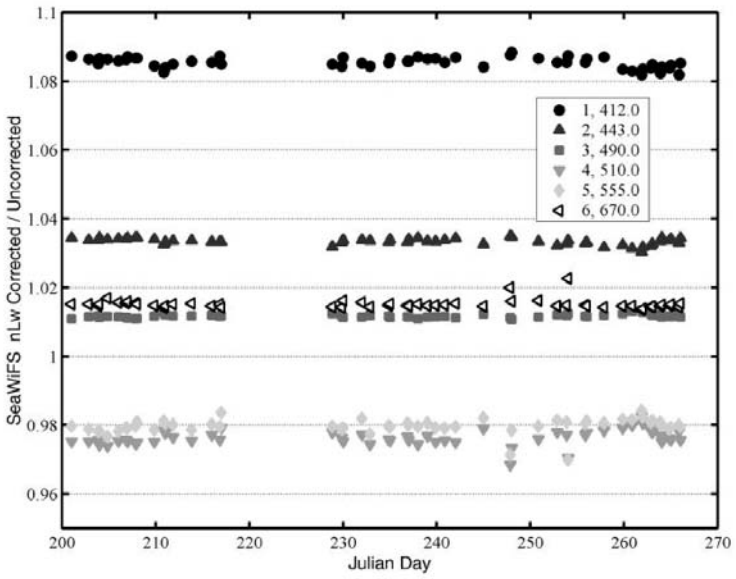

Fig. 5.36: Band-averaged Lw stray-light correction factors for SeaWiFS bands measured by MOBY during deployment 220.

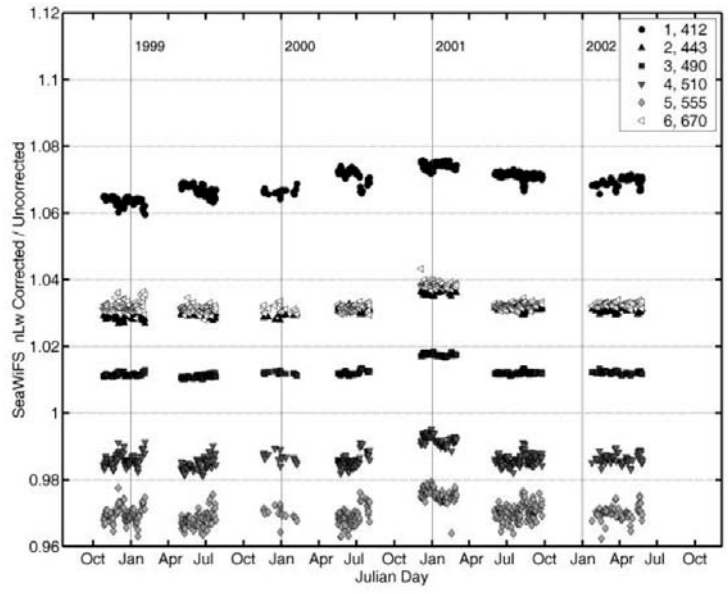

Fig. 5.37: Band-averaged Lw stray-light corrections for SeaWiFS bands measured by odd MOBY buoys from 1998 through 2002.

Impact on SeaWiFS

MOBY is used for the vicarious calibration of SeaWiFS bands 1 through 6 (Barnes *et al*. 2000). Any changes in MOBY-derived water-leaving radiances are directly reflected in SeaWiFS calibration coefficients for these channels. The effect of the MOBY stray-light correction is to increase the water-leaving radiance of SeaWiFS Bands 1 through 4, and decrease the radiance of Bands 5 and 6. SeaWiFS uses the Band 2 (443 nm) to Band 5 (555 nm) ratio to radiometrically determine chlorophyll *a* concentrations in oligotrophic waters (chlorophyll concentrations about 0.3 μg/l); the Band 3 (490 nm) to Band 5 ratio for mesotrophic waters (chlorophyll concentrations ranging from 0.3 μg/l to 1.5 μg/l); and the Band 4 (510 nm) to Band 5 ratio for eutrophic waters (chlorophyll concentrations > 1.5 μg/l) (O'Reilly *et al*. 1998). Correcting for stray light increases the band ratio in oligotrophic waters by 5 % to 6 % and approximately 3.5 % for waters with higher chlorophyll *a* concentrations. The change in band ratios corresponds to a 25 % to 35 % decrease in chlorophyll in oligotrophic waters and a 15 % decrease in mesotrophic and eutrophic waters. The stray-light correction of MOBY reduces global mean chlorophyll a concentrations measured by SeaWiFS by 15 % to 20 %. When combined with additional procedural changes implemented in the 4th reprocessing of the SeaWiFS data set in July 2002 (SeaWiFS 2002), the result was a mean monthly decrease in global chlorophyll a concentration of 6 %. In addition, the stray-light correction greatly reduced the magnitude of an issue with SeaWiFS measuring negative water-leaving radiance in coastal regions with complex aerosol distributions.

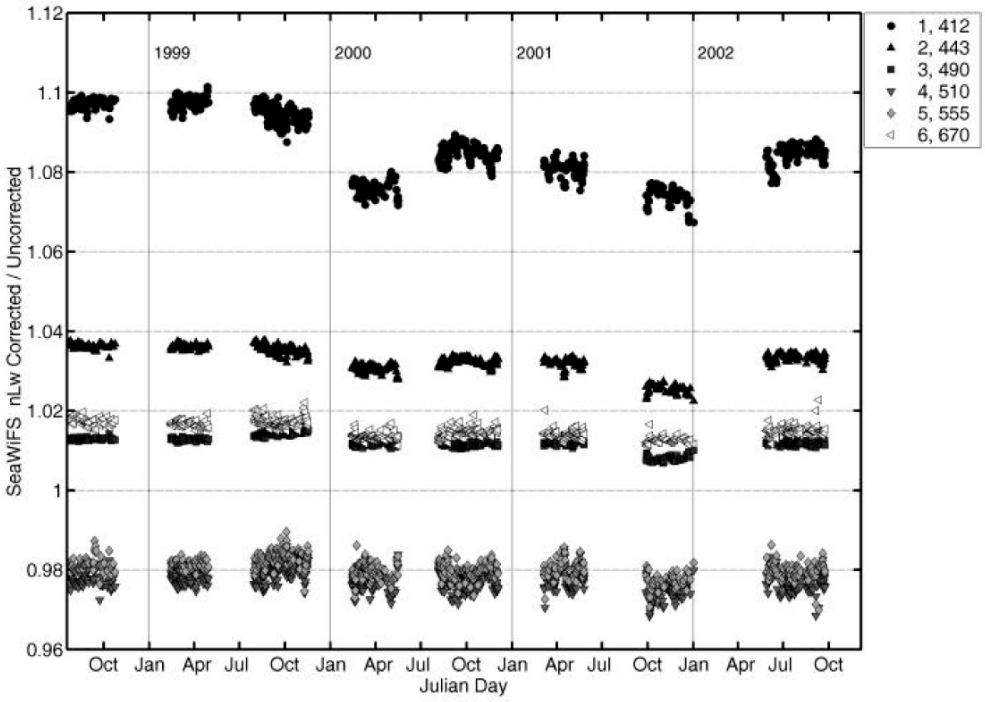

Figure 5.38: Band-averaged L_w stray-light-correction factors for SeaWiFS bands measured by even MOBY buoys from 1998 through 2002.

Implications for algorithm development

The derivation of remote-sensing-based ocean color data products such as chlorophyll *a* involve the integration of measurements by (1) the satellite sensor (*e.g*. SeaWiFS), (2) the vicarious calibration sensors (*e.g.* MOBY), and (3) the instruments used to develop the bio-optical algorithms relating the physical properties of the ocean (*e.g*. chlorophyll a concentration) to a radiometric measurement. Errors in measurements of any one of the three

components of the measurement chain will significantly impact the validity of the final data product. Instruments involved in ocean color measurements are typically calibrated against incandescent sources such as lamp-illuminated integrating spheres or reflectance plaques. These types of calibration sources have very different spectral distributions than the distribution of up-welling or water-leaving radiance and effects of stray light on the instrument response need to be considered for these instruments.

While considerable time and effort can be (and has been) expended to fully characterize and correct a satellite sensor or primary vicarious calibration station for stray light, it is much more difficult to extend the detailed characterization to the myriad instruments used by different groups to develop bio-optical algorithms. No general protocol has been developed to characterize and correct instrumentation used to develop bio-optical algorithms for stray light. However, effects of stray light are effectively canceled when the calibration source distribution approximates a measured ocean color spectrum. We have developed a radiometrically stable, spectrally tunable, solid-state calibration source for ocean color. This unique source approximates the spectral distributions of waters with varying chlorophyll concentrations, and may be used to calibrate, characterize, and to correct instruments' responsivities for stray light.

We have developed the prototype tunable solid-state source using Light Emitting Diodes (LEDs). (Brown *et al*. 2002). The source has 40 different, independently controlled LED channels comprised of 3 to 6 LEDs (depending on their output power) organized into 4 heads that mount onto 5 cm ports in the wall of an integrating sphere. The flux from each channel can be independently changed to model the spectral distribution of water-leaving radiance in different chlorophyll concentration waters. The output is monitored using a reference spectroradiometer integrated into the system. The source is under computer control and is designed to be automatically adjusted to match any desired input target spectrum, within the bandwidth limitations of the individual LEDs (~ 20 nm), to within approximately 5 % over the range from 390 nm to 550 nm.

The source has been tuned to match the water-leaving radiance from blue (oligotrophic), blue-green (mesotrophic), and green (eutrophic) waters, covering a wide range of chlorophyll concentrations. The target spectral distributions and the solid-state source output are shown in Figure 5.39. There is reasonable agreement over most of the spectral range. The sphere radiance is low below 390 nm. This is partially due to the low reflectance of the integrating sphere coating. With a new coating, we expect an order of magnitude increase in the radiance below 400 nm. The source is currently missing diodes at 360 nm, 435 nm, and 455 nm. The radiance around 550 nm is low due to weak diode emission; a problem that is easily addressed with the addition of extra 550 nm LEDs. The source stability and its applicability to the development of stray-light correction algorithms are currently under investigation.

We propose to correct instruments for stray-light errors in water-leaving radiance measurements using a variation on the basic approach developed for SeaWiFS by Wang, *et al*. (2001). Knowing the total spectral responsivity of the SeaWiFS bands, a stray light, or spectral out-of-band correction, is currently applied to each channel based on a semi-analytical water-leaving radiance model developed by Gordon for water with varying chlorophyll a concentrations (Gordon 1995; Wang *et al*. 2001). In this case, we don't know the total spectral responsivity of the instruments. Instead, we used the solid-state source to mimic the varying spectral water-leaving radiance spectral distributions and derive correction factors based on the ratio between the known radiance of the source (as measured by our reference spectroradiometer) and the radiance measured by the ocean color instruments.

5.8 SUMMARY

A simple iterative procedure was developed to correct MOBY measurements for stray light. Several fully operational MOBY systems were characterized *in situ* using a tunable laser-based, fiber-coupled integrating sphere source that was developed and installed at the MOBY field site at University of Hawaii Marine Center, Honolulu, Hawaii for this purpose. MOBY buoys with MOS204 and MOS205 detector systems were characterized and model slit-scatter functions developed. MOBY measurements of a Colored Source validated the stray-light-corrected measurements. In-water MOBY measurements of L_u and L_w were corrected for stray light, and the effect on SeaWiFS bands and derived chlorophyll-a concentrations were evaluated.

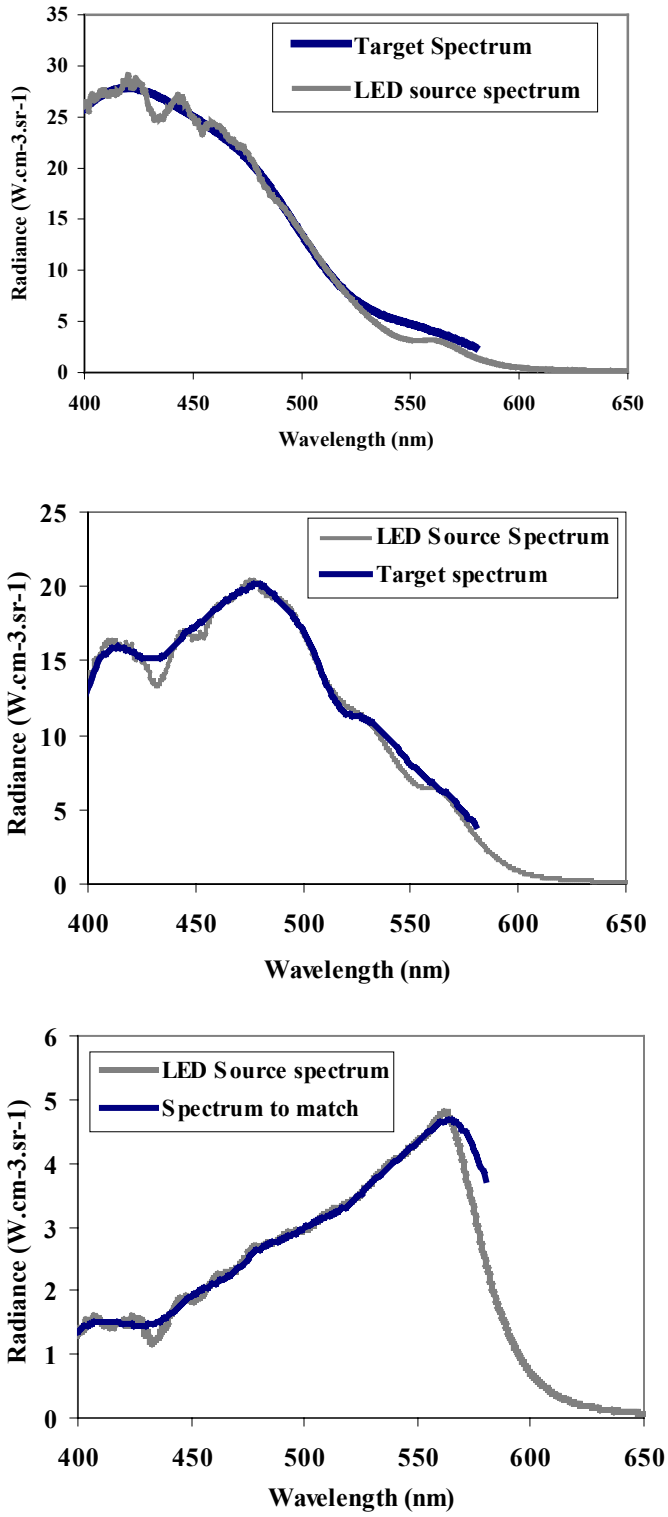

Figure 5.39: Target and LED source spectra for (a) blue, (b) blue-green and (c) green waters.

5.9 ACKNOWLEDGEMENTS

The authors gratefully acknowledge support for this work from the U.S. Air Force Metrology and NASA's SeaWiFS, SIMBIOS, MODIS and EOS Calibration/Validation program offices.

REFERENCES

Barnes, R. A., R. E. Eplee, Jr., W. D. Robinson, G. M. Schmidt, F. S. Patt, S. W. Bailey, M. Wang and C. R. McClain, 2000: The calibration of SeaWiFS on orbit, Proceedings of the SPIE, 4135, 281-293.

Brown, S. W., G. P. Eppeldauer and K. R. Lykke, 2000: NIST facility for spectral irradiance and radiance calibrations with uniform sources, Metrologia, 37, 579-582.

Brown, S. W. and Y. Ohno, 1999: NIST calibration facility for display colorimeters, Proc. SPIE, 3636, 162-169.

Brown, S. W., C. Santana and G. P. Eppeldauer, 2002: Development of a tunable LED-based colorimetric source, J. Res. Natl. Inst. Stand. Technol., 107, 363-371.

Butler, J. J., B. C. Johnson, S. W. Brown, H. W. Yoon, R. A. Barnes, B. L. Markham, S. F. Biggar, E. F. Zalewski, P. R. Spyak, J. W. Cooper and F. Sakuma, 1999: Radiometric measurement comparisons using transfer radiometers in support of the calibration of NASA's Earth Observing System (EOS) sensors. Sensors, Systems, and Next-Generation Satellites III. P. N. Slater. Bellingham, WA, Society of Photo-Optical Instrumentation Engineers. 3870: 180-192.

Clark, D. K., M. E. Feinholz, M. A. Yarbrough, B. C. Johnson, S. W. Brown, Y. S. Kim and R. A. Barnes, 2002a: Overview of the radiometric calibration of MOBY, Proceedings of the SPIE, 4483, 64-76.

Clark, D. K., H. R. Gordon, K. Voss, Y. Ge, W. Broenkow and C. Trees, 1997: Validation of atmospheric correction over the oceans, Journal of Geophysical Research, 102, 17209-17217.

Clark, D. K., M. A. Yarbrough, M. E. Feinholz, S. Flora, W. Broenkow, Y. S. Kim, B. C. Johnson, S. W. Brown, M. Yuen and J. L. Mueller, 2002b: MOBY, a radiometric buoy for performance monitoring and vicarious calibration of satellite ocean color sensors: Measurement and data analysis protocols. Ocean Optics Protocols for Satellite Ocean Color Sensor Validation, Rev. 3. J. L. M. a. G. S. Fargion. Greenbelt, MD, NASA/TM-2002-210004/Rev3-Vol2. 2.

Deschamps, P. Y., F. M. Breon, M. Leroy, A. Podaire, A. Bricaud, J. C. Buriez and G. Seze, 1994: The POLDER mission: instrument characteristics and scientific objectives, IEEE Trans. Geosci. Remote Sens, 32, 598-615.

Eppeldauer, G. P. and D. C. Lynch, 2000: Opto-mechanical and electronic design of a tunnel-trap Si- radiometer, J. Res. NIST, 105(6), 813-828.

Esaias, W. E., M. R. Abbott, I. Barton, O. B. Brown, J. W. Campbell, K. L. Carder, D. K. Clark, R. H. Evans, F. E. Hoge, H. R. Gordon, W. M. Balch, R. Letelier and P. J. Minnett, 1998: An overview of MODIS capabilities for ocean science observations, IEEE Trans. Geosci. Remote Sens, 36, 1250-1265.

Gordon, H. R., 1995: Remote sensing of ocean color: a methodology for dealing with broad spectral bands and significant out-of-band response, Appl. Optics, 34, 8363-8374.

Gordon, H. R., 1998: In-orbit calibration strategy for ocean color sensors, Remote Sens. Environ., 63, 265-278.

Habauzit, C., S. W. Brown, K. R. Lykke, B. C. Johnson, M. E. Feinholz, M. A. Yarbrough and D. K. Clark, 2003: Radiometric characterization and absolute calibration of the Marine Optical System (MOS) bench unit, Journal of Atmospheric and Oceanic Technology, 20(3), 383-391.

Hooker, S. B., C. R. McClain and A. W. Holmes, 1993: Ocean color imaging: CZCS to SeaWiFS, Marine Tech. Soc. Journal, 27, 3-15.

Isaacman, A., B. Franz and R. E. J. Eplee, 1999: An investigation of time variability in water-leaving radiances retrieved from ocean color measurements. ALPS99 Conference, Meribel, France.

Kostkowski, H. J., 1979: The relative spectral responsivity and slit-scatter function of a spectroradiometer. Self Study Manual on Optical Radiation Measurements, NBS Tech. Note 910-4. F. E. Nicodemus. Washington, DC, U.S. Department of Commerce: 1-34.

Mueller, J. (2002). personal communication.

O'Reilly, J. E., S. Maritorena, B. G. Mitchell, D. A. Siegel, K. L. Carder, S. A. Garver, M. Kahru and C. McClain, 1998: Ocean color chloropohyll algorithms for SeaWiFS, Journal of Geophysical Research, 103, 24937-24953.

SeaWiFS (2002). http://seawifs.gsfc.nasa.gov/SEAWIFS/RECAL/Repro4/.

Shumaker, J. B., 1979: Deconvolution. Self Study Manualon Optical Radiation Measurements, NBS Tech. Note 910-4. F. E. Nicodemus. Washington, DC, U.S. Department of Commerce: 35-90.

Walker, J. H., R. D. Saunders and A. T. Hattenburg, 1987: Spectral Radiance Calibrations, NBS Special Publication 250-1. Washington, DC, U.S. Government Printing Office.

Wang, M., A. A. Isaacman, B. A. Franz and C. R. McClain, 2002: Ocean-color optical property data derived from the Japanese Ocean Color and Temperature Scanner and the French Polarization and Directionality of the Earth's Reflectances: a comparison study, Appl. Optics, 41, 974-990.

Wang, M., B. A. Franz, R. A. Barnes and C. R. McClain, 2001: Effects of spectral bandpass on SeaWiFS-retrieved near-surface optical properties of the ocean, Appl. Optics, 40, 343-348.

Appendix A

Characteristics of Satellite Ocean Color Sensors: Past, Present and Future

Giulietta S. Fargion

Science Applications International Corporation, Beltsville, Maryland.

This appendix summarizes the essential operational characteristics of ocean color sensors of the past, present and future. Table A.1 lists general characteristics of past and presently operating ocean color sensors, including for each the satellite platform, country and agency, operational time period (actual or planned), orbit characteristics, spatial resolution at nadir, swath width, and tilt capabilities. Table A.2 lists the same information for ocean color sensors currently planned for launch and operation in the future. Table A.3 lists the center wavelength, spectral bandwidth (FWHM) and noise equivalent radiance resolution (NEΔL) for the ocean color bands of each of the sensors listed in Tables A.1 and A.2. Many of these sensors have additional bands, not listed here, addressing data requirements in terrestrial or atmospheric sciences. The information in these tables was updated from that published in IOCCG (1998). The sensor band data in Table A.3 should be used to expand Table 4.1 when specifying *in situ* instrument characteristics needed to support algorithm development and validation related to any of the other sensors, in addition to SeaWiFS, which fall within the SIMBIOS purview.

REFERENCES

IOCCG 1998: Minimum Requirements for an Operational, Ocean Colour Sensor for the Open Ocean. *Reports of the International Ocean-Colour Coordinating Group, No. 1.* IOCCG, Dartmouth, Canada, 46pp.

Table A1. Characteristics of past and present ocean-color sensors.

Sensor	**CZCS**	**OCTS**	**POLDER**	**MOS**	**SeaWiFS**	**OCM**
Platform	Nimbus-7	ADEOS-1	ADEOS-1	IRS-P3	OrbView-2	IRS-P4
Agency	NASA	NASDA	CNES	DLR	OSC/NASA	ISRO
Country	USA	Japan	France	Germany/India	USA	India
Operation Start	Oct. 1978	Aug. 1996	Aug. 1996	Mar. 1996	Sep. 1997	Nov. 98
Operation End	Jun. 1986	Jun. 1997	Jun. 1997			
Orbital Inclination	99.3	98.6	98.6	98.7	98.2	98.3
Equatorial Crossing Time (h)	12:00	10:41	10:41	10:30	12:00	12:00
Altitude (km)	955	804.6	804.6	817	705	720
Resolution at Nadir (km)	0.825	0.7	6 x 7	0.5	1.1	0.36
Swath (km)	1566	1400	2400	200	2800	1420
Tilt (degrees)	±20	±20	Variable	No	±20	±20
Direct Link	No	UHF/X-band	X-band	S-band	L-band	X-band
Recorded	Yes	X-band	X-band	None	S-band	Yes
Solar Calibration	No	Yes	No	Yes	Yes	Yes
Lunar Calibration	No	No	No	No	Yes	No
Lamp Calibration	Yes	Yes	No	Yes	No	Yes

Table A1 (continued). Characteristics of past and present ocean-color sensors.

Sensor	**OCI**	**OSMI**	**MODIS-TERRA**	**MISR**	**MERIS**	**MODIS-AQUA**
Platform	ROCSAT	KOMPSAT	EOS-AM1	EOS-AM1	Envisat	EOS–PM1
Agency	Taiwan	KARI	NASA	NASA	ESA	NASA
Country	Taiwan	Korea	USA	USA	Europe	USA
Operation Start	Feb. 1999	Jul. 1999	Dec. 1999	Dec. 1999	March 2002	June 2002
Operation End						
Orbital Inclination	35	98.13	98.2	98.2	98.5	98.2
Equatorial Crossing Time (h)	09:00/15:00	10:50	10:30	10:30	10:00	13:30
Altitude (km)	600	685	705	705	800	705
Resolution at Nadir (km)	0.8	0.85	1	0.25	1.2/0.3	1
Swath (km)	704	800	2330	360	1150	2330
Tilt (degrees)	No	No	No	Variable	No	No
Direct Link	S-band	X-band	X-band	No	X-band	X-band
Recorded	None	Yes	X-band	X-band	X-band	X-band
Solar Calibration	—	Yes	Yes	No	Yes	Yes
Lunar Calibration	—	No	Yes	Yes	No	Yes
Lamp Calibration	—	No	Yes	No	No	Yes

Table A2. Characteristics of future ocean-color sensors.

	GLI	POLDER-2	VIIRS
Platform	ADEOS2	ADEOS–2	NPP
Agency	NASDA	CNES	DoD/NOAA/NASA
Country	Japan	France	USA
Operation Start	Nov. 2002	Nov. 2002	2007
Orbital Inclination	98.6	98.6	98.6
Equatorial Crossing Time (h)	10:30	10:30	10:30
Altitude (km)	803	803	824
Resolution at Nadir (km)	1/0.25	6 x 7	0.74
Swath (km)	1600	2400	3000
Tilt (degrees)	±20	Variable	No
Direct Link	UHF/X-band	X-band	X-band
Recorded	X-band	X-band	TDRSS
Solar Calibration	Yes	No	Yes
Lunar Calibration	No	No	No
Lamp Calibration	Yes	No	No

Table A3. Summary of the spectral bands used for ocean-color applications. Center λ (nm), Bandpass (FWHM, nm), NEΔL (W m^{-2} sr^{-1} μm^{-1}).

CZCS			**OCTS**			**POLDER**			**MOS**			**SeaWiFS**		
Center λ	FWHM	NEΔL	Center λ	FWHM	NEΔL	Center λ	FWHM	NEΔL	Center λ	FWHM	NEΔL	Center λ	FWHM	NEΔL
443	20	0.208	412	20	0.186	443	20	0.138	408	10	0.192	412	20	0.092
520	20	0.173	443	20	0.109	490	20	0.147	443	10	0.124	443	20	0.077
550	20	0.166	490	20	0.089	565	20	0.088	485	10	0.148	490	20	0.056
670	20	0.094	520	20	0.121	670	20	0.063	520	10	0.141	510	20	0.049
750	100	0.040	565	20	0.091	763	10	0.090	570	10	0.150	555	20	0.043
			670	20	0.037	765	40	0.086	615	10	0.105	670	20	0.031
			765	40	0.057	865	40	0.034	650	10	0.141	765	40	0.019
			865	40	0.031	910	20	0.045	685	10	0.088	865	40	0.015
									750	10	0.102			
									815	10	0.034			
									870	10	0.033			
MISR			**MODIS**			**MERIS**			**OCI**			**OSMI**		
Center λ	FWHM	NEΔL	Center λ	FWHM	NEΔL	Center λ	FWHM	NEΔL	Center λ	FWHM	NEΔL	Center λ	FWHM	NEΔL
446	41	0.063	412	15	0.048	412.5	10	0.026	443	20	–	443	20	–
557	27	0.061	443	10	0.032	442.5	10	0.025	490	20	–	490	20	–
672	20	0.050	488	10	0.025	490	10	0.022	510	20	–	510	20	–
867	39	0.031	531	10	0.018	510	10	0.019	555	20	–	555	20	–
			551	10	0.019	560	10	0.016	670	20	–	670	20	–
			667	10	0.008	620	10	0.014	865	40	–	865	40	–
			678	10	0.007	665	10	0.013						
			748	10	0.009	681	7.5	0.014						
			870	15	0.006	709	9	0.011						
			469 *	20	0.145	779	14	0.008						
			555 *	20	0.127	870	20	0.007						
			645 **	50	0.170	890	10	0.011						
			858 **	35	0.123	900	10	0.010						
GLI			**OCM**			**POLDER-2**			**S–GLI**			**VIIRS**		
Center λ	FWHM	NEΔL	Center λ	FWHM	NEΔL	Center λ	FWHM	NEΔL	Center λ	FWHM	NEΔL	Center λ	FWHM	NEΔL
380	10	0.076	412	20	0.26	443	20	0.138	412	10	0.081	412	20	TBD
400	10	0.051	443	20	0.22	490	20	0.147	443	10	0.067	444	18	TBD
412	10	0.045	490	20	0.17	565	20	0.088	490	10	0.054	488	20	TBD
443	10	0.054	510	20	0.17	670	20	0.063	520	20	0.052	555	20	TBD
460	10	0.055	555	20	0.15	763	10	0.090	565	20	0.029	677	20	TBD
490	10	0.027	670	20	0.10	765	40	0.086	625	20	0.021	746	15	TBD
520	10	0.044	765	40	0.05	865	40	0.034	680	20	0.012	865	39	TBD
545	10	0.044	865	40	0.08	910	20	0.045	710	20	0.007	----------		
565	10	0.018							749	20	0.009			
625	10	0.017							865	20	0.006			
666	10	0.015										* Spatial resolution 0.5 km		
680	10	0.014										**Spatial resolution 0.25 km		
710	10	0.012										(others: 1 km)		
749	10	0.010												
865	20	0.007												

Appendix B

List of Acronyms

James L. Mueller

Center for Hydro-Optics and Remote Sensing, San Diego State University, California

AC9	A commercial device for measurements *in situ* of $a(\lambda)$ and $c(\lambda)$ at 9 wavelengths.
A/D	Analog-to-Digital
ADEOS	Advanced Earth Observing Satellite (Japanese)
AERONET	Aerosol Robotic Network (see Vol. II Chapter 4 and Vol. III, Chapter 5).
ALSCAT	ALPHA and Scattering Meter (Note: In older conventions, "ALPHA" corresponds to c(λ), the beam attenuation coefficient, in present usage.)
AMT	Atlantic Meridonial Transect, a research cruise series AMT-1, AMT-2, etc..
AOL	Airborne Oceanographic Lidar
AOP	Apparent Optical Properties (Section 2.4; Vol. I, Ch. 2)
AOT	Aerosol Optical Thickness
ARGOS	Not an acronym: the name given to the data collection and location system on NOAA Operational Satellites
ASCII	American Standard Code for Information Interchange
AVHRR	Advanced Very High Resolution Radiometer
AVIRIS	Advanced Visible and Infrared Imaging Spectrometer
BRDF	Bi-directional Reflectance Distribution Function
BSI	BioSpherical Instruments, Inc.
BNL	Brookhaven National Laboratory
CCD	Charge-Coupled Device
CDOM	Colored Dissolved Organic Material
CERT	Calibration Evaluation and Radiometric Testing
CHN	Carbon, Hydrogen, and Nitrogen
CIMEL	Name of a commercial sun photometer equipped with an automated sun tracking mechanism
CTD	Conductivity, Temperature, and Depth
CW	Continuous Wave
CZCS	Coastal Zone Color Scanner
DAS	Data Acquisition Sequence
DIW	Distilled Water
DOC	Dissolved Organic Carbon
DOM	Dissolved Organic Matter
DUT	Device Under Test
DVM	Digital Voltmeter
ECO-VSF	A commercial device for *in situ* determinations of $b_b(\lambda)$.
EOS	Earth Observing System
ER-2	Earth Resources-2, a research aircraft
ESA	European Space Agency
FEL	Not an acronym; a commercial bulb type designator of a lamp used, after suitable modification of its terminals, as a transfer standard of spectral irradiance
FOS	Fiber Optic Spectrometer

FOV	Field-of-View
FRSR	Fast Rotating Shadow-Band Radiometer
FSW	Filtered SeaWater
FWHM	Full-Width at Half-Maximum
GAC	Global Area Coverage
GASM	General Angle Scattering Meter
GF/F	Not an acronym; a specific type of glass fiber filter manufactured by Whatman
GLI	Global Line Imager, a future satellite ocean color sensor (Vol. VII, Appendix A)
GMT	Greenwich Mean Time
GOES	Geostationary Operational Environmental Satellite
GPIB	General Purpose Interface Bus
GPS	Global Positioning System
GSFC	Goddard Space Flight Center
HOBILABS	Hydro-Optics, Biology and Instrumentation Laboratories, Inc.
HPCE	High Performance Capillary Electrophoresis, in the present context, a proposed method for determining concentrations of phycobiliproteins.
HPLC	High Performance Liquid Chromatography, in the present context, a chemical method used to separate and measure concentrations of phytoplankton pigments in samples filtered from seawater
HydroScat	Not an acronym. Name of a commercial device for *in situ* determinations of $b_b(\lambda)$.
IAPSO	International Association for the Physical Sciences of the Ocean
ICES	International Council on Exploration of the Seas
IFOV	Instantaneous field-of-view
IOCCG	International Ocean Color Coordinating Group
IOP	Inherent Optical Properties (Section 2.4; Vol. I, Ch. 2)
IR	Infrared
ISS	Integrating Sphere Source
JGOFS	Joint Global Ocean Flux Study
LED	Light Emitting Diode.
LOA	Laboratoire d'Optique Atmosphérique
MDL	Method detection limit.
MER	Marine Environmental Radiometer
MERIS	Marine Environment Research Imaging Spectroradiometer (European Space Agency)
MICROTOPS	Name of a commercially available hand-held sun photometer
MISR	Multi-angle Imaging SpectroRadiometer
MLML	Moss Landing Marine Laboratories
MLO	Mauna Loa Observatory
MOBY	Marine Optical Buoy (Vol. VI, Chapter 2)
MOCE	Marine Optical Characterization Experiment
MODIS	Moderate Resolution Imaging Spectroradiometer
MOS	1. Modular Optoelectronic Scanner (German). 2. Marine Optical System, in the MOBY context (Vol. VI, Chapter 2 and elsewhere).
MS112	Not an acronym; name of a computer program used for SeaWiFS data processing
NAS	National Academy of Science
NASA	National Aeronautics and Space Administration
NASIC	NASA Aircraft/Satellite Instrument Calibration
NESDIS	National Environmental Satellite Data Information Service

NIMBUS	Not an acronym; name given to a series of NASA weather satellites
NIR	Near-Infrared.
NIST	National Institute of Standards and Technology
NOAA	National Oceanic and Atmospheric Administration
NOARL	Naval Oceanographic and Atmospheric Research Laboratory
NPP	National Polar Orbiting Operational Environmental Satellite System Preparatory Project.
NPR	NIST Portable Radiance source.
NRSR	Normalized Remote Sensing Reflectance
OCI	Ocean Color Imager
OCTS	Ocean Color and Temperature Sensor (Japanese)
OCS-5002	Optical Calibration Source (a commercial variant of SQM).
OFFI	Optical Free-Fall Instrument
OL4xx	Series of ISSs manufactured by Optronics Laboratories, Inc.
OMP-8	Not an acronym; a type of marine anti-biofouling compound
OSFI	Optical Surface Floating Instrument
OSMI	Ocean Scanning Multispectral Imager
PAR	Photosynthetically Available Radiation
PE	Phycoerythin
PEB	Phycoerythobilin chromophores
PUB	Phycourobilin chromophores
POC	Particulate Organic Carbon
POLBOX	A devices that transforms natural light to polarized light
POLDER	Polarization and Directionality of the Earth Reflectance (a French satellite radiometer)
PON	Particulate Organic Nitrogen
PREDE	Name of a commercial sun photometer equipped with an automated sun tracking mechanism
PSU	Practical Salinity Units
PTFE	Polytetrafluoroethylene, commonly known by the trade name Teflon
QA	Quality Assurance
QED	Quantum Efficient Detector
ROSIS	Remote Ocean Sensing Imaging Spectrometer, also known as the Reflecting Optics System Imaging Spectrometer (German)
ROV	Remotely Operated Vehicle
ROW	Reverse Osmosis Water
SCOR	Scientific Committee on Oceanographic Research
SeaBASS	SeaWiFS Bio-optical Archive and Storage System.
SeaWiFS	Sea-viewing Wide Field-of-view Sensor
SI	Standard International, as in “SI units”
SIMBAD	Name of a hand-held sun photometer and ocean surface radiance sensor (French)
SIMBIOS	Sensor Intercomparison for Marine Biology and Interdisciplinary Ocean Studies
SIMRIC	SIMBIOS Radiometric Intercalibration, a series SIMRIC-1, -2, of intercomparison experiments.
SIRCUS	Spectral Irradiance and Radiance responsivity Calibrations with Uniform Sources
SIRREX	SeaWiFS Intercalibration Round-Robin Experiment, a series SIRREX-1, -2, etc.
SLM	Standard Lamp Monitor
S/N	Serial Number
SNR	Signal-to-Noise Ratio
SPM	Total Suspended Particulate Material
SPO	SeaWiFS Project Office
SPSWG	SeaWiFS Prelaunch Science Working Group
SQM	SeaWiFS Quality Monitor
SST	Sea Surface Temperature
SXR	SeaWiFS Transfer Radiometer, a series of filter radiometers: SXR, SXR-II, etc.

TIROS	Television Infrared Observation Satellite
TOA	Top of the Atmosphere
TOMS	Total Ozone Mapping Spectrometer
TOVS	Total Ozone Vertical Sounder
T-S	Temperature-Salinity
UNESCO	United Nations Educational, Scientific, and Cultural Organizations
UK	United Kingdom, Great Britain
UPS	Un-interruptable Power Supply
UTC	Universal Time Coordinated
UV	Ultraviolet
UVB	Ultraviolet-B (a sub-range of UV wavelengths)
VIIRS	Visible and Infrared Imaging Radiometer Suite (to be flown on NPP)
VSF	Volume Scattering Function
VXR	Visible Transfer Radiometer, an instrument similar in concept to the SXR.
WETLABS	Western Environmental Technology Laboratory, Inc.
WMO	World Meteorological Organization
YES	Yankee Environmental Systems, Inc.

Appendix C

Frequently Used Symbols

James L. Mueller

Center for Hydro-Optics and Remote Sensing, San Diego State University, California

This appendix lists the definition of symbols that are used frequently throughout the ocean optics protocol document. Not included are the SI units (*e.g*. m, cm, nm, Km, mL, L, mg, μg, etc.), or specialized symbols that are defined locally for purposes of discussion in a particular segment of the text, and which do not appear elsewhere in the document. In the convention used throughout the protocols, variables are written in *italics*, with the exception of lower-case Greek symbols.

A or $A(\lambda)$	1. $A(\lambda)$ is spectral absorptance (Vol. I, Ch. 2, Sect. 2.4). 2. In HPLC chromatograms, A (with various super- and subscripts) is used to denote peak areas. 3. Altitude. 4. A general coefficient with varied usage as defined locally in the text
a	Area, but only when appearing without parentheses [*e.g*. as in Section 2.3 and Figure (2.3); Vol. I, Ch. 2].
$a(\lambda)$ or $a(z, \lambda)$	Spectral volume absorption coefficient (Vol. I, Ch. 2, Section 2.4) in m^{-1}. Frequently used subscripted variants are:

- $a_w(\lambda)$ spectral absorption coefficient of pure water
- $a_p(z, \lambda)$ spectral absorption coefficient due to suspended particles
- $a_g(z, \lambda)$ spectral absorption coefficient of substances dissolved in seawater, *e.g*. CDOM
- $a_g(z, \lambda)$ Non-pigmented particle absorption coefficient.
- $a_\phi(z, \lambda)$ Phytoplankton pigment spectral absorption coefficient.

$B(\lambda)$	Spectral scatterance, or $B(\lambda,\Psi,\phi)$ directional spectral scatterance (Vol. I, Ch. 2, Section 2.4)
$b(\lambda)$ or $b(z, \lambda)$	Spectral volume scattering coefficient in m^{-1} (Vol. I, Ch. 2, Section 2.4). Frequently used subscripted variants are:

- $b_w(\lambda)$ spectral volume scattering coefficient of pure water
- $b_r(\lambda)$ Raman volume scattering coefficient for pure water
- $b_p(z, \lambda)$ spectral volume scattering coefficient due to particles
- $b_b(z, \lambda)$ spectral volume backscattering coefficient
- $\tilde{b}_b(z,\lambda)$ normalized spectral volume backscattering coefficient

C^i_{Sample}	Individual pigment concentration (μg L^{-1}) (Vol V, Chapters 2 and 3)
C^i_{STD}	Concentration of a pigment standard(μg L^{-1}) (Vol V, Chapters 2 and 3)
Chl	Chlorophyll *a* concentration in mg m^{-3} or μg L^{-1}.
$c(\lambda)$ or $c(z, \lambda)$	Spectral beam attenuation coefficient [Vol. I, Ch. 2, equation (2.18)] in m^{-1}. Subscripted variants are the same as for $a(\lambda)$ and/or $b(\lambda)$.

$\hat{\mathbf{D}}$ Unit length vector indicating the direction of a detector, *i.e.* the reciprocal of the viewing direction for that detector, see *e.g.*, Figs. 2.1 and 2.2 of Vol. I, Ch. 2.

d 1. Earth-sun distance, where d_o indicates the annual average distance occurring on 3 January. 2. Distance of the lamp source from the collector surface in a radiometric calibration setup.

E Irradiance in μW cm^{-2} (Vol. I, Ch. 2, Sect. 2.3).

$E(\lambda)$ or $E(z, \lambda)$ Spectral irradiance in μW cm^{-2} nm^{-1} (Vol. I, Ch. 2, Sect. 2.3). Frequently used subscripted variants are:

- $E_d(z, \lambda)$ downward spectral irradiance
- $E_S(\lambda)$ Surface spectral irradiance, a synonym for $E_d(0^+, \lambda)$.
- $E_{sun}(z, \lambda)$ Direct solar spectral irradiance component of $E_S(\lambda)$
- $E_{sky}(z, \lambda)$ Diffuse sky spectral irradiance component of $E_S(\lambda)$
- $E_u(z, \lambda)$ downward spectral irradiance
- $\vec{E}(z,\lambda)$ vector spectral irradiance
- $\overset{o}{E}(z,\lambda)$ scalar spectral irradiance, also $\overset{o}{E}_d(z,\lambda)$ or $\overset{o}{E}_u(z,\lambda)$ (Vol. I, Ch. 2, Section 2.3)
- $E_N(\lambda, \theta_o)$ direct solar spectral irradiance, normal to the solar beam.

F 1. Used locally with subscripts to denote scale factors associated with various instrument response characteristics (especially in Vol. II, Ch. 3). 2. $F(z)$ is used to denote *in situ* chlorophyll a fluorescence. 3. Various factors in fluorometric determination of chlorophyll a concentration (Vol. V, Ch. 3).

$\overline{F}_o(\lambda)$ Extraterrestrial solar flux (above the atmosphere) when the earth-sun distance is at its annual mean.

$f(\lambda,...)$ A function relating IOP to irradiance reflectance $R(0^-, \lambda)$, and used together with the factor $Q(\lambda,\ldots)$ to remove the ocean's BRDF effects in determining $L_{WN}^{ex}(\lambda)$ (Vol. III, Ch. 4). The full functional dependence of the function is expressed $f\left[\lambda,(\theta_o,\tau_a,W),a(\lambda),\beta(\lambda,\Psi)\right]$. The symbol $f_o\left[\lambda,\tau_a,a(\lambda),\beta(\lambda,\Psi)\right]$ refers to the simplified case when the sun is at zenith.

$f'(\lambda,\cdots)$ Alternative form of $f(\lambda,\cdots)$, $f'(\lambda,\cdots) = f(\lambda,\cdots)\left[1-\frac{b_b(\lambda)}{a(\lambda)}\right]$ (Vol. III, Ch. 4).

$K(z, \lambda)$ Generic diffuse attenuation coefficient in m^{-1}. Frequently used variants are:

- $K_d(z, \lambda)$ Diffuse attenuation coefficient for $E_d(z, \lambda)$
- $K_u(z, \lambda)$ Diffuse attenuation coefficient for $E_u(z, \lambda)$
- $K_L(z, \lambda)$ Diffuse attenuation coefficient for $L_u(z, \lambda)$
- $K(\lambda)$ Remote sensing diffuse attenuation coefficient, $K_d(z, \lambda)$ for $E_d(z, \lambda)$ averaged over the first diffuse attenuation depth.

$L(\theta, \phi)$ Radiance in $\mu W\ cm^{-2}\ sr^{-1}$ (Vol. I, Ch. 2, Sect. 2.3).

$L(\lambda,\theta,\phi)$ or $L(z,\lambda,\theta,\phi)$ Spectral radiance in $\mu W\ cm^{-2}\ sr^{-1}\ nm^{-1}$ (Vol. I, Ch. 2, Sect. 2.3). When expressed without indicating angular dependence, *e.g.* as $L(\lambda)$, reference is made to nadir-viewing geometry. Frequently used subscripted variants are:

- $L_d(z,\lambda,\theta,\phi)$ downward spectral radiance
- $L_d^t(0^-,\lambda,\theta',\phi)$ downward spectral radiance transmitted across the air-sea interface
- $L_u(z,\lambda,\theta',\phi)$ upwelled spectral radiance
- $L_W(\lambda,\theta,\phi)$ Water-leaving radiance (at $z = 0^+$) transmitted upwards across the air-sea interface.
- $L_{WN}(\lambda)$ Normalized water-leaving radiance (at $z = 0^+$) (Gordon and Clark 1981; see Vol. III, Ch. 4).
- $L_{WN}^{ex}(\lambda)$ Exact normalized water-leaving radiance (at $z = 0^+$) (Morel and Gentili 1996; see Vol. III, Ch. 4).
- $L_{sfc}(\lambda,\theta,\phi,\theta_o,\phi_o)$ Spectral radiance leaving the surface at angles (θ,ϕ) for a given solar position (θ_o,ϕ_o).
- $L_{sky}(\lambda,\theta,\phi,\theta_o,\phi_o)$ Sky spectral radiance incident on the surface at (θ,ϕ) for a given solar position (θ_o,ϕ_o).
- $L_t(\lambda,\theta,\phi)$ Aperture radiance at TOA as measured by a satellite sensor.
- $L_{TOA}(\lambda,\theta,\phi)$ Same as $L_t(\lambda,\theta,\phi)$.

M or $M(\theta)$ Optical air mass.

$m(\lambda)$ Complex index of refraction $m(\lambda) = n(\lambda) + in'(\lambda)$ (Vol. I, Ch. 2, Sect. 2.5).

$n(\lambda)$ Real part of the complex refractive index, commonly referred to as simply the "refractive index" (Vol. I, Ch. 2, Sect. 2.5). A frequently used variant is $n_w(\lambda)$, the refractive index of water relative to that of air.

0_3 Ozone.

$OD(\lambda)$ Optical density, determined from transmission measurements in a spectrophotometer of a reference sample $V_o(\lambda)$ and a filter or dissolved sample $V(\lambda)$, calculated as $OD(\lambda) = \log_{10} V_o(\lambda) - \log_{10} V(\lambda)$. Used extensively in Vol. IV, Chapter 4 with subscripts denoting various types of samples and reference blank artifacts.

P Atmospheric pressure at the sea surface.

$P_a(\lambda, \Psi)$ Aerosol phase function, equivalent to $\tilde{\beta}(\lambda,\psi)$ (Vol. I, Ch. 2, Sect. 2.4).

$Q(\lambda,\theta',\phi;...)$ By definition, the ratio of upwelled spectral irradiance to upwelled spectral radiance just beneath the sea surface ($z = 0^-$). The full functional dependence of the quantity Q is expressed as $Q\left[(\lambda,\theta',\phi),(\theta_o,\tau_a,W),a(\lambda),\beta(\lambda,\Psi)\right]$ (Vol. III, Ch. 4), with simplified special cases:

- $Q_n\left[\lambda,\theta_o,a(\lambda),\beta(\lambda,\Psi)\right]$ For nadir viewing geometry
- $Q_o\left[\lambda,a(\lambda),\beta(\lambda,\Psi)\right]$ For nadir viewing geometry with the sun at zenith.

$R(z,\lambda)$ Irradiance reflectance, *i.e.* the ratio of $E_u(z, \lambda)$ to $E_d(z, \lambda)$ (Vol. I, Ch. 2, Section 2.7 and Vol. III, Ch. 4).

$R_{RS}(\lambda,\theta,\phi)$ Remote sensing reflectance, also sometimes denoted $R_{RS}(\lambda,\theta,\phi\in\Omega_{FOV};\theta_o)$ to indicate its dependence on a sensor's solid angle FOV and solar zenith angle (Vol. I, Ch. 2, Sect. 2.6 and Vol. III, Chapters 3 and 4). An important variant is exact normalized remote sensing reflectance $R_{RS}^{ex}(\lambda)$ as defined in equation (12.5) (Vol. III, Chapter 3).

R_s Peak resolution in HPLC protocols (Vol. V, Chapter 2).

r 1. Generic radial distance, or radius of circle or sphere. 2. Earth-sun distance. 3. Instrument radius in the context of instrument self shading.

$\hat{\mathbf{S}}$ Unit length vector defining the direction of a source, *e.g.* as in Figures 2.1 and 2.2 and related text in Vol I, Chapter 2.

S or $S(z)$ Salinity.

$\hat{\mathbf{T}}$ Unit length vector defining the direction of radiant flux transmittance from a source, $\hat{\mathbf{T}} = -\hat{\mathbf{S}}$, *e.g.* as in Figures 2.1 and 2.2 and related text in Vol. I, Chapter 2.

$T(\lambda)$ Spectral transmittance (Vol. I, Ch. 2, Section 2.4).

T or $T(z)$ Temperature

$t(z)$ Time at which an instrument is located at depth z during a profile.

$t(\lambda,\theta_o)$ Atmospheric transmittance of the direct solar beam.

V 1. Generically, Voltage in (V), *e.g.* for an instrument's response, as defined locally in the text. 2. In the context of sun photometry, $V(\lambda,\theta_o)$ is a photometer's response for airmass $M(\theta_o)$ and $V_o(\lambda)$ is the sensor's derived response for solar irradiance at TOA, *i.e.* for $M = 0$, as determined by the Langley-Bouguer method (Vol. II, Ch. 4). 3. Volume, in the context of absorption and pigment measurements from discrete water samples (Vol. IV, Chapter 4 and Vol. V, Chapters 2 and 3).

W Wind speed in m s^{-1}.

$(\hat{\mathbf{x}},\hat{\mathbf{y}},\hat{\mathbf{z}})$ Orthonormal basis vectors defining any local coordinate system, *e.g.*, as in Figures 2.1 and 2.2 and related text of Vol. I, Chapter 2.

z	Unless specified otherwise, the vertical coordinate in a local reference frame. Most often used to denote depth in m, but a more general usage is defined in several places in the text (see especially the generalized use of z in the coordinates of Fig. 2.2 and derivation of IOP in Section 2.4, Vol. I, Ch. 2). When z is used to indicate depth, $z = 0^+$ and $z=0^-$ refer to z=0 measured above and below the interface, respectively.
α	Angstrom coefficient (*e.g.* Vol. II, Ch. 4 and Vol. III, Ch. 5).
β	In the context of spectrophotometric measurements of absorption by particles concentrated on a glass-fiber filter [Vol. IV, Chapter 4, equations (4.6a) and (4.6b)], the correction factor for increased pathlength due to scattering within the filter. Also referred to as the "β-factor".
$\beta(\lambda,\psi)$	The spectral volume scattering coefficient (VSF), defined in Vol. I, Ch. 2, Sect. 2.4, is also denoted $\beta(z,\lambda,\psi)$ to indicate its variation with depth in the water column. Closely related quantities are $\tilde{\beta}(\lambda,\psi)$, the spectral volume scattering phase function, defined in Vol. I, Ch. 2 as the ratio of the VSF to the volume scattering coefficient [equation 2.22], and $\tilde{\beta}_w(\lambda,\psi)$, the molecular volume scattering phase function for sea water [equations (2.29) and (2.30)]. Other, more specialized forms of the VSF are defined locally as they occur in the text.
$\varepsilon(\lambda)$	Together with $\varepsilon_{sky}(\lambda)$ and $\varepsilon_{sun}(\lambda)$, model determinations of instrument self-shading errors in measurements of $L_u(0^-,\lambda)$ and $E_u(0^-,\lambda)$, as used in Vol. III, Ch.2, equations (2.16) through (2.30).
Φ	Radiant flux in, *e.g.*, μW (Vol. I, Ch. 2, Sect. 2.3).
ϕ	Generic symbol for azimuth angle, measured from the x-axis in the xy-plane (*e.g.* as in Figs. 2.1 and 2.2 of Vol. I, Ch. 2). When subscripted as ϕ_o, it denotes solar azimuth angle. A commonly used convention is to rotate the x-axis toward the sun, so that azimuth angles are measured relative to ϕ_o. Other, specialized uses of this symbol are defined locally as they occur in the text.
κ'_{xxx}	A family of subscripted coefficients used in instrument self-shading corrections to $L_u(0^-,\lambda)$ and $E_u(0^-,\lambda)$, via Vol. III, Chapter 2, equations (2.16) through (2.30).
λ	Wavelength, in nm unless specified otherwise.
χ,χ_p,χ_w	Model dependent scale factors used to relate VSF measurements at a single reference scattering angle Ψ^* to $b_b(\lambda)$.
Ψ	Scattering angle (Vol. I, Ch. 2, Section 2.2).

θ Generic symbol for zenith angle measured from the z-axis, as in Figures 2.1 and 2.2 of Vol. I, Ch. 2. Conventions for frequently used unprimed, primed, or subscripted, symbols are:

- θ zenith angle in air
- θ' zenith, or nadir, angle in water, related to θ by Snell's Law (Vol. I, Ch. 2, Sect. 2.5)
- θ_o solar zenith angle (in air), or sometimes that of any source.

$\rho(\lambda, \theta_o, \theta)$ BRDF of a diffuse reflecting surface, for radiant flux incident at zenith angle θ_o and reflected at angle θ, *e.g.*, as in Vol. II, Chapter 3, equation (3.6).

$\rho(\theta, \theta')$ and $\rho(\theta', \theta)$ Reflectances for radiances incident from above and below, respectively, on the wave roughened sea surface (Vol. I, Ch. 2, Sect. 2.5), where it is noted that $\rho(\theta, \theta') = \rho(\theta', \theta)$. Reflectance is sometimes written as, *e.g.*, $\rho(\theta, \theta', W)$ to explicitly indicate its dependence on wind speed. For a flat plane surface, these quantities converge to the Fresnel Reflectance $\rho_F(\theta, \theta')$ [Vol. I, Ch. 2 equations (2.35) and (2.36)].

$\Re(\theta', W)$ Term accounting for all effects of reflection and refraction at the sea surface [equation (4.17)] in determination of exact normalized water-leaving radiance (Vol. III, Ch. 4). The symbol $\Re_o$ denotes the simplified version of this term for nadir viewing geometry.

$\sigma_t(z)$ Specific density anomaly of seawater, a function of Temperature and Salinity.

τ In the context of fluorometric chlorophyll *a* analysis (Vol. V, Chapter 3), used - without functional notation - to quantify a fluorometer's sensitivity to phaeopigment fluorescence.

$\tau(\lambda)$ Total optical thickness of the atmosphere, with primary components:

- $\tau_a(\lambda)$ Aerosol optical thickness (AOT).
- $\tau_{O_3}(\lambda)$ Ozone optical thickness.
- $\tau_R(\lambda)$ Rayleigh optical thickness.
- $\tau_g(\lambda)$ Optical thickness of all absorbing gases (including Ozone).

Ω_{FOV} Solid angle FOV, in sr, of a particular sensor.

$\varpi(\lambda)$ or $\omega_o(\lambda)$ Single Scattering Albedo (Vol. I, Ch. 2, Sect. 2.4).